CRANFIELD UNIVERSITY

ALICE CHARLOTTE HILDA DANIELS

DESIGN, ANALYSIS AND FABRICATION OF A MOBILE ENERGY HARVESTING DEVICE TO SCAVENGE BIO-KINETIC ENERGY

SCHOOL OF APPLIED SCIENCES

PhD THESIS
Academic Year: 2009-2014

Supervisors: Prof. Meiling Zhu and Prof. Ashutosh Tiwari
May 2014

CRANFIELD UNIVERSITY

ALICE CHARLOTTE HILDA DANIELS

DESIGN, ANALYSIS AND FABRICATION OF A MOBILE ENERGY HARVESTING DEVICE TO SCAVENGE BIO-KINETIC ENERGY

SCHOOL OF APPLIED SCIENCES

PhD THESIS
Academic Year: 2009-2014

Supervisors: Prof. Meiling Zhu and Prof. Ashutosh Tiwari
May 2014

This thesis is submitted in partial fulfilment of the requirements for the PhD degree.
© Cranfield University 2014. All rights reserved. No part of this publication may be reproduced without the written permission of the copyright owner.

ABSTRACT

The increasing prevalence of low power consumption electronics brings greater potential to mobile energy harvesting devices as a possible power source. The main contribution of this thesis is the study of a new piezoelectric energy harvesting device, called the piezoelectric flex transducer (PFT), which is capable of working at non-resonant and low frequencies to harvest bio-kinetic energy of a human walking. The PFT consists of a piezoelectric element sandwiched between substrate layers and metal endcaps, the endcaps are specifically designed to amplify the axial force load on the piezoelectric element, instead of conventional designs of piezoelectric energy harvesters that focus on utilising resonant frequency in order to increase power harvested. This thesis presents the analyses, design, prototyping and characterisation of the PFT using a coupled piezoelectric-circuit finite element model (CPC-FEM) to show the energy harvesting capability of the proposed and developed novel device to harvest bio-kinetic energy. Prior to the study of the new PFT, an initial focus was given to a traditional Cymbal device to investigate its potential as a bio-kinetic energy harvesting device. To gain an understanding, effects of geometrical parameters and material properties of the device on its energy harvesting capability were studied and in doing so issues and problems were identified with the traditional Cymbal device for use as a bio-kinetic energy harvesting device. Its structural materials were not able to withstand higher than a 50N applied load and it was proposed that a small adhesion area connection in a fundamental part of the structure may have been at high risk of delamination. In order to study these, the CPC-FEM model was developed using the commercial software of ANSYS and validated by experimental methods. Later, based on a modelling and experimental study, a novel PFT was proposed and implemented to overcome the issues and problems of the traditional Cymbal device. For this initial study, the Cymbal was analysed by studying how key dimensional parameters affect the energy harvesting performance of the Cymbal. In addition to this, how piezoelectric material properties affect the energy harvesting performance were studied using the developed CPC-FEM model through comparisons of different piezoelectric materials and their electrical performances to aid with selecting high power producing materials for the final PFT design. It was found that (1) d_{31} is a more dominant material property over other

material properties for higher power output, (2) Figure of Merit (FOM) was more linear related to the power output than either the k_{31} or the d_{31}, and (3) ${\varepsilon^T}_{r33}$ had some role when the materials have an identical d_{31}; a lower ${\varepsilon^T}_{r33}$ was preferred. A combined FOM with d_{31} parameters is recommended for selection of piezoelectric material for a higher power outputs. The design of the new PFT is partly based on the traditional Cymbal however, the new PFT has more potential for withstanding higher forces due to an addition of substrate layers that reduced delamination risks. Using a similar approach to designing the traditional Cymbal, the new PFT was designed and tested with force frequencies of less than 5Hz and forces of up to 1kN. In the design process, the validated CPC-FEM was used 1) to analyse then utilise correlations between geometric parameters and power outputs, and 2) to ensure structural integrity by monitoring mechanical stress in the PFT. The PFT was retrofitted into a shoe and the harvested power was used to power an in-house developed wireless sensor module whilst the subject with a body weight of 760N was wearing the shoe and ran at 3.1mph (equivalent to 1.4Hz on the shoe), the PFT produced an average maximum power of 2.5mW over 2MΩ load and the power produced is able to power the wireless module approximately every 10 seconds.

ACKNOWLEDGMENTS

At its beginning this project was supplemented though technical guidance and support received from Dr Michele Pozzi at Cranfield University especially in terms of ANSYS guidance. Piezoelectric materials were kindly donation by Michael Riedel at Johnson Matthey, Plc and also PI Inc. Thanks to Pete Siriputtaiwon for the artistic interpretation images that were used in this report. Great thanks to my colleagues for sharing their time and expertise, Alessandro Giuliana, Vlad Marsic and Alfredo Canziani. Alessandro Giuliana and Vlad Marsic thank you. Thanks to Mrs Emily Pike-Wilson and Keith Withers at Brunel University in helping run my high frequency experiments of which the results did not make it into this report. The author also gives thanks to a small part of financial support from SmartWater: "Smart Sensor Network with energy harvesting for real time monitoring in urban water infrastructure" of FP7-People-2-12-IRSES project of EC318985. In the early stages financial support was given from IMRC-135 (Cranfield's Innovative Manufacturing Research Centre) via EPSRC (Engineering and Physics Science of Research Council in the UK). I would like to thank my mother Sarah Daniels who encouraged me to study engineering. I would like to thank my father Dr Paul Daniels, mother and Mark Kerr for their unreserved and generous financial support for my studies leading to this PhD. I would like to thank my sisters Prudence Daniels, Katy Brookes and Julia Broom for helping me keep perspective, all those phone calls that changed the bad or boring days into brilliant ones and being there for ups and downs; the break up with my boyfriend and when Dad kicked the bucket. Especially now I write-up this thesis, I am indebted to my boyfriend Dr Chamith Halahakoon and his earnest family who's diligence in life has given me the support I need for the final stretch of this PhD. Final thanks go to my supervisors Professor Meiling Zhu and Professor Ashutosh Tiwari, for the opportunity, the support and the belief.

LIST OF PRESS & PUBLICATIONS

Journals

[1] **A. Daniels**, M. Zhu and A. Tiwari, "*Evaluation of Piezoelectric Material Properties for a Higher Power Output from Energy Harvesters with Insight into Material Selection Using a Coupled Piezoelectric-Circuit Finite Element Method*", Transactions on Ultrasonics, Ferroelectrics, and Frequency Control, Vol. 60, No.12 (2013) 2626-2633.

International conferences

[2] **A. Daniels**, A. Giuliano, M. Zhu and A. Tiwari, "*Modeling, validation and design analyses of a piezoelectric Cymbal transducer (PCT) for non-resonant energy harvesting*", IEEE International Conference on Internet of Things, Beijing, China, August 20-23rd (2013) 1665-1667.

[3] **A. Daniels**, M. Zhu and A. Tiwari, "*Design, analysis and testing of a piezoelectric flex transducer for harvesting bio-kinetic energy*", Journal of Physics, PowerMEMS conference, London, UK, Vol. 476, No. 1, December 03-06th (2013) 012047.

Press

[4] A Bullock. Can electricity from the human body replace batteries? British Broadcasting Corporation BBC, online article, Costing The Earth. (Sept, 2012). URL: http://www.bbc.co.uk/news/science-environment-19470850 [last accessed Oct 2013].

TABLE OF CONTENTS

ABSTRACT 3
ACKNOWLEDGMENTS 5
LIST OF PRESS & PUBLICATIONS & PRESS 6
LIST OF FIGURES 9
LIST OF TABLES 16
NOMENCLATURE 17
1 CHAPTER 1 Introduction 22
1.1 Introduction 22
1.2 Energy Harvesting 27
1.3 Aim 30
1.4 Objectives 30
1.5 Thesis Structure 31
2 CHAPTER 2 Literature Review 34
2.1 Energy Harvesting 35
2.2 Bio-kinetic Energy 37
2.3 Bio-kinetic Energy Harvesting Devices 42
2.4 Harvesting from Foot Fall 46
2.5 Transduction Techniques for Bio-kinetic Energy 54
2.5.1 Electromagnetic vs. piezoelectric 55
2.5.2 Piezoelectric materials and shoe-based bio-kinetic energy harvesting 55
2.6 The Cymbal Device 56
2.6.1 Origin of the Cymbal and it's use as actuators 56
2.6.2 Cymbal-like devices 59
2.6.3 Cymbals used as EHDs 61
2.6.4 Cymbal function 63
2.7 Review on Cymbal Device Modelling and Simulation 66
2.8 Introduction to Piezoelectric Material Selection 72
2.9 Contributions & Novelty 76
2.10 Methodology 80
3 CHAPTER 3 Modelling, Validation & Analysis of The Cymbal Device 82
3.1 CPC-FE Model for the Cymbal Device Energy Harvesting Analyses 84
3.2 Model Validation 88
3.2.1 Cymbal fabrication 88
3.2.2 Experimental set-up 89
3.2.3 Results & discussions 90
3.2.4 Summary 93
3.3 Cymbal Structural Parameter Design Analyses on Energy Harvesting Performance using the CPC-FE model 94
3.3.1 Effects of the connected resistive load 94
3.3.2 Effects of experimental impedance 96
3.3.3 Effects of angle of the endcap 97
3.3.4 Effects of join length of endcap 101
3.3.5 Effects of PZT disk thickness and diameter 102
3.3.6 Effects of multi-layering of PZT disk 104

3.4 Summary 106
4 CHAPTER 4 Material Selection for Enhancement of Power output 108
4.1 Introduction 108
4.2 Piezoelectric Material Analyses and Selection using the CPC-FE model 108
4.2.1 Model configuration 108
4.2.2 Approach to the study 109
4.2.3 Results & discussions 113
4.2.4 Summary 125
4.3 Endcap Material Analyses and Selection using CPC-FE model 126
4.3.1 Introduction 126
4.3.2 Results & discussions 126
4.3.3 Summary 132
5 CHAPTER 5 Developed Novel Piezoelectric Flex Transducer (PFT) 133
5.1 Design of PFT using the CPC-FE model 135
5.1.1 Approaches to the study 135
5.1.2 Model configuration 138
5.1.3 Simulation results and PFT design analyses 140
5.1.4 Summary 152
5.2 Fabrication of the PFT 154
5.3 Testing the PFT 159
5.3.1 Set-up 159
5.3.2 Results & discussions 161
5.4 Demonstration of PFT in an Application 173
5.4.1 Demonstration set-up 175
5.4.2 Results & discussions 180
5.5 Summary 185
6 CHAPTER 6 Discussion and Conclusions 186
6.1 Discussions 186
6.2 Conclusions 198
6.3 Challenges 200
6.4 Further Work 200
REFERENCES 203
APPENDICES 212

LIST OF FIGURES

Figure 1.1 Cymbal device for harvesting machine waste vibrations developed by Kim et al Left: piezoelectric disk sandwiched between top and bottom metallic endcaps, right: a photo of fabricated Cymbal device. 25

Figure 1.2 Schematic of the PFT when a downward compressive force is applied. 26

Figure 1.3 Benefits of Mobile Energy Harvesting Technology for Wireless Sensing. 27

Figure 1.4 From left to right, Lance Corporal Mathew Sampson and Lance Corporal Jody Samways wearing their Personal Role Radios, Helmand Province, Afghanistan, Operation Herrick XV. Photo courtesy of LCP Mathew Sampson (taken by Private Rob Appell).....28

Figure 2.1 Photo of piezoelectric cantilever based harvester, 1) harvester with its proof mass 2) aluminium holder 3) accelerometer for testing 4) mount for shaker testing.....36

Figure 2.2 Types of energy produced by the human body. 38

Figure 2.3 Prosthetic foot that uses a spring to recover energy and aid in walking 38

Figure 2.4 Mass imbalance oscillation generator on sheep's heart 40

Figure 2.5 (a) Magnetometer taking measurement near elbow in shielded room (b) Magnetomyogram spectra.....40

Figure 2.6 RF measurement area over Lookout Mountain, USA.....41

Figure 2.7 Solar vest.....41

Figure 2.8 Using cockroach as a biofuel-cell 41

Figure 2.9 Electrical power generated by potential wearable piezoelectric, electromagnetic and electrostatic EHDs in terms of year of publication.....42

Figure 2.10 Mechanical power generation and absorption profiles at the ankle for 47

Figure 2.11 (a) acceleration measured perpendicular to the ground of the heel of the foot during gait with integrated velocity, speed of gait was 10 kmph, (b) acceleration perpendicular to the ground of the heel of the foot during gait, speed of gait was 6 kmph and (c) voltage output from shoe-integrated screen-printed piezoelectric shoe insole EHD, at a gait of 1strike/second, open circuit voltage contribution from only the piezoelectric elements at the sole of the foot. 48

Figure 2.12 Electrical power generated by bio-kinetic EHDs embedded into a shoe in terms of year of publication. 49

Figure 2.13 The Moonie transducer 57

Figure 2.14 Cymbal as a pump. Inset; Cymbal 57

Figure 2.15 An array of Cymbal's is driven at ultrasonic frequencies to excite the a drug to be delived through the skin of the patient. The drug then travels through the skin of the patient....58
Figure 2.16 Slotted Cymbal....58
Figure 2.17 Drawing of a Piezoelectric metal cavity (PMC) actuator....59
Figure 2.18 Photograph of Cymbal-type DAM....60
Figure 2.19 Schematic of rectangular Cymbal transducer....60
Figure 2.20 Rectangular Cymbal array for transdermal insulin delivery....61
Figure 2.21 Cymbal device with a) Cymbal before assembly, b) assembled Cymbal, and c) cross-section of Cymbal in μm....62
Figure 2.22 Schematic of the Cymbal structure....63
Figure 2.23 Axis orientation used in this system and more commonly used axis orientation....64
Figure 2.24 Example of d constant definitions in relation to the more commonly used axis orientation....64
Figure 2.25 Left: Illustration of uni-morph, Right: Illustration of Single degree of freedom model....68
Figure 2.26 Equivalent circuit for a single degree of freedom electromechanical system....69
Figure 3.1 (a) Schematic of the Cymbal, (b) 2D Force analysis of the Cymbal....83
Figure 3.2 (a) Section of Cymbal in the developed CPC-FEM showing boundary conditions, and (b) Developed CPC-FEM; results of static simulation showing Von Mises Stress force Cymbal under 50N load. Top middle: axis coordinates used in CPC-FEM....85
Figure 3.3 Cross-section of Cymbal....88
Figure 3.4 The experimental setup using the loading machine to test the Cymbal with a photo of the fabricated Cymbal inset....89
Figure 3.5 Experimental set-up for testing of the Cymbal, where the Cymbal is placed in the loading machine and a 50N compressive force with 2 and 5Hz is applied the Cymbal....89
Figure 3.6 Comparisons between the experimental and simulated results of the power, voltage and current verses the electrical resistive load for a Cymbal excited at 2Hz and 5Hz under a 50N compressive force load. PCT refers to Piezoelectric Cymbal Transducer....92
Figure 3.7 Simulated results of the electric responses of powers, voltages and currents over a range of electrical resistive loads for two different frequency ranges of 1-10Hz and 50-150Hz....95
Figure 3.8 Simulation results of electrical responses of power, voltage and current verses internal angle of the endcaps, where the force magnitude, the

force frequency and the electrical resistance were 50N, 2Hz and 8MΩ, respectively. 98

Figure 3.9 Simulation results of electrical responses of power, voltage and current verses join length between the PZT disk and the endcap, where the force magnitude, the force frequency and the electrical resistance are 50N, 2Hz and 8MΩ....101

Figure 3.10 Simulation results of electrical responses of power, voltage and current verses PZT thickness of Cymbal and Cymbal 2, where each data point represents the electrical output over an optimal resistance for the given dimensions. The force magnitude and the force frequency were 50N and 2Hz respectively. 103

Figure 3.11 Simulation results of electrical responses of power, voltage and current for multi-layers of the PZT disk of the Cymbal, where each layer is connected in parallel, and the force magnitude, the force frequency and the total PZT thickness were kept fixed at 50N, 2Hz and 1mm, respectively. 104

Figure 3.12 Equivalent electrical circuit of piezoelectric structure....105

Figure 3.13 Studied parameters effecting Cymbal energy harvesting performance. 106

Figure 4.1 CPC-FEM model used in the study....109

Figure 4.2 Electrical power output vs. elastic compliance of piezoelectric materials: (a) for all the materials listed in Table 4.1 and (b) for soft PZT and hard PZT materials only....114

Figure 4.3 Electrical power output vs. different piezoelectric constants: (a) for piezoelectric strain constants d_{31}, (b) for piezoelectric voltage constants g_{31} for all the materials listed in Table 4.1, and (c) for g_{31} of soft PZT and hard PZT materials only. 116

Figure 4.4 Electrical power output vs. relative dielectric constant for all the materials listed in Table 4.1 whilst connected to their respective optimal resistances. 118

Figure 4.5 Relationship between relative dielectric constant εTr33 and piezoelectric constant d31: (a) for all the materials listed in Table 4.1 and (b) for soft PZT and hard PZT materials only....119

Figure 4.6 Dominant effect of d31 on power output for selected materials with a similar εTr33 for 4 grouped materials....121

Figure 4.7 Effect of relative dielectric strain constant εTr33 on power output for selected materials with 3 sets of identical d31. 121

Figure 4.8 Power output vs. electromechanical coupling coefficient k31 for the materials listed in Table 4.1 whilst connected to their respective optimal resistances. 122

Figure 4.9 Power output vs. FOM: (a) for all the materials listed in Table 4.1, and (b) for soft PZT and hard PZT, and PVDF materials. 124

Figure 4.10 Simulated electrical power response of PFT for different endcap materials and thicknesses based on harmonic analyses; PFT is under a 1kN force at 2Hz with a fixed base. Power calculation is based on the PFT connected to a 10MΩ resistor in parallel. All other materials and dimensions are the same as in Table 5.1. 127

Figure 4.11 Simulated Von Mises stress of PFT around apex bend for different endcap materials and thicknesses. PFT is under a 1kN force with fixed base (Static non-linear analysis). Other PFT dimensions can be found in Table 5.1. 128

Figure 4.12 A screen-shot of the Von Mises stress in the endcap elements based on static non-linear simulation with the endcap loaded at 1kN. The labels show high stress concentrations occurring in the bent profiles of the endcap, where the endcap is 0.5mm thickness and made from Stainless steel 304 128

Figure 4.13 Simulated electrical power response of PFT for different endcap materials and thicknesses. Graph excludes results where stress exceeded safety factor 2. PFT under a 1kN force at 2Hz with fixed base (Harmonic Analysis). Power calculation based on the PFT connected in parallel to a 10MΩ resistor. Other PFT dimensions can be found in Table 5.1. 129

Figure 4.14 Simulated stress in PZT for different endcap thicknesses based on static non-linear analysis, where the PFT is under a 1kN force with a fixed base and each point on the graph corresponds to the maximum stress that occurs along the centre in the z-direction (length-direction) in the PZT. Insert, the stress distribution along the central length-direction of the PZT, where the peaks correspond to the endcap-PZT contact point. Other PFT dimensions can be found in Table 5.1. 131

Figure 5.1 Function of the PFT when a downward compressive force is applied. 134

Figure 5.2 A Photo of the PFT showing its general structure and materials. 135

Figure 5.3 CAD sketch of the PFT developed in the CPC-FEM. 137

Figure 5.4 PFT in CPC-FEM showing boundary conditions and how electrical resistor is connected in parallel with PFT. Top left: axis coordinates used in CPC-FEM. 139

Figure 5.5 Simulated electrical output of the PFT verses piezo-element thicknesses, where the PFT is subjected to a 1kN force at 2Hz. For each different piezo-thickness the optimal resistance was used, and dimensions of the PFT can be found in Table 5.1 and for the material properties in Table 5.2. 142

Figure 5.6 Simulated electrical output of the PFT verses join lengths, where the PFT was subject to a 1kN force at 2Hz, whilst connected in parallel to

an 8MΩ resistor, dimensions of the PFT can be found in Table 5.1, and for the material properties in Table 5.2. 143

Figure 5.7 Simulated electrical output of the PFT verses electrode length, where the PFT was subject to a 1kN force at 2Hz. For each different electrode length the optimal resistance was used, dimensions of the PFT can be found in Table 5.1 and for the material properties in Table 5.2. 145

Figure 5.8 Simulated electrical output of the PFT verses internal angle of the endcaps, where the PFT was subjected to a 1kN force at 2Hz, each curve represents a different thickness of the piezo-element, and dimensions of the PFT can be found in Table 5.1 and for the material properties in Table 5.2. 148

Figure 5.9 Simulated Von Mises Stress around the apex bend of the endcap for the endcap thickness of 2mm, where the PFT was subject to a force of 1kN at 2Hz. 150

Figure 5.10 Simulated electrical output of the PFT verses substrate thickness, where PFT was subjected to a 1kN force at 2Hz, and dimensions of the PFT can be found in Table 5.1 and for the material properties in Table 5.2 151

Figure 5.11 Structure of PFT. 154

Figure 5.12 Resistance welded endcap. 156

Figure 5.13 Laser welded Endcaps. 156

Figure 5.14 Measruing voltage produced by PFT under force excitation of loading machine; PFT electrically connected over a resistive load, voltage measured over resistive load using multimeter with data proccesing on laptop using Agilent Technologies LtD software. 159

Figure 5.15 The electrical response of a PFT verses the load resistance where the PFT was subjected to a force of 2Hz at three different force magnitudes, the PFT had laser welded endcaps and a partial electrode area (52mmx30mm), and the error bars are based on standard deviation from experimental results of three identical PFTs. 162

Figure 5.16 The electrical response of a PFT verses load resistance, where the PFT was subjected to a force of 2Hz at three different force magnitudes, the PFT had resistance welded endcaps and a partial electrode area (40mmx30mm), and error bars were based on standard deviation from experimental results of two identical PFTs. 163

Figure 5.17 The electrical response of a PFT verses load resistance, where the PFT was subjected to a force of 2Hz at three different force magnitudes, the PFT had resistance welded endcaps and a full electrode area (52mmx30mm), and error bars based on standard deviation from experimental results of three identical PFTs. 164

Figure 5.18 The electrical response of 2 different PFTs verses load resistance, were the PFTs were subject to a 1kN force load at two different

frequencies, the two types of PFT were one with a full electrode area and one with partial electrode area (both with resistance welded endcaps), and error bars were based on standard deviation experimental results; full electrode based on three devices and partial electrode based on 2 devices. 166

Figure 5.19 Resistance spectrum graph when input parameters were varied in the CPC-FEM of the PFT. Unless stated otherwise dimensions and material properties of the PFT can be found in Table 5.1 and Table 5.2, respectively. For material properties of the adhesion layer see Table 5.9. ... 167

Figure 5.20 Comparision of simulation and experiemntal results of PFT resistance spectrum response, for PFT under a force load at 2Hz over two differnt force loads 1kN and 0.75kN. Simulation is based on worst case senario input parameters for PFT. Experimental results from Section 5.3.2 when PFT was tested in the loading machine. 171

Figure 5.21 Comparision of simulation and experiemntal results of PFT resistance spectrum response, for PFT under a force load at 5Hz over two differnt force loads 1kN and 0.75kN. Simulation is based on worst case senario input parameters for PFT. Experimental results from Section 5.3.2 when PFT was tested in the loading machine. 172

Figure 5.22 Reaction force from ground was obstructed from making contact with PFT due to the thickness of the sole material. 173

Figure 5.23 (a)-(c) Sketches showing progression of PFT positing within shoe/boot. 174

Figure 5.24 (a)-(c) Photographs showing progression of PFT positing within shoe/boot. 174

Figure 5.25 System level flow; PFT converting Bio-kinetic energy to electrical energy to power a wireless sensor module which in-turn transmits sensor data to a base station. 175

Figure 5.26 Low power consuming wirless module with intergrated sensor array 176

Figure 5.27 Jennic LtD wireless intergrated transiever compliant with IEEE 802.15.4 protocol at 2.4GHz frequency. 176

Figure 5.28 (a) Test 1: Establishing the electrical performance of the PFT when connected to a load resistor in parallel, the voltage across the load resistor was measured whilst the subject was running on the treadmill, (b) simplified circuit diagram. 177

Figure 5.29 (a) Test 2: Ascertaining the cold-start time and time between each transmission by interpreting the voltage measured across the wireless modules internal capacitor using a multi-meter, sensor data was also recorded on the laptop, (b) simplified circuit diagram. 178

Figure 5.30 (a) Treadmill used for test the energy harvesting system, (b) wireless module stored in pocket of subject during testing and, (c) wires

transferring power between wireless module and PFT tracked up leg and held in place with insulation tape. 179

Figure 5.31 Test 1: Voltage measured across a range of resistors connected in parallel to PFT (in shoe). Subject was exerting a 760N force at a frequency of 1.4Hz, (a) calculated power (b) measured voltage, and (c) calculated current. 180

Figure 5.32 Test 1: Voltage measured across a 4MΩ resistor connected in parallel to PFT. Subject was exerting a 760N force at a frequency of 1.4Hz. 181

Figure 5.33 Test 1: Voltage measured across a 4MΩ resistor connected in parallel to PFT. Subject was exerting a 1000N force at a frequency of 1Hz. MS, TO and SP denote the mid-stance, toe-off and swing-phase periods of the gait cycle. 182

Figure 5.33 Test 2: Voltage across 2mF wireless module capacitor due to power supplied by PFT when subject ran at 1.4Hz exerting approximately 760N on PFT. Inset, magnified plot of voltage fluctuations, fluctuations due to power used by each transmission. 183

Figure 5.34 Test 2: Two transmissions of sensor data received via the transceiver..... 184

Figure 6.1 Drawing of half cross-section of Cymbal structure. 232

LIST OF TABLES

Table 1.1 Weight of spare batteries carried by a typical british army section soldier for 24 hour patrol (second in command). 29

Table 2.1 Typical power requirments of some applications. 37

Table 2.2 Overview of human based EHDs. 44

Table 2.3 EHDs integrated into shoes. 51

Table 2.4 Articles on the Cymbal that focus on the performance characteristics of frequency response. 66

Table 2.5 Articles on the Cymbal that focus on electrical perfomance. 67

Table 2.6 Methodologies proposed for modelling piezoelectric [99]. 70

Table 3.1 Material properties used in the developed CPC-FEM. 87

Table 3.2 Most effictive dimensional parameters chosen based on Cymbal CPC-FEM results and also the dimensional parameters used in the Cymbal CPC-FEM simulations. 87

Table 3.3 Strains in the Cymbal compared with a PZT disk. 99

Table 3.4 Shape factor compared with the effective piezoelectric constant. 100

Table 3.5 Key design aspects to improve Cymbal. 107

Table 4.1 Key piezoelectric material properties used in CPC-FEM analyses, associated material properties, optimal load resistances and associated power outputs. 112

Table 4.2 Piezoelectric material data origin. 113

Table 4.3 Endcap materials used in investigation. 126

Table 4.4 Endcap thickness allowed when Von Mises stress in endcap is bellow yield strength (SF2). 130

Table 5.1 Dimensional parameters used in the PFT CPC-FEM. 137

Table 5.2 Material properties of materials used in the PFT CPC-FEM. 138

Table 5.3 General relationships and limiting factors for key parameters studied. 153

Table 5.4 PFT parts list. 154

Table 5.5 Costing estimation for single PFT. 155

Table 5.6 Physical variation in PFTs that were fabricated. 155

Table 5.7 Fabrication of PFT with laser welded endcaps and partial electrode. 157

Table 5.8 Force and frequency combinations used in loading machine test of single PFT. 161

Table 5.9 Material properties of structural adhesive used in CPC-FEM. 168

Table 5.10 Affect of PFT CPC-FEM input parameter variation on PFT CPC-FEM power output when the PFT is connected to a parallel resistance of 10MΩ. 170

NOMENCLATURE

Acronyms

2D	Two Dimensional
3D	Three Dimensional
AC	Alternating Current
APDL	ANSYS, Inc. Programing Design Language
BPS	British Pound Sterling
CO2	Carbon Dioxide
CPC-FEM	Coupled Piezoelectric-Circuit finite Element Model
CPU	Central Processing Unit
DAM	Displacement Amplification Device
DAQ	Data acquisition card
DC	Direct Current
DFOM	Dimensionless Figure of Merit
DL	Del Piezo Specialties, LLC
DMG	Denison Mayes Group
EHD	Energy Harvesting Device
FEA	Finite Element Analysis
FEM	Finite Element Model
FOM	Figure of Merit
GPS	Global Positioning System
GSM	Global System for Mobile Communications
HS	Heel Strike period of the gait cycle
IEEE	Institute of Electrical and Electronics Engineers
LCP	Lance Corporal
LLC	Limited Liability Company
LTD	Limited Company
MEHD	Mobile Energy Harvesting Device
MEMS	Micro Electrical Mechanical System
MFC	Macro Fiber Composite
MP3	MPEG-1 Audio Player 3
MS	Mid Stance period of the gait cycle
NASA	National Aeronautics and Space Administration
Nd:YAG	Neodymium-Doped Yttrium Aluminum Garnet
NI	National Instruments
PA	Pennsylvania
PB	Prototype Board
PCT	Piezoelectric Cymbal Transducer
PEH	Piezoelectric Energy Harvester
PFT	Piezoelectric Flex Transducer

PID	Proportional Integral Derivative Controller
PLC	Public Limited Company
PMC	Piezoelectric Metal Cavity
PRR	Personal Role Radio
PSI	Piezo Systems, Inc.
PVC	Poly Vinyl Chloride
PVDF	Polyvinylidene Fluoride
PZN-PT	Lead Zinc Niobate-Lead Titanate (single crystal)
PZT	Lead Zirconate Titanate
RF	Radio Frequency
RMS	Root Mean Square
SDOF	Single Degree Of Freedom
SF	Safety Factor
SM	Steiner & Martins, Inc.
SP	Swing Phase period of the gait cycle
SPARK	Soldier Power Regeneration Kit
SPEM	Sumitomo Metal Electronics Devices, Inc.
SPICE	Simulation Program with Integrated Circuit Emphasis
TO	Toe Off period of the gait cycle
Tr|O2	Disaccharide Trehalose and Oxygen
TV	Television
UDL	Universally Distributed Load
UK	United Kingdom
ULP	Ultra Low Power
USA	United States of America
USD	United States Dollar

Abbreviations

deg	Degrees
Eq	equation
et al	and others
Exp	Experimental
hr	Hour
min	Minute
mph	miles per hour imperial unit
piezo	Piezoelectric
sec	Second
vs	verses

Symbols

£	British Pound Sterling
Ø	Diameter
№	Number
™	Registered Trademark
®	Unregistered trademark

Variables

A	amplification factor due to Cymbal endcaps
A_c	force amplification factor of the Cymbal
A_e	the electrode area
C	capacitance of piezoelectric element in PFT
c^E	piezoelectric elastic constant at constant electric field
C_{Full}	capacitance of piezoelectric element in PFT with full electrodes
C_p	capacitance (piezoelectric)
$C_{Partial}$	capacitance of piezoelectric element in PFT with partial electrodes
d	piezoelectric strain constant
D	total diameter of Cymbal or length of PFT
D_{11}	equivalent damping stiffness in equivalent circuit method
D_a	apex diameter endcap
D_c	cavity diameter of endcap
d_e	distance between the electrodes
d_{33}^{eff}	equivalent piezoelectric strain constant
D_w	width of PFT
e	piezoelectric stress constant
E	Young's Modulus
ε_r	piezoelectric relative permittivity
ε^S	piezoelectric dielectric constant at constant strain
ε^T	piezoelectric dielectric constant at constant stress
ε_{r33}^T	piezoelectric relative dielectric at constant stress
F	applied force
F_x	force in *x*- direction
F_y	force *y*- direction
g	piezoelectric stress constant
H	endcap internal height
θ	internal angle in of the endcaps
I	electrical current
I_{rms}	electric current rms
J	length of join between endcap and piezoelectric material
k	electromechanical coupling coefficient
K_{11}	equivalent stiffness in equivalent circuit method
ζ_m	mechanical damping ratio
μ	Poisson's ratio
M_{11}	equivalent mass in equivalent circuit method
m_{eff}	approximate effective mass

N	number of samples
P_{avg}	average power
R_p	leakage resistance (piezoelectric)
Q_{Full}	charge of piezoelectric element in PFT with full electrodes
$Q_{Partial}$	charge of piezoelectric element in PFT with partial electrodes
ρ	Density
R	resistive part of impedance
R_{eq}	equivalent resistance of the resistive load and leakage resistance
R_{Full}	resistance of piezoelectric element in PFT with full electrodes
R_l	resistive load (piezoelectric)
$R_{Partial}$	resistance of piezoelectric element in PFT with partial electrodes
s^E	piezoelectric elastic compliance at constant electric field
σ_y	yield strength
t_c	endcap thickness
Θ_1	electromechanical coupling mass in equivalent circuit method
t_p	piezoelectric thickness
v	voltage
V_{Full}	voltage output of PFT with full electrodes
$V_{Partial}$	voltage output of PFT with partial electrodes
V_{rms}	voltage rms
w	relative displacement
w_B	base displacement
ω_N	natural frequency
X	reactive part of impedance
φ	shape coefficient
Z	Impedance

Constants

ε_0	permittivity of free space

CHAPTER 1

1.1 Introduction

This thesis encompasses the study, design, analysis and fabrication of a novel mobile energy harvesting device (EDH) to scavenge bio-kinetic energy and demonstrates that, the studied device is capable of harvesting sufficient amounts of energy from movements of the human body to power a custom-developed wireless sensor module. No industrial funding was used in conjunction with this thesis. This thesis begins with the study of an existing device called the Cymbal, and follows the development of the Cymbal device through incremental and logical design improvement steps along with their associated findings therefore, leading to the development and fabrication of a final novel device, the piezoelectric flex transducer (PFT). The final and novel device presented becomes geometrical dissimilar to its Cymbal origin, thus it becomes capable of transducing high force energy (up to 1kN) and therefore is well suited to harvesting energy from the movements of the human body, in particular. Coupled piezoelectric-circuit finite element modelling (CPC-FEM) (ANSYS version 13) developed in this thesis was the principle design tool used.

The value of mobile energy harvesting is in the benefits of autonomy. The monetary and environmental costs are also reduced i.e., batteries become redundant reducing resources used, time and associated waste. It is unclear whether EHDs will ever meet the growing energy demands of portable consumer electronics as computing central processing units (CPUs) are continually pushed to run more intensive processes at higher speeds. Current devices designed are still only able to satisfy the energy needs of low power consuming applications such as some pacemakers, health monitoring systems and sensors. However, significant developments in microelectronic technology have provided many ultra-low-power (ULP) devices that can be powered by energy harvesting technology [1], [2], [3], [4]. For instance, a ULP wireless module has been

developed that uses 2.3mW for data transmission and 1.8mW in receiving mode [2]. This new surplus of ULP devices has created large interests in the research and development of energy harvesting technology [5].

To harvest energy from the low frequency energy sources of the human body provides some challenges. Often lower frequency sources are less energy rich e.g. if there were two vibrational sources with the same amplitude but different frequency levels then the lower frequency vibration would have less energy. If the EHD is required to be relatively small in size (common for mobile EHDs) then it is likely to be far from its resonant frequency when operating, thus difficult to utilise the resonant modes of the structure to improve output electrical performance. And finally, if the source of kinetic energy is at low frequency then the resulting transducer electrical signal will also be at low frequency causing high internal impedances which is currently undesirable for charging batteries.

Until the power outputs of bio-kinetic mobile EHDs increase to a usable level for current technology, of a few milliwatts, they can be used to power low power consumption devices e.g. a wireless sensing system. It is then more beneficial to take a system level design approach i.e., designing the whole system to be a low power consuming at every level. Developing the power management systems is a research area in itself. One example developed by Prof. Zhu's Energy Harvesting Research Group [6] includes the following:

- using low power consuming electronics,
- using control systems to isolate components when they are inactive/in sleep mode,
- developing low power consuming algorithms for microcontrollers, and
- choosing simple architecture communication protocols that has low power consumption.

Other techniques include impedance matching between EHDs and the connected power management circuit and the end of users. In the final testing demonstration of this thesis, a custom-developed wireless sensor module that included the aforementioned power management techniques was used. This wireless sensor module was connected to the novel PFT for the purpose of a demonstrating the capabilities of the final device

presented in this thesis. Power management solutions can help improve the power available to the application but this is out of the scope of the thesis.

This thesis involves the study of a new piezoelectric EHD, which is capable of working at non-resonant and low frequencies to harvest bio-kinetic energy of human walking. This approach involves considering how physical parameters both geometrical and material properties effect energy harvesting performance. In this thesis a desirable energy harvesting performance is characterised by increased power, less focus is given to the voltage-current characteristic curves. Also, the power stated in this thesis is the power calculated over a range of resistive loads therefore it gives a realistic estimation of the energy harvesting capability of the piezoelectric based devices. In studying individual physical parameters of EHDs a general trend of how the devices behaved was also gained. The behavioural characteristics of devices, in particular the initially studied Cymbal device, were understood and then issues and problems as a potential bio-kinetic EHD were recognised and consequentially, overcome.

With potential as a bio-kinetic EHD an initial focus was placed on the study of an existing piezoelectric based device, commonly used as an actuator, called the Cymbal. This is because it uses a force amplification mechanism, rather than a resonant mechanism, and it is potentially capable of working at non-resonant and low frequencies to harvest bio-kinetic energy from movements of the human body. Some attention was given to the Cymbal's energy harvesting capability and also to how the piezoelectric transducer is elastically deformed through its amplification structure. The Cymbal has the ability to amplify the elastic deformation of the piezo-element through its structure and so it can be used to work at non-resonant frequencies to harvesting bio-kinetic energy. Kim *et al* [7] reported that the addition of a top and bottom endcap to a piezoelectric disk gave an enhanced electrical output of 40 times more than using a piezoelectric disk alone. This statement was confirmed later in this thesis by using a Cymbal CPC-FEM developed, where an enhanced electrical output of 39 times was noted.

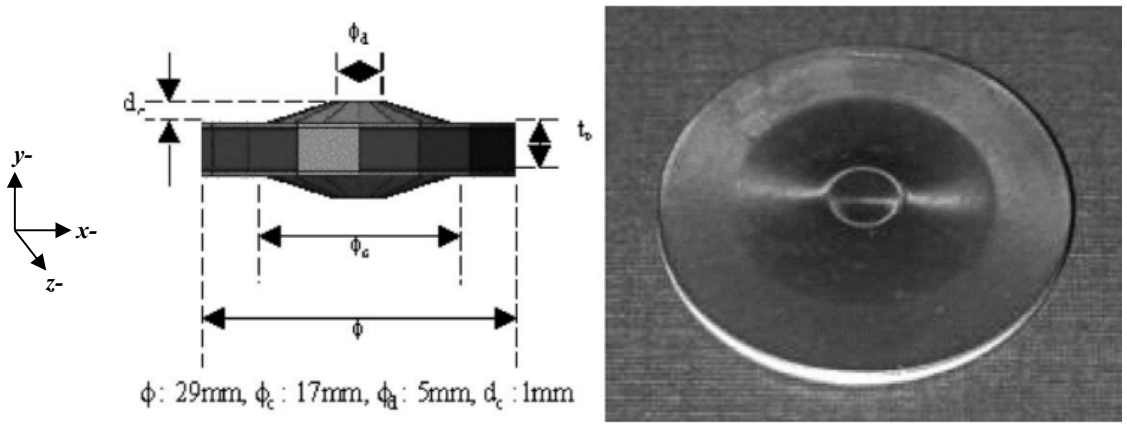

Figure 1.1 Cymbal device for harvesting machine waste vibrations developed by Kim *et al* [7] Left: piezoelectric disk sandwiched between top and bottom metallic endcaps, right: a photo of fabricated Cymbal device.

The Cymbal working principle is explained below. The Cymbal consists of a piezoelectric element sandwiched between two metal endcaps, which are specifically designed to amplify the axial loaded force on the piezoelectric element. When excited, the endcaps deform the piezoelectric disk in the *x*-, *y*- and *z*-directions. The co-ordinates used in this thesis correspond to the convention initiated by the ANSYS simulations. The applied force in the *y*-direction generates some elastic deformation in the piezoelectric material (at the endcap-piezoelectric disk interface) and thus also a charge on the electrodes due to the contribution of d_{33} piezoelectric strain constant. Secondly, the force in the *y*-direction is converted and amplified to the *x*- and *z*-directions due to the small angle of the endcaps and so generates a strain and charged due to the contribution of d_{31} piezoelectric strain constant. Hence an equivalent strain constant d_{33}^{eff}, can be written as $d_{33}^{eff} = d_{33} + |A\ d_{31}|$ [7], where A is dependent on endcap leverage contributions, and *A*=cavity radius/cavity depth. The metal endcaps are essentially functioning as mechanical force amplifiers to increase the force that acts on the piezoelectric disk and so increase the elastic strain energy stored in the piezoelectric disk for energy harvesting. Though not explicitly mentioned in the literature, the endcaps of the Cymbal provide an additional degree of freedom for the piezoelectric disk, allowing it to elastically deform more freely as opposed to if it were restrained with a fixed base. When studying the design of the Cymbal in this thesis, only the geometrical effects on power output were considered. Having said this, a result of

changing the piezoelectric disk dimensions led to a change in the electrical characteristics of the Cymbal. Due to the vulnerability of the adhesion layer it was not thought possible for the Cymbal to be designed to withstand more than 50N loading before mechanical failure, which is significantly less than what would be the required for footfall force of 1kN. Identifying this limitation led to the development of a new device, called the piezoelectric flex transducer (PFT).

Based on the concept of the Cymbal device, the PFT has a top and bottom metallic endcap that work to actuate a central piezoelectric element. Unlike the Cymbal the PFT has an additional substrate layering which has enabled the device to be scaled up and therefore withstand forces of up to 1kN. The substrate layering reduces the risk of delamination by increasing the adhesion contact area. The PFT has a rectangular shape for an improved packing factor, though this may vary between applications.

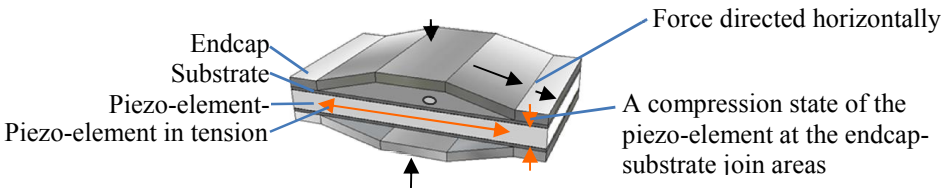

Figure 1.2 Schematic of the PFT when a downward compressive force is applied.

The PFT consists of a piezoelectric element sandwiched between substrate layers and two metal endcaps. The stainless steel endcaps have two main functions: 1) to amplify and redirect the downward applied mechanical force to a horizontal force so that the majority of the available force acts to stretch piezo-element horizontally, the converse action happens when the force is removed and the PFT tends back to its original state, and 2) to not be constrained along the underside the piezo-element and thus suspend the piezo-element and substrate so that they can operate more freely, generally speaking a higher elastic deformation or strain corresponds to a higher charge produced.

The Cymbal study in the literature did not include an extensive material selection process. As material properties is an important factor effecting energy harvesting performance, a study was carried out in this thesis on piezoelectric material selection criteria for EHDs, which helped with selecting a piezoelectric material for the PFT. This

piezoelectric material selection work takes up a chapter in this thesis and included using a CPC-FEM of a simplified EHD to compare 25 different piezoelectric materials. Material selection of the endcaps and substrates were based on findings from comparing different metals using a CPC-FEM of the PFT. In summary CPC-FEMs were used to design and analyse the novel piezoelectric flex transducer's (PFTs) performance with focus on some key dimensional parameters and material properties. The PFT was fabricated, retrofitted into a shoe and the energy generated was used to power a wireless sensor module whilst the subject wearing the shoes ran at approximately 3.1mph.

1.2 Energy Harvesting

The value of mobile energy harvesting is in the benefits of energy autonomy. Combing mobile energy harvesting and wireless sensing technology mean that for example, a health monitoring system may be installed with no reliance on an outside power supply. Moreover, when mobile energy harvesters are combined with wireless capabilities it enables the retrofitting of sensor systems into difficult to access areas, thus allowing some projects to becomes more feasible prospects. Therefore, mobile energy harvesting could be considered a vital part of remote and harsh environment sensing systems of the future.

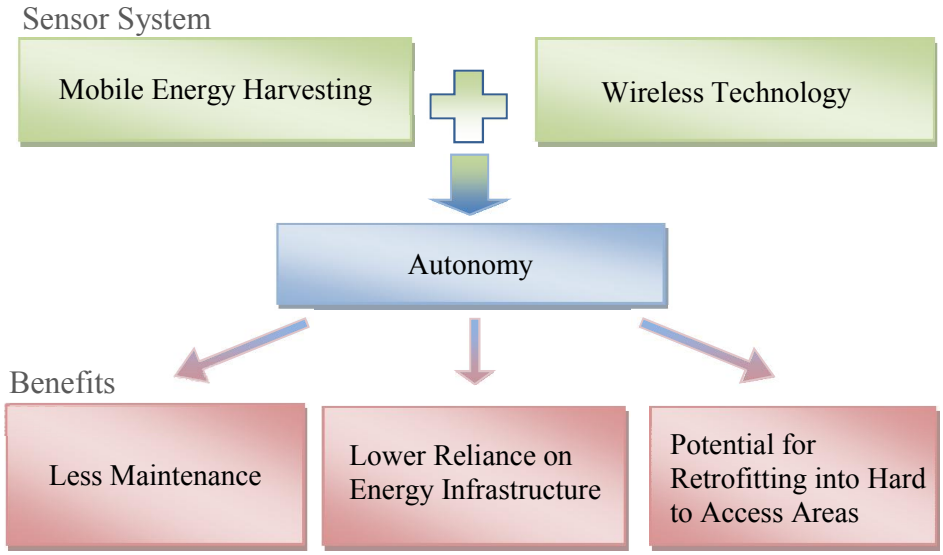

Figure 1.3 Benefits of Mobile Energy Harvesting Technology for Wireless Sensing.

In the developed world the modern human is becoming increasingly reliant on its mobile phone, the mountaineer on its GPS and the soldier on its communications equipment. The apparent reliance of our society upon portable devices is demonstrated by the mobile/cellular phone, which is one of the most commonly owned portable electrical devices and has over 4.6 billion subscriptions worldwide [8]. Based on the reliance of portable electrical devices it is not difficult to imagine the vast number of applications a mobile energy harvesting device (MEHD) utilising human waste energy may have e.g. to power mobile phones, GPS, mp3 player. However, this research area still hasn't directly demonstrated that energy harvesting can directly power these applications with no need for batteries. Moreover, a general consumer may have reservations about wearing a MEHD just to power their mobile phone. Until MEHDs become highly discreet a MEHD is more likely to benefit specialised systems such as in defence, mountaineering or as part of a wearable health monitoring system [9], for example integrating a MEHD with a health monitoring system would be of benefit due to reduced maintenance for the user (battery changes).

In theory a compact MEHDs can be retrofitted into many applications if it meets power requirements. Some applications may regard energy harvesters with more value due to their situation. For instance, personal role radios PRRs are issued to every soldier—and are worn according to the patrol commanders discretion—when the battery runs out on a soldier's PRR, safety is greatly compromised. The volatile battle field often creates situations where patrol missions are away from base for unpredictable and extended periods of time.

Figure 1.4 From left to right, Lance Corporal Mathew Sampson and Lance Corporal Jody Samways wearing their Personal Role Radios, Helmand Province, Afghanistan, Operation Herrick XV. Photo courtesy of LCP Mathew Sampson (taken by Private Rob Appell)[10].

If a patrol is forced from returning to base, a MEHD/system is of direct and significant value to sustain communications equipment. In addition to its power producing capabilities a MEHD could also help reduce soldier fatigue by reducing the battery related weight that is carried. To give an idea of weight; a typical British army section soldier (second in command) carries 2.78kg in spare batteries alone. In the British army a section is a small military unit made up of eight soldiers.

Table 1.1 Weight of spare batteries carried by a typical british army section soldier for 24 hour patrol (second in command).

Equipment	Amount	Battery Type	Weight (g)
Personal Role Radio (500m Range)	4 to 6	AA	92-138
Global positioning system	4	AAA	92
Head torch/Maglite	3	AAA	69
Night Sight	2	Lithium AA	30
Helmet Mounted Night Vision Goggles	1	Lithium AA	15
Bowman,Personal communication radio (1-2mile Range)	1	Battery Cassette (10xAA)	1200
Improvised Explosive Device Detector	9	D	1332
Total			2870

Source: Lance Corporal Mathew Sampson, British Army[11].

With such obvious gains for defence related applications i.e., soldiers, a device has already been proposed. The exchange of batteries with a MEHD the PowerWalk™ M-series, is reported not only to lighten the weight carried by a soldier but could save up to $135 in batteries, assuming 200 mission days per year, the cost saving adds up to $27,000 per soldier per year [12]. With contribution from a device on each leg the total power produced was 12W. The supporting literature for this device concluded that for 6 individual people tested whilst wearing the device on one leg walking at a speed of 1.5 m/s that 4.8± 0.8 W [13] could be generated.

1.3 Aim

The research aim was to design, analyse and develop an EHD capable of harvesting sufficient energy from movements of the human body to power a wireless sensor module.

1.4 Objectives

1. Identify key parameters of the Cymbal (an existing device) that affect its suitability and performance as an EHD using a CPC-FEM as a design tool.

2. Fabricate and test a Cymbal device with the intention of validating the CPC-FEM developed.

3. Develop a piezoelectric material selection criteria using a simplified version of the CPC-FEM used for the Cymbal study.

4. Design a new EHD whilst considering key performance related parameters identified in the Cymbal study, the new EHD must withstand forces associated with human gait (1kN at 2Hz).

5. Fabricate and demonstrate the EHD by retrofitting it into the sole of a shoe, harvesting bio-kinetic energy from gait to power a wireless sensor module.

1.5 Thesis Structure

The work in this thesis started in Chapter 3 by focusing on studying the behaviour of the cymbal device and determining its applicability for harvesting bio-kinetic energy. In other words, could the Cymbal be designed to withstand the associated forces of specific human body movements? On determining that the Cymbal was not able to be designed for such an application work on the Cymbal stopped. However, in learning about how the Cymbal functioned and how to tailor the design a new device was developed. A lot of time was invested in generating new ideas and finding solutions to the limitations that the Cymbal possessed. Multiple attempts and design ideas were produced before the final device was decided upon. Ideas were tested using the CPC-FEM. During this same period of time the work in Chapter 4 carried out on piezoelectric material selection using the CPC-FEM was also done. It was thought to be important work for use in the final design. The other reason for doing the tasks in the same time period was so that if one area of the thesis was not succeeding then it could be rested and other parts would become productive instead. The ability to come back to a piece of work after a week not only gave new and helpful perspective but also allowed for constant productivity. The work done in Chapter 5 was built upon the work in previous chapters. Although design ideas for the final device were generated during the time of the material selection work in Chapter 4, the final design was further tailored for performance later on. This design work along with the fabrication and testing of the final device was the last work to be carried out in this thesis, Chapter 5.

Chapter 1 introduces the thesis and presents its main Aim and 5 objectives.

Chapter 2 presents a literature review. This is an overview of the power outputs and types of energy produced by the human body with an insight into some EHDs, transduction mechanisms and design modelling approaches. Some focus is on the Cymbal device. Its variations in structure and application are presented along with an explanation of how the Cymbal functions as an EHD. Design approaches applicable to piezoelectric EHDs are introduced and discussed concluding that the CPC-FEM used in this thesis was a sensible approach. Although finite element modelling can be problematic for simulations of non-linear electrical circuit components these problems

did not apply in this thesis due to the simple electric circuit used. The benefit of using the CPC-FEM was that it is capable of handling the 3D modelling of a EHDs complex shape and account for electromechanical coupling. Following this, existing material selection criteria is also introduced and discussed. The literature review in Chapter 2 concludes with a methodology and a section discussing research questions that were raised during the literature review, it explains how the thesis answers these questions, what contributions have been made, and the novelty of specific contributions by work in the thesis.

Chapter 3 is concerned with investigating the Cymbal device and its suitability for harvesting bio-kinetic energy. The modelling approach using the CPC-FEM of the Cymbal is explained and the model is validated by experiment. The CPC-FEM of the Cymbal is then used to analyse the Cymbal structure gaining an understanding of how it functions. Moreover, key design parameters were identified that had a direct effect on electrical power output. The chapter is then concluded and explains how the scaling of the Cymbal device to enable it to withstand higher working forces, such as those associated with bio-kinetic energy in particularly gait, becomes problematic due to the vulnerability in its structure. This vulnerability is the adhesive join interface between the endcap and piezoelectric element.

The first section in Chapter 4 presents a study where a CPC-FEM was developed to investigate key piezoelectric material properties and their effect on power output of a piezoelectric EHD. Results are presented and there is a discussion that focuses on the comparison of multiple piezoelectric materials on merit of the power output they produced. The section is then concluded. The second part of Chapter 4 is concerned with the comparison of metal based materials for possible use in the endcap structures. A CPC-FEM of a PFT was used to compare the effect that different metals used to make the endcaps had on power output performance. Moreover, the study also investigated what the minimum thicknesses of endcap could be before compromising the structural integrity of the PFT. Results were presented, discussed and concluded. Findings from both sections of this chapter were implemented in material selection decisions in later chapters.

Chapter 5 presents the development of the new PFT. Introducing the chapter is an explanation of the design approach that gives insight into similarities between the Cymbal and PFT and therefore explains what parameters that had been previously investigated during Chapter 3. The configuration of the CPC-FEM developed for designing the PFT is explained. The CPC-FEM is then used to analyse the effects structural parameters have on power output performance of the PFT. The results of the analysis of the PFT are then discussed and concluded by presenting a final design of the PFT. Following this, a detailed fabrication process of the PFT is shown. The PFT is then tested using a loading machine as a kinetic energy input. Test results are presented and discussed, as part of this a comparison between the experimental test results and the CPC-FEM results are presented. Furthermore a short section is included that investigated how the CPC-FEMs power output is sensitive to specific input parameter variation. Finally, the PFT is tested in an application were the PFT is retrofitted into the sole of a shoe and harvests bio-kinetic energy from foot fall during gait to power a wireless sensor module. The results are presented and discussed. Finally, the chapter is concluded.

Chapter 6 presents a summary of the research performed in this thesis. The structure of the discussion follows the objectives set out by this thesis. It's explained how each objective is achieved, what its main outcomes are and what the resulting contributions to research are. Following this the thesis is concluded. Finally, based on limitations of this thesis, recommendations for further work are suggested.

CHAPTER 2

This Chapter provides a background to this thesis. The literature was assessed to provide a quantitative overview of the power outputs and types of energy produced by the human body with an insight into some EHDs, transduction mechanisms and design modelling approaches.

According to the literature, energy associated with foot fall was relatively high in comparison to other sources, except arms movements which were just 10% lower than foot fall. 12 devices used for harvesting energy from foot fall were reviewed by comparing their methods of transduction and power output. To further investigate the practicalities of the different transduction techniques i.e., size and weight, the overview was then broadened to include devices used to harvest energy from the human body, as opposed to just foot fall or leg swing.

Different transduction techniques were then discussed concluding that piezoelectric and electromagnetic are the most appropriate for harvesting foot fall. These two transduction techniques are then compared concluding that piezoelectric transduction offers small displacements with the ability to extract energy from a high magnitude force at low frequency.

In this thesis it is assumed that energy from foot fall/heel strike is due to the compressive force exerted on the ground through foot-ground contact when in gait and not due to the momentum in the swing phase of the foot in gait. The Cymbal device was then investigated through the literature and with an additional interpretation and explanation of its physical function developed in this thesis.

Different approaches to piezoelectric harvester design were introduced which helped explain why the CPC-FEM was used as a design tool in this thesis.

Finally, a background of piezoelectric material selection was given suggesting that the application of the CPC-FEM could be used to compare many different piezoelectric materials. For instance, by using the CPC-FEM and simulating the same harvester but

made of different piezoelectric material would enable a comparison of materials with a more accurate measure of performance i.e., power output.

2.1 Energy Harvesting

Large scale energy harvesting

The modern human is heavily reliant on energy, which is commonly provided by the burning of fossil fuels in the form of natural gas, coal and petroleum. Due to the large scale population and human densities, a considerable amount of CO2 has released from burning fossil fuels and considered internationally to be of detriment to the environment. Nuclear power releases minimal amounts of CO2 during operation. However, it does produce the by-product of nuclear waste, a substance complex to dispose of. Moreover, nuclear power plants are potential hazards; there has been the 1986 Chernobyl disaster in the Ukraine and the 2011 Fukushima disaster in Japan. Wind-power, hydro-power and solar-power are common renewable resources that produce no CO2 during operation. However, if a CO2 life-cycle assessment were to be carried out it would highlight the substantial CO2 contributions to the environment produced during a renewable products manufacture and installation. Though the amount of CO2 produced by the human population is excessive and may be altering the earth climate artificially, some critics argue that the earth is following a natural cycle regardless of man-made CO2.

Small scale energy harvesting

This thesis focuses on small scale energy harvesting. A MEHD is a device that can convert ambient energy into useful energy. MEHDs tend be used for harvesting waste energy. For instance, vibrational energy that would otherwise dissipate through the atmosphere evolving into sound then finally heat. Vibration energy is so common that there has been a range harvesters designed with a variety of different transduction mechanisms of electro-static, electromagnetic and piezoelectric. Transduction techniques are described in more detail later on in this literature review. Zhu et al [14] designed and developed a vibrational energy harvester, this piezoelectric cantilever beam device resonated at a matched frequency to the energy source in order to maximise its power output.

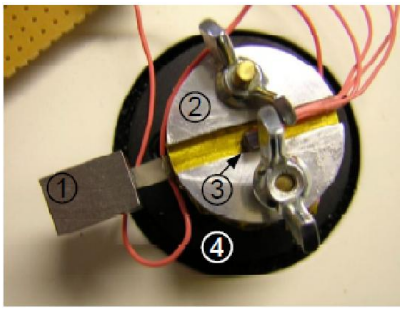

Figure 2.1 Photo of piezoelectric cantilever based harvester, 1) harvester with its proof mass 2) aluminium holder 3) accelerometer for testing 4) mount for shaker testing [14].

Power Requirements

An important category of possible applications for harvesters is the wireless communication node. As they provide a convenient solution to transmit data wirelessly, wireless nodes are found throughout domestic and industrial products and systems. Associated with being the lowest power consumer Blue-tooth is a common wireless technology that works in the frequency range of 2402-2480MHz. Another popular communication frequency is the Global System for Mobile Communications (GSM) frequencies which work in the 2100MHz range. As shown in Table 2.1, a Bluetooth wireless node can operate around 5-18mW depending on the quality of the signal needed.

Table 2.1 Typical power requirments of some applications.

System	Power (W)
Low-power microcontroller chip [15]	0.001
Bluetooth communication signal [16]	0.005-0.018
Embedded CPU board [15]	1
Implantable pacemaker [16]	4.80 x 10-6
Small portable FM radio [17]	0.03
Low-end MP3 [16]	0.327
TV remote control [17]	0.1
Notebook computer [15]	10
	121
Average power use over 24 hours [15]	

If a harvester cannot produce enough power to meet the needs of an application it could be used to supply the idle power consumed by application. Idle power consumption occurs during stand-by and sleep modes of electrical appliances.

2.2 Bio-kinetic Energy

The human body is a biological system comprised of many organ systems each with their own individual yet co-dependent function. Over years of evolution the human and its ancestral relatives have developed many ways to interact with the world around it. Assuming the human is only a product of this world it follows that many of the energies that flow through the world also flow though humans, if they are to interact. The forms of energy known to be produced by the human body are thermal, kinetic (force & sound), bio-chemical, electromagnetic, and bio-magnetic energy, shown in Figure 2.2.

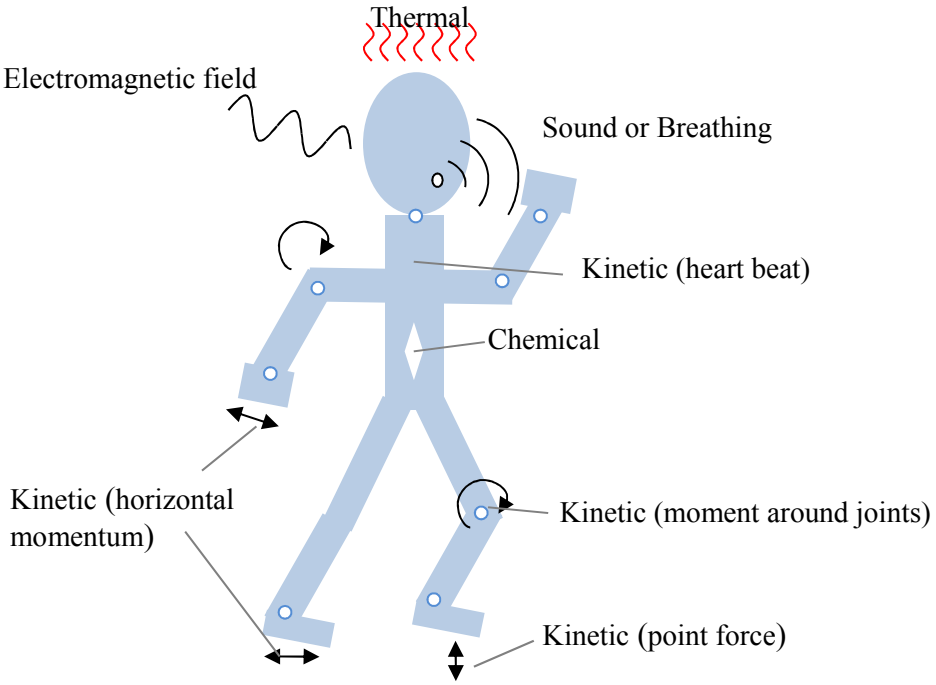

Figure 2.2 Types of energy produced by the human body.

It has been demonstrated, using electromagnetic transduction [18], that 3μW of breathing energy from human was able to be harvested without impeding breathing flow. Heat from the human body has also been shown to harvest 250μW from a thermoelectric wristwatch [19] and separately 0.31mW from a thermoelectric shoe implant [20]. A prosthetic total knee implant demonstrated by Platt *et al* [21] harvested 1.6mW. Further from this, a prosthetic leg that harvests the energy from its swing phase damping has the potential to produce 0.2-0.54W [22]. Prosthetic feet are now in the development stage and are becoming increasingly complex in structure [23], shown in Figure 2.3, opening up the possibility of integration or retrofitting of an EHD into prosthetic feet.

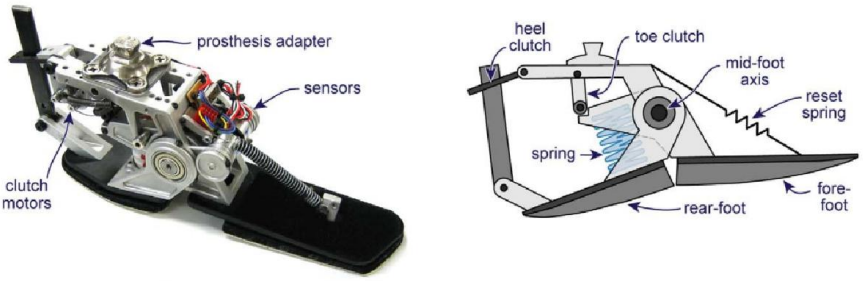

Figure 2.3 Prosthetic foot that uses a spring to recover energy and aid in walking [23].

There has been research into EHDs that scavenge kinetic energy/bio-kinetic energy in order to power pacemakers. A design has been proposed by Karami *et al* in the USA [24]; the zig-zag design is a MEMS cantilever based structure that utilises resonance for enhancing power outputs. The zig-zag device is designed not to impede the heart and thus aims to harvest vibrations in the area of the heart and not directly from the heart. A healthy heart is expected to beat with consistency between cycles, however, the frequency profile of each cycle is complex with a spectrum of vibration frequencies and amplitudes associated with it. Karami *et al* explains that "the frequency spectrum of heart beat oscillations spread from fractions of a hertz to about 50Hz." The zig-zag device was designed to operate at 39Hz, this is not to say that the heart rate was 39Hz but simply a component of the heart beat caused some vibration in the body or the zig-zag device of 39Hz. Using an analytical model based on mechanical and electrical governing principles the power output of such a zig-zag device harvesting frequencies of 39Hz was 10μW.

Zurbuchen *et al* [25] in Switzerland demonstrated a mass imbalance oscillation generator (or eccentric oscillating weight) on the heart of a sheep which converted the hearts kinetic energy to electrical energy via electromagnetic transduction, it harvested 30μW in vitro and 16.7μW in vivo, see Figure 2.4, which was claimed to be sufficient to power the latest low power consuming pacemakers. The mass imbalance oscillation generator could have been tested in the vicinity of the heart—much like Karami *et al*'s proposal. By testing in the vicinity of the heart the harvester would then not impede an already compromised heart. The assumption that the heart is already compromised is based on the initial need for the pacemaker.

Testing of an EHD by Roberts *et al* [26] in the UK has also been carried out on a pig's heart. Although there has yet to be published work on human testing, this field of human body energy harvesting research is promising and spans many different institutions across the world.

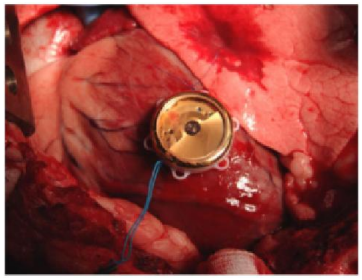

Figure 2.4 Mass imbalance oscillation generator on sheep's heart [25].

The body produces an Electromagnetic field or biomagnetic field, which is potential energy source, however, it is extremely weak. Cohen et al found the field of the heart was 5x10-7 which is "one-millionth of the earth's steady magnetic field" [27].

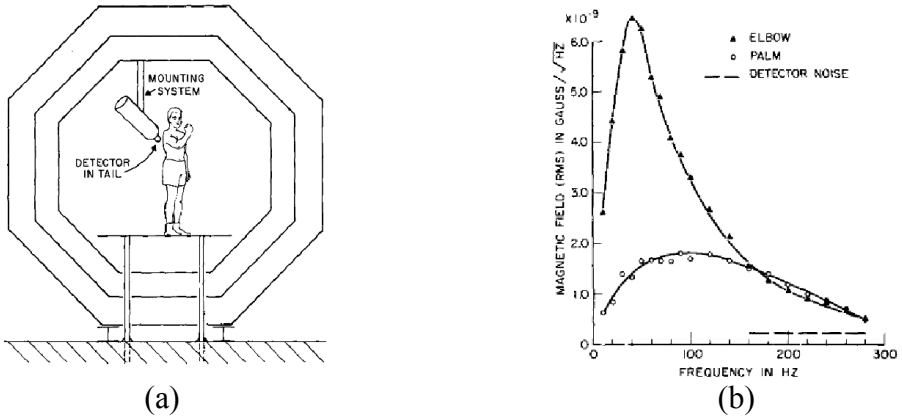

(a) (b)

Figure 2.5 (a) Magnetometer taking measurement near elbow in shielded room (b) Magnetomyogram spectra [27].

Although the body gives off a weak magnetic field, if the human body is regarded as an antenna itself, then it could be used to harvest energy from Radio Frequencies (RF) used in both radio and television transmissions. An RF power density study was carried out by Burch et al in response to public health concerns over proximity to antennas with raised brain cancer cases. With line of sight of an antenna up to 1km away a power of 2.92μW/cm2 [28] was reported. Therefore, this study inadvertently demonstrates the potential for energy harvesting of RF for low power consuming applications.

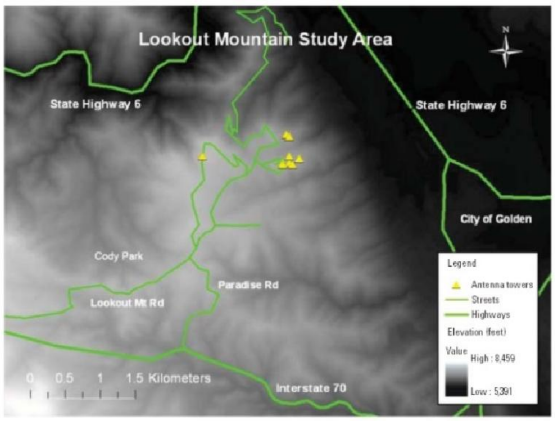

Figure 2.6 RF measurement area over Lookout Mountain, USA [28].

A further extension of this perception that the body is much like an antenna, in a solely outdoor environment it therefore lends itself as being a surface for harvesting solar energy. There are such devices that use the photovoltaic effect to harness the sun's rays; costing around 205USD this solar vest has 4 panels in its rear that can produce up to 4.2W [29].

Figure 2.7 Solar vest [29].

Figure 2.8 Using cockroach as a biofuel-cell [30].

Harvesting of chemical energy from living organisms has been reported [30]. Electrodes were inserted into a blood sinus in the abdomen of a species of cockroach (Discoid Cockroach). These specialised electrodes were part of a Tr|O2 biofuel cell that is fuelled by the disaccharide trehalose and oxygen from the atmosphere. The bio-fuel cell was able to generate approx. 55µW/cm2 which rose to approx. 100µW/cm2 after 45 minutes

[30]. This type of energy harvesting contributes to a research aim to exploit chemical energy to power a range of in vivo sensors to gather data that may aid clinicians in medical diagnostics.

2.3 Bio-kinetic Energy Harvesting Devices

Romero et al [31] looked at 23 different papers of piezoelectric, electrostatic and electromagnetic based devices suitable for portable or wearable applications and concluded that actual devices with sizes around 1cm3 produce hundreds of microwatts and generators with sizes over 10cm3 produce mill watts of power. Figure 2.9 is an adaption of the Romero literature collection with additional papers; only papers that used devices suitable for harvesting energy from the human body in the last 13 years are presented here. The list of devices with pictures and extra detail in Table 2.2 all feature in Figure 2.9.

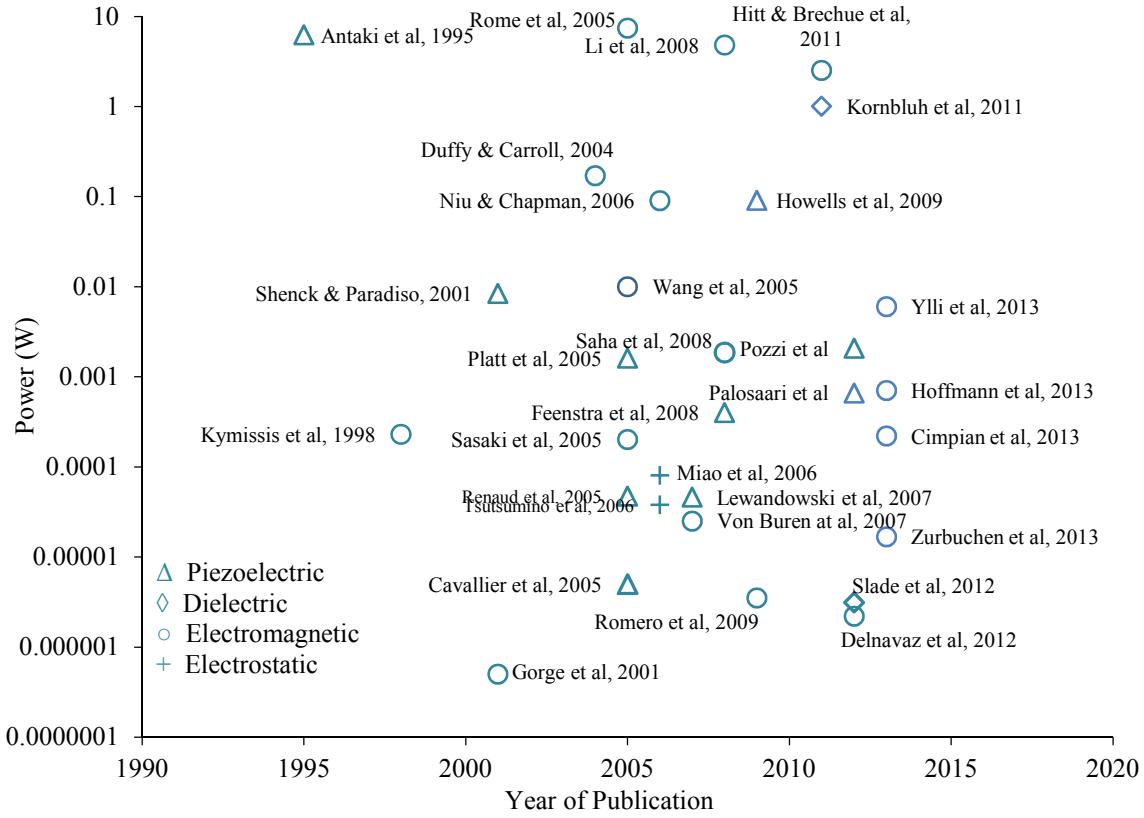

Figure 2.9 Electrical power generated by potential wearable piezoelectric, electromagnetic and electrostatic EHDs in terms of year of publication. [32][33] [34] [35] [36] [37] [38] [39] [40][41] [42][37]

Table 2.2 shows a list of harvesters designed to harvest energy from the human body from the kinetic energy of breathing and walking to the thermal energy from the surface of the skin. There are many factors to consider when designing a bio-kinetic harvester. One of the key performance factors is power output as it dictates what application is feasible for the device to power. Other factors include interaction with the user, robustness of the harvester and ability to cope with environmental factors. The thermo electric generator (TEG) that was integrated into a shoe [20] gives an opportunity to explain these factors in more detail. Although the TEG does not cause disruption in terms of size when retrofitting into the shoe there are some negative interactions with the user that are apparent e.g., the comfort of the user is compromised as without a control system to limit the function of the TEG it would not only pump waste heat from the user but also start to pump core heat from the user. The TEG also has environmental limitations, as it is a heat pump it needs a heat gradient between the user temperature and the ambient temperature to function. If it is a hot day then the heat gradient will be more difficult to achieve seeing at the person is likely to be overheating and the air temperature would also be hot. For extremely cold days the user would be warmer than the ambient temperature which would create a high temperature gradient however, on a cold day the user would find discomfort in giving its much needed thermal energy away. Surprisingly the human breathe harvester [18] does not impede breathing or require extra exertion by the user. However, it is unlikely that the positive aspect of generating 3μW from breathing outweighs the disruptive nature of wearing a face mask. The leg brace harvester designs of Li *et al* [43] and Slade *et al* [44] may also provide some discomfort in use. The leg brace by Li *et al* was able to harvest 4.8W, however, the light pressure and resulting friction caused by the leg brace during leg swings would be likely to cause skin soreness over long periods of time. Although there may also be some uncomfortable pressure on the limbs, the partially shoe embedded (housed on a connection between ankle and foot) electromechanical device called the ‘soldier Power Regeneration Kit’ or SPaRK was capable of producing 2.5W during a fast walk of 4.8 km/hour (3mph) [45].

After the literature search the highest power producing device found was a back-pack integrated electromagnetic generator that produced an approximate average power of

7.37W [46]. One down side to this back-pack integrated device is that it weighs 5.6kg. When considering a typical British army section soldier carries 2.78kg in spare batteries, depending on the mission length, the army may still choose to send the soldier on a mission with batteries.

Although the higher power producing MEHDs are not necessarily fully shoe-embedded, the current devices in the literature are still either heavy, bulky or require a slight exoskeleton which may not suit the user. This thesis attempts to develop a device that can be retrofitted into a shoe with low impact for the user i.e., little to no adaption time needed and no loss of comfort for the user.

Table 2.2 Overview of human based EHDs.

Picture	Energy Type and Source	Transduction Type	Device Descriptions
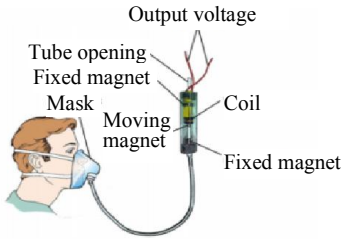	Energy: Kinetic Source: Breathing Date: 2012	Electromagnetic	A free magnet is actuated by pressure fluctuation during breathing, produced 3µW [18].
	Energy: Thermal Source: Wrist Date: 2007	Thermoelectric or Seebeck Effect	The five-to-seven indoor wrist watch produced an average power of 250µW [19].
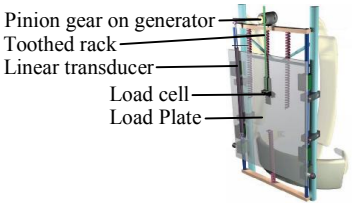	Energy: Kinetic Source: Gait Date: 2005	Electromagnetic	A toothed rack connected to the load of a backpack transfers vertical movement of the toothed rack to a pinion gear attached to a DC motor acting as a generator; producing an approximate average power of 7.37W [46].

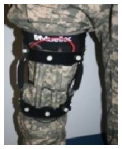	Energy: Kinetic Source: knee swing Date: 2012	Dielectric elastomer	Dielectric elastomer or Electro active polymers EAPs; for one leg brace during a brisk walk produced an average power of 3.13µW [44].
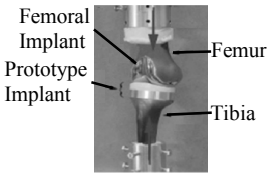	Energy: Kinetic Source: Knee compression Date: 2005	Piezoelectric	Piezoelectric transducer integrated into a total knee replacement prosthetic, produced 1.6mW [21].
	Energy: Kinetic Source: Knee Swing Date: 2008	Electromagnetic	Adapted leg brace with rotational kinetic energy recovery via electromagnetic transduction produces and average power of 4.8W [43].
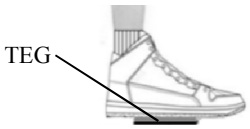	Energy: Thermal Source: Foot Date: 2013	Thermoelectric or Seebeck Effect	Thermoelectric generator in testing use a male subject 0.31mW over a 20Ω load [20].
	Energy: Kinetic Source: Gait Date: 2010	Electromagnetic	In gait a nylon cord is used to put on a low-pitch ball-screw which in-turn spins a generator producing an average power of 2.5W during a fast walk of 4.8 km/hour (3mph) [45].

2.4 Harvesting from Foot Fall

Although the body produces many types of energy, the majority of papers published focus on harvesting kinetic energy or bio-kinetic energy. This is not to say that kinetic energy should be the only focus, its high amount of interest is more likely a consequence of kinetic energy being the most abundant form of waste energy given by the human body and in a general sense it is easier to harvest higher amounts of energy from an abundant source than a sparse source. A study by Starner [15] shows the highest mechanical power outputs from the human body whilst walking were from arm movements and foot fall, producing 60W and 67W, respectively [15]. These movements can be predictable and follow a pattern, although this pattern itself may be complex this has not deterred research.

There are many piezoelectric based energy harvesters known in the research community, many of which work at resonance in order to increases power output. For harvesting bio-kinetic energy however, this frequency range of piezoelectric harvesters becomes relatively low i.e., Shenck et al [47] tested a bio-morph shoe based device that worked at 0.91Hz, the orthopaedic implant based device by Platt et al [21] was tested at 1Hz and a backpack strap based device by Feenstra et al [48] operated at 5Hz. In terms of working forces harvesters by both Shenck et al [47] and Platt et al [21] were designed to operate under an applied force of 900N, the backpack strap based device by Feenstra et al [48] operated at around 220N.

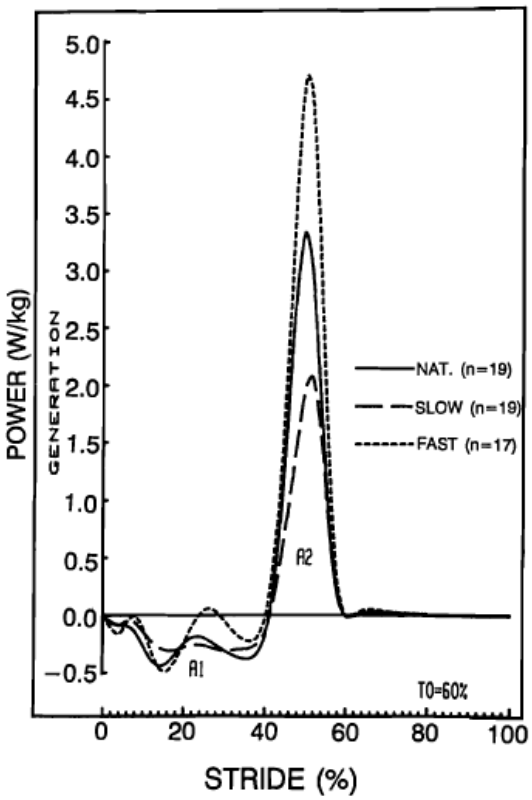

Figure 2.10 Mechanical power generation and absorption profiles at the ankle for three walking-speed cadences: natural, slow and fast. A1 is the absorption of energy as the plantar flexors lengthen and the leg rotates forward over the foot, TO=toe-off. A2 is the push-off power by concentric plantar flexor activity [49].

From medical based research Winter et al [49] reported the instantaneous mechanical power (per kg of a person) generated by the ankle at three different speeds. In Figure 2.10, A1 is the absorption of energy or region of negative power when there is eccentric plantar flexion; the foot moves away from the body so that the angle between the shin and top of the foot increases, little exertion is made by the foot during this movement. As the foot moves back, heel-off starts to occur and directly following this is the pre-swing phase where the toe starts to lift off (TO=toe-off). During TO (A2) there is concentric plantar flexion where the foot is again moving away from the body but this time also producing a burst of propulsive energy, during this phase the foot is pushed into the ground in order to provide lift for the leg. This A2 phase represents over 75% of all energy generated in the stride period [49] and is shown as the large peak in power on the graph in Figure 2.10.

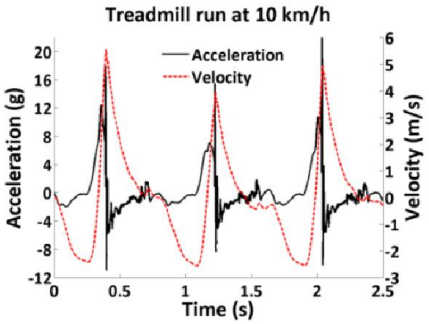

(a)

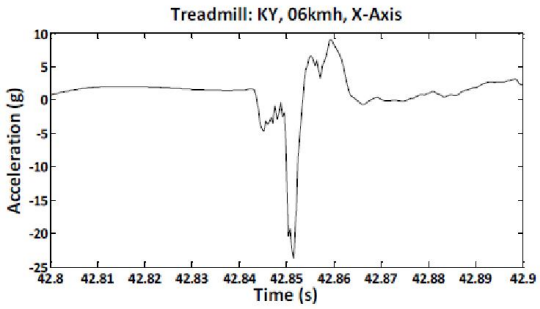

(b)

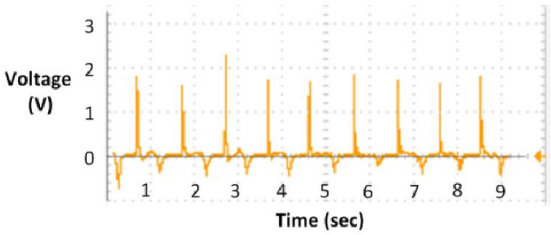

(c)

Figure 2.11 (a) acceleration measured perpendicular to the ground of the heel of the foot during gait with integrated velocity, speed of gait was 10 kmph [50], (b) acceleration perpendicular to the ground of the heel of the foot during gait, speed of gait was 6 kmph [51] and (c) voltage output from shoe-integrated screen-printed piezoelectric shoe insole EHD, at a gait of 1strike/second [52], open circuit voltage contribution from only the piezoelectric elements at the sole of the foot.

A similar profile to the one in Figure 2.10 can be seen in Figure 2.11 (a) & (b) where acceleration measurements were taken during experimental testing of shoe-integrated EHDs. Figure 2.11 (c) shows the output voltage of a shoe-integrated screen-printed piezoelectric shoe insole EHD.

As mentioned previously in a study by Starner [15] the highest mechanical power outputs from the human body whilst walking were found to be from arm movements and foot fall, producing 60W and 67W, respectively [15]. The high powers harvested from foot fall and/or gait stated by the Starner study [15] are reflected in the high proportion of EHDs in Figure 2.9 that use devices integrated into shoes i.e., the graph in Figure 2.9, shows a large range of EHDs where by a high proportion of devices are demonstrated as EHDs retrofitted into shoes. Extracting the shoe based EHDs from Figure 2.9 to give Figure 2.12 we are left with 11 existing papers. The list of devices with pictures and extra detail in Table 2.3 all feature in Figure 2.12.

It was due to the Starner [15] study that this thesis focused on harvesting energy from foot fall as the high power available from the process of walking was an attractive energy resource to harness.

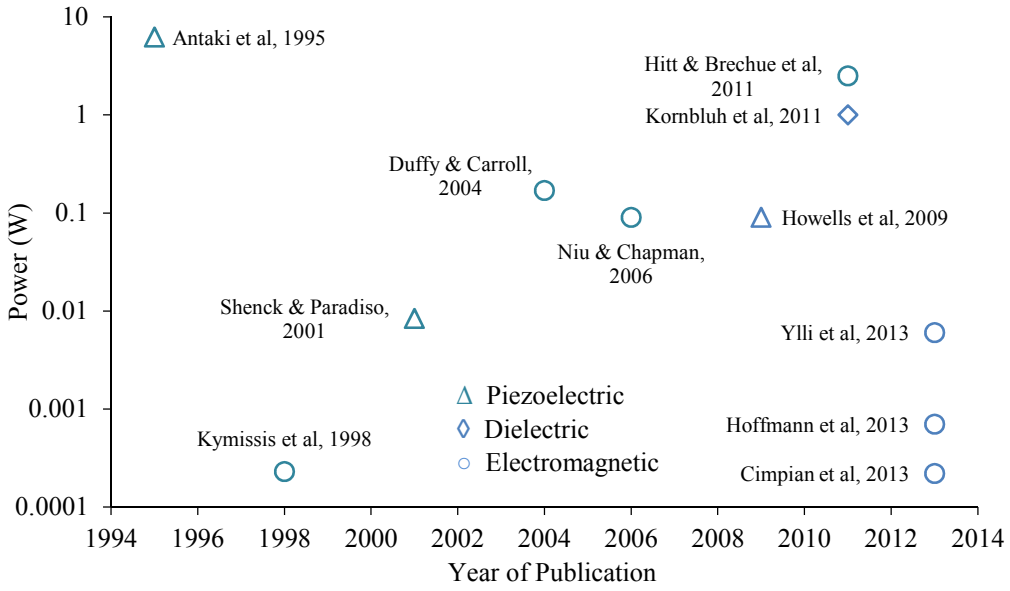

Figure 2.12 Electrical power generated by bio-kinetic EHDs embedded into a shoe in terms of year of publication.

The following devices discussed can be found listed with extra detail in Table 2.3. Table 2.3 presents shoe-based harvesters as opposed to the more general harvesters of human body energy presented in Table 2.2. There have been multiple approaches to integrating an EHD into a shoe with variations on transduction techniques. Antaki *et al* [53] placed a shaft like piezoelectric device that spanned the length of the shoe and used a hydraulic force amplifier acting on a piezoelectric stack. When comparing to other devices listed in Table 2.3, this device was able to produce a relatively high power of 6.2W. Another shaft like device spanning the length of the foot, this time electromagnetically based, produced a much lower power of 170mW [54]. A possible draw-back of these devices is the overall stiffening of the shoe sole. A stiffening of the shoe sole could impede walking, however, steel toe-cap boots or thick soled shoes would suffer less of a downgrade in comfort with a this type of retrofitted EHD. There have also been devices that sit external to the shoe, Hitt *et al* [45] developed an electromagnetic based device that utilises the waste energy of the ankle rotation during foot fall, almost working as an external Achilles tendon, this SPaRK device produced a relatively high power of 2.5W. Another device also placed external to the shoe is by Kymissis *et al* [55], however, this electromagnetic device produced a relatively low power of 0.23mW. These externally based devices are both bulky and the SPaRK device would have the potential to not cause skin irritation through friction over time but could also be hazardous if its multiple brackets and straps caught to things during a soldier's mission.

If one was to focus on devices with less disruption to the user we generally see lower powers harvested. There is the low-profile piezoelectric based device that is integrated into a section of the sole of a shoe by Shenck *et al* [47], this device only managed to harvest 1.3mW. Another low bulk device is the electromagnetic based device integrated into the sole of the shoe by Ylli *et al* [50] that was able to harvest 10mW. By far the best compromise between bulk and power output is the dielectric elastomer based device integrated into the sole of a shoe by 1W Kornbluh *et al* [56], this device could harvest 1W.

From the devices presented in Table 2.3, there is little to no mention of design approach, specifically whether designs were designed to be robust by assuring that

working stresses of the devices do not exceed yield stresses. No mention of safety factors was made either, which is a good indication of conservative and robust outcomes. In addition to this, stating a safety factor may also aid when attempting to compare a harvesters power output. For instance, if there are two piezoelectric harvesters both with the same power output but one has a safety factor of two, it suggest that the harvester with a safety factor of two operates with almost double the efficiency.

Considering the impact that a bulky shoe based harvester may have on the user, this thesis attempts to develop a device that can be retrofitted into a shoe with low impact for the user with the addition of design considerations such as a safety factor that insures the working stress of the final device design do not exceed half it yield stress.

Table 2.3 EHDs integrated into shoes.

Picture	Energy Type and Source	Transduction Type	Device Descriptions
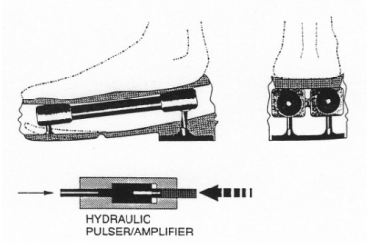	Energy: Kinetic Source: Heel strike Date: 1995 Authors: Antaki et al	Piezoelectric	A hydraulic force amplifier actuates a piezoelectric stack all integrated into a shoe; initial experiments show that 6.2W could be generated [53].
	Energy: Kinetic Source: Gait Date: 2010 Authors: Hitt et al	Electromagnetic	In gait a nylon cord is used to put on a low-pitch ball-screw which in-turn spins a generator producing an average power of 2.5W during a fast walk of 4.8 km/hour (3mph) [45].
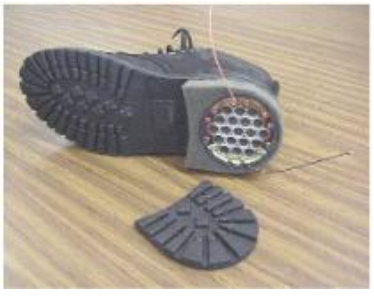	Energy: Kinetic Source: Heel-strike Date: 2011 Authors: Kornbluh et al	Dielectric Elastomer	During gait a dielectric elastomer which is also used to seal a coupling gel inside a frame structure is forced to deform through holes in the frame under the pressure

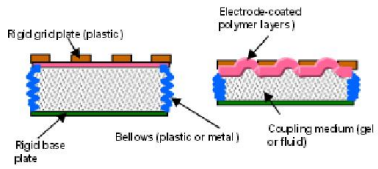			exerted by heel strikes. Although with no accompanying results this shoe-integrated dielectric elastomer is said to be capable of producing 1W during gait [56].
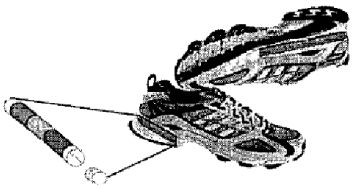	Energy: Kinetic Source: Gait Date: 2004 Authors: Duffy et al	Electromagnetic	Sliding magnetic and stationary coils (150 turns) running the length of the shoe could generate 170mW of power every second for two steps [54].
	Energy: Kinetic Source: Gait Date: 2006 Authors: Niu et al	Electromagnetic	Foot motion slide generator produced an average power of 90mW [57].
	Energy: Kinetic Source: Heel strike Date: 2009 Authors: Howells et al	Piezoelectric	Heel strikes turn teeth of the cog wheel which in-turn deflect four PZT-5A bimorph stacks simultaneously to generate electrical energy of up to 90mW [58].
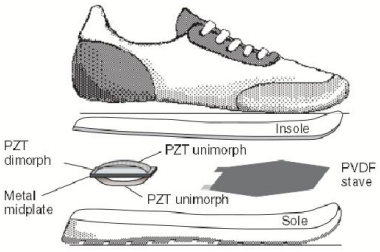	Energy: Kinetic Source: Heel strike Date: 2001 Authors: Shenck et al	Piezoelectric	Two devices integrated into a shoe producing 8.4mW from uni-morph piezoelectric structure and 1.3mW from stave [47].

			An electromagnetic generator consisting of a pipe with two external coils of wire wrapped around each end with a central magnet that moves freely within the tube. Acceleration due to heel strike causes the magnet to move and induce a voltage in the coil windings. When retrofitted into the show the device was able to harvest an average power of 6mW at a walking speed of 2.5mph. Moreover, at a faster walking speed of 3.7mph the device was able to produce and average power of 10mW [50].
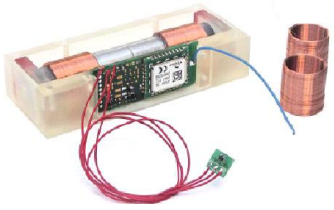	Energy: Kinetic Source: Heel strike/swing Date: 2013 Authors: Ylli et al	Electromagnetic	
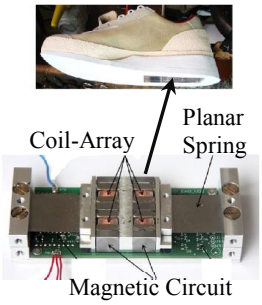	Energy: Kinetic Source: Heel strike Date: 2013 Authors: Hoffmann et al	Electromagnetic	A magnetic circuit is suspended between two cantilevers, heel strike causes the magnetic circuit to move relative to the fixed magnets. At a walking speed of 1Hz a continuous average power of 0.7mW was harvested [51].
	Energy: Kinetic Source: Heel strike Date: 1998 Authors: Kymissis et al	Electromagnetic	Electromagnetic generator mounted on a shoe produced an average power of 0.23mW [55].

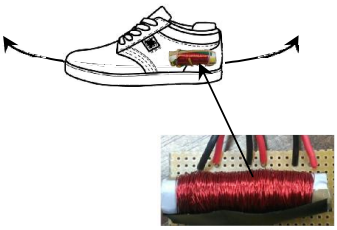	Energy: Kinetic Source: Heel strike/swing Date: 2013 Authors: Cimpian et al	Electromagnetic	Pipe containing a free moving magnet that induces a voltage in wire coils during the swing phase of the foot during gait, for a running speed of 6.2mph the device harvested an average continuous power of 0.22mW[59].
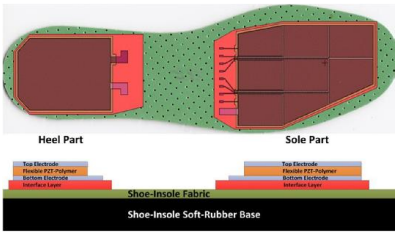	Energy: Kinetic Source: Heel strike Date: 2013 Authors: Almusallam et al	Piezoelectric	The screen-printed piezoelectric device produced 2 Volts in open-circuit [52].

2.5 Transduction Techniques for Bio-kinetic Energy

Energy harvesting is becoming a large area of study and many papers have been published that cover a wide range of harvesting techniques. Energy can be harvested from ambient sources such as kinetic (vibration or impact force) [60], [61], [62], [14] and fluid flow [63] by using one of the three most popular transduction mechanisms: piezoelectric [48], electromagnetic [64] and electrostatic [65]. Electromagnetic [66], Thermal [62], [67], solar [68] and radio frequency energy [69] can also be harvested by using specific devices. Furthermore, combinations of transduction mechanisms, also known as hybrids, have been recently reported. For example, piezoelectric and electromagnetic transduction techniques have been combined [70], [71] to harvest kinetic energy, and the combination of piezoelectric with magnetostrictive [72] transduction techniques, to harvest electromagnetic energy has been reported. Dielectric elastomers have also showed promise with recent papers relating to bio-kenetic energy harvesting [56] & [44].

The two papers representing electrostatic transduction, see Figure 2.9, both produced a small amount of power, both were made using MEMS fabrication techniques and are relatively small in size (micrometer range). As Romero *et al* [31] demonstrated, device size is proportional to power output which could explain why the electrostatic devices were such low power producers, this is because they were small in size. Power has been focused on here as a measure of fitness, however, efficiency and power density are also indicators of a successful device. It can be more challenging to compare devices on such merits if all the detail for calculation isn't presented within the papers.

2.5.1 **Electromagnetic vs. piezoelectric**

Although the data set in Figure 2.12 is small, it shows that since 1994 to 2013, 7/11 shoe based devices have been electromagnetic compared with 4/11 based on piezoelectric transduction. Therefore, the higher power producing devices are dominantly electromagnetic transduction and second to this, piezoelectric. Experiments using electromagnetic transduction are likely popular due to their inherent simplicity and cheap construction. Electromagnetic devices also tend to have a low internal impedance which is often a specification when linking an EHD with a battery charging circuit. Conversely, high performance piezoelectric material is often expensive and unless used in a multi-layer configuration has very high internal impedances.

If the power outputs of electromagnetic devices and piezoelectric devices are compared it is clear that electromagnetic devices generally produce higher power outputs, moreover, they produce a more usable current level than piezoelectric devices (that historically produce low current unless a multilayer configuration is employed). In terms of output power the electromagnetic device would seem superior based on harvesters in current literature.

2.5.2 **Piezoelectric materials and shoe-based bio-kinetic energy harvesting**

However, another important factor when designing or choosing an EHD is the device suitability with its input energy (source of waste energy). In the context of bio-kinetic energy harvesting, in particular with device-shoe integration, I will compare kinetic energy source scenarios. Electromagnetic devices tend require large displacements at

low force, however piezoelectric transducers can take considerably higher forces and displace to a much lesser degree. For the application of integrating an EHD into a shoe a piezoelectric transducer would seem more suitable than an electromagnetic transducer; the piezoelectric transducer provides the capabilities of being able to work under the high forces of body weight and displace very little, thus utilising the force input and also providing no loss of comfort (through lesser displacement) to the person wearing the specialised shoe. Piezoelectric devices also tend to be more compact or have potential to be more compact whereas the power produced by electromagnetic devices is proportional to the amount of wire turns making many electromagnetic devices bulky. Therefore, piezoelectric material was thought to be a good candidate as a transduction mechanism for the shoe-based MEHD.

2.6 The Cymbal Device

During the early stage of this thesis, an existing device called the Cymbal was studied because it has the ability to deform the piezo-element relatively effectively and it has a potential to be used for bio-kinetic energy harvesting. Kim *et al* [7] reported that the addition of a top and bottom endcap to a piezoelectric disk gave an enhanced electrical output, about 40 times more than using a piezoelectric disk alone, this claim was later confirmed by using the CPC-FEM developed in this thesis.

The Cymbal uses mechanical force amplification via its endcaps, this is not the only use of force amplification, as mentioned previous Antaki *et al* reported a piezoelectric stack integrated in a shoe with hydraulic amplification that produced a relatively high power output when compared to other shoe-integrated devices [53].

2.6.1 **Origin of the Cymbal and it's use as actuators**

The fundamental structure of the Cymbal was a more compliant adaption to the moonie [73], its predecessor, seen in Figure 2.13. Simply by removing some of the endcap material, force transfer between the endcaps and PZT disk was found to be more effective.

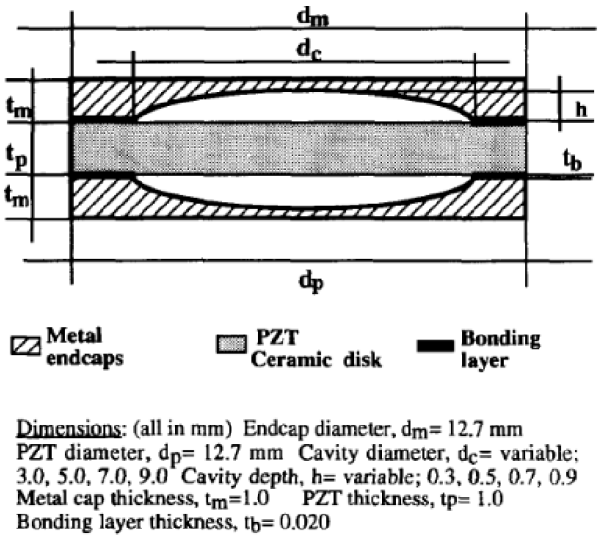

Figure 2.13 The Moonie transducer [73].

The Cymbal as a structure is not new; Cymbals have been used as actuators, such as hydrophones [74][75], pumps [76] as seen in Figure 2.14, and in ultrasonic drug delivery as seen in Figure 2.15.

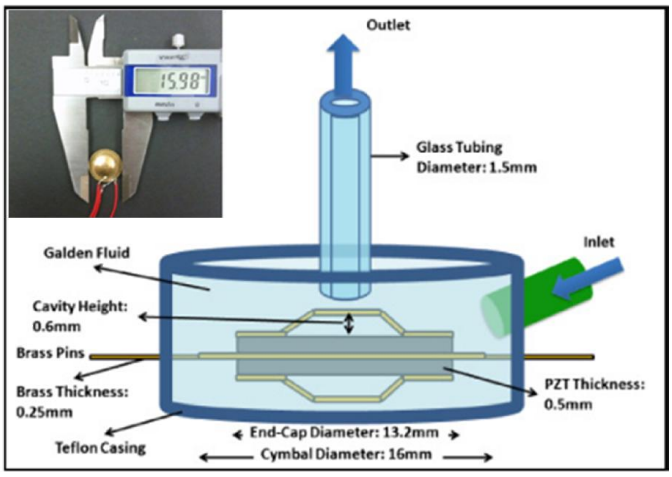

Figure 2.14 Cymbal as a pump. Inset; Cymbal [76].

Figure 2.15 An array of Cymbal's is driven at ultrasonic frequencies to excite the a drug to be delived through the skin of the patient. The drug then travels through the skin of the patient [77].

The slotted-Cymbal [78], shown in Figure 2.16, is an example of the extent to which the Cymbal has been adapted. The slotted-Cymbal is a much like the original Cymbal but has many slots in its top and bottom endcaps that release the tangential stresses allowing for more flexibility in the structure. The slots allow for the resonant frequency of the Cymbal to be lower and the displacement of the endcaps to be higher, which are the desired characteristics for certain hydrophones where high acoustic-powers at low frequencies are required. Although the slots were an advantage for lower resonant frequency and having a higher efficiency of force transfer between the endcaps and piezoelectric disk, the amount of slots was found to affect the rigidity of the structure and 24 slots was stated as a stated as a sufficient trade-off. No clear indication of generative force magnitudes were given as the slotted-Cymbal was designed for actuator purposes, however, it is likely that its working force range is low and therefore would not be suitable for harvesting bio-kinetic energy.

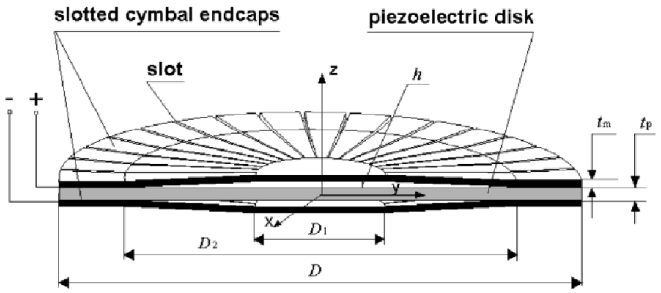

Figure 2.16 Slotted Cymbal [78].

2.6.2 **Cymbal-like devices**

Many variants of the Cymbal have been reported and are mentioned here on merit that they claim to be related to the Cymbal in function.

A device similar to the Cymbal but named a Piezoelectric metal cavity PMC has been reported by Lam *et al* [79]. The reason why the PMC is similar to the Cymbal is that it uses electrical contributions of both d_{33} and d_{31} from of a piezoelectric disk. Figure 2.17 shows the PMC; a circular shaped actuator with a two exterior uni-morph piezoelectric disks upon respective brass substrates with a steel ring sandwiched in-between. In theory this PMC could be made by attaching two piezoelectric based buzzers (readily available) either side of a steel ring. The steel ring acts to hold the outer piezoelectric-substrate layers in a simply supported state and also to combine the magnitudes of the deformation efforts of both top and bottom piezoelectric-substrate pairs. The PMC generated 16μm under a ±77V driving voltage. A point of interest in this paper was that it described how it calculated the effective piezoelectric coefficient of the PMC. The effective piezoelectric coefficient d_{33} was obtained for both the PMC and for a Cymbal of similar size. First, the charge generated by the actuator in response to an applied static load normal to its surface was measured and plotted (Force vs. Charge). Then the slopes of these curves were used to determine the d_{33} (pC/N). The PMC had a higher effective coefficient (~40,000 pC/N) than the Cymbal (d_{33} ~20,000 pC/N). During the experiment of obtaining the effective coefficient a pre-stress of 3N was applied to the PMC and Cymbal, however, they were not demonstrated to work under forces exceeding 0.6N, which would mean the PMC would be unsuitable for harvesting bio-kinetic energy.

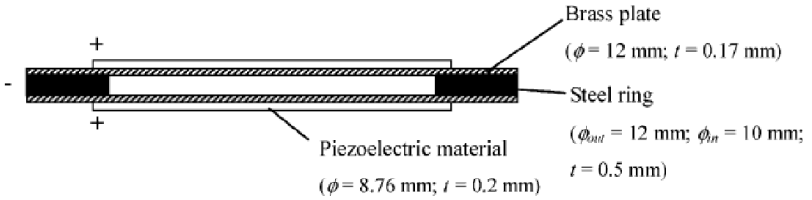

Figure 2.17 Drawing of a Piezoelectric metal cavity (PMC) actuator [79].

The displacement amplification device (DAM) is described as a modified Cymbal mechanism used in a micro punching system [80]. The orientation of the piezoelectric material in the DAM was not stated, therefore, its similarity in terms of how the piezoelectric material operated was not determined. The DAM combines 3 'Cymbal-like' structures to give a high speed displacement. In addition to the piezoelectric orientation (poling direction) not being known, the DAM differs to the original Cymbal design in the following ways; the shape is rectangular and not circular, it also has closed ends, whereas the Cymbal has PZT running right to the edges. Even though the DAM seems to differ from the Cymbal it was felt important to mention on the basis that it was explained as a modified Cymbal.

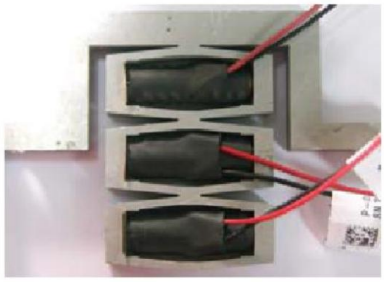

Figure 2.18 Photograph of Cymbal-type DAM [80].

Following on the trend of variants on the Cymbal device, there are Cymbals based on rectangular shape [81]. Figure 2.19 shows a cross section of a rectangular Cymbal that is able to produce 14mW at 500Hz (load resistor 74Ω, force 0.55N).

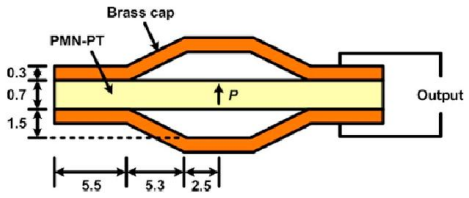

Figure 2.19 Schematic of rectangular Cymbal transducer [81].

Another rectangular shaped Cymbal reported is the rectangular Cymbal array. Shown in Figure 2.20 this non invasive drug delivery system is a suggested improvement to the Cymbal array previously mentioned and depicted in Figure 2.15 [77]. The array is

driven at ultrasonic frequencies to excite the drug to be delived, the drug then travels through the skin of the patient. The rectangular array was found to be more effective at dispering the drug that was to be delivered (which was a desired characteristic). This device was designed for high frequency and low force which would render it unsuitable for bio-kinetic energy harvesting, however, it is interesting to see that changing the shape of the Cymbal works well for some applications. The Cymbal was origionally circular and this succesful demonstration of a rectangular configuration posses the question, does the Cymbal have to be defined by its shape or instead can it be defined soley by the nature of which it deforms its piezoelectric element?

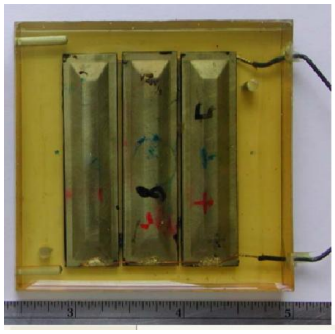

Figure 2.20 Rectangular Cymbal array for transdermal insulin delivery [77].

2.6.3 **Cymbals used as EHDs**

Now Cymbal's will be discussed in terms of their applicability as EHDs. Cymbal's have been experimentally studied as EHDs to harvest energy from high frequency car vibrations [60], [81]. In terms of the force capability of the Cymbal, Kim *et al* [7] reported that a Cymbal of approx. Ø30mm could not withstand forces higher than 50N [81], in a similar study Kim *et al* reported testing a cymbal at 70N. Although 70N is a higher working for than any of the Cymbals in actuator applications it is still small in comparison to forces associated with the human body in gait (1000N). A study by Palosaari *et al* [82] reported testing of a Cymbal at 24.8N, which again is relatively low for forces associated with the human body in gait.

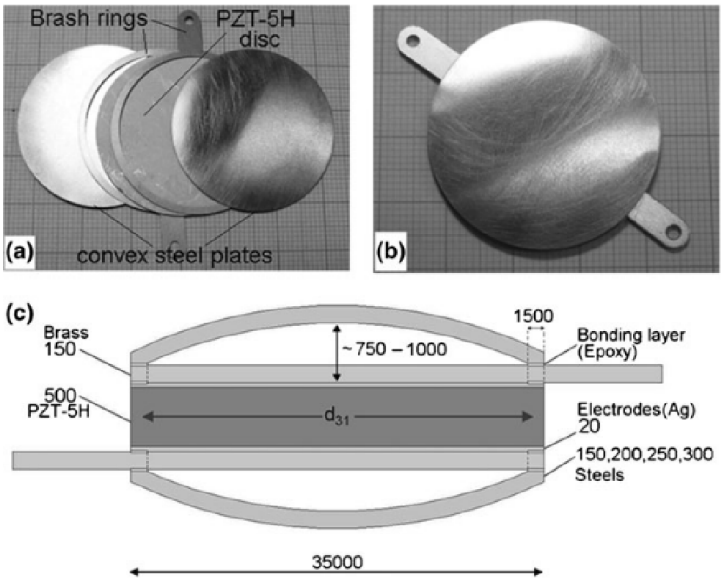

Figure 2.21 Cymbal device with a) Cymbal before assembly, b) assembled Cymbal, and c) cross-section of Cymbal in µm

At the beginning of this thesis the Cymbal structure in the transducer form had not been used to harvest energy from low frequency energy sources such as in the 1-10Hz range, which is why this thesis chose to study its potential further. However, a paper by Palosaari *et al* [82] was published in 2012 that suggested the use of the Cymbal for retrofitting into the shoe. The Cymbal was not demonstrated in a shoe application and instead tested with a force load applied by using a computer controlled piston drive system. The Cymbals of Ø35mm was tested at a low frequency and force of 1.19Hz and 24.8N and from this harvested 0.27mW. Two initial questions were posed, 1) why the Cymbal can enhance the power output? And 2) could the Cymbal be used as an EHD to harvest lower frequencies 1-10Hz and forces common to human gait for scavenging waste bio-kinetic energy.

2.6.4 **Cymbal function**

A Cymbal consists of a piezoelectric disk sandwiched between two metal endcaps with shallow cavities. The brass endcaps act as a mechanical force amplifier to increase the force that acts on the piezoelectric disk in the *x*- and *z*-direction. When excited, the endcaps deform the piezoelectric disk in the *x*-, *y*- and *z*-directions. Please note, the co-ordinate systems chosen for use throughout this thesis originated from the ANSYS model.

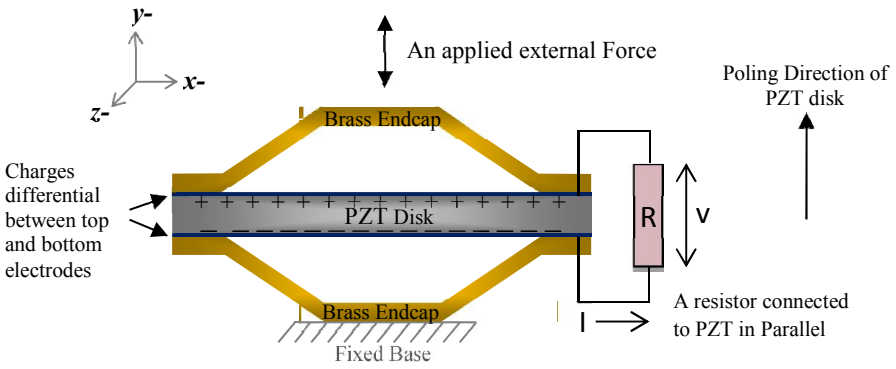

Figure 2.22 Schematic of the Cymbal structure.

The applied force in the *y*-direction produces some charge due to the piezoelectric effect of the d_{33} piezoelectric strain constant. Due to the angle of the endcaps, the force is amplified in the *x*- and *z*-directions and produces the charge due to the d_{31} piezoelectric strain constant. Hence an equivalent strain constant, d_{33}^{eff}, can be written as follows [7]: Where *A* is related to on the endcap leverage.

$$d_{33}^{eff} = d_{33} + \left| A d_{31} \right| \tag{1}$$

$$A = \frac{cavity\ \ radius}{cavity\ \ depth} \tag{2}$$

As mentioned previously the co-ordinate systems chosen for use throughout this thesis originated from the ANSYS model. However, it is different from the more commonly used axis orientation. Figure 2.23 shows the difference between the axis orientation used in this thesis and the more commonly used axis orientation. The only difference is that the poling direction used in this thesis is in the *y*-direction as opposed to the *z*-direction.

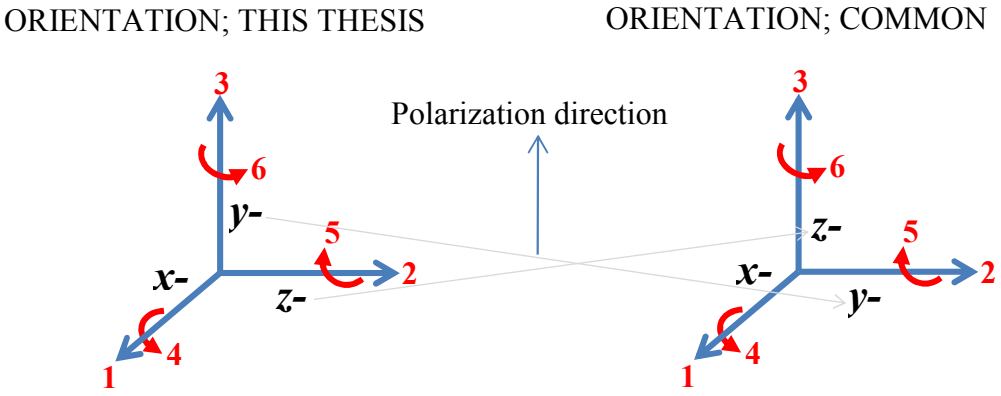

Figure 2.23 Axis orientation used in this system and more commonly used axis orientation.

Figure 2.24 shows how different *d* constants are defined according to the commonly used axis orientation.

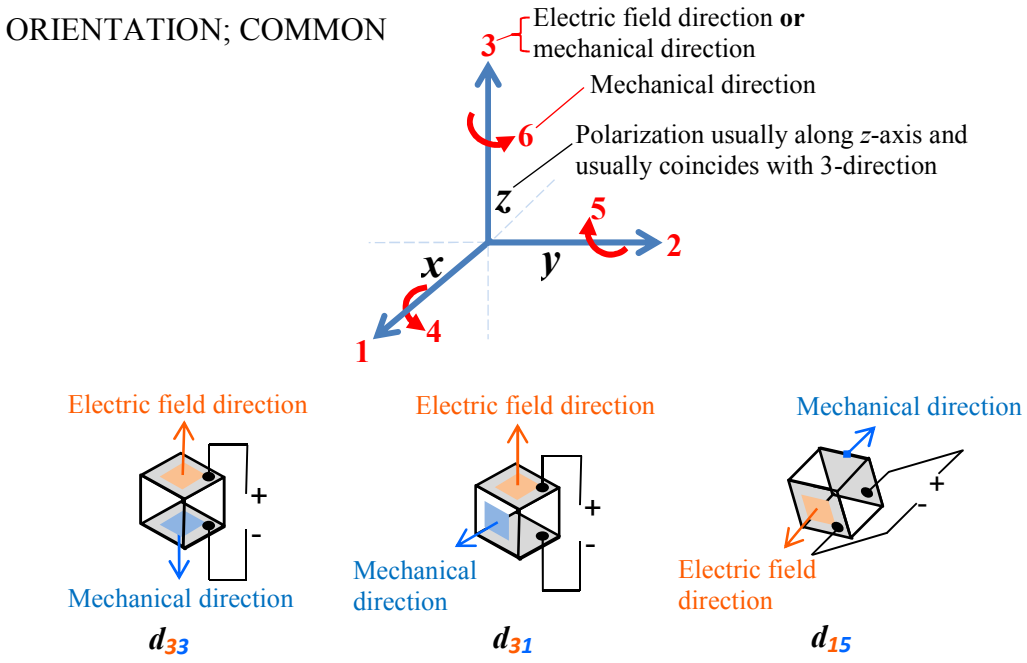

d*direction electrodes are perpendicular to, direction of applied stress* ***or*** *induced strain*

Figure 2.24 Example of *d* constant definitions in relation to the more commonly used axis orientation.

2.7 Review on Cymbal Device Modelling and Simulation

The finite element model used in this thesis was a couple piezoelectric-circuit finite element model (CPC-FEM). The CPC-FEM was used to design the novel PFT later presented in this thesis. The following section will focus on what modelling approaches have been used to previously study the Cymbal. The same reasons as to why the CPC-FEM was a suitable to study the Cymbal were also true for the study of the PFT device.

Many parameter studies have been carried out involving the Cymbal transducer and/or actuator that focus primarily on physical aspects such as resonance behaviour and mechanical stress states.

Table 2.4 Articles on the Cymbal that focus on the performance characteristics of frequency response.

Paper Focus	Frequency Range	Approach	Electrical Related output studied
Design parameters effecting performance, Dogan (2006)[83]	10-200kHz	FEM	-
Parameters affecting performance, Haijun (2010)[84]	0-6kHz	FEM vs. Exp	-
Resonance behaviour and fabrication concerns, Meyer (2002)[85]	20-60kHz	FEM vs. Exp	-
Resonance Characteristics, Shilin Wu (2009)[86]	20-100KHz	Analytical vs. FEM	-
Mechanical approach to defining effective piezoelectric coefficient, P Ochoa (2002)[87]	-	Analytical vs. Exp	-
Selecting materials to control resonance, Tressler (1997)[88]	10-50kHz	Analytical vs. Exp	-

Research of the Cymbal has been carried out using analytical modelling, numerical modelling (FEM) and experimental techniques. The Cymbal has been experimentally studied where focus was on output power e.g., a Cymbal was demonstrated to harvest 100mW from automotive vibrations [60] (under 70N loading at 200Hz over at 200kΩoptimal resistor) and in a separate study for harvesting low frequency compressions [89] producing 0.27mW (under 24.8N at 1.19Hz over 3.6MΩoptimal). Of

the studies that included numerical modelling (FEM) focus was mainly on the effects relating to resonance behaviour of the Cymbal structure [84], [85] and [88]. Some numerical modelling (FEM) studies of the Cymbal did provide a form of electrical analysis i.e., Ochoa et al [90] looked at the relationship between mechanical stress and electrical potential distribution, however, focus was on the characteristics of the relationship and not of quantifying the electrical output. Another numerical study, by Zhao et al [91], investigated the potential the Cymbal device had as an EHD when embedded into a pavement, electrical output was in the form of electrical energy (measured in Joules). From an energy-harvesting perspective it is important to know the power output of a device so that you can gauge its appropriateness for application.

Table 2.5 Articles on the Cymbal that focus on electrical perfomance.

Paper Focus	Frequency Range	Approach	Electrical Related output studied
Energy harvesting of automotive vibrations, Kim (2006)[60]	10-200Hz	Analytical vs. Exp	Power
Energy harvesting Cymbal embedded in pavement, Zhao (2010)[91]	20Hz	FEM	Joules
Energy harvesting low frequency and low force, Palosaari (2012)[89]	1.19Hz	Exp	Power
Energy harvesting of automotive vibrations, Kim (2004)[92]	50-150Hz	Exp	Power
Mechanical stress study including bonding layers, Ochoa (2005)[90]	100Hz + 31kHz	FEM	Electrical Potential Distribution

Separate from the Cymbal domain there are design methods that can help predict piezoelectric electrical behaviours. An analytical approach by Dutoit et al [93] involves simplifying the mechanical structure to a single degree of freedom (SDOF) representation and develops governing equations based on both the mechanical equations of motion and the piezoelectric constitutive equations.

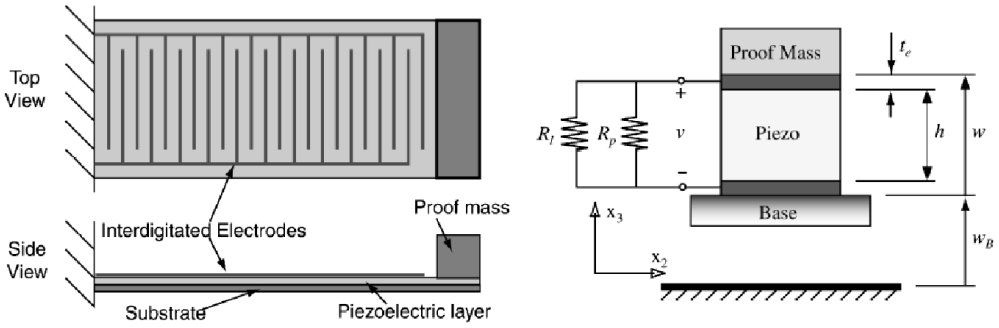

Figure 2.25 Left: Illustration of uni-morph, Right: Illustration of Single degree of freedom model [93].

The coupled governing equations are,

$$\ddot{w} + 2\zeta_m \omega_N \dot{w} + \omega_N^2 w - \omega_N^2 d_{33} v = -\ddot{w}_B \tag{3}$$

$$R_{eq} C_p \dot{v} + v + m_{eff} R_{eq} d_{33} \omega_N^2 \dot{w} = 0 \tag{4}$$

Where w is the relative displacement, w_B is the base displacement, v is the voltage, ζ_m is the mechanical damping ratio, ω_N is the natural frequency of the device, m_{eff} is the approximate effective mass, R_{eq} is the equivalent resistance of the resistive load and leakage resistance, R_l and R_p respectively, and finally the C_p is the piezoelectric capacitance. The governing equations were then evaluated using Laplace transforms to give the magnitudes of displacement, voltage and power output.

In a comprehensive review paper, Erturk et al [94] points out issues with many analytical modelling approaches and stresses that overly simplistic assumptions have been made in many distribution parameter solutions that lead to incorrect solutions. The distribution parameter solution is an extension and/or improvement to a specific analytical approach in order to improve accuracy of the final solution. The paper proceeds to address the issues it highlighted, even so, the analytical approach has been described as problematic for harvesters with complex structures. Therefore, at present, it can be stated that the analytical approach is appropriate for calculating outcomes for harvesters with low mechanical and electrical complexity for instance, simplistic

geometry and linear electrical components. In addition to these limitations the analytical approach is associated with the design of harvesters working at resonance.

The equivalent circuit method is a simplified representation of the core mechanical and electrical elements of a system. Figure 2.26 is an equivalent circuit where the mechanical contributions of a piezoelectric cantilever beam (with a single degree of freedom) is represented on the right-hand side and the electrical contributions on the left-hand side.

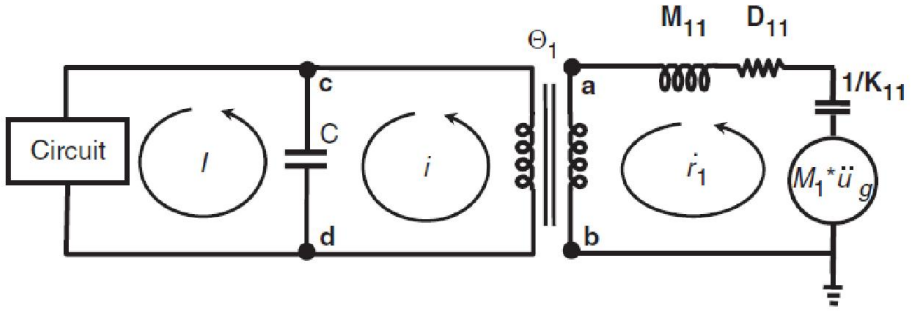

Figure 2.26 Equivalent circuit for a single degree of freedom electromechanical system [95].

Elvin and Elvin [95] used the analytical approach from Roundy and Wright [96] to determine the equivalent mechanical contributions. The equivalent mass M_{11}, stiffness K_{11}, damping stiffness D_{11} and electromechanical coupling Θ_1 of the mechanical elements are represented by an inductor, capacitor, resistor and ideal transformer, respectively, within the circuit. Once both mechanical and electrical equivalent circuit parameters are defined, the open source software program Simulation Program with Integrated Circuit Emphasis (SPICE) was used to evaluate the system.

Although the mechanical structure was of low complexity, the numerical modelling or system-level approach of Elvin and Elvin [95] by using SPICE, extended the capabilities to include non-linear electrical circuit components. Non-linear components are common to power management systems i.e., transistors which are used to make bride rectifiers.

Describing it as a tedious process, Yang and Tang [97] avoid completely the analytical approach for determining the mechanical contributions and instead use a more complete system-level approach to do so. Yang and Tang [97] explain in more detail how

identification of the required mechanical parameters for the equivalent circuit method was done by using Finite Element Modelling before using circuit modelling (SPICE) to evaluate the performance of the energy harvester. In separate work to the one previously mentioned, Elvin and Elvin [98] also used a system-level approach to determine the mechanical and electrical contributions. In addition, batch processing via Matlab software enabled the coupling of FEM and SPICE simulations, the general protocol is as follows:

- the mechanical structure is solved as a FEM with appropriate excitation to gain outputs of displacements and piezoelectric coupling voltage,
- the equivalent circuit in SPICE is updated with the latest coupling voltage from the FEM solution, a new coupling voltage is then extracted along with the coupling force from SPICE,
- the coupling force is then input into the FEM and so on until the time history is satisfied.

A Limitation pointed out in the study by Elvin and Elvin was that FEM-SPICE coupling is carried out at the end of each time step, so for accurate solutions computational cost is great.

A table of methodologies for piezoelectric modelling by Yang and Tang [97] aids the designer by outlining the appropriate design approach depending on the level of complexity of the mechanical and/or electrical constituents of the harvester. The design approaches range from purely analytical to a complete system-level approach.

Table 2.6 Methodologies proposed for modelling piezoelectric [97].

Mechanical condition / Energy harvesting circuit	Simple (e.g., uniform beam with unimorph/bimorph configuration, simple boundaries)	Complex (e.g., non-uniform beam with complex profile boundaries)
Only linear elements included (resistor, capacitor, and inductor)	Analytical model	System-level FEM
Non-linear elements (e.g., rectifier, DC-DC converter, and energy storage module) included	Equivalent circuit model (with parameters determined by theoretical model analysis)	Equivalent circuit model (with parameter identified by FEM)

It would be easy to conclude that from Yang and Tang's table [97] that the approach leading to the most accurate performance predictions with capabilities compatible to designing harvesters with mechanical and electrical complexity matching existing harvesters in industry would be a system-level approach for both electrical and mechanical elements. However, it could be said that there are still gains to be had in using a more modular approach due to the high complexity of electrical and mechanical elements exclusively. Therefore, the partially exclusive study of the mechanical or electrical elements of a harvester are still of some merit. For instance, if the aim was to focus on design of the mechanical aspects of a harvester in particular the effects on power output when there are changes in dimensions, geometry and of material properties with consideration of structural integrity, then it would be appropriate to use FEM as a single design tool.

When designing a harvester using a FEM with a basic electrical circuit Zhu et el [99] was able to investigate phenomena relating to electromechanical coupling. Later Pozzi et al [100] also used the CPC-FEM approach to design a piezoelectric based harvester with leg swing in gait being the energy source. When comparing results from the CPC-FEM against experimental data they were in good agreement. Zhu et el developed and validated [14] a CPC-FEM of a piezoelectric cantilever beam connected to a load resistor and found that the electrical and mechanical outputs of the cantilever were significantly dependant on one another. The load resistor was shown to have an effect on the current output, voltage output, power output and beam vibrational characteristics (vibrational amplitude and resonance) of the harvester. Furthermore, some specific phenomena were identified, contrary to the literature, results showed that the maximum power output does not appear at the optimal resistance, and also the maximum power output does not appear in conjunction with the maximum vibrational displacement.
Zhu et el also highlights the importance of ascertaining the out power output for determining the harvesters' suitability for any given application. The CPC-FEM developed (using ANSYS) in this thesis allows for the Cymbal structure along with its connected electrical circuit to be simulated. This enabled the CPC-FEM to be used as a design tool to explore the merits of varying dimensional and electrical variables of the Cymbal to investigate its electrical performance. It is an accurate design approach due

to the model being a full 3D representation of the Cymbal and its connecting circuit. Although modelling papers of the Cymbal have been carried out, this thesis shows results from a full 3D model of a Cymbal-like structure directly connected to an electric circuit to account for coupling between the piezoelectric disks physical and electrical behaviours during its operation. In summary, the CPC-FEMs developed in this thesis were able to account for mechanical and electrical inputs and simulate mechanical and electrical outputs. This enabled an understanding of the performance and structural integrity of the EHDs studied and also to measure useful electrical quantities from them such as, current voltage and power over a connected load resistor. An FEA software package called COMSOL was initially considered for use in this thesis however, ANSYS was a more favourable choice due to the better teaching resources and support available for ANSYS at Cranfield University. Moreover, as previously mentioned CPC-FEMs for two different EHDs were validated by experiment which showed the potential of ANSYS as an accurate design tool.

2.8 Introduction to Piezoelectric Material Selection

In order to design a harvester with a high energy density, a number of design approaches have been used to design the PEHs, for example,

- Selection of suitable piezoelectric material properties, i.e., a high piezoelectric strain constant "d", a high piezoelectric stress constant "g" and a high electromechanical coupling coefficient "k" for achieving a high energy transduction rates of PEHs [7,92];
- Impedance matching technique for efficient extraction of energy from PEHs [7];
- Optimisation of geometry of the PEHs for effective elastic deformation/straining [101].

It is well known that a high piezoelectric strain constant "d" has been used as a parameter to select a suitable piezoelectric material in design of PEHs in the literature. This is because one of the physical meanings of d is the short circuit charge collected on the electrodes of PEHs to a unit applied mechanical stress. It is obvious that the

higher the d, the higher the possible charge collected in the short circuit. Since charge is a quantity related to electrical power, it can be said that piezoelectric material with a high d can potentially produce a higher power. Therefore, a high value of d of a material property has been used for selection criteria. Similar to the d, the g is also used to select a suitable piezoelectric material in design of PEHs in the literature. This is because one of the physical meanings of g is the open circuit voltage produced across the electrodes of PEHs to a unit applied mechanical stress. It is, again, obvious that the higher the g, the higher the electrical voltage produced across the electrode in the open circuit. Since the voltage is also related to the electrical power, piezoelectric material with a high "g" can also potentially lead to a higher power output from PEHs and therefore it is also used in selection criteria of piezoelectric material for design of PEHs. It should be mentioned that, in spite of their different physical meanings, d and g are related to each other, that is,

$$g = \frac{d}{\varepsilon^T} \tag{5}$$

Where ε^T is the dielectric constant measured at a constant stress. Higher "d" and "g" constants of a piezoelectric material favour either a larger current in the short circuit or a larger voltage in the open circuit and therefore, they are sought after for design of a higher power output from PEHs.

Furthermore, because of the physical meanings of d and g, the product of d and g, i.e., dg, can, in a some way, represent the electrical power output from PEHs under an excitation. Thus, the dg has primarily been used as a figure of merit (FOM) for the selection of piezoelectric material for generating a higher power output from PEHs in the literature, i.e., [102],

$$\text{FOM} = dg = \frac{d^2}{\varepsilon^T} \tag{6}$$

From the above analyses, it is not difficult to find that the d, g, and FOM were derived either in the short circuit or in the open circuit, or in mixed open with short circuit conditions and therefore the FOM doesn't mean the electrical power generated by PEHs. This is because the electrical power generated is the product of the electrical current and the electrical voltage produced in one circuit, not in two different circuits, the open and short circuits, in which the power generated is zero. This raises a basic question: how do these piezoelectric material properties relate to the power output from PEHs and what kind of piezoelectric material properties are more effective to be used for power generation. Chapter 4 will make an attempt at answering these questions.

In addition to d, g and FOM, the electromechanical coupling coefficient k has also been commonly used for selection of a suitable piezoelectric material in design of PEHs in the literature. This is because k^2 is defined as the ratio of the converted energy from mechanical to electrical form, and vice versa, that is,

$$k^2 = \frac{\text{Electrical energy stored}}{\text{Mechanical energy applied}} \text{ or } k^2 = \frac{\text{Mechanical energy stored}}{\text{Electrical energy applied}} \tag{7}$$

and the relation to the piezoelectric material properties, taking the "31" mode as an example, is

$$k_{31}^2 = \frac{d_{31}^2}{s_{11}^E \varepsilon_{33}^T} \tag{8}$$

Where k_{31} is the electromechanical coupling coefficient of piezoelectric materials in the "31" mode, and s_{11}^E is the elastic compliance measured at a constant electric field, and ε_{33}^T is the dielectric constant measured at a constant stress. Although k represents the electromechanical coupling capability between mechanical and electrical and vice versa, how k_{31} is related to the power generation is also a question to be studied.

A number of research scientists have carried out research in this area, Bilgen *et al* [103] did a study based on cantilevered uni-morph beams and an experimental approach to investigate the actuation and energy harvesting capability of a number of different piezoelectric materials, and concluded that, for the same type of materials, the MFC type of uni-morph beams has the highest actuation capability but the lowest energy harvesting capability. Priya [104] provided a dimensionless figure of merit (DFOM) to try to answer the question of which piezoelectric composition is better to be used for energy harvesting based on similar beams but an analytical approach, which can be used in routine material evaluation. Kim *et al* [7] used the first physical principle approach to analyse how the electrical power available in piezoelectric transducers is related to piezoelectric material properties of the FOM (as in Eq (6)) and g, and further based on 5 different materials, including PVDF (PVDF-piezoelectric film), PZN-PT (single crystal), hard PZT and soft PZT, and high g, to conclude that a material with a higher FOM and a higher g can generate a higher voltage and a higher power when the piezoelectric material is directly used either for energy harvesting or for sensing. It is this same FOM (as in Eq (6)) that was further studied in this thesis. It seems that there is a lack of quantitative study on how the piezoelectric material properties are related to energy harvesting capability. With the present progress of the research community in modelling and simulation, this question could be answered by use of a CPC-FEM, proposed by the paper [99]. The questions proposed are; can the CPC-FEM be used to calculate the power output of PEHs directly connected to a load resistor and can the CPC-FEM be used to evaluate key piezoelectric material properties and associated data s_{11}, d_{31}, g_{31}, ε^{T}_{r33}, k_{31} and FOM so that correlations relating to power output can be identified if present?

2.9 Contributions & Novelty

This section presents the research questions raised by the literature review and explains the action taken to answer the questions and the resulting contributions to the research field that were made.

Question 1

Why can the Cymbal enhance power output?

Action

To answer this question a CPC-FEM was developed and validated by experiment. This CPC-FEM was then used to design and analyse a Cymbal. Using the CPC-FEM it was found that the physical parameters of the Cymbal had significant effects on the power output from the Cymbal. Reducing the thickness, join length and angle of the endcaps led to higher power outputs. In terms of changing parameters relating to the piezoelectric disk, in general when increasing the piezoelectric thickness the voltage increased, the current decreased and the curve of power reached a peak with a steady decline. Using the CPC-FEM, a shape factor was developed. The shape factor highlights how the extent of elastic deformation, in the form of strain, in the PZT disk due to the endcaps, allows the Cymbal device to have a higher power output than a PZT alone.

Contributions

Although previous work has been published using the CPC-FEM approach, this thesis developed the first 3D CPC-FEM of a Cymbal and also validated the CPC-FEM by experiment. The distinguishing feature of this work is that no CPC-FEM of Cymbal type geometry has been published until now. This is significant as the CPC-FEM is able to simulate a realistic model that includes mechanical inputs and meaningful electrical outputs such as current, voltage and power. Another contribution this thesis has made is expanding the understanding of how the Cymbal functions and identifying key design parameters related to electrical power performance. A conference paper based on the design of a Cymbal using a CPC-FEM for energy harvesting was published as a conference paper [105].

Question 2

Could the Cymbal be used as an EHD to harvest lower frequency (1-10Hz) and high forces common to human gait for scavenging waste bio-kinetic energy?

Action

The CPC-FEM was used to design a Cymbal to withstand upto 50N at 2Hz. A Cymbal was designed, fabricated and tested. It was suspected that for a Cymbal to be robust during operation it could not be designed and manufactured to withstand higher forces much more than 50N without changing its configuration. Therefore this research question was not directly answered but later on in this thesis a new device based on the Cymbal was developed. Interestingly, Palosaari *et al* [82] also developed a Cymbal with the intention of integrating it into the shoe and also designed it to withstand much lower forces of 24.8N than are available during foot fall. This work was carried out around the same time as work in this thesis.

Contributions

The Cymbal in this thesis had varied success when comparing to other Cymbals in the literature. The Cymbal in this thesis produced a 0.12mW power output for an applied force of 50N at 2Hz but for the lowest frequency test of a Cymbal by Kim *et al* [7] at 10Hz their Cymbal produced approx. 0mW. The Cymbal in this thesis did not produce a higher power than a Cymbal in a study by Palosaari *et al* [82] were it was reported that testing of a larger Ø35mm Cymbal at 1.19Hz under a force of 27.1N produced 0.27mW (measured over parallel resistor of $3.5M\Omega_{optimal}$). However, the Cymbal in this thesis was able to withstand higher forces which may widen its range for application.

Question3

Can the CPC-FEM be used to calculate the power output of PEHs directly connected to a load resistor and used to evaluate piezoelectric material properties for a higher power output with insight into material selection, in order to help in selecting a suitable piezoelectric material for the final design proposed?

Action

A CPC-FEM was developed and used to compare 25 different piezoelectric materials including single crystal, PVDF, and soft and hard PZT. The power outputs associated with key piezoelectric material properties of s_{11}, d_{31}, g_{31}, ε_{r33}^{T}, and associated material properties of FOM and k_{31} were studied using the CPC-FEM.

Contributions

Kim *et al* [7] used the first physical principle approach to analyse how the electrical power available in piezoelectric transducers is related to piezoelectric material properties of the FOM and g based on 5 different materials, to conclude that a material with a higher FOM and a higher g can generate a higher voltage and a higher power. However, results in this thesis showed that the g constant had a poor correlation with power output when studied over 25 different piezoelectric materials. Furthermore, results showed the d_{31} constant was a more dominant material property over other material properties for enhanced power output and the FOM was a more linear related property to power output than either the coupling coefficient k_{31} or d_{31} alone. No single materials parameters were able to be recommended, combined high values of FOM with d_{31} materials properties was recommended for selection of piezoelectric material for a higher power outputs in the context of energy harvesting of low frequency energy sources. Using the comparison data of 25 different material properties a high power producing material was able to be chosen for the novel EHD designed in this thesis.

As a result of failing to answer the research question 2 led to the final question, which is linked to the main aim of this thesis.

Question 4

Can the CPC-FEM be used to solve limitations of the Cymbal according to the application set out in this thesis?

Action

Using a CPC-FEM approach, time was spent to modify the Cymbal by adding substrate layers between endcap and piezoelectric element to reduce delamination risks thus allowing higher force loads to be applied. Also, by changing the shape of device allowed for more effective use of space in the shoe cavity (larger electrode plate areas of the piezoelectric element tend to have a higher power output). The outcome of this design work was that a novel harvester called the PFT was created. This new PFT could also withstand forces of up to 1kN at 2Hz. The PFT was then fabricated, tested using a loading machine and also demonstrated to power a wireless sensor module from scavenged bio-kinetic energy thus meeting the aim of the thesis.

Contributions

Although the PFT cannot produce as higher output as other piezoelectric shoe-integrated devices, it does have two advantages in combination which are 1) a small and compact configuration at 52x30x16.3mm and 2) a robust structure that can withstand 1kN. A significant contribution of this thesis that will benefit others is the approach that was used to design the novel PFT. This approach included the following:

- developing a 3D CPC-FEM,
- identifying key parameters of the harvester relating to power performance by using the CPC-FEM as an analysis tool,
- refining the design based on these findings,
- designing a physically robust harvester using stress analysis from the CPC-FEM, and
- using the CPC-FEM a material selection tool.

2.10 Methodology

This methodology demonstrates how research questions from the literature review were raised and how the aim and objectives of this thesis were proposed and persuade. A flow chart of the methodology can be found in the appendices.

The Aim of this research was to design, analyse and developed an EHD capable of harvesting sufficient energy from movements of the human body to power a wireless sensor module. At first an existing device was studied that lead to the first research questions proposed from the literature review which were; why can the Cymbal enhance power output and could the Cymbal be used as an EHD to harvest energy from lower frequencies (1-10Hz) and higher forces associated with the human gait? To answer these questions the Cymbal device was studied using ANSYS multi-physics finite element software, where by a CPC-FEM of a Cymbal was developed. The exploration that the CPC-FEM of the Cymbal allowed meant that knowledge and understanding of the Cymbal was gained in terms of its electrical and mechanical performance and its physical limitations. A conference paper based on these findings was published in order to share the work. Furthermore, it was found that the addition of the endcaps to the piezoelectric disk to form a Cymbal device improved its power output by 39 times compared with using a piezoelectric disk alone.

The second research question posed was; could the CPC-FEM be used to calculate the power output of PEHs directly connected to a load resistor and be used to evaluate piezoelectric material properties for a higher power output?
In response to this question a CPC-FEM of simplified EHD was developed using ANSYS multi-physics software and used to compare 25 different piezoelectric materials. The correlations between key material properties and the EHDs power output were studied and the most robust indicators of power output were found to be FOM and piezoelectric strain constant d_{31}. A journal paper was published in order to share this work with the wider research community. In terms of contribution to this thesis, the findings of the study were applied where by a piezoelectric material with a high FOM and high d_{31} were chosen to be used in the final device design.

Combing the both the work carried out in the material selection study and the investigation into the Cymbal, which included validating a Cymbal CPC-FEM and understanding its strengths and weaknesses, a new device was developed in order to meet the Aim of this thesis.

A lot of time was spent using CPC-FEMs to generate new device designs and to find ways to solve the limitations of Cymbal according to the application set out in this thesis. To increases bonding strength between the endcaps and piezoelectric element a substrate layer was added. The shape of device was changed to allow for easier fabrication and more effective use of space in the shoe cavity (larger electrode plate areas of the piezoelectric element tend to have a higher power output). Following extensive design work using a CPC-FEM, that included varying dimensions to give enhanced power output, the final device was fabricated. Testing of the PFTs was done using a loading machine to apply the input kinetic energy. The PFT was also demonstrated by retrofitting it into a shoe and harvesting energy from gait to power a wireless sensor module. To share this work a conference paper was published and journal paper was submitted.

CHAPTER 3

Modelling, Validation & Analysis of the Cymbal Device

This chapter covers modelling, validation and analysis of an existing piezoelectric based device called the Cymbal, where key variables and design features relating to its performance were studied. A CPC-FEM was developed and then used as a design tool to investigate some parameters that had effects on the electrical output of the device and to discover the feasibility of the Cymbal as a MEHD. The CPC-FEM configuration used in this thesis simulates the mechanical aspects of the EHD but also a basic electrical circuit connected to the EHD, in this instance, a load resistor in parallel with the piezoelectric element.

A brief outline of this chapter is as follows:

- CPC-FEM configuration
- Validation of the CPC-FEM
- Design Analyses of the Cymbal
- Summary

Cymbal Description

The Cymbal device studied in this chapter consists of a piezoelectric disk sandwiched between two metal endcaps with shallow cavities, as shown in Figure 3.1 (a). The metal endcaps act as mechanical force amplifiers to increase the force that acts on the piezoelectric disk, thus, increase the elastic strain energy stored in the piezoelectric disk for energy harvesting. The Cymbals characteristics enable it to harvest from relatively low frequency energy sources without need of working at a resonant mode.

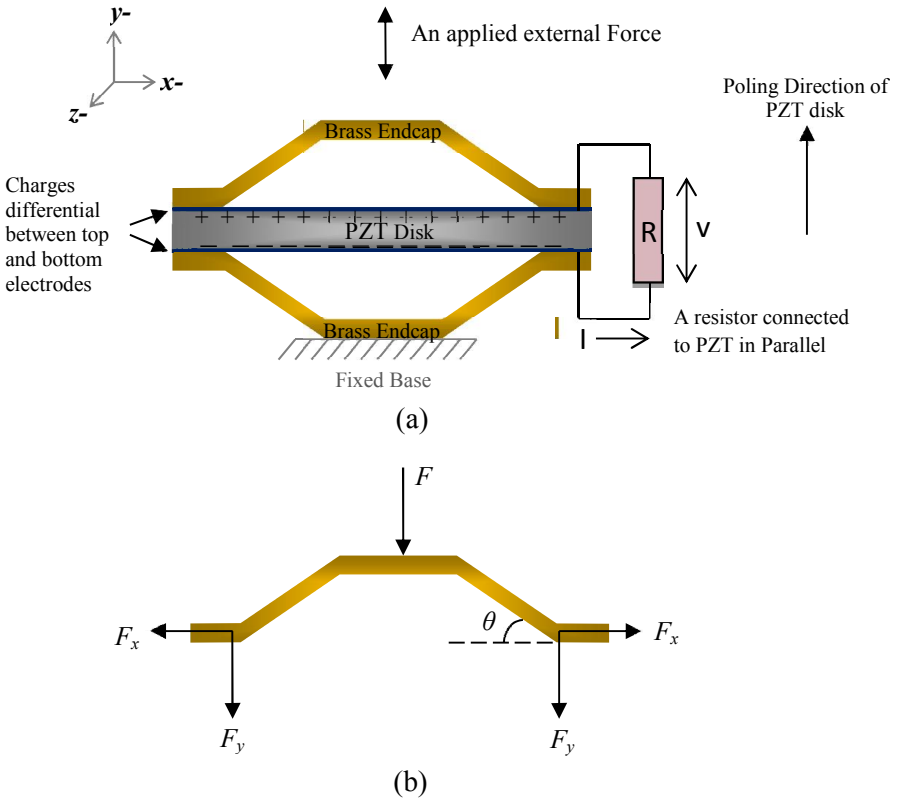

Figure 3.1 (a) Schematic of the Cymbal, (b) 2D Force analysis of the Cymbal.

The amplification principle of the Cymbal can be analysed based on the force analysis in Figure 3.1 (b); where F_x and F_y are the horizontal force and downward force as a result of the applied force F and θ is the angle in radians of the endcaps. This approach of explaining amplification principle is greatly simplified as it assumes that the Cymbal—a 3D cicular structure—is 2D.

$$F_y = \frac{F}{2} \tag{9}$$

$$F_x = \frac{F}{2}\frac{1}{\tan\theta} \cong \frac{F}{2\tan\theta} \tag{10}$$

Therefore, the ratio of F_x to F can be written as,

$$A_c = \frac{F_X}{F} \cong \frac{1}{2\tan\theta} \tag{11}$$

Where A_c is the defined force amplification factor of the Cymbal. From Eq (11), it can be seen that A_c depends on the angle of the endcaps, the smaller the angle of the endcaps, the larger the force amplification factor. Because θ of the Cymbal is very small, the electrical output of the Cymbal can be significantly increased through the piezoelectric effects of d_{31} and d_{33} of the piezoelectric strain constants. Later, this chapter will study how the electric output is affected by the angle of the endcaps base on the modelling approach. After modelling data was analysed an angle of 12° was chosen.

3.1 CPC-FE Model for the Cymbal Device Energy Harvesting Analyses

ANSYS (Version 13), a multi-physics finite element analysis (FEA) software package was used to develop a CPC-FEM of the Cymbal. The CPC-FEM includes the physical structure of the Cymbal and a load resistor connected in parallel with a piezoelectric disk of the Cymbal. The CPC-FEM has the ability to calculate the electrical output of the Cymbal under an external force excitation, such as the voltage, current and power produced.

Figure 3.2 (a)-(b) shows the developed FEM of the Cymbal with meshes, which consisted of the Cymbal connected to a load resistor. Three element types were used in the FEM. Firstly, the element type used for the PZT disk was SOLID226; a hexahedral element type comprised of 20 nodes. SOLID226 is a couple-field element type that is capable of analysing piezoelectric structural performance, it can also tolerate irregular shapes e.g., the mesh shape became irregular when revolving a 3D rectangular section into the PZT disk of the Cymbal. Secondly, SOLID95 was used for the endcaps; also a hexahedral type element comprised of 20 nodes. It should be mentioned that the elements of SOLID226 and SOLID95 have been specifically selected to have the same

element structures and numbers of nodes to ensure their inter compatibility. Finally, CIRCU94 was used for the resistor element connected to the piezoelectric disk.

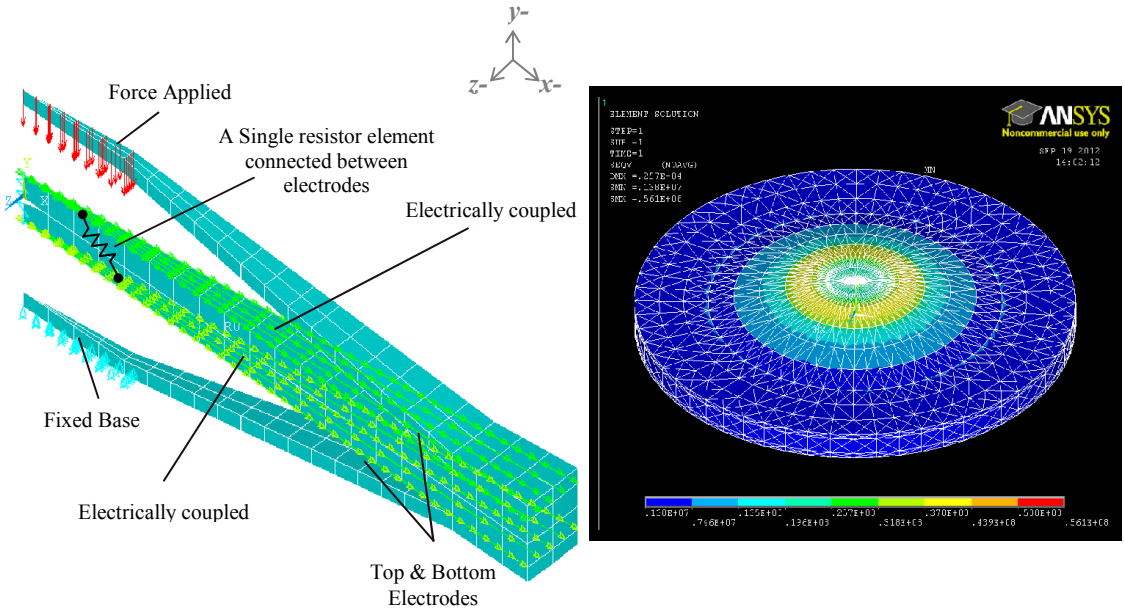

Figure 3.2 (a) Section of Cymbal in the developed CPC-FEM showing boundary conditions, and (b) Developed CPC-FEM; results of static simulation showing Von Mises Stress force Cymbal under 50N load. Top middle: axis coordinates used in CPC-FEM.

The material properties and geometric parameters of the Cymbal are listed in Table 3.1 and Table 3.2 for the developed model and the parametric definitions are shown in Figure 3.3. For an explanation of how the piezoelectric material was input using APDL please refer to Appendix 2. The Cymbal dimensions in Table 3.2 are the result of many dimensional refinements for improved power output. Each dimension was first individually varied until an optimal value was found whilst also considering limitations of yield stress and manufacturing difficulty. After an optimal or best value was found for each dimension the simulations were then repeated with this whole set of optimal value dimensions, of which the graphical representation of these results are shown in Figure 3.6- Figure 3.11. The reason why the chosen dimensions were studied was because they were assumed to be the most simplified set of dimensions needed to model

a Cymbal. Each dimension was investigated with the same rigour. The Cymbal was modelled with the lower endcap fixed and a universally distributed load (UDL) applied to the upper surface of the upper endcap. It was assumed that the thickness of the electrodes were very thin and could be ignored in the model; only the electrical voltages and charges on the electrode surfaces needed to be considered. Thus, during the modelling, the nodes of the electrode surfaces were electrically coupled to ensure an equal electrical potential across the electrode surface. This meant that each node was electrically connected to its neighbour, with the same electric potential. It was also assumed that the thickness of the adhesion layers between the endcaps and the PZT disk was very thin and so could be ignored in the model. The piezoelectric material chosen was a type of PZT (VIBRIT 420, Johnson Matthey Plc, Germany), which have a large electromechanical coupling coefficient, 0.34. Brass was selected to be used for the endcaps, rather than steel. This was because brass was thought to be more compliant and thus more easily deformed, therefore it was more effective at transferring force from the metal endcaps to the PZT disk. A safety factor of 2 was used when designing the endcaps and the stress in the piezoelectric disk did not exceed 10MPa. This value was determined through static analysis using the CPC-FEM. The extent of deformation of the endcaps and piezoelectric disk was in the order of 10s of microns therefore, it was assumed that deformation was not a satisfactory or valuable indicator of mechanical failure; consequently no such results are present in this Thesis.

Table 3.1 Material properties used in the developed CPC-FEM.

Brass: Red Brass UNS C23000, MatWeb, LLC		
Young's Modulus (GPa)	E	115
Yield Strength (MPa)	σ_y	435
Density (Kg/m3)	ρ	8750
Poisson's Ratio	μ	0.307
Piezoelectric Material: VIBRIT 420 Johnson Matthey Plc		
Elastic Compliance (x10-12 m2/N)	s_{11}	15.4
	s_{12}	-5.7
	s_{13}	-6.5
	s_{33}	18.7
	s_{44}	45
	s_{66}	54.6
Relative Dielectric Constant (constant stress)	ε_{r11}^{T}	1600
	ε_{r33}^{T}	1600
Density (Kg/m3)	ρ	7600
Piezoelectric strain constants (x10-12 m/volt)	d_{15}	525
	d_{31}	-160
	d_{33}	355
Piezoelectric Coupling Coefficient	k_{31}	0.34
Mechanical quality factor	Q	100

Table 3.2 Most effictive dimensional parameters chosen based on Cymbal CPC-FEM results and also the dimensional parameters used in the Cymbal CPC-FEM simulations.

		Simulated		Experimental
		Cymbal 1	Cymbal 2	Cymbal 1
Total Diameter (mm)	D	30	22.5	30
Cavity Diameter (mm)	D_c	20	15	20
Apex Diameter (mm)	D_a	6	4.5	6
Height (mm)	H	1.5	1.125	1.5
Caps Thickness (mm)	t_c	0.33	0.33	0.33
PZT Thickness (mm)	t_p	1	0.75	1
Join Length (mm)	J	5	3.75	5
Angle of the Endcap (°)	θ	12	12	12

*Cymbal 2 is a variant of Cymbal 1 that was used to investigate diameter changes.

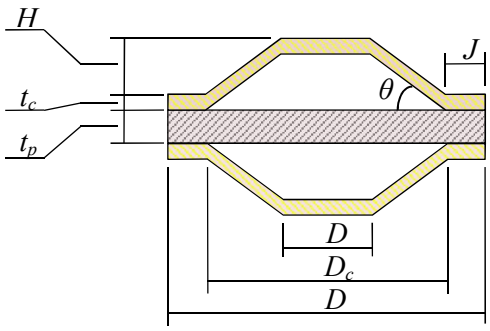

Figure 3.3 Cross-section of Cymbal.

3.2 Model Validation

3.2.1 Cymbal fabrication

Cymbal fabrication process: firstly, circular disks were cut from a brass shim and were stamped to form the endcaps. A Ø2mm hole was drilled into the flange of each endcap to enable an electrical connection to be made through to the PZT electrodes. Once the endcaps were made, a PZT disk was carefully bonded between them using a structural adhesive, 3M DPD-460. With a thin layer of adhesive applied to endcaps and PZT disk, the parts were then stuck together, left for up to 5 hours under a 1.2Kg weight and baked for 20 minutes at 90°C. Finally, wires were fed through the Ø2mm pre-drilled holes to the PZT electrodes and bonded with silver epoxy to ensure connectivity.

3.2.2 **Experimental set-up**

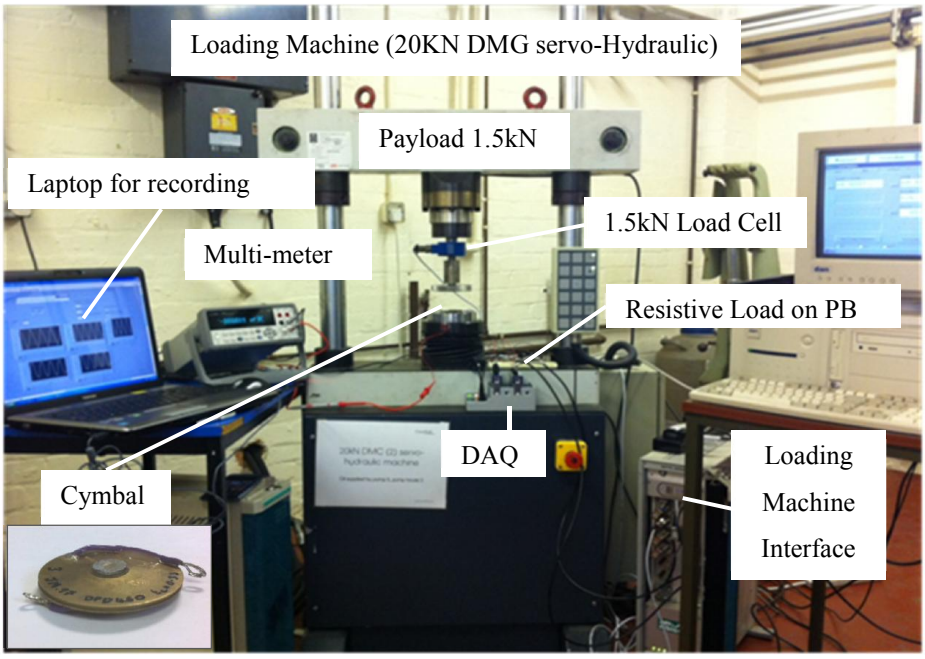

Figure 3.4 The experimental setup using the loading machine to test the Cymbal with a photo of the fabricated Cymbal inset.

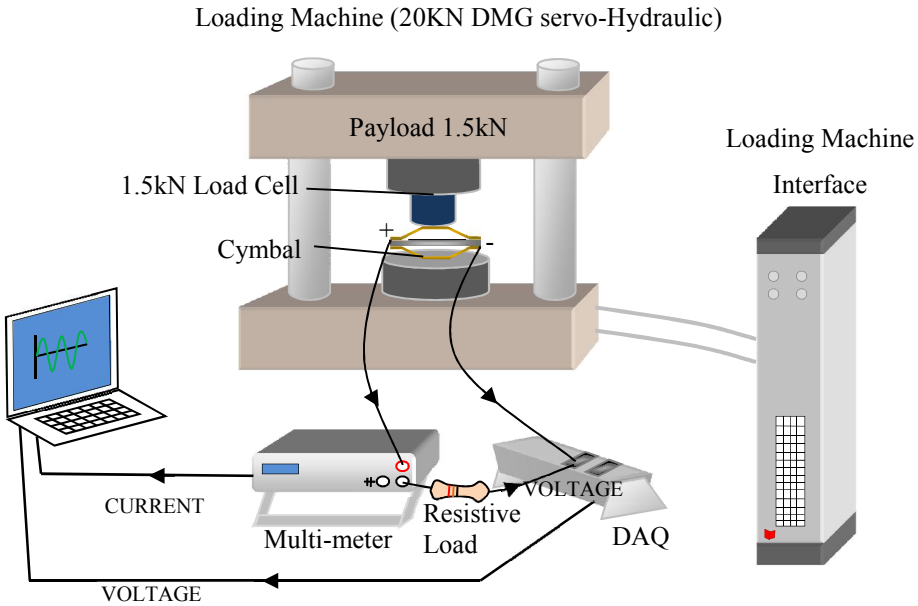

Figure 3.5 Experimental set-up for testing of the Cymbal, where the Cymbal is placed in the loading machine and a 50N compressive force with 2 and 5Hz is applied the Cymbal.

shows the fabricated Cymbal 1, see Table 3.2 for more details of Cymbal 1, and the experimental setup for testing the electric output performance of the Cymbal. During experimental measurements, the Cymbal was electrically connected to a range of resistive loads in-turn and a 20kN DMG servo-hydraulic loading machine (Denison Mayes Group, UK) with a 1.5kN payload was used to physically excite the Cymbal. In addition, a data acquisition card, DAQ NI-9222 (National Instruments, UK), was used in conjunction with LabVIEW™ software to record the electric output generated from the Cymbal. A 1.5kN load cell was used to monitor the force exerted on the Cymbal. To acquire the test results; the Cymbal was placed in the loading machine and excited with a known force magnitude and frequency, the Cymbal was electrically connected to a potential divider (to protect the DAQ) and a load resistor, the connection then ran into the DAQ NI-9222 to read a voltage, finally, a LabView program recorded the voltage and accounted for the effects of the potential divider. Later the current and power was calculated using the appropriate load resistor in the calculation. A potential divider was used as the DAQ only had an input capability of ±10Volts and an internal resistance of 1GΩ. A multi-meter was also used to measure the current, a power was then calculated using this current measurement, however the results have not been included in this thesis as their purpose was only to check against the power that was derived from the voltage and they were in good agreement.

3.2.3 **Results & discussions**

An ANSYS Parametric Design Language (APDL) code was specifically developed to be used to obtain simulation results of the electrical output of the Cymbal. The electrical outputs studied here are the voltage, current and power generated through the connected electrical load resistor due to the external force excitation. All the simulation results obtained from the developed model were based on harmonic analyses. To validate the model developed in the following section a Cymbal (Cymbal 1) was fabricated and tested, and results were compared with modelling results from the CPC-FEM.

Figure 3.6 shows the electrical resistive load spectrum results from the CPC-FEM of a Cymbal and experimental results of Cymbal 1. Figure 3.6 (a)-(c) shows power, voltage and current results, where the electric voltage was measured from the testing, the electric power and current were calculated from the measured voltage across the electrical resistive load, and the amplitude of the applied force was 50N. Generally speaking, the simulation results agree well with the experimental results. The simulation results and experimental results both show a similar trends and similar magnitudes. The Cymbal tested was designed to withstand a force of 50N, it was assumed that forces exceeding 50N may compromise the adhesive bond between the endcap and piezoelectric disk. Although not shown here, testing was carried out at a facility at Brunel University using a servo-hydraulic loading machine that was used to apply force loading of up to 50Hz on the Cymbal. During this testing the Cymbal was subject to higher frequencies until failure was observed. At 50Hz, 50N the endcaps of the Cymbal collapsed inward. This suggested that the brass material used to make the endcaps was inadequate at higher frequencies. Surprisingly the adhesive bond layer seemed to suffer very little. A more accurate way of concluding the adhesion layer was intact would be to view a cross-section of it under microscope or electron microscope. If the Cymbal is to be used to scavenge from a high frequency energy source a more suitable endcap material or thickness of endcap should be found. As the endcaps failed due to large scale deformation, a material with a higher stiffness and/or yield strength is advised in future.

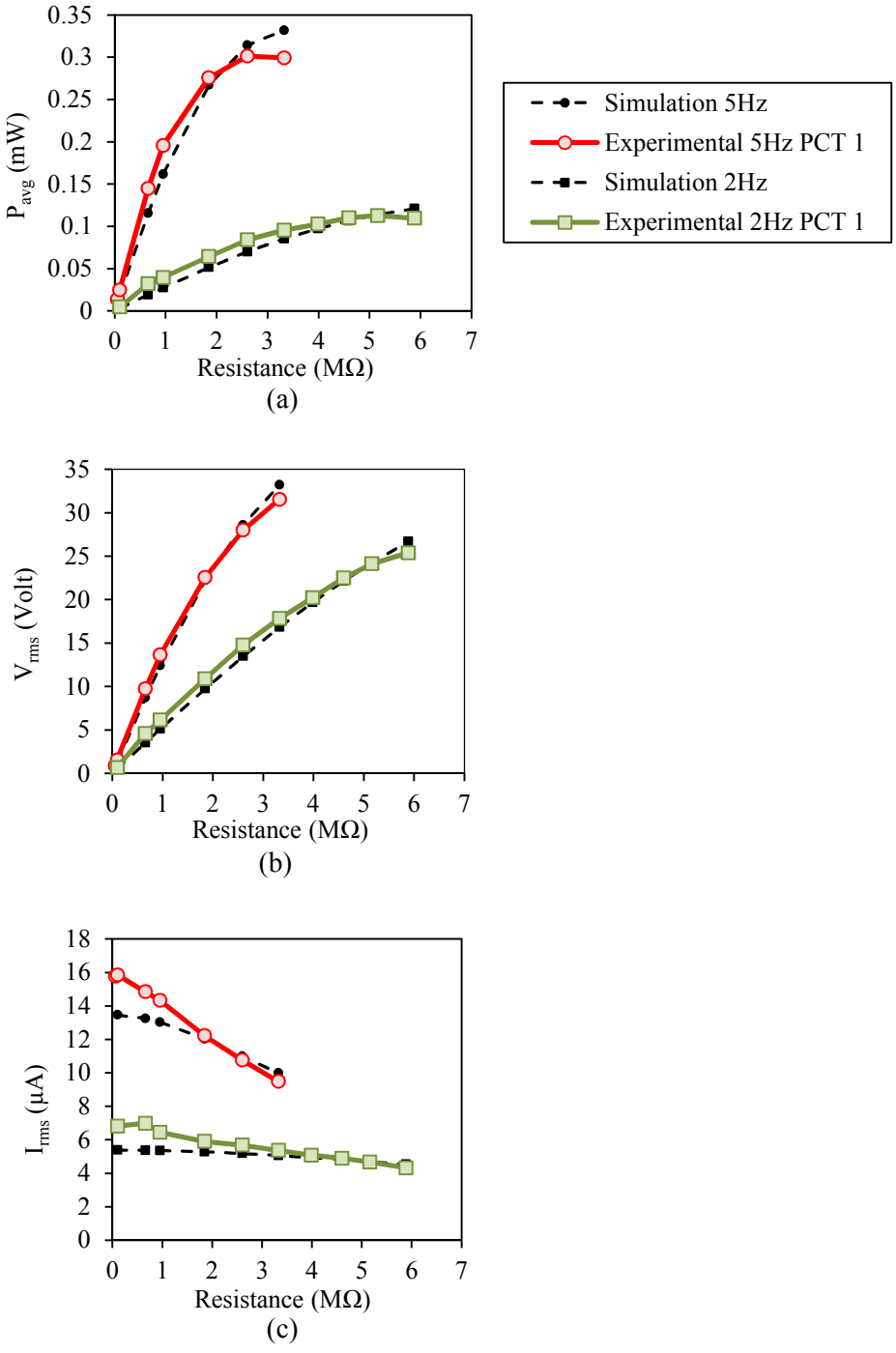

Figure 3.6 Comparisons between the experimental and simulated results of the power, voltage and current verses the electrical resistive load for a Cymbal excited at 2Hz and 5Hz under a 50N compressive force load. PCT refers to Piezoelectric Cymbal Transducer.

3.2.4 **Summary**

The validation experiment showed that the CPC-FEM results were in good agreement with the experimental results; therefore suggesting that the CPC-FEM is suitable to be used for design and analysis of the Cymbal to maximise its power output.

Parts of the Cymbal structure could have been designed to withstand higher forces than 50N i.e., making the endcaps and piezoelectric disk thicker would have increased their resistance to mechanical failure. However, the Cymbal was not designed to withstand forces higher than 50N as the adhesion area between the endcaps and piezoelectric disk was thought to be at high risk of failure; therefore based on this assumption it is concluded that the Cymbal is not suitable to harvest energy of forces higher than 50N. During testing the brass endcaps of the Cymbal collapsed at 50Hz force excitation, suggesting that for higher frequency applications the endcap material choice should be reviewed. The failure mode of the endcap was a gradual deformation where by the endcap became flattened.

3.3 Cymbal Structural Parameter Design Analyses on Energy Harvesting Performance using the CPC-FE model

The validated model described in the previous section was used for the analyses of effects of varying the geometric parameters and the electrical loads on the electrical outputs of the Cymbal. Figure 3.7- Figure 3.11 show the simulated results for varying the electrical load values and dimensions of both the endcaps and PZT disk under a 50N excitation force, where all other dimensional parameters and material properties of the Cymbal were kept fixed, unless otherwise stated. It should be noted that the voltage and current presented on all graphs are the root mean squared value (rms), the voltage amplitudes over the resistor are extracted directly from simulated harmonic simulation results, and the electrical powers and the electric currents are calculated from the simulated voltage, and the average power is calculated using Eq (12).

$$P_{avg} = \frac{V_{rms}^2}{R} = \frac{V^2}{2R} \tag{12}$$

3.3.1 Effects of the connected resistive load

Figure 3.7 (a)-(c) shows the electrical responses of the Cymbal over a range of resistive loads for the frequency range of 1-10Hz. From Figure 3.7 (a)-(c), it can be observed that with an increase in electrical resistive load there was an increase in voltage and a decrease in current. Moreover, the power output increased with increased frequency; an increased frequency of excitation force means more deformation cycles (higher mechanical energy input) and when there is an increased mechanical input there is an increased electrical output. Based on the power curve in Figure 3.7 (a) which was relatively flat in climax, the optimal resistance value from a Cymbal excited at 2Hz was found to be around $10M\Omega_{optimal}$. From Figure 3.7 (a), it can be further observed that there is an optimal resistance value of $2M\Omega_{optimal}$ for a Cymbal excited at 10Hz. For the lower frequencies, the peak in power becomes less apparent due to heavier damping effects.

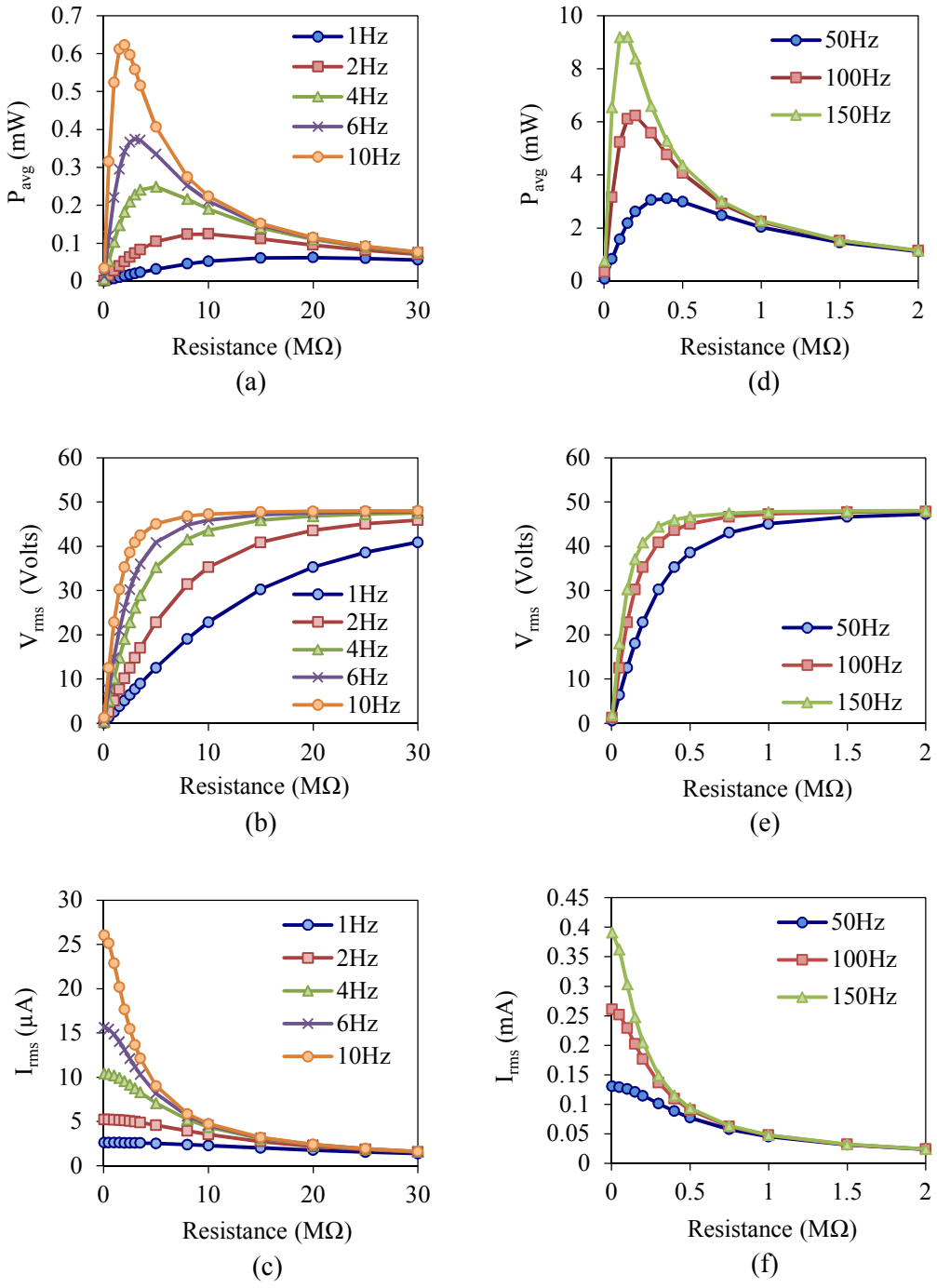

Figure 3.7 Simulated results of the electric responses of powers, voltages and currents over a range of electrical resistive loads for two different frequency ranges of 1-10Hz and 50-150Hz.

Figure 3.7 (d)-(f) shows the electrical responses of the Cymbal over a range of resistive loads for the frequency range of 50-150Hz, which have similar characteristics to the lower frequency range of 1-10Hz; the optimal resistance for 50Hz, 100Hz and 150Hz were 0.4MΩ, 0.2MΩ and 0.15MΩ respectively.

3.3.2 **Effects of experimental impedance**

In order to check the CPC-FEM results with further experimental results the impedance of Cymbal 1 was measured at 2Hz and 150Hz using a PSM1700 frequency response analyser (Newtons 4th Ltd., UK). The impedance for the Cymbal at 2Hz was measured at 9.89MΩ whereas the power peak in Figure 3.7 (a) was 10MΩ. The capacitance was measured at 8.05nf. The resistive and reactive parts of the impedance were also measured; contribution from the reactive compared to the real part of the impedance was higher. Where $|Z|$ is the modulus of the impedance, R the resistive part and X the reactive part,

$$|Z| = \sqrt{R^2 + X^2} \tag{13}$$

The contributions are as follows,

$$|9.89\,M\Omega| = \sqrt{191\,k\Omega^2 + 9.89\,M\Omega^2} \tag{14}$$

The reactive part of the impedance had a greater contribution to the impedance than the resistive part, which meant that changing only the resistive part of the impedance to find the highest power was a somewhat crude method for investigating lower frequency excitations of the Cymbal. What the method in this thesis does is assumes that choosing the optimal resistance gives and optimal resistive load. However, this approach still serves a purpose when focus is mainly on investigating mechanical parameters with some consideration of power output characteristics and is most accurate at higher frequencies.

The internal impedance of the Cymbal at 150Hz was measured at 0.138MΩ, compared to the power peak in Figure 3.7 (d) 0.15MΩ. The capacitance was measured at 7.64nf.

The real and reactive parts of the impedance were more equal in magnitude than results at the lower 2Hz frequency,

$$|0.138\,M\Omega| = \sqrt{2.75k\Omega^2 - 138.8k\Omega^2} \qquad (15)$$

3.3.3 **Effects of angle of the endcap**

Figure 3.8 shows the simulation results of the power, voltage, and current for changing the angle of the endcaps, where the force magnitude, the force frequency and the electrical resistive loads were 50N, 2Hz and 8MΩ, respectively. The angle of the endcaps was varied by changing the height of the endcaps. From Figure 3.8 (a) it can be observed that the electrical power increases with a decrease in angle (of the endcaps), for example, when the angle was reduced from approx. 25° to 5°, the power was increased from 0.08mW to 0.38mW. It should be mentioned that, when changing the angle of the endcaps, all the other parameters were kept fixed except the height of the endcaps.

Figure 3.8 (a) clearly shows that the power output increases with the decrease of the angle. This can be partly be explained by Eq (10) for the horizontal force F_x, in Figure 3.1 (b). The smaller the angle of the endcaps, the higher the force in the horizontal direction, F_x. A reason why the Cymbal is more efficient with utilising the horizontal force compared with the vertical force is simply because of the Cymbal configuration, that is, having the PZT disk suspended means that not only is it more free to deform in the horizontal direction but also the majority of the PZT volume is effected by horizontal forces (due to its flat profile).

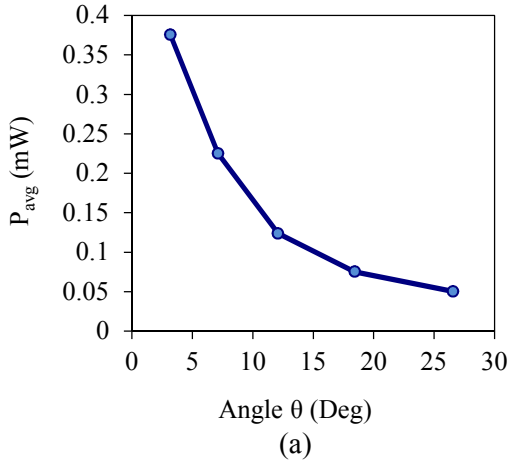

(a)

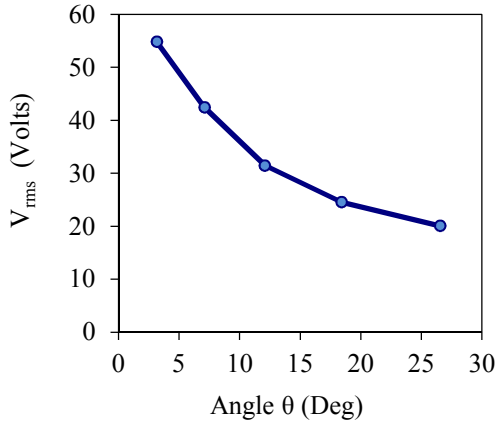

(b)

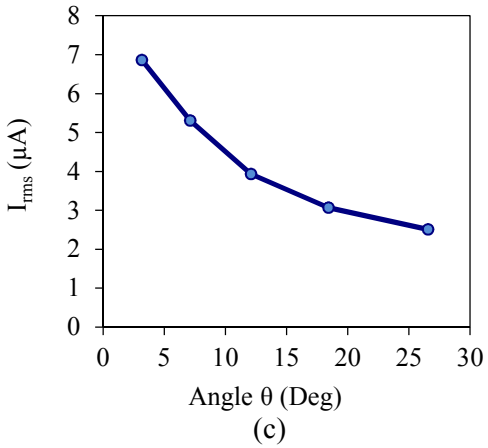

(c)

Figure 3.8 Simulation results of electrical responses of power, voltage and current verses internal angle of the endcaps, where the force magnitude, the force frequency and the electrical resistance were 50N, 2Hz and 8MΩ, respectively.

In summary, reducing θ , results in the increase of the power output of the Cymbal due to leverage effects and Figure 3.8 (a) demonstrates the result.

In order to explain and quantify the amplification effect the angle change had, Table 3.3 compares the mechanical strain in a lone PZT disk with the strain in the piezoelectric part of a Cymbal (under the same excitation force of 50N). In this case PZT has been used as an abbreviation for piezoelectric seeing as the piezoelectric material used in the CPC-FEM does comprise of Lead zirconate and titanate.

Table 3.3 Strains in the Cymbal compared with a PZT disk.

	Amplification Factor in Literature, A [7]	Amplification Factor Derived, A_c Eq (11)	ε_x (μS)	ε_y (μS)
PZT Disk alone (no endcaps)	0	0	3.25	-2.5
Cymbal	6.6	2.3	40	-40

As seen in Table 3.3, the Cymbal has substantially more strain than the lone PZT disk. A compressive force corresponding to the negative direction in ANSYS was applied to both the disk and Cymbal which is the reason for the negative y-direction strain output. The strain in the *x*-direction corresponds to a horizontal or radial strain. Though not shown here, the strain in the *z*-direction is also a radial strain and is equal to the strain in the *x*-direction. A relationship has been presented in literature that pairs endcap related force amplification with the piezoelectric strain constant, called the equivalent strain constant, d_{33}^{eff} [7].

$$d_{33}^{eff} = d_{33} + \left| A\ d_{31} \right| \tag{16}$$

Where A is dependent on the angle of endcaps' leverage contributions, thus the d_{33}^{eff} quantity demonstrates how d_{31} contributes to the piezoelectric constant through the angle of the endcaps and A_c is the Amplification Factor Derived in this thesis and is, Eq (11).

This thesis pairs strain with its respective piezoelectric strain constant and proposes a shape factor φ to demonstrate the positive effects of the endcaps.

$$\varphi = d_{33}\ \varepsilon_y + \left| d_{31}\ \varepsilon_X \right| \tag{17}$$

Table 3.4 Shape factor compared with the effective piezoelectric constant.

	d_{33}^{eff} [50]	φ	Vrms (Volts)
PZT Disk alone	515	1407	0.32
Cymbal	723	20600	12.6
Disk:Cymbal	1:1.4	1:14.6	1:39
% Difference	29%	93%	98%

To study the shape factor φ introduced above, the equivalent strain constant and the voltage generated from the PZT disk alone and the Cymbal are all calculated based material properties in Table 3.1 and voltage results using the validated CPC-FEM.

The simulated voltage produced by the PZT disk alone was 98% smaller that the voltage produced by the Cymbal; a similar percentage was reflected in the shape factor difference, see Table 3.4, therefore the shape factor highlights how strain observations in Cymbal design are important in understanding the reason for electrical performance variations. It should be noted that the force applied was 50N at 2Hz, and the electric resistive load connected to the PZT disk alone and the Cymbal were both set at 2.5MΩ (any values could have been chosen along as they remained constant for both set-ups in the comparison).

3.3.4 **Effects of join length of endcap**

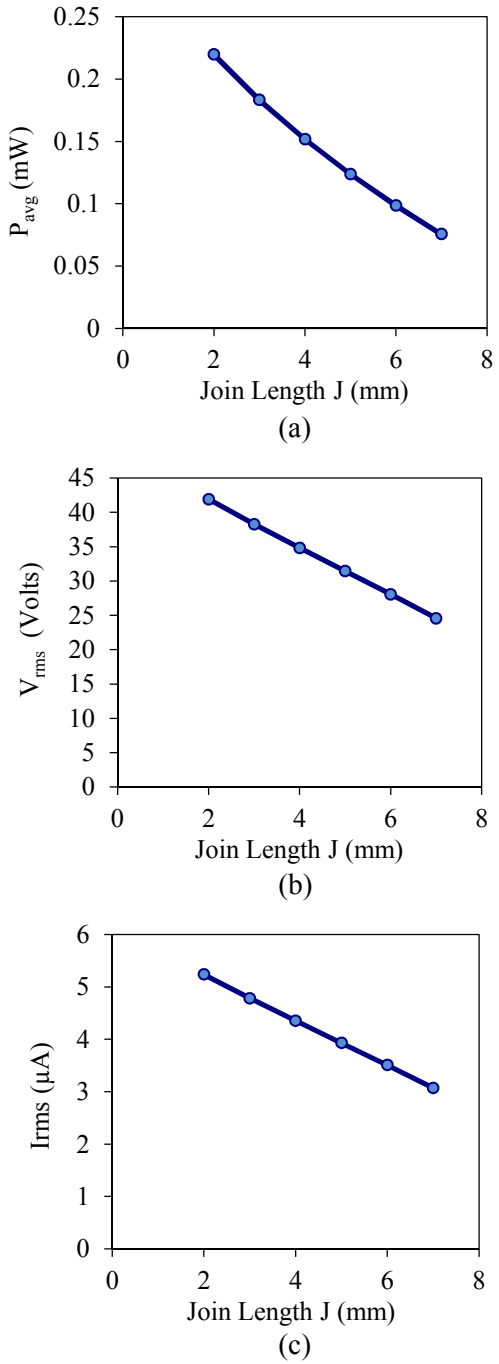

Figure 3.9 Simulation results of electrical responses of power, voltage and current verses join length between the PZT disk and the endcap, where the force magnitude, the force frequency and the electrical resistance are 50N, 2Hz and 8MΩ.

Figure 3.9 shows simulation results of the power, voltage and current for changing the join length between the PZT disk and the endcaps. The join length is used for bonding between the endcaps and PZT disk and when increased from 2mm to 7mm the power output decrease from 0.22mW to 0.05mW, respectively. This means that the smaller the join length, the larger the power output. A possible reason for this is that with a reduced join length more of the PZT is able to be elastically deformed, thus resulting in higher power outputs. It should be mentioned that, when changing the join length, the cavity diameter D_c was changed but the angle of the endcaps was kept fixed at 12° to avoid any effects of increased/decreased leverage on the simulation results. To keep the angle fixed, the apex diameter D_a was changed in proportion to D_c. Therefore, this change in cavity diameter did not affect the performance of the device through leverage and only had the desired and isolated effect of varying join length.

3.3.5 **Effects of PZT disk thickness and diameter**

Figure 3.10 shows the simulation results of the power, voltage and current for changing the PZT thickness of the Cymbal and Cymbal 2. Dimensions can be found in Table 3.2. Each data point represents the electrical output over a fixed load resistance for the given dimensions. From Figure 3.10, it can be observed how the electrical power output, the electric voltage and the electric current of the Cymbal changed with a change in PZT thickness and diameter; the smaller the diameter, the higher the electric power output. Furthermore, it can also be observed that there is an optimal PZT thickness that gives a maximum power output.

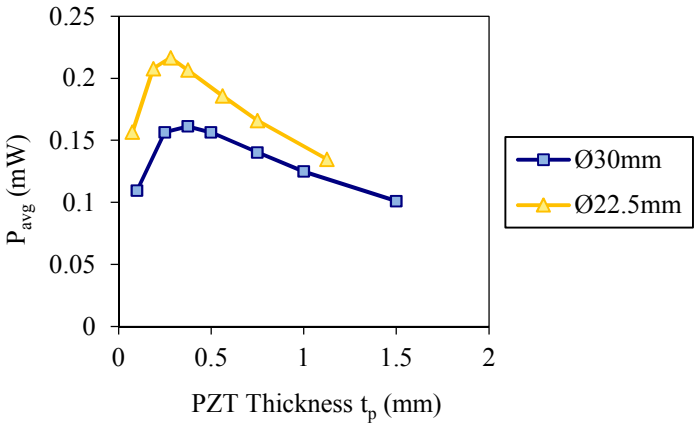

(a)

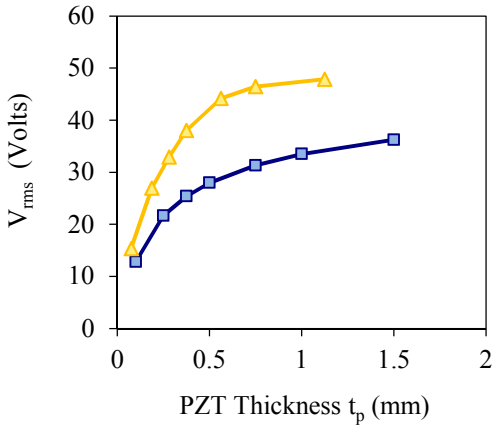

(b)

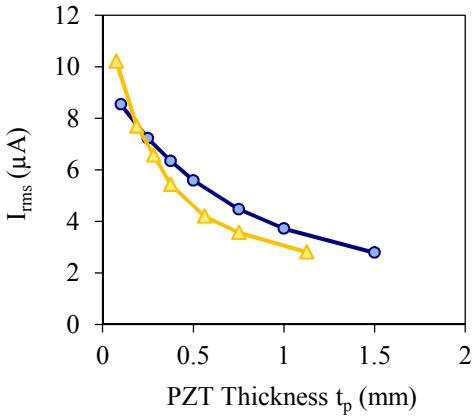

(c)

Figure 3.10 Simulation results of electrical responses of power, voltage and current verses PZT thickness of Cymbal and Cymbal 2, where each data point represents the electrical output over an optimal resistance for the given dimensions**.** The force magnitude and the force frequency were 50N and 2Hz respectively.

3.3.6 **Effects of multi-layering of PZT disk**

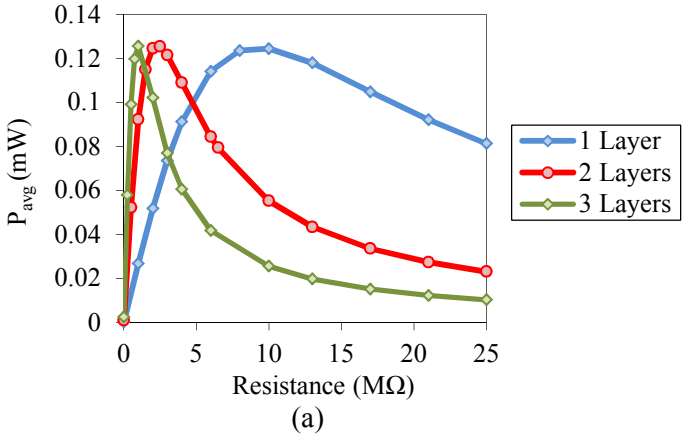

(a)

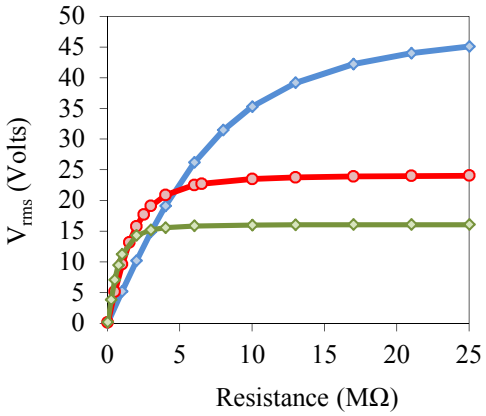

(b)

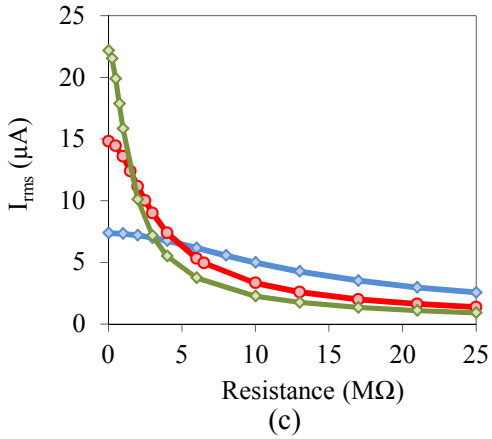

(c)

Figure 3.11 Simulation results of electrical responses of power, voltage and current for multi-layers of the PZT disk of the Cymbal, where each layer is connected in parallel, and the force magnitude, the force frequency and the total PZT thickness were kept fixed at 50N, 2Hz and 1mm, respectively.

Figure 3.11 shows the simulation results for multi-layers of the PZT disk of the Cymbal, where each layer is connected in parallel, and the force magnitude, the force frequency and the total PZT thickness were kept fixed at 50N, 2Hz and 1mm, respectively. From Figure 3.11, it can be observed that the maximum power output almost remained constant in spite of the changing number of layers that divided up the PZT disk. Although the increased layering doesn't increase the power output it does provide some benefits, the peak in power for devices with increased layers occurred earlier along the resistance spectrum, thus the more the layers, the lower the input impedance. This is an important factor when designing the Cymbal for specific applications with low impedance requirements; the multi-layered PZT structure can be used to reduce the optimal working impedance. Figure 3.11 (b) & (c) also show how the voltage and current are affected by the multi-layered PZT structure. For multi-layered structures with the layers connected in parallel, the total piezoelectric resistance will be decreased, resulting in a smaller optimal impedance the more the element is divided into layers, for a given source excitation frequency. Figure 3.12 shows the equivalent piezoelectric circuit which includes elements of resistance, capacitance and inductance.

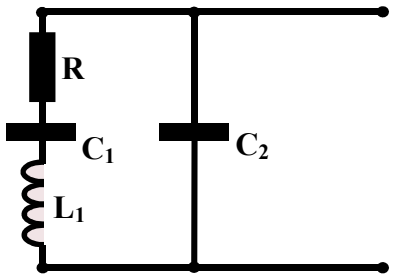

Figure 3.12 Equivalent electrical circuit of piezoelectric structure [106].

Although multi-layering is beneficial in terms of tailoring the impedance of a device, it does have some more practical disadvantages. With multiple layering comes multiple electrodes and thus a small reduction in power output due to the extra electrode material there is to strain. Moreover, it could also be argued that with multiple layers there is a higher likelihood of delamination between layers. Finally the monetary cost of producing a multilayer piezoelectric ceramic—at this point in time—is a considerable amount higher than manufacturing a monolithic piezoelectric ceramic.

3.4 Summary

In this section an existing Cymbal device was studied to assess its feasibility as an EHD and to identify some design characteristics that could be utilised in later design developments. Using a CPC-FEM it was found that the electrical resistive load and select physical parameters of the Cymbal had significant effects on the power output from the Cymbal; reduced thickness, join length and angle of the endcaps led to higher power outputs. Modelling results of the CPC-FEM were in good agreement with experimental results. The shape factor introduced in this chapter demonstrated why the Cymbal was more effective than simply using a piezoelectric disk in the d_{33} mode. Due to the vulnerability of the adhesion layer it was not possible for the Cymbal to be designed to withstand more than 50N loading before mechanical failure which is a significantly less than the required footfall force of 1kN, however, a Cymbal of dimensions Ø30x4.6mm with an endcap thickness of 0.33mm was able to harvest 0.12mW of power under a 50N force at 2Hz (10MΩ).

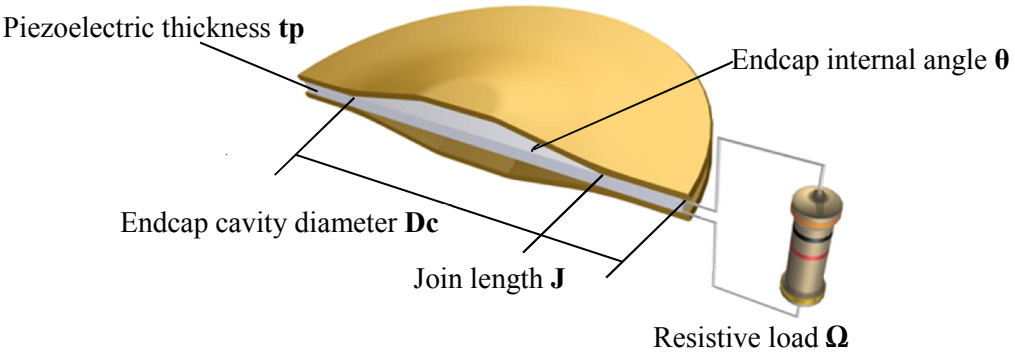

Figure 3.13 Studied parameters effecting Cymbal energy harvesting performance.

Through the design study a number of key variables and design features relating to the Cymbal's performance were recognised. These key variables have been included in the following table.

Table 3.5 Key design aspects to improve Cymbal.

Mechanical Changes • Use of endcaps with PZT disk improves electrical performance • Reduction in internal angle of endcaps improves leverage effects on PZT disk • Reduction in endcaps-PZT disk Join length allows greater flexing of PZT disk • Increased cavity diameter sees positive effects from both reduced join length and increased angle • Reduced endcap thickness allows for more effective force transfer
Electrical Changes • Impedance matching is important for optimal power output • Multi-layering can lower internal impedance of PZT disk
Mechanical & Electrical Interrelated Changes • For lower PZT impedance, PZT disk thickness should be minimised (application dependant)

It should be mentioned that this section did not look into an obvious group of parameters that were thought likely to affect a piezoelectric EHDs performance. The material properties of the piezoelectric element is of great importance as it governs how effective the material is at converting between kinetic and electrical energies. This next chapter shows a comparison of piezoelectric materials in the context of energy harvesting by using the CPC-FEM to study a simplified piezoelectric harvester structure.

CHAPTER 4

4.1 Introduction

The aim of this thesis was to design a device that could harvest bio-kinetic energy. So far, an existing device called the 'Cymbal' has been studied; various physical parameters where studied to investigate their effect on electrical performance in an energy harvesting context. The material properties however, were not studied. In this chapter material selection is considered. Material selection was investigated for two of the main elements in the final device. The bulk material of the final device was comprised of piezoelectric material as the transducer element and a metallic outer frame acting to control the exerted external input force. Therefore, presented in the following order are the reasons for choosing a specific piezoelectric material and a specific endcap material.

A brief outline of this chapter is as follows:

- Selection process of piezoelectric material
- Selection process of endcap material

4.2 Piezoelectric Material Analyses and Selection using the CPC-FE model

In this section the CPC-FEM was used to shed light on existing piezoelectric material selection criteria and create informed knowledge to aid the material selection process. For background on this chapter please referrer to the literature review Section 2.8 of Introduction to Piezoelectric Material Selection.

4.2.1 Model configuration

The CPC-FEM was used to calculate the power dissipated by an optimal resistive load connected directly to a piezoelectric energy harvester (PEH) while simultaneously calculating the electrical and mechanical related responses, such as the voltage and the current, and the stress and the strain. Similarly to the Cymbal study, commercially

available FEA software (ANSYS Inc. Canonsbury, PA) was used to develop the CPC-FEM for the study. To reduce computational time, a simple rectangular piezoelectric plate under a low frequency excitation was used as a harvester for this study.

Figure 4.1 shows the CPC-FEM specifically developed for this study, where the piezoelectric plate was poled in the thickness direction and had dimensions of 60mm in length, 40mm in width and 1mm in thickness. The electrodes on the piezoelectric plate were connected to an optimal load resistor, and a sinusoidal force of 500N at a low frequency of 2Hz was applied at the ends of the plate. The element SOLID226 was used to model the 3D piezoelectric plate and the circuit element CIRCU94 was used to model the optimal load resistor connected to the electrodes of the piezoelectric plate. To create the electrodes on the top and bottom of the piezoelectric plate the nodes were electrically coupled for each surface to ensure the identical voltage across the surface.

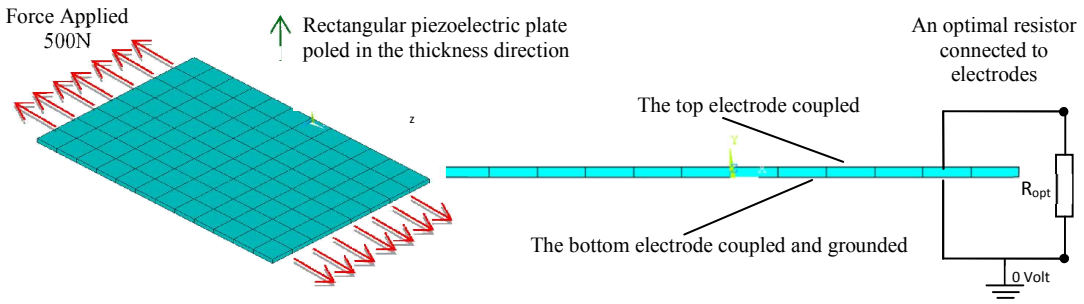

Figure 4.1 CPC-FEM model used in the study

4.2.2 **Approach to the study**

To study how power generation capability was linked to piezoelectric material properties, 25 different piezoelectric materials were selected, including a signal crystal, a PVDF (PVDF-piezoelectric film), 12 soft PZTs and 11 hard PZTs. The terms soft and hard refer to its electrical properties, not its mechanical properties. Hard piezoelectric materials usually have lower piezoelectric constant values, lower dielectric constants, lower dielectric losses, better linearity and are harder to de-polarise. In contrast to this, soft piezoelectric materials tend to have high piezoelectric constant values, high dielectric constants, high dielectric losses, poor linearity and are easier to de-polarise.

The governing equations for piezoelectric behaviour are the electromechanical constitutive equations. In a specific form of these equations by [107] it can be deduced that the only piezoelectric constants involved are; s^E, d and ε^S which are the elastic compliance, piezoelectric constants (relating strain and electric field) and dielectric constants, respectively. Therefore, the piezoelectric material properties chosen for study are based on this group of parameters named here as 'key material properties'. For a more detailed explanation of the piezoelectric constitutive equation discussed here, please see Appendix 2.

Of the 25 piezoelectric materials studied and sourced from companies listed in Table 4.2, all of the material properties are input into the model but only the key material properties, which were related to the plane stress state, and the associated material properties, i.e., s_{11}, d_{31}, g_{31}, ε^T_{r33}, k_{31}, FOM, are listed in Table 4.1.

Initially, an alternative to this study was proposed; to acquire data for one piezoelectric material and then to artificially vary each material property systematically to investigate relationships with power output e.g., to keep all but one of the material properties constant and therefore to test that single material property in a meaningful range, then repeat the process with focus on a different material property. A disadvantage with this approach is; it would be a study of an artificial piezoelectric material and would therefore not reflect what was possible in real terms. The study carried out in this chapter uses real piezoelectric material data, with the majority of data sourced from piezoelectric manufacturers. The method used was to input all of the necessary material properties into the CPC-FEM of the simple harvester and run a harmonic simulation to obtain the power output. The only output of the CPC-FEM was the power output.

The mechanical quality factor and dielectric loss were not considered in this study as they are typically characterised at 1 kHz and therefore they are less relevant for lower frequency and quasi-static energy harvesting away from resonant states.

It should be kept in mind that the PEH gives different power outputs when connected to different value load resistors. In order to give a fair comparison for all the materials studied, the maximum power output of the PEH connected to its optimal resistive load

is used to analyse the links between power generation capability and piezoelectric materials properties in this thesis. Hence, for each different material input into the CPC-FEM there was a respective optimal resistance. In order to find the optimal resistive load for the PEH, the harmonic analyse of the PEH connected to different value load resistors was first carried out for all the materials studied so as to find the optimal resistance value that provided the highest power output from the PEH. These optimal resistive loads are listed in Table 4.1 with their corresponding power outputs. The optimal resistive load was found using data extracted from the output data of CIRCU94 for each material, also listed in Table 4.1.

The graphs in this chapter are scatter plots, with the addition of the hard and soft groups being identified. In this respect they may resemble a material selection chart or Ashby plot which, for example, may plot density against strength and group the classes of material together (polymers, composites, metals and alloys). Ashby plots may also use a logarithmic scale and contain additional guidelines for specific selection purposes. Seeing as there few material categories to identify within the data in this chapter it was not thought appropriate to attempt to make an Ashby plot.

Table 4.1 Key piezoelectric material properties used in CPC-FEM analyses, associated material properties, optimal load resistances and associated power outputs.

			CPC-FEM INPUTS							CPC-FEM OUTPUT
Type	Ref №	Material Name	Elastic Compliance s_{11} (x10^{-12})	Piezoelectric strain constant $\|d_{31}\|$(x10^{-12} m/V)	Piezoelectric voltage constant $\|g_{31}\|$(x10^{-3} Vm/N)	Relative Dielectric Constant $\varepsilon_{r33}{}^{T}$	Piezoelectric Coupling Coefficient k_{31}	FOM $d_{31}{}^{2}/\varepsilon_{33}{}^{T}$ (x10^{-12})	Optimal resistive Load (MΩ_{opt})	Output power P_{avg} (mW)
Single Crystal	1	PZN-PT	66.6	1330	18.3+	8200§	0.59	24.36	0.16	9.93
PVDF	2	PVDF	333	20	188+	12§	0.11	3.76	310	4.42
PVDF	2.1	PVDF'	333	20	188+	12§	0.11	3.76	2.9	0.082
HARD PZT	3	DL-40	10	48	15	350	0.27	0.74	12	0.87
HARD PZT	4	DL-41	10.2	65	14	520	0.3	0.92	8	1.07
HARD PZT	5	DL-42	11.1	81	12.2	750	0.3	0.99	6	1.14
HARD PZT	6	DL-43	11.5	105	11	1050	0.33	1.19	4	1.39
HARD PZT	7	DL-43 HD	11.2	120	11	1250	0.34	1.3	3	1.53
HARD PZT	8	DL-44	13.3	125	11.8	1200	0.33	1.47	4	1.68
HARD PZT	9	DL-45	12.9	131	11	1350	0.34	1.44	3	1.68
HARD PZT	10	DL-47	11.4	135	9.2	1650	0.33	1.25	3	1.41
HARD PZT	11	DL-45HD	13.1	150	11	1550	0.35	1.64	3	1.88
HARD PZT	12	DL-48	10.9	150	6.4	2650	0.3	0.96	2	1.06
HARD PZT	13	DL-46	15	153	11.9	1450	0.35	1.82	3	2.12
SOFT PZT	14	DL-50	16.1	180	11.3	1800	0.36	2.03	2	2.35
SOFT PZT	15	DL-50HD	15.4	191	11.1	1950	0.37	2.11	2.1	2.44
SOFT PZT	16	DL-51	15.5	210	10.5	2250	0.38	2.21	1.9	2.54
SOFT PZT	17	SM410	15.4	210	10.3*	2000	0.36	2.49	2.2	2.86
SOFT PZT	18	SPEM 5C	17	210	10.8*	2400§	0.345	2.08	1.6	2.42
SOFT PZT	19	DL-52	15	235	9.6	2750	0.39	2.27	1.5	2.61
SOFT PZT	20	DL-52HD	14.4	255	8.9	3230	0.4	2.27	1.4	2.58
SOFT PZT	21	DL-53	16.4	275	9.3	3350	0.4	2.55	1.3	2.91
SOFT PZT	22	DL-53HD	15.1	300	8.8	3850	0.42	2.64	1.2	2.96
SOFT PZT	23	DL-54HD	15.1	320	7.9	4600	0.41	2.51	1.3	3.47
SOFT PZT	24	PSI-5H4E	16.1	320	9.5	3800	0.44	3.04	1	3.50
SOFT PZT	25	SM211	16.1	320	6.7	5400	0.41	2.14	0.8	2.47

§ assumed constant stress for calculations

+calculated using $g=d/\varepsilon^{T}=d/\varepsilon_r{}^{T}\varepsilon_0$

*Original data from manufacturer, but when calculated using $g=d/\varepsilon^{T}$; $g_{31SM410}$=11.9 x10^{-3} Vm/N $g_{31SPEM5C}$ = 9.9 x10^{-3} Vm/N

Table 4.2 Piezoelectric material data origin.

Prefix	Company	Country
DL	DeL Piezo Specialties, LLC. [108]	USA
SPEM	Sumitomo Metal Electronics Devices, Inc. [109]	Japan
PSI	Piezo Systems, Inc. [110]	USA
SM	Steiner & Martins, Inc. [111]	USA

4.2.3 **Results & discussions**

Based on the power outputs listed in Table 4.1, the results between the electrical power output and their key piezoelectric material properties and the associated material properties of s_{11}, d_{31}, g_{31}, ε_{r33}^{T}, k_{31}, and FOM are presented in Figures Figure 4.2-Figure 4.9. This section will evaluate the effect of piezoelectric material properties on power output, provide understanding of how the power generation of the materials relates to the piezoelectric material properties, and give insight to material selection.

4.2.3.1 Effect of S_{11} on power output

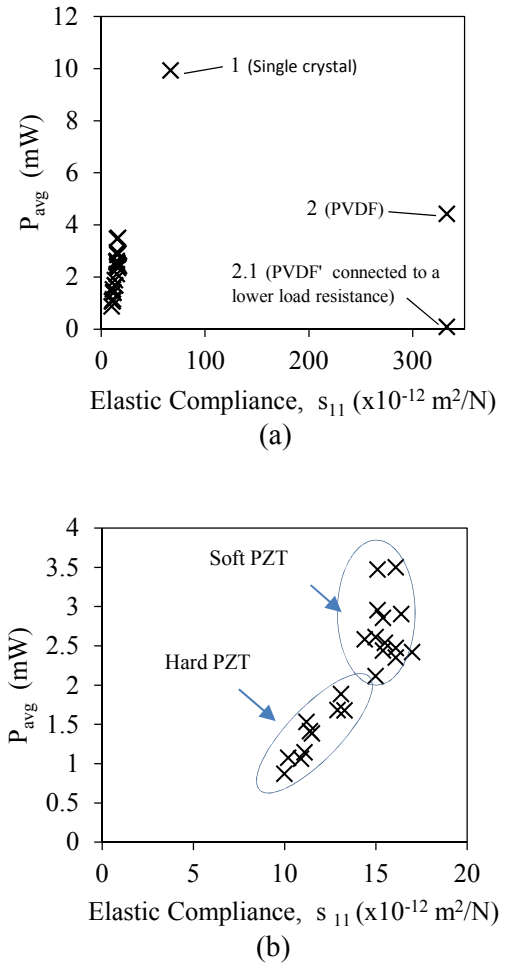

Figure 4.2 Electrical power output vs. elastic compliance of piezoelectric materials: (a) for all the materials listed in Table 4.1 and (b) for soft PZT and hard PZT materials only.

Figure 4.2 shows the electrical power output vs. elastic compliance of piezoelectric materials, s_{11} whilst connected to their respective optimal resistances, where Figure 4.2 (a) is for all the materials listed in Table 4.1, and Figure 4.2 (b) is for soft PZT and hard PZT materials only so as to clearly show the results from these two material sets. It can be observed that there is no clear correlation between the elastic compliance and the power output for the materials studied but it could be concluded that the signal crystal material generated more power than other the materials, and the soft PZTs were better than hard PZTs in terms of higher electrical power output. From Figure 4.2 (b), it can

also be observed that there is no obvious link between the power output and the piezoelectric material properties. Therefore, the material property of elastic compliance can't be used as a parameter for piezoelectric material selection.

The labels Hard and soft in all of the graphs in this chapter refer to electrical properties. Since compliance is the inverse of stiffness, Figure 4.2 (b) shows that the two groups hard and soft are roughly distinct, electrically softer piezoelectric materials tend to be more compliant and therefore less stiff. It would be inaccurate to state that electrically soft materials are generally mechanically soft. Mechanically soft materials are partly characterised by their ability to be cut, moulded or compressed which suggests they yield to pressure easily, whereas materials with a low stiffness (high flexibly) are not defined as having a low yield point. It was expected that the hard materials may have a higher stiffness than the softer materials seeing as harder piezoelectric materials are typically more able to withstand higher stresses that softer piezoelectric material. One of the most prominent differences in manufacture between hard and soft piezoelectric materials is the different doping that they undergo. The doping affects the electrical and mechanical properties. However, a definitive answer could not be found as to why the doping affects stiffness.

4.2.3.2 Effect of d_{31} on power output

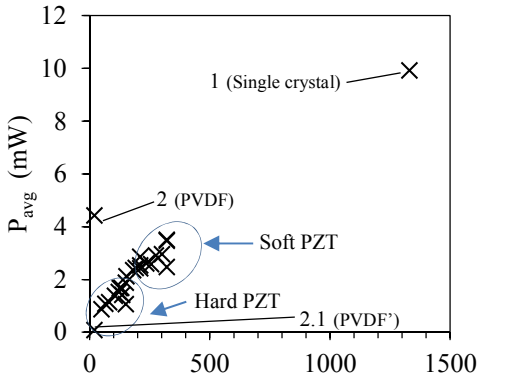

(a)

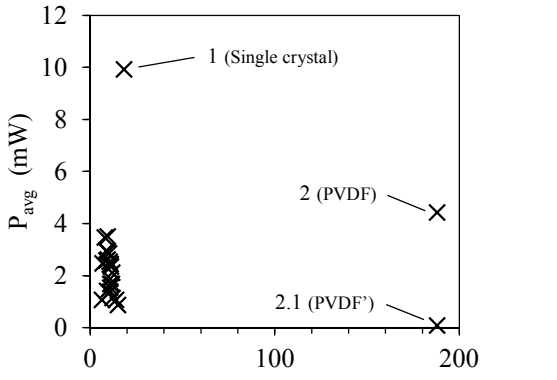

(b)

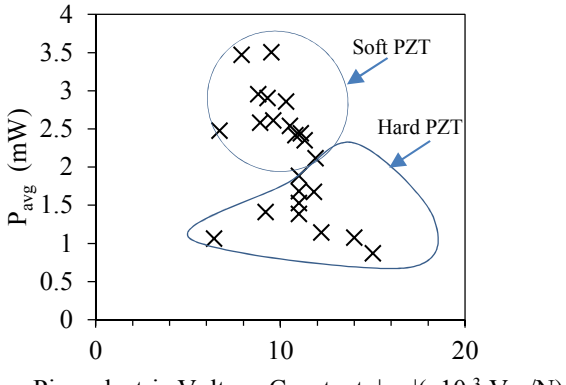

(c)

Figure 4.3 Electrical power output vs. different piezoelectric constants: (a) for piezoelectric strain constants d_{31}, (b) for piezoelectric voltage constants g_{31} for all the materials listed in Table 4.1, and (c) for g_{31} of soft PZT and hard PZT materials only.

Figure 4.3 (a) shows the relationship between d_{31} and the power output, i.e., the higher the d_{31}, the higher the power output for all the materials listed in Table 4.1 except the PVDF material. This is a reasonable trend because, as discussed before, d_{31} represents the charge collected over the electrodes of the PEH to every unit of applied mechanical stress (in short circuit). Figure 4.3 (a) also shows that the single crystal generates more power than other materials and the soft PZTs are better than hard PZTs in their electrical power output due to their higher d_{31}. However, the PVDF material does not follow the trend because it has a very small d_{31} of 20 x10^{-12} m/V and produces a high power output. This exceptional case could be viewed as unrealistic as the optimal load connected to the PEH with the PVDF material was 310MΩ, which is too high to be used to deliver power to applications. For comparison, a similar load resistor to the soft and hard PZT materials of 2.9MΩ was used for the PVDF and the result obtained shows that the PVDF material produces a very small amount of electrical power, around 0.08mW.

Figure 4.3 (b) shows the relationship between g_{31} and the power output. For a better understanding Figure 4.3 (c) excludes PVDF and single crystal materials. From Figure 4.3 (c), it can be observed that there is no clear relationship between g_{31} and power. This suggests g_{31} can't be used as a parameter for piezoelectric material selection, which is not the case mentioned in some literature [7].

4.2.3.3 Effect of ε^{T}_{r33} on power output

Figure 4.4 shows the correlation of the relative dielectric constant ε^{T}_{r33} to the power output. It seemed that the relative dielectric constant ε^{T}_{r33} contributed to the power output as it increases, suggesting that the PEH with a high ε^{T}_{r33} tended to produce a higher power. This was thought inconsistent with both k_{31} and the FOM criteria mentioned above. In Eq (5) Eq (6) and Eq (8), it is clearly stated that the PEHs with a higher ε^{T}_{r33} produce a lower power output as ε^{T}_{r33} is in the denominator in these equations. In order to understand if this is true, further studies on the relationship between ε^{T}_{r33}, d_{31} and their effects on power output are presented below.

Quick Reference

Eq (5) $g = \frac{d}{\varepsilon^{T}}$ Eq (6) $\text{FOM} = dg = \frac{d^2}{\varepsilon^{T}}$ Eq (8) $k_{31}^2 = \frac{d_{31}^2}{s_{11}^{E}\varepsilon_{33}^{T}}$

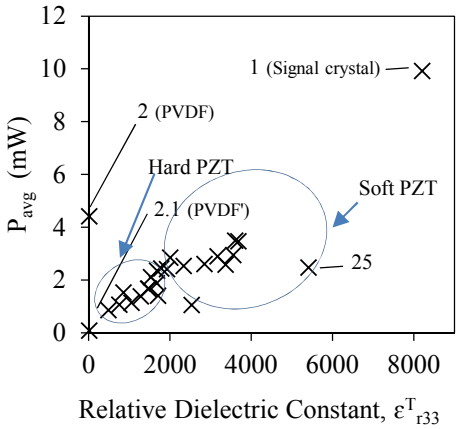

Figure 4.4 Electrical power output vs. relative dielectric constant for all the materials listed in Table 4.1 whilst connected to their respective optimal resistances.

4.2.3.4 Relationship between ε^{T}_{r33} & d_{31} and their effects on power output

Figure 4.5 shows the relationship between the relative dielectric constant ε^{T}_{r33} and the piezoelectric strain constant d_{31}. There is a general trend showing that a higher d_{31} normally has a higher ε^{T}_{r33} for most of the materials listed in Table 4.1. This can be used to, in part, to understand why the above suggestion is not consistent with the one that the k_{31} and the FOM suggest in Eq (6) and Eq (8).

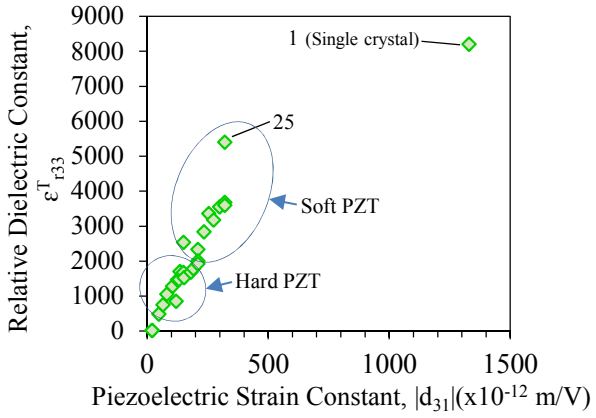

(a)

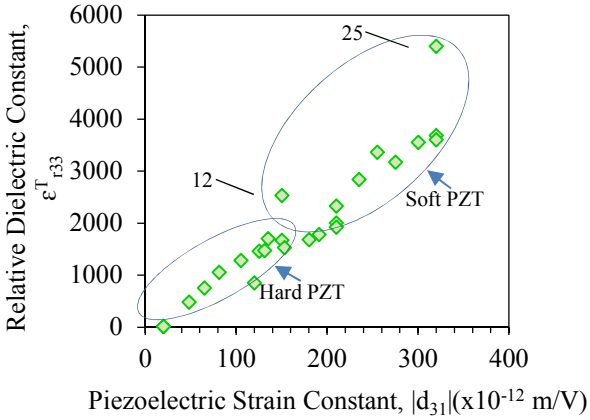

(b)

Figure 4.5 Relationship between relative dielectric constant εTr33 and piezoelectric constant d31: (a) for all the materials listed in Table 4.1 and (b) for soft PZT and hard PZT materials only.

To understand true effect of ε_{r33}^{T} on power output, in Figure 4.6 and Figure 4.7, materials with a similar ε_{r33}^{T} for 4 grouped materials were used to show the dominant effect of d_{31} , not ε_{r33}^{T} on the output power. As previously shown in Figure 4.4, there is a somewhat misleading trend that an increase in ε_{r33}^{T} gives rise to an increase in power. Interestingly, Figure 4.6 suggests that d_{31} is a more dominant parameter than ε_{r33}^{T} for gaining a higher power output; this can be seen by looking at the four groups of ε_{r33}^{T} in Figure 4.6, the higher power output occurs when a higher value of piezoelectric strain constant d_{31} is present whether ε_{r33}^{T} is high or low in its group.

In order to confirm that a lower ε_{r33}^{T} leads to a higher output power, we need to isolate the dominant effect of d_{31}. In Figure 4.7, the materials with 3 sets of identical d_{31} were selected to show the effect of ε_{r33}^{T} on the output power. Figure 4.7 shows that the materials with a lower ε_{r33}^{T} have a higher power output for piezoelectric materials with identical values of d_{31}. In addition, it is interesting to observe Material 18, which has a lower d_{31} and a lower ε_{r33}^{T}, produced a similar amount of power output to Material 25, which has a higher d_{31} and a higher ε_{r33}^{T}. This shows that a lower ε_{r33}^{T} leads to a higher power output, which is consistent with that Eq (6) and Eq (8). Combining Figure 4.6 and Figure 4.7, it can be concluded that d_{31} is a dominant piezoelectric material property in regards to power output and therefore, d_{31} of material property can be used as a parameter for piezoelectric material selection.

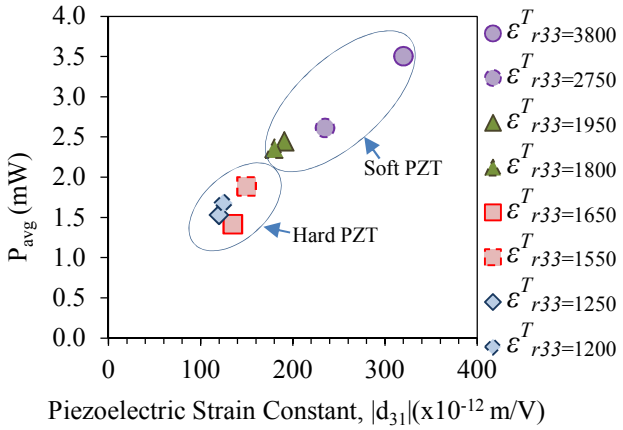

Figure 4.6 Dominant effect of d_{31} on power output for selected materials with a similar ε^{T}_{r33} for 4 grouped materials.

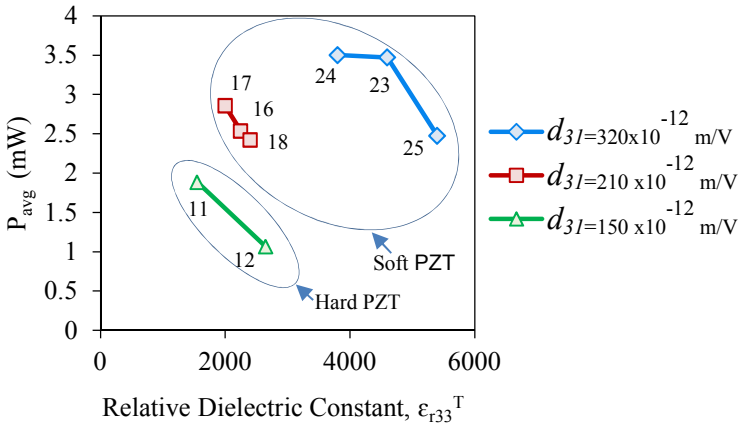

Figure 4.7 Effect of relative dielectric strain constant ε^{T}_{r33} on power output for selected materials with 3 sets of identical d_{31}.

4.2.3.5 Effects of k_{31} on power output

Figure 4.8 shows a plot of the electromechanical coupling coefficient k_{31} for each material against its respective power produced. There is a general trend that a higher k_{31} has a higher power output for all the materials studied here. But for an identical k_{31} of the materials, the power output can be different. For example, Materials 14 and 17 have an identical k_{31} of 0.36 but the power outputs for these two materials are 2.35mW and 2.85mW, respectively. If one uses k_{31} as a selection parameter of piezoelectric material, what are the other parameters to be considered for a higher power output when selecting materials. From Table 4.1 we see that Material 17 has a higher d_{31} than Material 14. So once again, this confirms the previous conclusion drawn from Figure 4.6 and Figure 4.7.

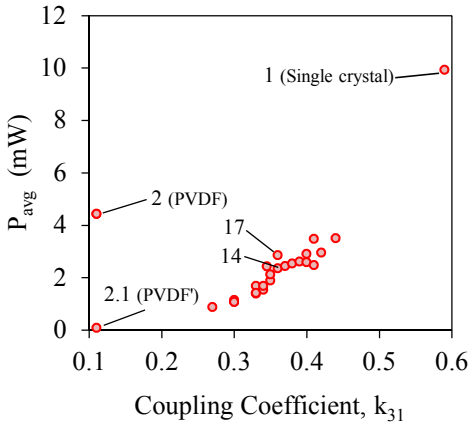

Figure 4.8 Power output vs. electromechanical coupling coefficient k31 for the materials listed in Table 4.1 whilst connected to their respective optimal resistances.

4.2.3.6 Effects of FOM on power output

Figure 4.9 shows a plot of the FOM for all the selected materials against their respective power output produced. There is a moderate linear relationship between the FOM and the power output for all the materials studied here. But for Materials 23 and 17 with a similar FOM, the power output is different, that is, Materials 23 and 17 have FOM of 2.51 and 2.49 but the power outputs for these two materials are different, that is, 3.47mW and 2.86mW, respectively. This suggests that it is not rigorous approach to use FOM as the sole key parameter for piezoelectric material selection and therefore, other parameter(s) should be considered. As seen in Table 4.1 Material 23 has a higher d_{31} than Material 17. Therefore, combined materials properties could be used for selection of piezoelectric material for a higher power output from the PEHs. For example, in the case of choosing between Materials 23 and 17, first you would notice that the FOM are very close in value, you may sway towards Materials 23 as it's FOM is marginally higher, however, once assessing their respective d_{31} values this would cement the choice of using Material 23.

Compared with Figure 4.8, Figure 4.9 shows that the FOM quantity ($d_{31}^{\ 2}/\varepsilon_{33}^{T}$) was more linearly related to the power output than either the coupling coefficient k_{31} or d_{31} alone. Although the majority of data points in Figure 4.9 show a linear trend for Power vs FOM there are three outlier materials; 1, 2.1 and 23. Due to these unexplained outliers no single materials parameters were able to be recommended as selection criteria. However, the obtained CPC-FEM results suggested, combined FOM with d_{31} materials properties can be best used for selection of piezoelectric material for generation of a higher power output from the PEHs. That is, for best results to choose a material with the highest FOM and if the FOM is similar between materials choose the one with the higher d_{31} also.

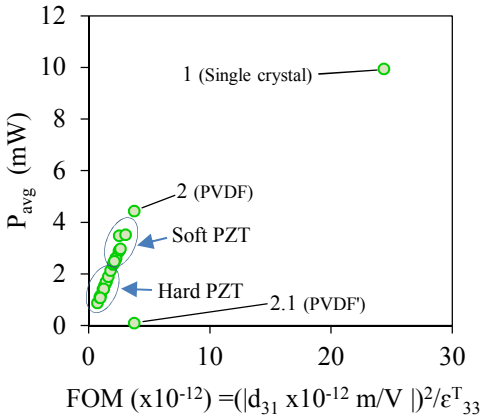

(a)

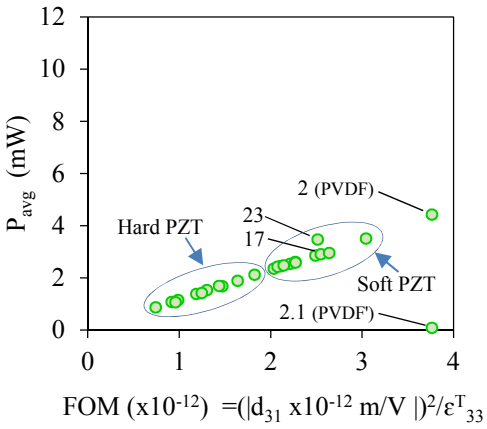

(b)

Figure 4.9 Power output vs. FOM: (a) for all the materials listed in Table 4.1, and (b) for soft PZT and hard PZT, and PVDF materials.

4.2.4 **Summary**

In studying the power outputs of 25 different piezoelectric materials using a CPC-FEM, It was found that (1) d_{31} is a more dominant material property over other material properties for enhanced power output, (2) FOM was a more linear related value to power output than either the coupling coefficient k_{31} or d_{31} alone, and (3) the relative dielectric constant ε_{r33}^{T} had some role when comparing materials with an identical piezoelectric strain constant d_{31}; a lower relative dielectric constant ε_{r33}^{T} was preferred. No single materials parameter were able to be recommended as selection criteria, however, combined FOM with d_{31} materials properties was recommended for selection of piezoelectric material for a higher power output from the PEHs. In terms of choosing a PZT material for use in the final device—presented in a following chapter—the material with the highest power output was PSI-5H4E (d_{31} 320x10^{-12} m/V, FOM 3.04, 3.5mW). However, in reality a material is also chosen based on some extra factors; whether the product can be made to specific dimensions, lead time and monetary cost. Therefore another high performing material was chosen, DL-53HD (d_{31} 300x10^{-12} m/V, FOM 2.64, 2.96mW). DL-54HD was initially chosen but the supplier suggested that the piezoelectric material DL-53HD would perform more consistently over time.

4.3 Endcap Material Analyses and Selection using CPC-FE model

4.3.1 Introduction

Due to their combined elastic behaviour and high yield strength, 5 metal based materials were investigated using a CPC-FEM. The CPC-FEM encompassed the entirety of the piezoelectric flex transducer PFT design that is presented in the next section, although only the material and thickness of the endcap was varied here. Dimensions and further material properties used in the CPC-FEM for this section can be found in Table 5.1. This investigation used a two part modelling approach, 1) harmonic analysis to distinguish the effect of endcap material type on electrical performance and, 2) static analysis to ascertain which material and thickness of endcap performs best.

Table 4.3 Endcap materials used in investigation.

Material Name	Young's Modulus (GPa)	Density (kg/m3)	Poisson's Ratio	Yield Strength (MPa)
AK Stainless Steel 304 (Austenitic) [112]	193	8030	0.24	251
Stainless Steel 304 [113]	193	8000	0.3	205
Aluminium Alloy 1100c [113]	69	2710	0.33	34
Copper Alloy C17200 [113]	128	8250	0.3	195
Titanium Alloy Ti-5Al-2.5Sn [113]	110	4480	0.34	760

4.3.2 Results & discussions

4.3.2.1 Effect of endcap material on electrical performance

There are two main categories of bulk material in the PFT, firstly the ‘active part’ or piezoelectric element and secondly the ‘passive part’ or metal framing. A reduction in mass of the passive part of the PFT means more of the input energy (force input) is available for dissipation across the active part, thus the PFT becomes a more efficient transducer. The effect of reducing the mass is reduced stiffness which in-turn provides

less resistance to elastic deformation and thus improved kinetic to electrical energy transfer. Figure 4.10 demonstrates clearly that reducing the thickness—and therefore and stiffness—of the passive part of the PFT increases its electrical power output. It was not certain what overall quantitative effect the material choice of endcap would have on overall PFT performance. This is why each metal alloy was compared over the same endcap thickness range, Figure 4.10. This comparison revealed only small differences in overall electrical performance of the PFT for each alloy tested. It could be concluded that all of the 5 metal based materials gave the same performance for an endcap thicknesses bellow 1mm. The difference between the metals became most prominent at the highest thickness tested, 3mm, at this point there was a range 2.9-4.2mW power output between metals.

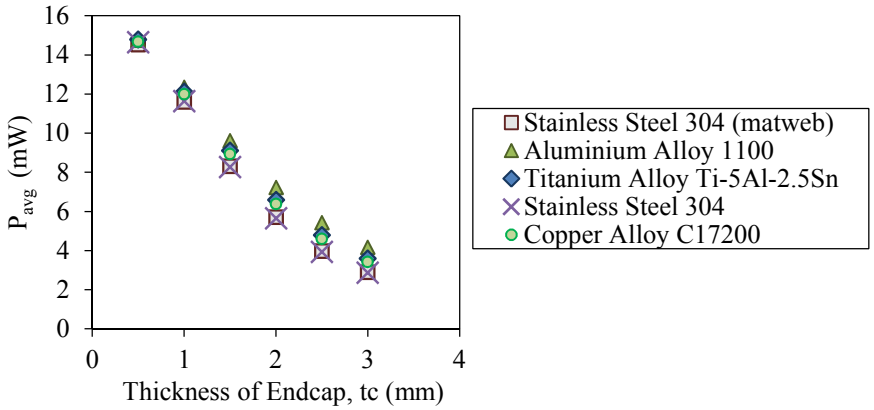

Figure 4.10 Simulated electrical power response of PFT for different endcap materials and thicknesses based on harmonic analyses; PFT is under a 1kN force at 2Hz with a fixed base. Power calculation is based on the PFT connected to a 10MΩ resistor in parallel. All other materials and dimensions are the same as in Table 5.1.

Figure 4.10 shows a correlation between Young's modulus and power output, for each of the 5 metals at an endcap thickness of 3mm, the most stiff alloys (stainless steel) performed worse and the least stiff alloy (aluminium) performed best. It was expected that the more compliant alloys would perform best as they provide less resistance to elastic deformation, which means less energy is wasted during operation. The main conclusion drawn from Figure 4.10 is the endcap thickness is dominant over the endcap material type in terms of their effect on performance. This suggests that the geometry is important than the actual material used.

4.3.2.2 Electrical performance limitations due to mechanical stress

At this point it would seem sensible to choose any of the 5 metals as long as it was the thinnest measure. However, when drastically changing the stiffness of any given structure its structural integrity should also be considered. Figure 4.11 shows that reducing the endcap thickness had a considerable effect on the stress occurring around the bend points of the endcap.

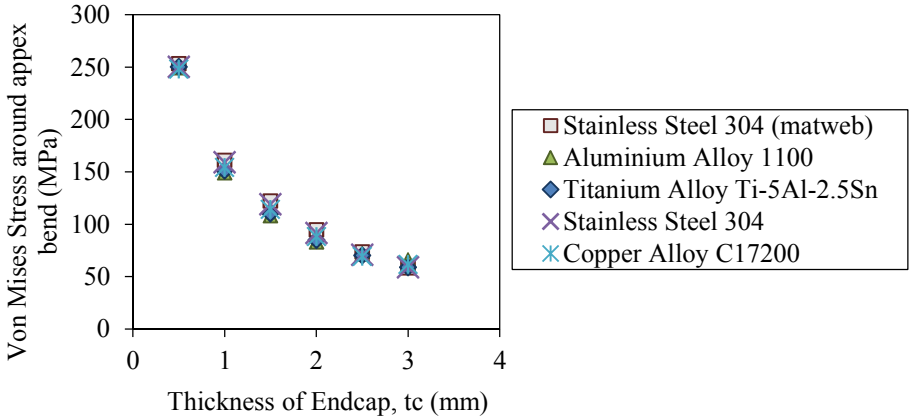

Figure 4.11 Simulated Von Mises stress of PFT around apex bend for different endcap materials and thicknesses. PFT is under a 1kN force with fixed base (Static non-linear analysis). Other PFT dimensions can be found in Table 5.1.

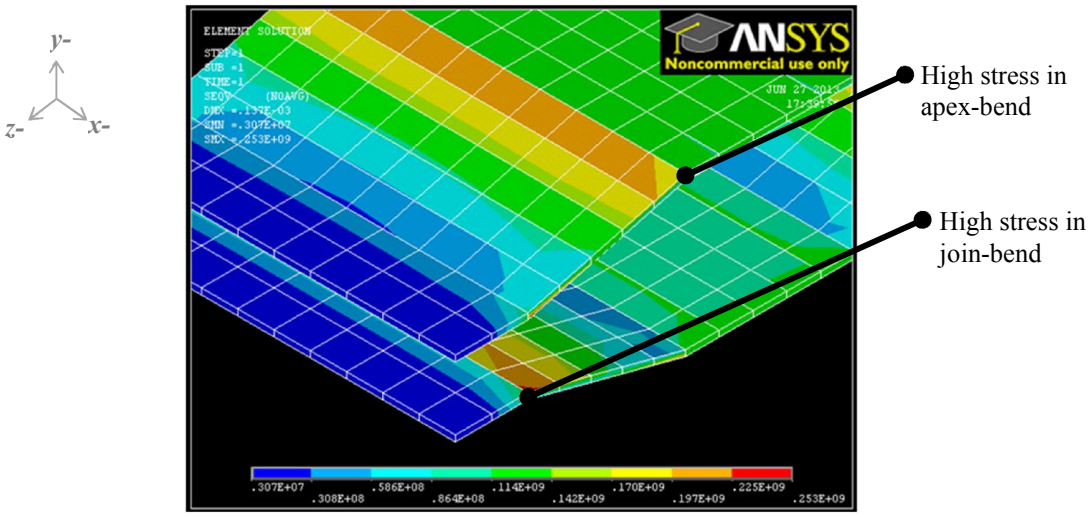

Figure 4.12 A screen-shot of the Von Mises stress in the endcap elements based on static non-linear simulation with the endcap loaded at 1kN. The labels show high stress concentrations occurring in the bent profiles of the endcap, where the endcap is 0.5mm thickness and made from Stainless steel 304 [112].

When static analysis of the PFT was carried out the high stresses occurred at local points. In regards to just the endcaps, these high stress areas were on the bends of the endcaps, both around the apex and near the join bend. This was to be expected as a bend is essentially an interface that houses conflicting force directions which is conducive to a high stress state, in addition to this, the corner and crease areas of a sharp bend are relatively small leading to stress concentrations.

Now considering a failure criteria based on any stress in the endcap not exceeding half the yield stress, then a safety factor of 2 (SF2), the metals were compared once more. Although there are more detailed approaches in determining appropriate safety factors, the final device was considered a non-critical structure due to its low risk levels of financial loss and injury if it failed and therefore a safety factor of 2 was decided suitable. However, it must be stated that the loads applied on the device in practice may be slightly less predictable if used to harvest energy from walking. In contrast to this however, fatigue is also less of an issue due to the low working frequency of the final device.

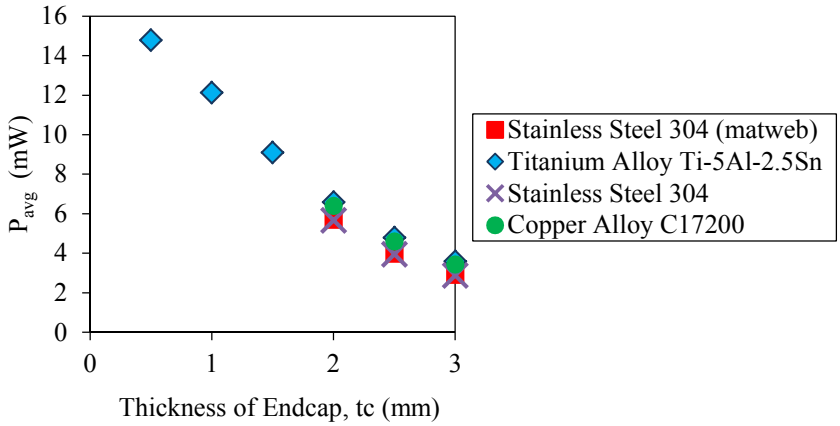

Figure 4.13 Simulated electrical power response of PFT for different endcap materials and thicknesses. Graph excludes results where stress exceeded safety factor 2. PFT under a 1kN force at 2Hz with fixed base (Harmonic Analysis). Power calculation based on the PFT connected in parallel to a 10MΩ resistor. Other PFT dimensions can be found in Table 5.1.

Figure 4.13 shows that titanium was able to withstand the high forces present in the thinnest endcap tested of 0.5mm, therefore, it enabled the PFT to perform to the highest level, 14.8mW. Secondly the copper and stainless steel alloys performed similarly but were not able to be made from an endcap thinner that 2mm before exceeding the failure criteria of a SF2 on the yield stress. The Aluminium alloy was not included in Figure 4.10 as it exceeded the SF2 even for an endcap as thick as 3mm. It could however be argued that the other Aluminium alloys have a higher yield strength and would have fared better in this study having been chosen. A limiting factor of this study is the amount of alloys investigated. Regardless of this, it is clear from this study, out of the alloys investigated, a low Young's modulus/Stiffness was desired for compliance reasons, however, more dominant than this was possessing a high yield strength so that the thinnest endcap possible could be used.

Table 4.4 Endcap thickness allowed when Von Mises stress in endcap is bellow yield strength (SF2).

Material Name	Yield Strength (MPa)	Yield Strength SF2 (MPa)	Minimum Endcap Thickness Allowed (mm)	Von Mises Stress around apex of Endcap (MPa)
Stainless Steel 304 [112]	251	126	2	94.6
Stainless Steel 304 [113]	205	103	2	91.4
Aluminium Alloy 1100 [113]	34	17	Fail	Fail
Copper Alloy C17200 [113]	195	98	2	88.1
Titanium Alloy Ti-5Al-2.5Sn [113]	760	380	0.5	250

4.3.2.3 Effects of the endcap thickness on PZT stress

As mentioned earlier, a change in stiffness of any part of a structure will cause an overall structural behaviour change i.e., reducing the thickness of the endcaps altered the mechanical stress throughout the PFT. Therefore, as a caution the relation between endcap (material and thickness) and stress in the PZT was also investigated. 15MPa was used at the yield stress of the PZT. Two materials for the endcaps were looked at; titanium was chosen for its high yield strength and stainless steel for its relative low cost. A static non-linear analysis of the PZT part of the PFT was carried out, see Figure 4.14.

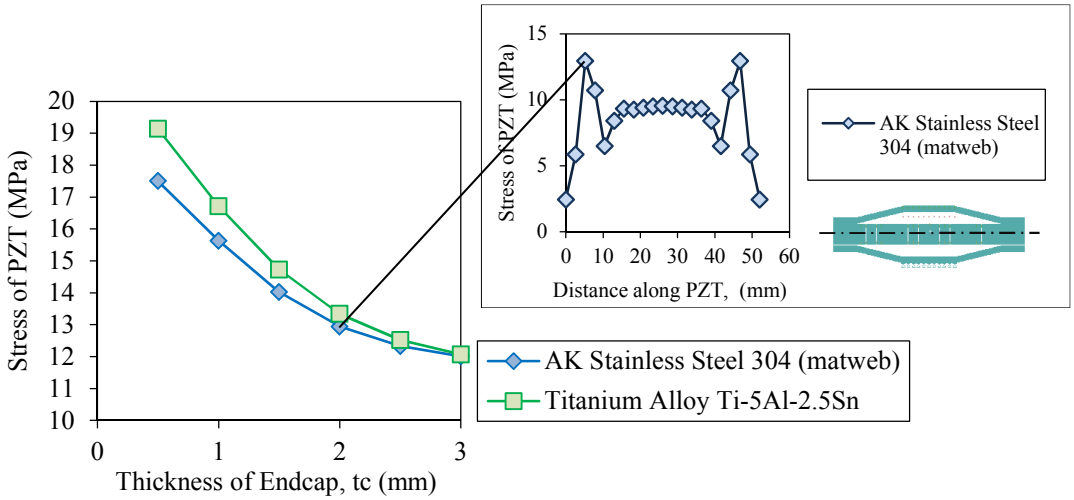

Figure 4.14 Simulated stress in PZT for different endcap thicknesses based on static non-linear analysis, where the PFT is under a 1kN force with a fixed base and each point on the graph corresponds to the maximum stress that occurs along the centre in the z-direction (length-direction) in the PZT. Insert, the stress distribution along the central length-direction of the PZT, where the peaks correspond to the endcap-PZT contact point. Other PFT dimensions can be found in Table 5.1.

Figure 4.14 shows a stress comparison in the PZT of two types of PFT, one with titanium endcaps and one with steel endcaps for a range of thicknesses. For the PFT with titanium endcaps (2mm thick) the stress in the PZT was at 13.34MPa and the corresponding power output was 6.7mW (power output from harmonic simulation in Figure 4.13). For the PFT with stainless steel endcaps (2mm thick) the stress in the PZT was at marginally less at 12.94MPa and the corresponding power output was also less at 5.7mW (power output from harmonic simulation in Figure 4.13).

Although the PFT with the titanium endcaps produced 1mW more than the PFT with the stainless steel endcaps for a similar stress level in the PZT element, stainless steel was chosen over titanium as the material of choice for the endcaps. Ideally titanium would have been chosen as it performed best out of the 5 alloys investigated and was considerably lighter, however stainless steel was more readily available and cheaper.

4.3.3 **Summary**

In selecting a suitable material for the endcaps to be made from, 5 metal alloys were investigated using a CPC-FEM and were chosen due to their combined elastic behaviour and high yield strengths. Early on, a correlation between endcap thickness and power output was identified. In fact, endcap thickness was shown to have a greater effect on electrical performance than the endcaps material type (in the narrow amount of materials investigated). This however, did not mean that any material could have been chosen as there was a limit to the thickness each material could withstand when scrutinised in a structural integrity context. Combing considerations of stress present in the endcaps—for certain thicknesses and material types—with the resultant stress in the PZT element, titanium performed best. Even so, stainless steel was actually chosen due to its lower cost, this meant a possible loss of 1mW power output compared to if titanium endcaps had been used.

CHAPTER 5

Piezoelectric Flex Transducer (PFT)

This Chapter covers the design, fabrication, testing of a PFT. A CPC-FEM of the PFT was used as a design tool and a sensitivity study of the CPC-FEM was carried out. A loading machine was used to investigate the electrical performance of the PFT when a specified force magnitude and frequency was applied to it. The PFT was also retrofitted into a shoe and demonstrated to power a wireless sensor module.

A brief outline of this chapter is as follows:

- CPC-FEM configuration
- Design Analyses of the PFT
- Fabrication of the PFT
- Testing of the PFT using a loading machine
- Investigating sensitivity of CPC-FEM
- Comparison of CPC-FEM results to loading machine results
- Testing of the PFT in an application
- Summary

It was proposed that the studied Cymbal device in the previous chapter could not be scaled-up to withstand higher forces, which was the requirement for harvesting bio-kinetic energy, thus changes were made to the Cymbal device that led to a new design called the PFT.

The Cymbal device was originally designed to take a maximum force of 50N. There is a vulnerable interface between the endcap flange and the piezoelectric disk of the Cymbal device. It's a particularly vulnerable interface because all the force from the endcaps is

transferred across it to the piezoelectric disk. A force transfer across an interface is a likely candidate for mechanical failure by way of delamination. The PFT design aimed to increase the area of this interface, thus spreading the load and reducing the mechanical stress experienced by the adhesion layer. To increase the area of the interface a substrate layer was added, this substrate was welded to the endcap and bonded to the piezo-element using a structural adhesive. Therefore, the bonding area covered the entire surface of the piezo-element and not just the edge as previously done in the Cymbal design. Further from the addition of a substrate, the PFT design varies in general form. The PFT has been made rectangular for an increased packing factor and also to maximise the use of space with the sole of a shoe, which was its original intended location for it.

The PFT consists of a piezoelectric element sandwiched between two metal endcaps with shallow cavities. The stainless steel endcaps have two main functions, 1) to amplify and redirect the downward applied mechanical force to a horizontal force so that the majority of the available force acts to stretch piezo-element horizontally, the converse action happens when the force is removed and the PFT tends back to a physically neutral state, and 2) to suspend the piezo-element and substrate so that they can actuate more freely, generally speaking a higher elastic deformation or elastic strain is beneficial in piezoelectric material as it corresponds to a higher charge produced.

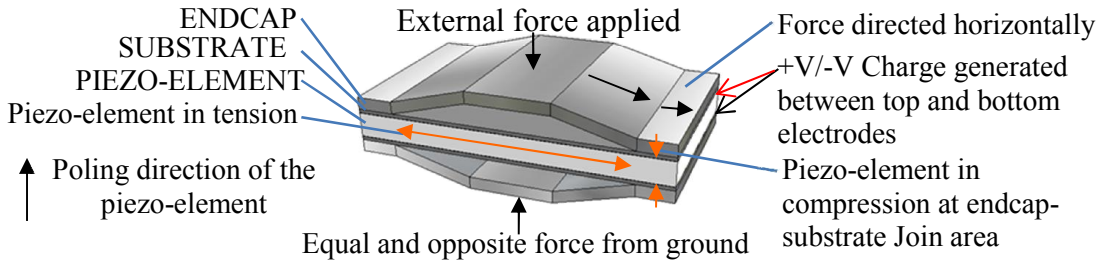

Figure 5.1 Function of the PFT when a downward compressive force is applied.

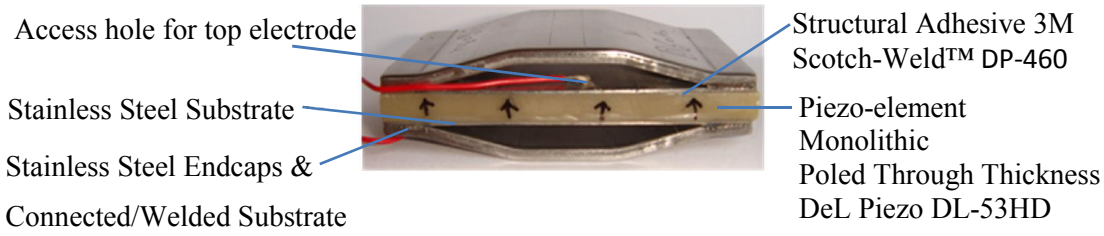

Figure 5.2 A Photo of the PFT showing its general structure and materials.

5.1 Design of PFT using the CPC-FE model

5.1.1 Approaches to the study

Having studied the effects of key parameters of the Cymbal device regarding performance it was beneficial to investigate some of the same parameters for the PFT along with parameters specific to the PFT. Multi-layering was not considered in the PFT study for two reasons. Firstly, it does not help to increase power output although; it does change the voltage, current and optimal resistance. Secondly, any gains from electrical tailoring can be an insufficient trade-off as multi-layering adds a considerable amount of complexity during fabrication.

Parameters picked from Cymbal Study to be used in PFT study:

- Thickness of piezoelectric element.
- Endcap internal angle.
- Join length.

The material property choices of the piezo-element and endcaps have been discussed in previous sections, of which stainless steel was selected for the endcaps and DL-53HD for the piezo-element. The substrate material is kept identical to the endcap material to enable a strong bond such as welding.

Findings from Material Selection Study to be used in new PFT design:

- Piezoelectric material choice.
- Endcap material choice.

Additional parameters to be part of PFT study:

- Electrode coverage.
- Thickness of endcap in conjunction with endcap internal angle.
- Substrate layer.

Another parameter studied was the electrode coverage as it was suspected that a partial electrode that excludes inactive piezoelectric material may be beneficial (Section 5.1.3.3). In the Cymbal device parameter study the endcap thickness and internal angle were studied independently. However, it was decided that their interaction should also be investigated, thus, the endcap thickness and internal angle were studied in combination. Although the substrate layering was a relatively simplistic addition to the structure, any added material associated with deflection in the structure will inevitably absorb some of the energy input and thus needs some consideration in the design analysis, hence it was briefly studied here.

During this design analysis all parameters remained constant apart for the highlighted parameter or parameters being investigated. Unless otherwise stated the geometric parameters and material properties of the PFT are listed in Table 5.1 and Table 5.2, respectively.

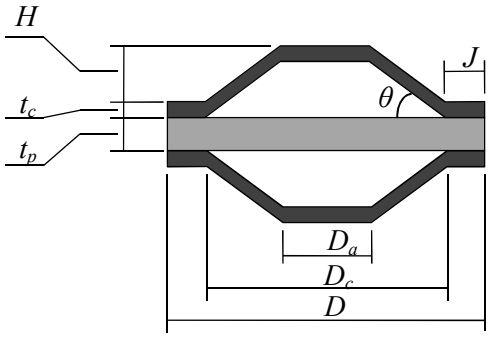

Repeat of Figure 3.4 parameter names of Cymbal and PFT are identical.

Table 5.1 Dimensional parameters used in the PFT CPC-FEM.

Total Length (mm)	D	52
Cavity Distance/Length (mm)	D_c	40
Width (mm)	D_w	30
Apex Distance/Length (mm)	D_a	14
Height (mm)	H	3.5
Caps Thickness (mm)	t_c	2
Piezo Thickness (mm)	t_p	4
Join Length (mm)	J	6
Angle of the Endcap (°)	θ	8.75

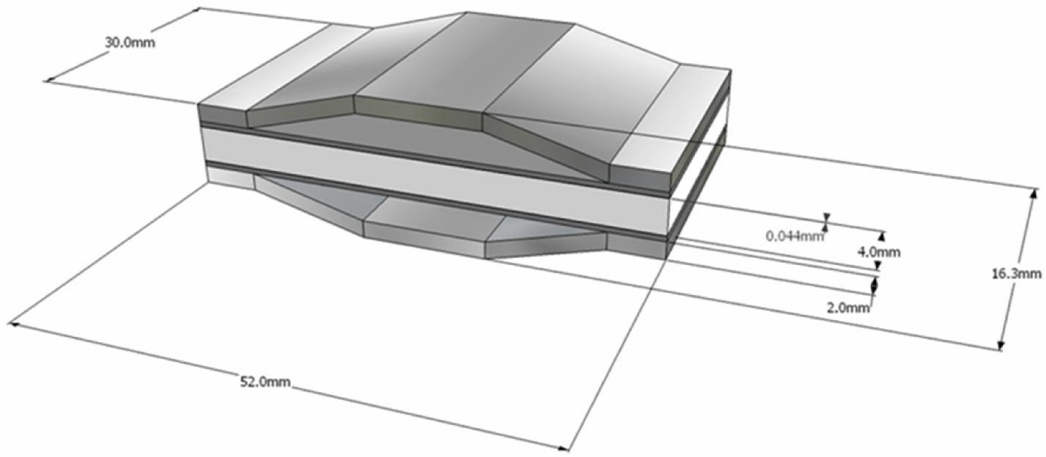

Figure 5.3 CAD sketch of the PFT developed in the CPC-FEM.

Table 5.2 Material properties of materials used in the PFT CPC-FEM.

AK Stainless Steel: Austenitic stainless steel 304, MatWeb, LLC	
Young's Modulus (GPa)	
E	193
Yield Strength (MPa)	
σ_y	215
Density (Kg/m3)	
ρ	8030
Poisson's Ratio	
μ	0.24
Piezoelectric Material: DeL Piezo DL-53HD	
Elastic Compliance (x10-12 m2/N)	
s_{11}	15.1
s_{12}	-4.5
s_{13}	-9.4
s_{33}	24.8
s_{44}	37.1
s_{66}	39.2
Relative Dielectric Constant (at the constant stress)	
ε_{r11}^{T}	3550
ε_{r33}^{T}	3850
Density (Kg/m3)	
ρ	7900
Piezoelectric strain constants (x10-12 m/volt)	
d_{15}	810
d_{31}	-300
d_{33}	680
Piezoelectric Coupling Coefficient k_{31}	0.42
Mechanical quality factor Q	20

5.1.2 **Model configuration**

ANSYS (Version 13), a multi-physics finite element analysis (FEA) software package was used to develop a CPC-FEM of the PFT. The CPC-FEM was similar in configuration to the previous Cymbal device model and included the general structure of the PFT and a load resistor connected in parallel with the piezo-element of the PFT. Running a harmonic analysis the CPC-FEM had the ability to calculate the electrical output of the PFT whilst it was subject to an external force excitation, such possible

outputs were; the peak voltage, current and power produced. Static analysis was also carried out to establish the mechanical stress of the PFT.

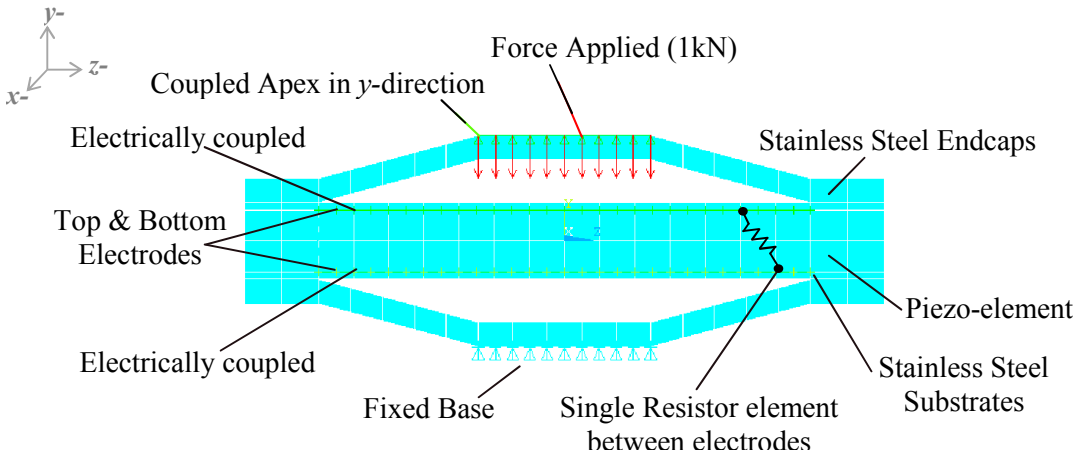

Figure 5.4 PFT in CPC-FEM showing boundary conditions and how electrical resistor is connected in parallel with PFT. Top left: axis coordinates used in CPC-FEM.

Figure 5.4 shows the developed CPC-FEM of the PFT with meshes, which consisted of the PFT connected to a load resistor. Three element types were used in the CPC-FEM. Firstly, the element type used for the piezo-elemenet was SOLID226; a hexahedral element type comprised of 20 nodes. SOLID226 is a couple-field element type that is capable of analysing piezoelectric structural performance. Secondly, SOLID95 was used for the endcaps and substrate layer; also a hexahedral type element comprised of 20 nodes. It should be mentioned that the elements of SOLID226 and SOLID95 have been specifically selected to have the same element structures and numbers of nodes to ensure their inter compatibility. Finally, CIRCU94 was used for the resistor element connected to the piezo-element. The PFT was modelled with the lower endcap fixed and a universally distributed load (UDL) applied to the upper surface of the upper endcap. The force applied to the top endcap was 1kN, this is an approximation of what a solider might exert on the ground. For an explanation of how the piezoelectric material was input using APDL please refer to Appendix 2.

As the thickness of the electrodes were very thin and they were ignored in the model; only the electrical voltages and charges on the electrode surfaces were considered. Thus, during the modelling, the nodes of the electrode surfaces were electrically coupled to ensure an equal electrical potential across the electrode surface. This meant that each

node was electrically connected to its neighbour, much like creating a short circuit over the surface. It was also assumed that the thickness of the adhesion layers between the endcaps and the piezo-elememt was very thin and so were ignored in the model.

5.1.3 Simulation results and PFT design analyses

In the following set of results, average power output of the PFT is used as a measure of fitness and is calculated using Eq (12).

5.1.3.1 Piezo-element Thickness

The first parameter that was studied was the thickness of the piezo-element. Figure 5.5 (a) shows how the power output increases with an increase in piezo-thickness for a PFT under a 1kN force load at 2Hz. The piezo-element thickness range studied was 0.5-9mm, which approximately corresponded to a power range of 2-5mW, a voltage range of 80-449V, a current range of 53-24μA and an optimal resistance range of 1.5-19MΩ. The trend of power in Figure 5.5 (a) peaks at around 5.7mW which corresponds to a PFT with a piezo-thickness of 5mm (12MΩ). When the thickness of the piezo-element is changed it affects the inherent capacitance and internal resistance of the PFT, this results in a variation of voltage and current produced by the PFT shown in Figure 5.5 (b) & (c). As the thickness of the piezo-element is increased the capacitance decreases and the internal resistance increases. It is important to note for circumstances where further integration with power management systems is required that for thicker piezo-elements comes an inherently higher optimal resistance e.g. for a piezo-element 0.5mm thick the optimal resistance was 1.5MΩ and for a piezo-elements 9mm thick the optimal resistance was 19MΩ, see Figure 5.5 (a).

Along with the piezo-thickness, the corresponding optimal resistance and mechanical stress was also considered in the selection process. Form Figure 5.5 (a) we see that the highest power output was 5.7mW at a thickness of 5mm (12MΩ), however, a thickness of 4mm was chosen for reasons that a minor reduction in power gave a major reduction in optimal resistance. The PFT with a piezo-thickness of 4mm only produced 0.1mW

less power compared to the 5mm thick piezo-element but the optimal resistance was reduce by 2MΩ to 10MΩ, this was seen as a sufficient compromise. Of course, the optimal resistance of any piezo-element can be reduced for the same power output if multi-layering of the electrodes is used in place of a monolithic piezo-element used here (see Section 3.3.6), but decreasing optimal resistance using multi-layering was not seen worthwhile enough for the potential increasing structural complexity. The approach used was crude in the sense that first the power levels and associated optimal resistances were established and afterwards the thickness was picked based on a compromise of the two parameters. As previously mentioned the mechanical stress was also closely monitored, the stress intensity of the piezo-element (4mm thick) was 12.94MPa, which was considered a low risk stress level for operation, see inset graph in Figure 4.14.

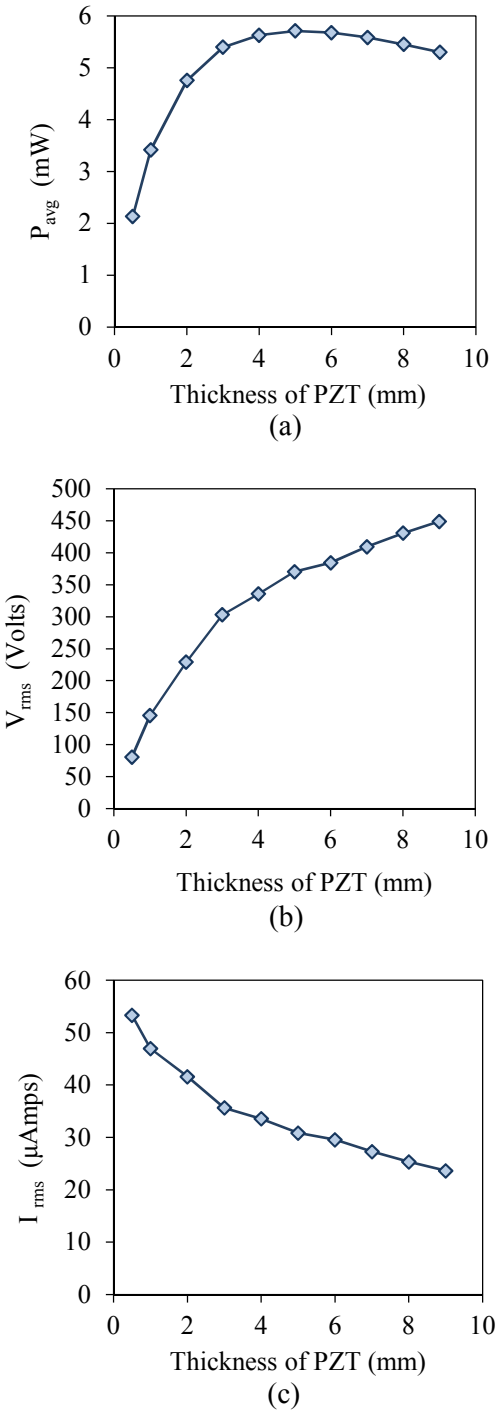

Figure 5.5 Simulated electrical output of the PFT verses piezo-element thicknesses, where the PFT is subjected to a 1kN force at 2Hz. For each different piezo-thickness the optimal resistance was used, and dimensions of the PFT can be found in Table 5.1 and for the material properties in Table 5.2.

5.1.3.2 Endcap Flange/Join Length

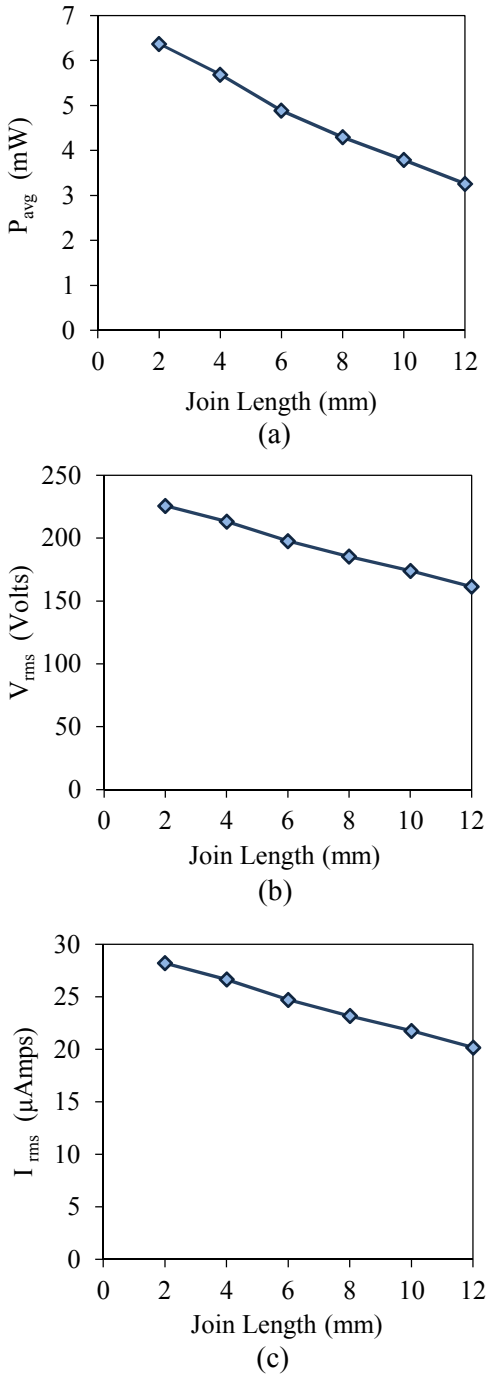

Figure 5.6 Simulated electrical output of the PFT verses join lengths, where the PFT was subject to a 1kN force at 2Hz, whilst connected in parallel to an 8MΩ resistor, dimensions of the PFT can be found in Table 5.1,Table 5.1 Dimensional parameters used in the PFT CPC-FEM. and for the material properties in Table 5.2.

The results shown in Figure 5.6 (a)-(c) are for the electrical outputs produced by the PFT when the join lengths on the PFT endcaps were changed. When changing between 2-12mm there was an approximate variation in power of 3.1mW, a variation in voltage of 65V and a variation in current of 8μA.

Figure 5.6 (a) shows that a reduced join length (flange area between endcap and substrate) is beneficial for increased power outputs. There was no change in internal angle when changing the join length, the compensating dimension was the apex length of the endcap. One reason for the beneficial effects of smaller a join length was that with smaller join lengths there was less detrimental clamping of the piezo-element. Where clamping and/or griping of the piezo-element occurs there is reduced deflection causing there to be less energy for transduction. Although deflection is related to strain, the stress levels may in some way represent the energy input to the piezo-element and thus also, the difference in activity between parts of the piezo-element. A lack of stress in the clamped region can be observed in the inset graph in Figure 4.14, this Figure shows a dramatic reduction in stress in the clamped region compared with the non-clamped region.

Figure 5.6 (b) & (c) shows how the voltage and current produced by the PFT both increase with a decrease in join, this was expected as the internal properties of the piezo-element remained constant, it was only the force applied to the piezo-element that changed (due to join length changes).

According to Figure 5.6 (a) a smaller join length is desired, however, the join had to be large enough for a join to be possible during fabrication, 6mm was the join length settled on as it allowed for multiple joining techniques that included; spot welding, laser welding along the edges of the join region and for a small nut and bolt configuration. The nut and bolt configuration was not pursued as it would have meant drilling holes in the piezo-element and machining done without specialised cutting tools was avoided because of the risk of mirco-cracks that could cause early mechanical faliure. Also the weight bearing nuts would have increased the risk of a pull-out mechanical failure mode in both the piezo-element and substrate-endcap parts.

5.1.3.3 Electrode Length/Coverage

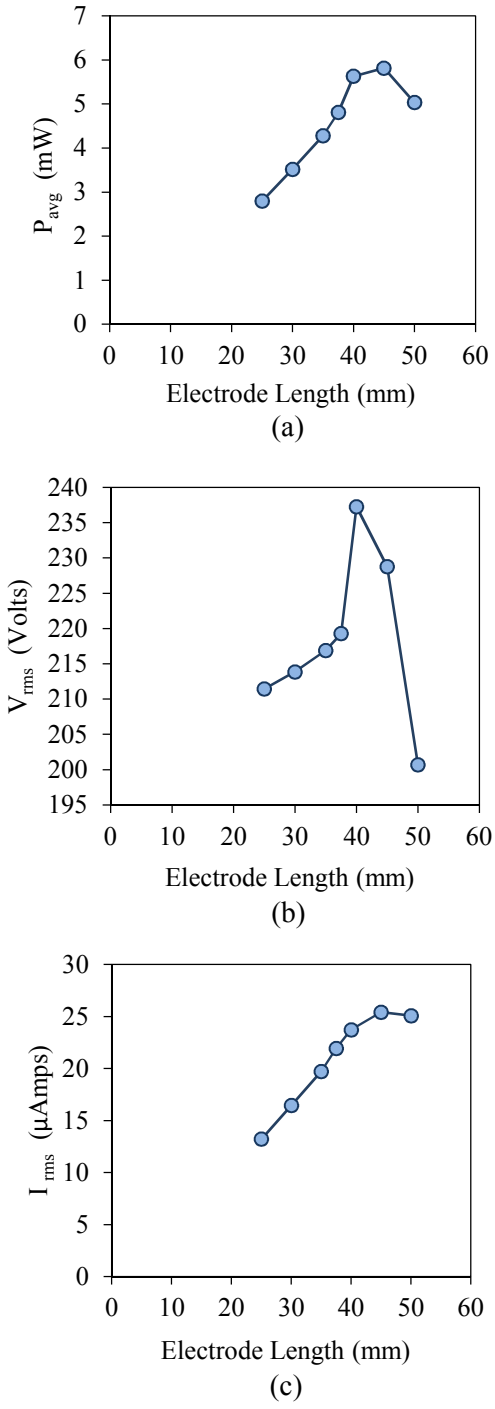

Figure 5.7 Simulated electrical output of the PFT verses electrode length, where the PFT was subject to a 1kN force at 2Hz. For each different electrode length the optimal resistance was used, dimensions of the PFT can be found in Table 5.1 and for the material properties in Table 5.2.

.

Figure 5.7 (a) shows how the power output varied with the electrode length. To clarify, changing the electrode length effectively changed the electrode area (as the CPC-FEM was in 3 geometrical dimensions). The electrode length was varied between 25-50mm, 50mm being an almost complete electrode covering. When compared to a 25mm coverage a 40mm coverage length gave 2.8mW more power, 26V more voltage and 10.5μA more current. When the electrode area coverage was varied across the piezo-element top and bottom region, results showed that the most effective coverage was one that excluded the clamped region of the piezo-element. Therefore in the graph of Power vs. Electrode length, Figure 5.7 (a), the most effective area was around 40mm, which is the distance measured along the PFT that excludes the lengths of the join, otherwise known as the cavity length. The trend-line in Figure 5.7 (a) was not smooth due to the accuracy of the optimal resistances used.

The suspected reason for why a partial electrode (covering just the cavity area) is more effective than a full electrode is as follows:

On the surface of the piezo-element sits the electrode, with a full electrode PFT the electrode covers the full surface of the top and bottom of the piezo-element, with the partial electrode PFT the electrode covers (on the top and bottom of the piezo-element) the cavity area. This cavity area excludes the area bellow where the endcap flange meets the substrate; this join area is effectively clamped and thus contributes negligible charge when the PFT is in use (because there is reduced deflection in the clamped region). If the join region contributes negligible charge then,

$$Q_{Partial} = Q_{Full} \tag{18}$$

where Q is charge in Coulombs, subscript partial is short-hand for partial electrode and full short-hand for full electrode. Also, the capacitance of the partial electrode PFT is smaller as its electrode area is smaller,

$$as, \quad C = \varepsilon_0 \varepsilon_r \frac{A_e}{d_e} \quad then, \quad C_{Partial} < C_{Full} \tag{19}$$

where ε_0 is the permittivity of free space, ε_r the relative permittivity, A_e the electrode area and d_e the distance between the electrodes.

Given that the capacitance of the partial electrode PFT is smaller than the capacitance of the full electrode, to satisfy $Q_{Partial} = Q_{Full}$, then by way of the reduced capacitance of the partial electrode PFT the partial electrode PFT should produce a higher voltage,

$$\begin{aligned} &given, \quad Q_{Partial} = Q_{Full} \\ &and, \quad C_{Partial} < C_{Full} \\ &and, \quad Q = V_{Partial}\ C_{Partial} = V_{Full}\ C_{Full} \\ &then, \quad V_{Partial} > V_{Full} \end{aligned} \tag{20}$$

Where Q is the charge, V is the voltage and C the capacitance.

Not only did the voltage in Figure 5.7 (b) follow a similar trend to the power output in Figure 5.7 (a) but so did the current produced in Figure 5.7 (c). This is contrary to the behaviour of the PFT electrical output when changing the piezo-element thickness in which the voltage and current levels act opposite to one another, as the voltage increase the current decreases. Following a similar route the explanation for why the current increased as the voltage increased is as follows. However, this explanation is not fully satisfying as it does not explain how the voltage and current are able to increase in unison.

$$\begin{aligned} &given, \quad Q_{Partial} = Q_{Full} \\ &and, \quad C_{Partial} < C_{Full} \\ &and, \quad Q = IR_{Partial}\ C_{Partial} = IR_{Full}\ C_{Full} \\ &then, \quad IR_{Partial} > IR_{Full} \end{aligned} \tag{21}$$

The PFT with a partial electrode of 45mm gave the highest power performance at 5.8mW, however a PFT with a partial electrode of 40mm length producing 5.6mW was instead chosen. The 45mm length electrode would have been chosen if it wasn't for a regretful mistake in reading the graph.

5.1.3.4 Endcap Internal Angle and Thickness

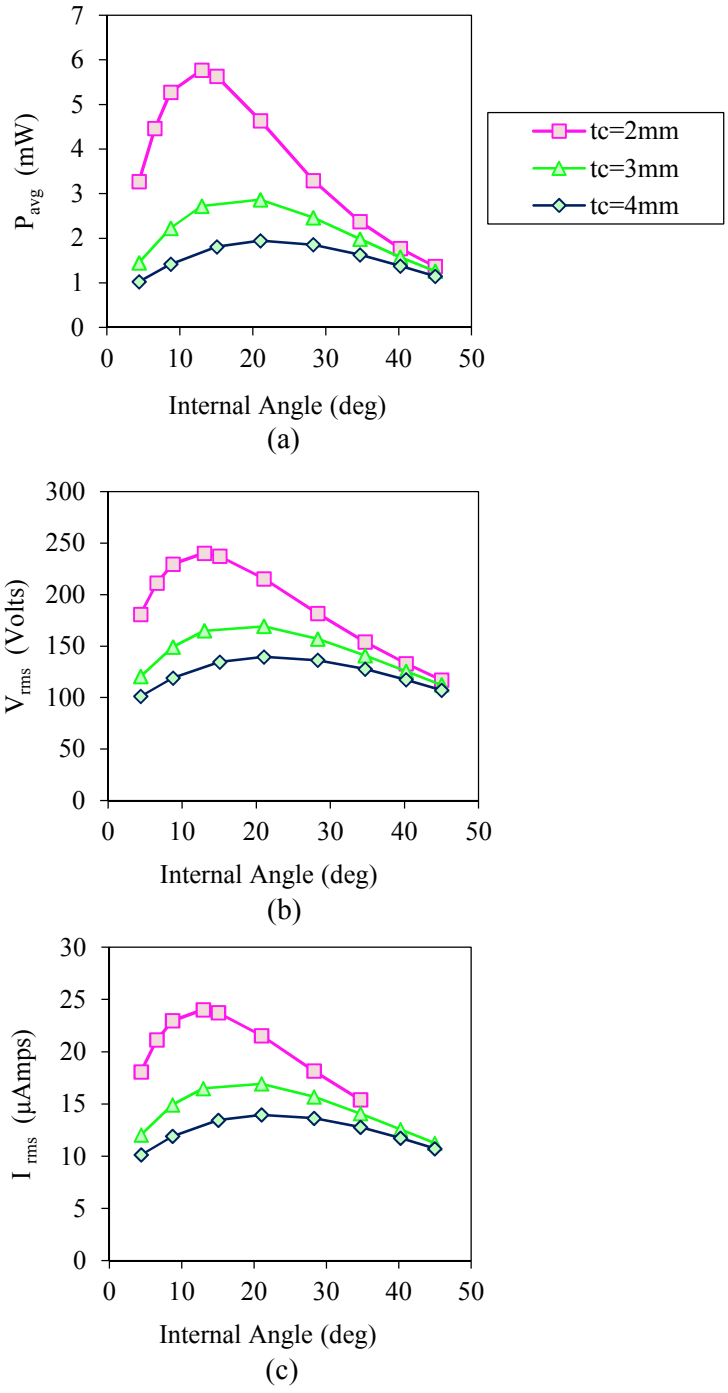

Figure 5.8 Simulated electrical output of the PFT verses internal angle of the endcaps, where the PFT was subjected to a 1kN force at 2Hz, each curve represents a different thickness of the piezo-element, and dimensions of the PFT can be found in Table 5.1 and for the material properties in Table 5.2

The graph in Figure 5.8 (a) shows the effects of using different endcap internal angles with each trend representing a different endcap thickness. Firstly, the results in Figure 5.8 (a) show that in general, thinner endcaps cause a higher power output, the reason being that with less endcap material to resist elastic deformation there is more energy available to be absorbed by the piezo-material, thus causing a greater power output from the PFT.

The second most prominent observation to be made from Figure 5.8 (a) is that a reduction in the internal angle of the endcaps caused an increase in power output. When the internal angle was reduced, more of the force applied to the PFT was directed horizontally along the piezo-element (due to leverage) as opposed to simply being directed downward to cause a tighter clamping between the join areas, and seeing as the force is more efficiently used by the PFT in the horizontal direction (see Section 3.3.3) this causes a greater power output of the PFT. There is a reduction in power output as the internal angle becomes very small, this is because the very small angles are in a sense unrealistic and the resulting deflection of the endcap apex is enough to allow contact between the apex and the substrate cavity surface. Essentially the endcap collapses and the force is not used in the more efficient way possible, which is for it to be directed to stretch the piezo-element in the horizontal direction.

Looking at the interaction between the two parameters in Figure 5.8 (a), thickness and internal angle of endcaps, it can be observed that the effect of the endcap internal angle is more pronounced for thinner endcaps, this is simply because reducing the thickness reduces the stiffness of the endcaps which in-turn allows the endcaps to move more easily in the way that their shape dictates. In other words, the shape defines the form of movement and the stiffness dictates the extent of freedom of movement.

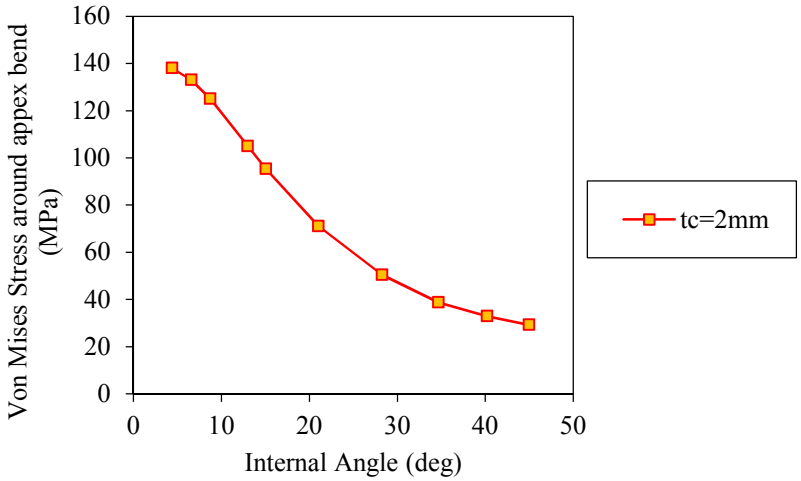

Figure 5.9 Simulated Von Mises Stress around the apex bend of the endcap for the endcap thickness of 2mm, where the PFT was subject to a force of 1kN at 2Hz.

In choosing an endcaps thickness for the PFT it was clear from the observations discussed that a minimised endcap thickness and internal angle would be best. The factor that dictated the limit of these two parameters was the maximum mechanical stress. Following that the stainless steel used had a yield of 125MPa (with SF2 applied) the thinnest endcap and internal angle chosen was 2mm and 8.7° respectively, see Figure 5.9 (a).

5.1.3.5 Substrate Layer Thickness

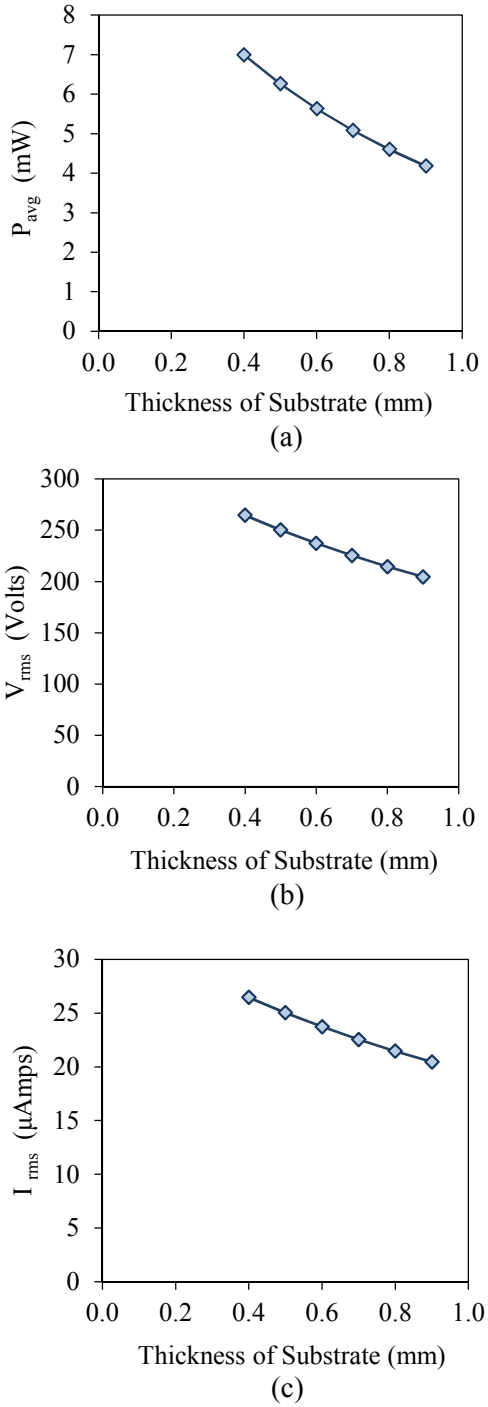

Figure 5.10 Simulated electrical output of the PFT verses substrate thickness, where PFT was subjected to a 1kN force at 2Hz, and dimensions of the PFT can be found in Table 5.1 and for the material properties in Table 5.2.

Figure 5.10 (a) shows the electrical output of the PFT for different thicknesses of substrate. The simulations included both top and bottom substrate, thus during the simulation for a substrate of 0.6mm thickness, both the top and bottom were made to be 0.6mm each. As expected, a thinner substrate resulted in higher power outputs. When the substrate was thinner, more of the applied kinetic energy was able to be distributed to both the endcaps and more importantly to the piezo-element, which is the kinetic to electrical transducer part of the PFT.

The selection process involved choosing a minimal substrate thickness, as minimising thickness led to increased power output, see Figure 5.10 (a). The stress in the substrate even for a substrate thickness of 0.4mm was 82.3MPa which was well with the yield stress of the stainless steel used in the CPC-FEM of 125MPa (thats with a SF2 applied). The limit to how thin the substrate could be was mostly a result of fabrication issues. If the substrate was too thin then the difficulty of the weld increased and also the strength of the weld could be compromised. A manageable thickness for fabrication was thought to be 0.6mm, the fabrication/joining method was either to be resistance or laser welding. Both were experimented with.

5.1.4 **Summary**

This design analysis section has focused on studying key dimensional parameters to use in the final PFT design with the aid of CPC-FEM. The design analysis of the PFT includes work from previous chapters by way of material selection and some key dimensional parameters highlighted by studying the Cymbal. These exact differences between parameters studied for design of the PFT and design of the Cymbal are discussed in Section 5.1.1. The parameters studied included the thickness of piezoelectric element or piezo-element, the endcap Join length, the electrode length/coverage, the thickness of endcap in conjunction with endcap internal angle and the substrate layer thickness, a summary of their details can be found in the following table.

Along with the refining of the dimensional parameters of the PFT the mechanical stress levels were also monitored and the resulting in a PFT design capable of withstanding

1kN at 2Hz, thus making applications such as integrating into to the sole of a shoe possible. Based on the CPC-FEM results, the PFT was then fabricated and tested. At best the CPC-FEM predicts that the PFT could produce 5.6mW under an applied for of magnitude 1kN and frequency 2Hz.

Table 5.3 General relationships and limiting factors for key parameters studied.

	Values Chosen	General relationships between the parameters studied and the power output	Limiting Factors
Thickness of piezoelectric element	4mm	Thicker piezo-elements tended to produce higher power outputs in the range studied, but there was also a peak in the trend to be considered.	For very thick piezo-elements the internal resistance can be problematic for some applications of the PFT.
Endcap join length	6mm	Smaller join lengths gave increased power output.	The join length had to be long enough to ensure fabrication was possible.
Electrode length	40mm	Choosing a length that excludes the inactive piezoelectric material is desired for higher power outputs.	No secondary considerations.
Thickness of the endcap	2mm	Thinner endcaps enhance positive effects of smaller internal angles. Thinner endcaps give higher power outputs.	Very thin endcaps approached yield strength.
Internal angle of endcap	8.7°	Smaller internal angles give higher power outputs.	Very small angles suffered endcap collapse.
Substrate layer thickness	0.6mm	Thinner substrates gave higher power outputs.	Very thin substrates had increased fabrication difficulty.

5.2 Fabrication of the PFT

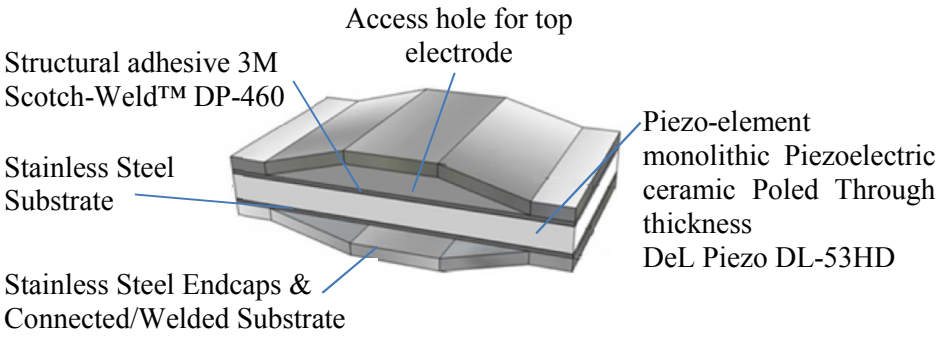

Figure 5.11 Structure of PFT.

The PFT's fabricated and tested were based on the designed produced from the modelling results. There was a restriction due to materials thus allowing 8 PFT's to be fabricated. The PFT was fabricated from the following constituents summed up in the table.

Table 5.4 PFT parts list.

№	Part
1x	DL-53HD Piezoelectric element (poled thickness direction, 2 electrodes)
2x	Stainless steel endcap
2x	Stainless steel substrate
2x	Structural Adhesive Layer (3M Scotch-Weld™ DP-460)
2x	Electrical connection (Circuit Works® silver epoxy)
2x	10cm length of copper wire Ø0.5mm (PVC coated)

The stainless steel endcaps were subcontracted by a metal sheet bending specialist (Rye-Guard Services LtD, UK). The DL-53HD piezoelectric element was tailor made (DeL Piezo Specialties LLC, USA). Most costs were relatively low for the device fabrication with the highest cost per device being the piezoelectric element costing £28.73 (not including shipping or wire fee). The second highest cost was the subcontracted endcaps at £4.50 each, thus £9 per device.

Table 5.5 Costing estimation for single PFT.

	Unit Price* (BPS,£)	Quantity	Cost (BPS,£)
DL-53HD Piezoelectric element	38.5	1	38.5
Stainless steel endcap	4.5	2	9
Stainless steel substrate	0.5	2	1
Structural adhesive Layer (3M Scotch-Weld™ DP-460)	30	1/24	1.25
Electrical connection (Circuit Works® silver epoxy)	50	1/24	2.08
10cm length of copper wire Ø0.5mm (PVC coated)	n/a		
Total			51.83

*Including Shipping, Duty, Wire Fee

One of the intentions of testing was to compare PFT performance of resistance welded vs. laser welded endcaps and also PFTs with a partial electrode vs. PFTs with a full electrode. Seeing as the resistance welds were quicker, cheaper and easier to carry out, more of the PFTs made incorporated this resistance weld design feature. For continuity all of the PFTs involved in comparing electrode covering amount were made using resistance welded endcaps; 3 with a full electrode and 2 with a partial electrode.

Table 5.6 Physical variation in PFTs that were fabricated.

Number	Resistance Weld	Laser Weld	Partial Electrode	Full Electrode
3	√			√
2	√		√	
3		√	√	

In fabrication, two different types of endcap-substrate bond were used. The first was a resistance weld and the second was a laser weld.

Figure 5.12 Resistance welded endcap.

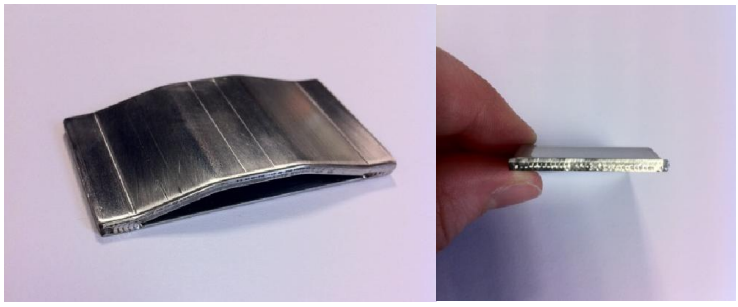

Figure 5.13 Laser welded Endcaps.

The reason for carrying out two different weld approaches was to see if the weld type had an effect on the performance of the device. Resistance welding is a more common form of welding compared with laser welding, however the quality and repeatability of the laser weld is superior. The main physical difference between the two endcaps after welding were the resistance welded endcap had indents that were present on the substrate side of the endcap (a distortion cause by the actual weld point), whereas the laser welded endcap kept its smooth substrate surface.

The Laser welding was carried out by Dr Wojciech Suder in the Welding Institute at Cranfield University using a 300W Nd:YAG pulsed Laser source (JK Lasers, UK) with a pure shield Argon (BOC Plc, UK). After clamping of the endcaps pieces, the laser beam was optically focused to a circular 0.5mm spot. The laser spot was moved along the weld length pulsing at a frequency of 0.8Hz and speed 20mm/min to gain a 50% overlap between weld spots, this created a seemingly continuous weld between the endcap pieces. To create the resistance weld join Ø16mm electrodes with a Ø1.5mm tip were pressed over the flange part of the endcap pieces and exposed to an electrical signal with a power of 12.6 kVA for approx. 1second.

Table 5.7 Fabrication of PFT with laser welded endcaps and partial electrode.

Picture	Description
	Ø2mm hole drilled in through substrate layer for both top and bottom endcap and burrs removed. Substrate side sanded to roughen surface for gluing using medium grade sand paper; aluminium oxide paper-baked Flexovit 80 grit.
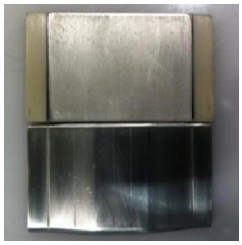	Join length of Electrode removed using wet-and-dry sand paper with very fine grade.
	Remaining Electrode scored with Stanley knife to improve adhesion between endcaps and PZT.
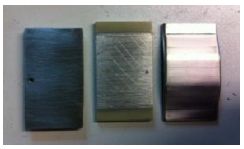	Every component was then cleaned thoroughly with acetone. Then on each side of the PZT element the electrode through-hole connection point was marked and checked for alignment. A Graphite pencil was used due to its good electrical conductivity.
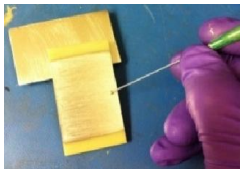	A spot of Circuit Works® silver epoxy (CW2400) was then placed over the through-hole mark point using a needle as a fine spatula. This silver epoxy spot meant that the through-hole spot was claimed and electrical access could be guaranteed when the PZT element was finally glued to its endcaps.
	3M Scotch-Weld™ DP-460 structural adhesive was then put on all four connecting faces of the device; PZT element top and bottom and top and bottom endcap substrate face. The adhesive was carefully smeared over the entire face, in addition a saddle of adhesive was built up along the central axis of each face; this meant that when the faces joined and compressed, the glue would steadily flow outwards towards the sides of the device. This controlled the flow of the adhesive and was thought to reduce the likelihood of air-bubbles, which would be of structural detriment. Air-bubble

boundaries may cause stress concentrations which makes them possible sites for crack initiation.

A basic clamp was made to ensure good midway adhesion between the PZT element and substrate. The clamp beams were treated with a release agent (Loctite® Frekote® FRP-NC®) to prevent the structural epoxy from sticking to them, 3 coats were applied with 20 minute intervals. Before the device parts were bought together the clamp beams were slotted through the endcaps-substrate gaps, then all of the parts were carefully put in place and the clamp beams were fastened together with two bolts.

As soon as the clamp was fastened on the PFT it was then put in a vice for secondary clamping overnight for approx. 14 hours. After 1-2 hours of being in the vice clamp the PFT was checked and an excess leakage of adhesive was wiped from round the sides.

After having left the PFT in the vice for 14 hours it was then removed. By this stage more adhesive had usually leaked onto the clamps again but was tougher compared with 12 hours previous. With a scalpel blade the semi-set glue was sliced off the clamps. The clamps were then loosened fully and wriggled to check they were not stuck to the PFT.

Having checked the clamp was not adhered to the PFT, the clamp was then re-tightened and the PFT was placed in a convection oven on an electrically resistive surface (safety measure). The PFT was then baked bringing it up to 90°C in cautionary steps; ambient to 50°C in 10mins, then to 70°C in 10mins, then to 90°C in 10mins and held at 90°C for 20mins. After baking the device was allowed to cool to ambient temperature slowly.

PVC coated Ø0.5mm wires were then glued through to the electrodes using Circuit Works® silver epoxy (CW2400).

5.3 Testing the PFT

The first testing of the PFTs involved measuring the power output of each device that was made; with the input energy coming from a mechanical loading machine. Testing involved the use of a loading machine, where the force input magnitude and frequency exerted onto the PFT was able to be controlled.

5.3.1 Set-up

Testing was carried out in Cranfield University laboratory space.

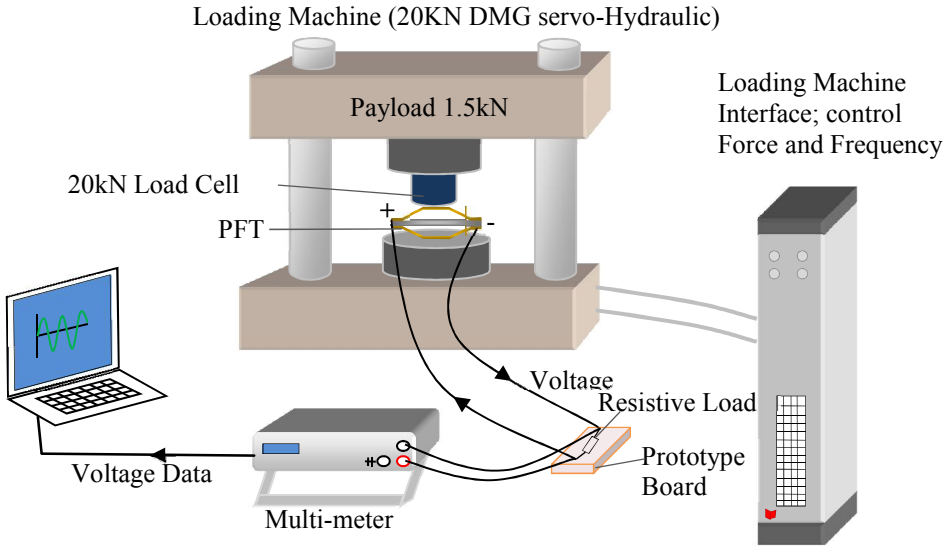

Figure 5.14 Measruing voltage produced by PFT under force excitation of loading machine; PFT electrically connected over a resistive load, voltage measured over resistive load using multimeter with data proccesing on laptop using Agilent Technologies LtD software.

During experimental measurements, the PFT was electrically connected to a range of resistive loads in-turn and a 20kN DMG servo-hydraulic loading machine (Denison Mayes Group, UK) with a 1.5kN payload was used to physically excite the PFT. A 20kN load cell was used to monitor the force exerted on the PFT. Each PFT was individually tested by placing it into a 20kN DMG servo-hydraulic loading machine, the PFT was connected to a load resistor which in-turn was connected and therefore measured by a multi-meter (on the voltage setting). The voltage was measured over a range of resistors with different resistive values to give a response spectrum in order to

identify the optimal resistive value for connecting to the device. Although the voltage was measured by the multi-meter, the multi-meter was also connected to a computer and Agilent Technologies software was used to process the data from it, in this case only the voltage. In order to gain the instantaneous voltage the multi-meter was set to read DC voltage, this meant that the multi-meter passed data equivalent to a sinusoidal voltage signal to the Agilent software. This sinusoidal signal had a minor variation in peak values, thus it would have been inaccurate to read any one of the peak voltages and use this to calculate the rms voltage simply ($V_{rms} = V_{peak} / \sqrt{2}$). Instead the rms or average voltage was calculated by using a number of samples that comprised the sinusoidal wave with multiple peaks. This sinusoidal wave was averaged to give the rms voltage as follows,

$$V_{rms} = \frac{1}{N}\sqrt{\sum_{i=1}^{N} x_i^2} \qquad (22)$$

Where, N is the number of samples and x is the magnitude of the voltage sample.

This electrical resistance response spectrum was recorded for each device over 3 different force loads at 2 different force frequencies. Therefore, for a single device, the spectrum response was recorded 6 times over a combination of loading forces and frequencies 0.5-1kN and 2-5Hz.

Table 5.8 Force and frequency combinations used in loading machine test of single PFT.

		Load (kN)		
		0.5	0.75	1
Freq. (Hz)	2	√	√	√
	5	√	√	√

5.3.2 **Results & discussions**

As mentioned previously, each PFT was individually tested over a range of forces and frequencies. Figure 5.15 to Figure 5.17 show the power outputs of a PFT when excited at 2Hz, each trend-line representing the three force loading magnitudes (0.5, 0.75 and 1kN). The error bars on each trend-line represent a standard deviation based on results from other devices with identical endcap-substrate weld type and electrode area covering, see Table 5.6 for exact numbers of each variant of PFT.

Three central questions will be addressed in this results section.

1. Did the endcap-substrate weld type affect electrical performance?
2. Did the electrode area affect electrical performance?
3. How did the CPC-FEM results compare?

The loading machine was thought to perform best at low frequencies (1-2Hz) and thus had a limited performance at 5Hz and higher.

5.3.2.1 Effects of Endcap-substrate weld and Electrode Variation

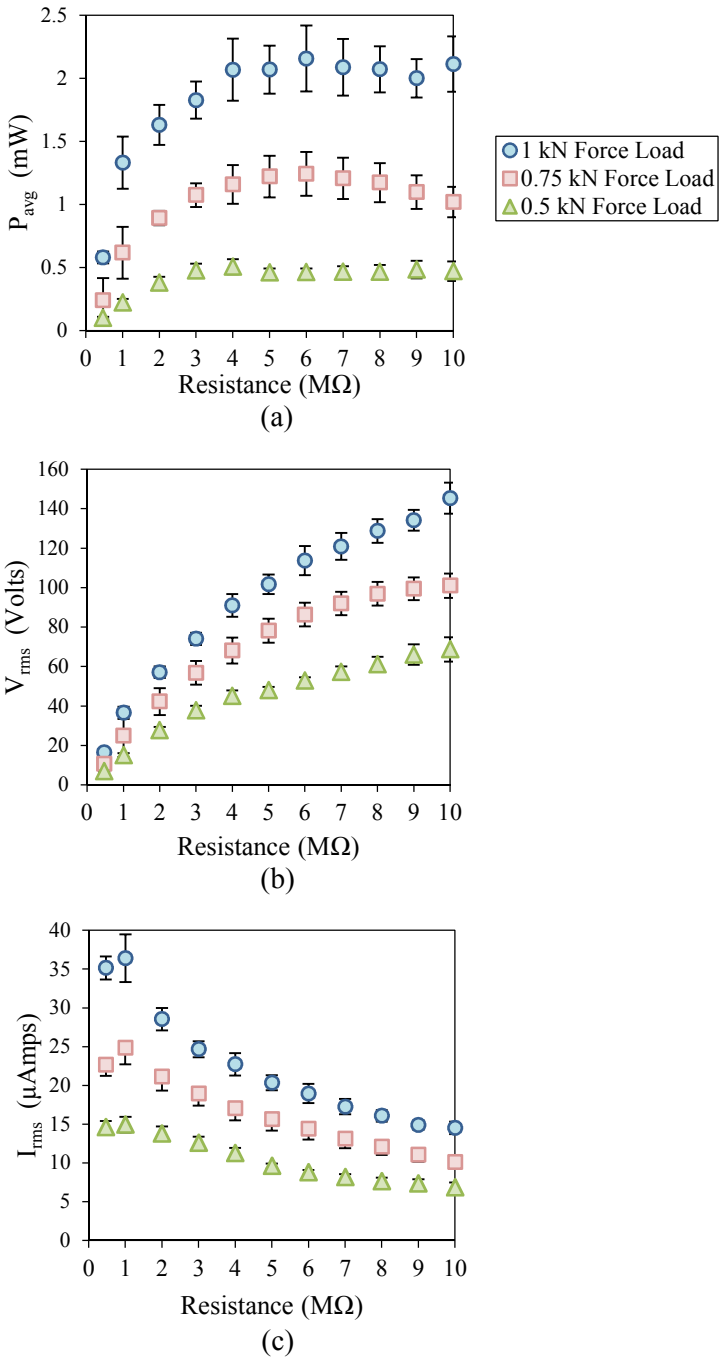

Figure 5.15 The electrical response of a PFT verses the load resistance where the PFT was subjected to a force of 2Hz at three different force magnitudes, the PFT had **laser** welded endcaps and a **partial electrode** area (52mmx30mm), and the error bars are based on standard deviation from experimental results of three identical PFTs.

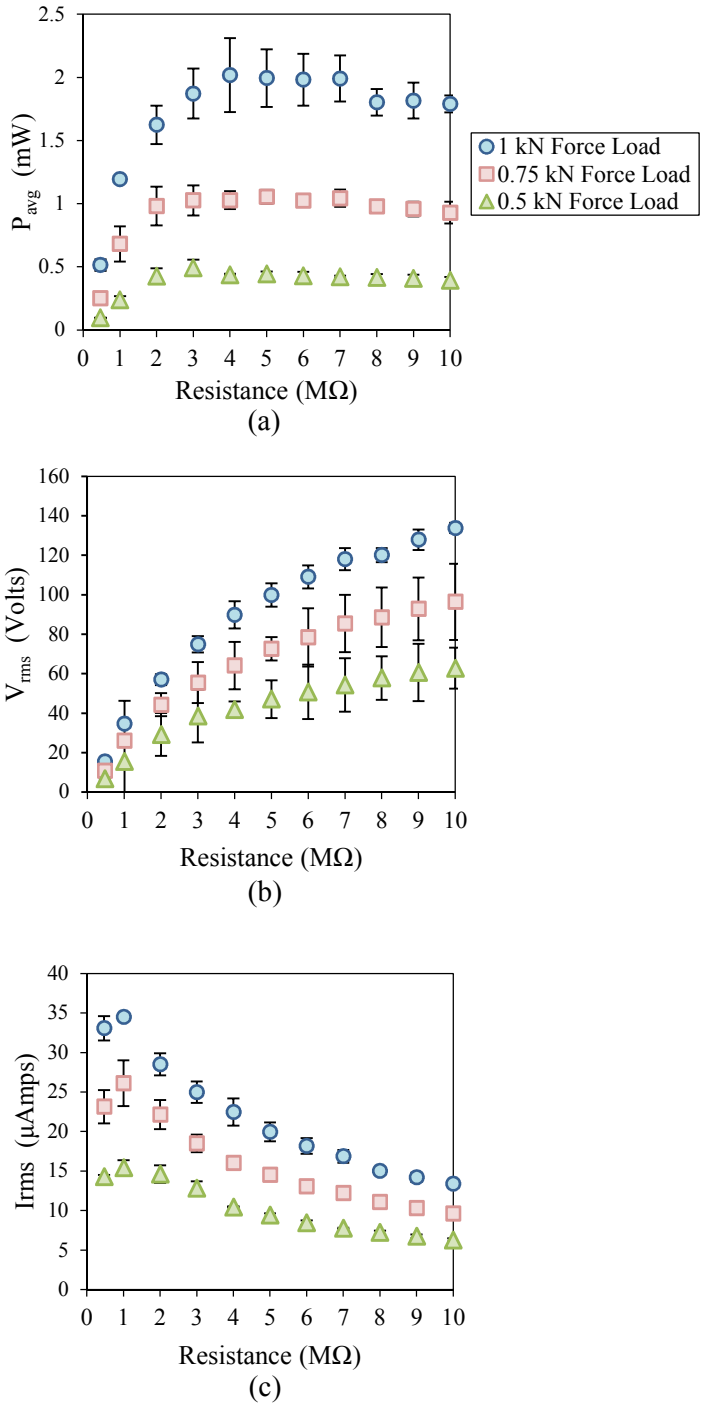

Figure 5.16 The electrical response of a PFT verses load resistance, where the PFT was subjected to a force of 2Hz at three different force magnitudes, the PFT had **resistance** welded endcaps and a **partial electrode** area (40mmx30mm), and error bars were based on standard deviation from experimental results of two identical PFTs.

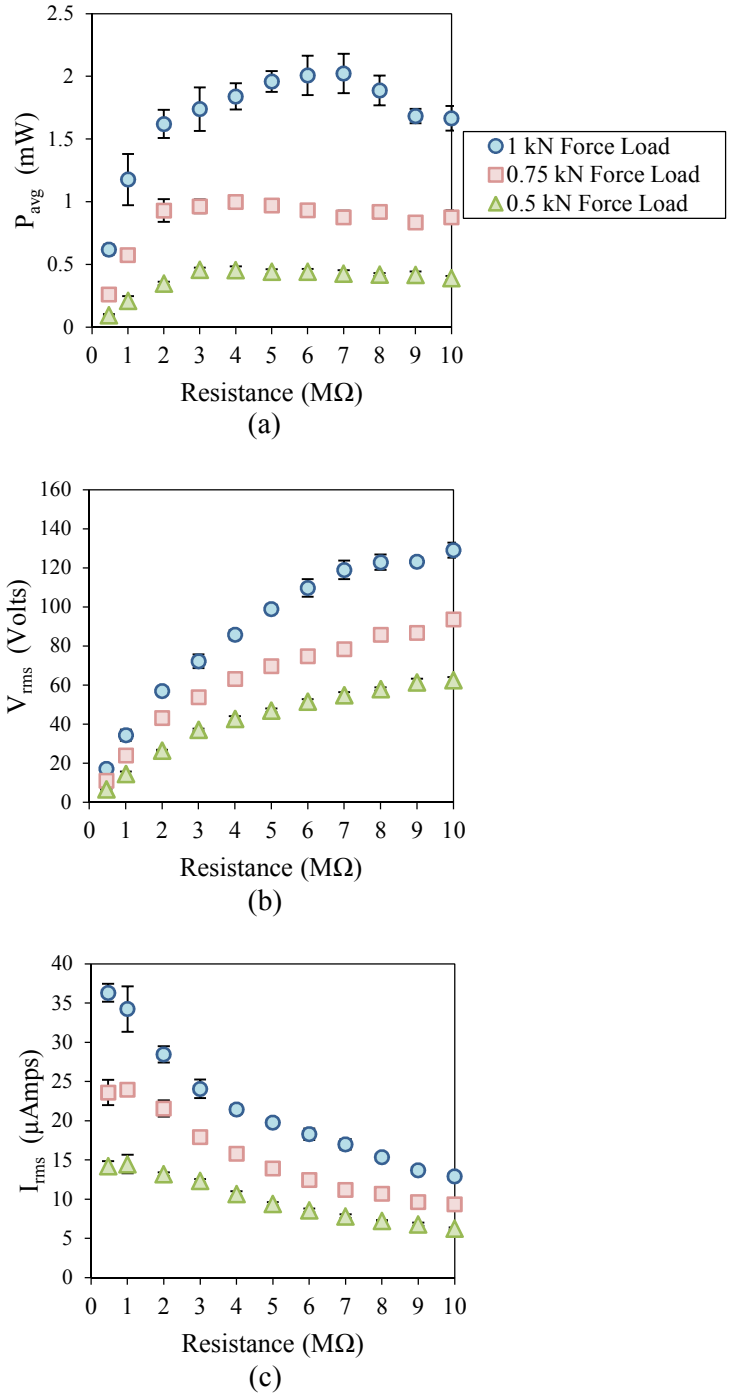

Figure 5.17 The electrical response of a PFT verses load resistance, where the PFT was subjected to a force of 2Hz at three different force magnitudes, the PFT had **resistance** welded endcaps and a **full electrode** area (52mmx30mm), and error bars based on standard deviation from experimental results of three identical PFTs.

As can be seen from Figure 5.15 (a), Figure 5.16 (a) and Figure 5.17 (a) the three variants of PFT; Laser welded endcaps with partial electrodes, resistance welded endcaps with a partial electrodes and resistance welded endcaps with a full electrodes all performed similarly. The peak in power range in PFTs with laser welded endcaps and partial electrodes was 1.63mW (6MΩ, 2Hz, 1kN) at worst and 2.15mW (6MΩ, 2Hz, 1kN) at best. The power range in PFTs with resistance welded endcaps and a partial electrodes was 1.69mW (6MΩ, 2Hz, 1kN) at worst and 1.98mW (6MΩ, 2Hz, 1kN) at best. The power range in PFTs with resistance welded endcaps and full electrodes was 1.7mW (6MΩ, 2Hz, 1kN) at worst and 2mW (6MΩ, 2Hz, 1kN) at best. Due to the similarity of each PFT in terms of all electrical outputs at 2Hz loading for a multiply of force magnitudes, it can be deduced that endcap-substrate weld type and also electrode area coverage did not have any noticeable effect on PFT power output in the 2Hz force frequency range. This was contrary to the CPC-FEM results in Section 5.1.3.30, which showed how electrode coverage had an effect on the electrical output even at 2Hz.

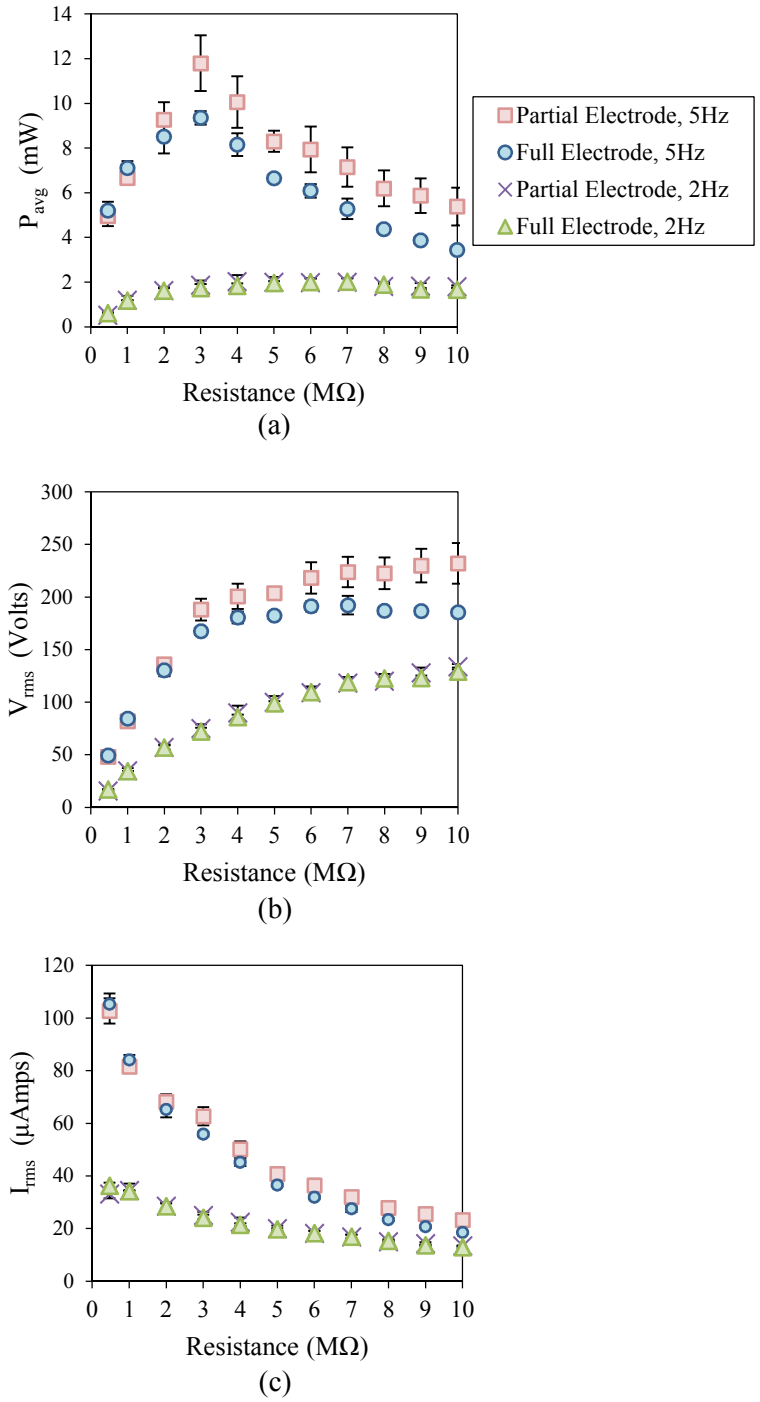

Figure 5.18 The electrical response of 2 different PFTs verses load resistance, were the PFTs were subject to a 1kN force load at two different frequencies, the two types of PFT were one with a full electrode area and one with partial electrode area (both with resistance welded endcaps), and error bars were based on standard deviation experimental results; full electrode based on three devices and partial electrode based on 2 devices.

When observing the power outputs of the PFTs (both with resistance welds) with different electrode area coverage, the resulting power outputs were similar at 2Hz but at 5Hz there was a small but noticeable difference. The PFTs with a partial electrode produced a higher voltage and a higher current (and therefore power) than the PFTs with a full electrode when they were all tested with a 5Hz force exerted on them. The findings in Figure 5.18 therefore suggest that the effect of a partial electrode becomes less apparent when testing with exerted force frequencies around 2Hz.

5.3.2.2 Comparing of PFT test results with CPC-FEM

CPC-FEM Sensitivity

Before comparing the CPC-FEM results of the PFT with the experimental results of the PFT subject to force in a loading machine, the sensitivity of the CPC-FEM was briefly studied.

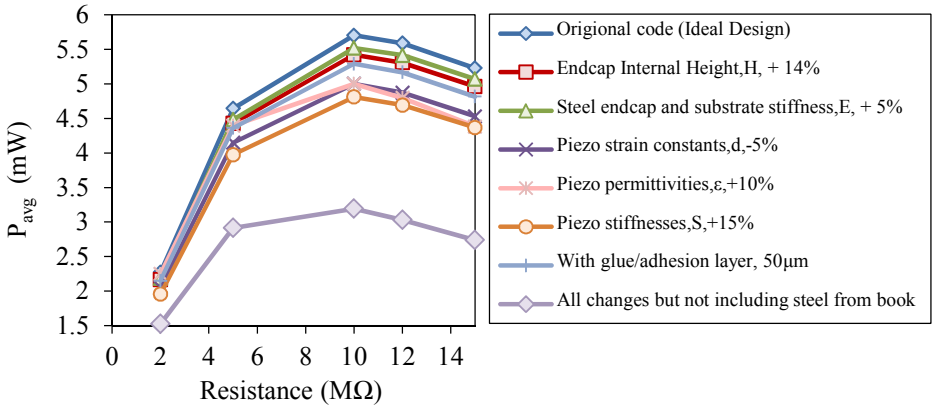

Figure 5.19 Resistance spectrum graph when input parameters were varied in the CPC-FEM of the PFT. Unless stated otherwise dimensions and material properties of the PFT can be found in Table 5.1 and Table 5.2, respectively. For material properties of the adhesion layer see Table 5.9.

When the PFT was fabricated its dimensions were checked and the internal heights of the endcap were found to be 0.5mm more than what was expected considering the tolerance range specified, this resulted in the fabricated PFTs not matching the geometry specified by the design analysis. When checking the sensitivity of the CPC-FEM results of the PFT, this 0.5mm increase in height amounted to a decrease of

0.28mW in power, see Figure 5.19. Thus subsequent comparisons between simulated results and experimental results included this variation in height.

Figure 5.19 is a graph showing the sensitivity of the CPC-FEM of the PFT to some changes in the input variables. The three main materials that comprise the PFT in reality are the piezo-element, the endcaps and substrate (both made of the same material) and the adhesion layer. Hence, the piezoelectric properties and the shared endcap and substrate material were varied and compared to the original CPC-FEM of the PFT in the design analysis section. A simulation was also carried out to show what effect a thin adhesion layer may have.

The piezoelectric properties that were varied were the piezoelectric strain constants (d_{31}, d_{33} and d_{15}), relative permittivity ($\varepsilon_{r11}\varepsilon_{11}$ and ε_{r33}) and stiffness (s_{11}, s_{12}, s_{13}, s_{33}, s_{44} and s_{66}). Based on ranges given by the manufacturers only the worst case scenario was chosen for simulation i.e., the manufactures advised that the piezoelectric strain constant may vary by ±5%, thus the simulation results in Figure 5.19 deducted 5% from each of the three strain constants input. All of the variations in piezoelectric material properties were typical variation values provided by the manufacturer. The variation chosen for the stainless steel was an approximation.

Table 5.9 Material properties of structural adhesive used in CPC-FEM.

Structural Adhesive [114]	
Young's Modulus (GPa) E	22.7
Density (Kg/m3) ρ	1100
Poisson's Ratio μ	0.4

Greatest CPC-FEM sensitivity to some of the input parameters varied was found to be the piezoelectric constants variation, in which deducting 5% from each of the three piezoelectric constants caused the output power to of the PFT to reduce by 12.3%. Variation in the piezoelectric materials also caused other significant power output variations in the CPC-FEM, increasing the permittivity values by 10% caused a 12.3% reduction in power output and increasing the stiffness of the piezoelectric material by 15% caused an almost proportional decrease in power output by 15.7%. The additions of a thin adhesion layer caused a power output decrease of 7.25%. One of the lesser sensitive changes to the CPC-FEM was increasing the stiffness of the endcaps and substrate material by 5% which only caused a 3.2% decrease in power output. When running a simulation with all of the changes applied to the input parameters listed in Table 5.10 their combined effects on the output power gave an overall decrease in power of 44%.

Figure 5.19 shows trends of power output verses load resistance of a PFT for a number of different input parameter variations as well as the power output of an original code and the power output for a PFT simulation where all of the input parameters were varied at the same time, this lead to the combined variation of 44%, as mentioned previously. However, if the power outputs for each individual input parameter change, shown in Figure 5.19 over a 10MOhm resistor are added together (endcap internal height, Steel endcap stiffness, piezoelectric strain constant etc.), this combined power compared to the power output from the original code gave a difference of 56%. A reason for this is that the input parameters are dependent on one another. Optimisation software could be used to vary multiple parameters and therefore investigate the relationships between input parameters in greater detail.

Table 5.10 Affect of PFT CPC-FEM input parameter variation on PFT CPC-FEM power output when the PFT is connected to a parallel resistance of 10MΩ.

Input Variable to PFT CPC-FEM	Amount input variable was changed	Effect on power output when changing corresponding input variable
Original CPC-FEM	0%	0%
Endcap Internal Height, H	14%	5%
Steel endcap and substrate stiffness, E	5%	3.2%
Piezoelectric strain constants, d	-5%	12.3%
Piezoelectric permittivity's, ε	10%	12.3%
Piezoelectric stiffness's, s	15%	15.7%
With glue/adhesion layer, 50μm	N/A	7.2%
All changes		44%

Comparison of CPC-FEM with test results

Figure 5.20 shows a comparison of simulated results from the CPC-FEM of the PFT with experimental results of the PFT for identical loading conditions. The CPC-FEM is based upon the 'ideal' input parameters using in the design analysis section. Similarly, Figure 5.21 shows a comparison between CPC-FEM and experimental results but for a higher force frequency of 5Hz as opposed to 2Hz as in Figure 5.20.

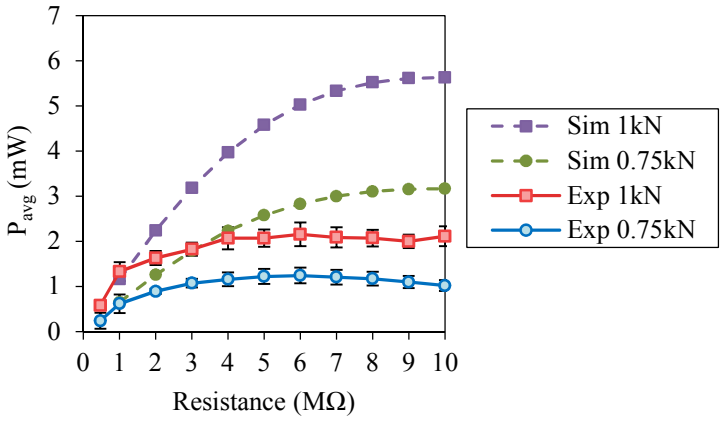

Figure 5.20 Comparision of simulation and experiemntal results of PFT resistance spectrum response, for PFT under a force load at 2Hz over two differnt force loads 1kN and 0.75kN. Simulation is based on worst case senario input parameters for PFT. Experimental results from Section 5.3.2 when PFT was tested in the loading machine.

From the graph in Figure 5.20 where a PFT was subject to a force magnitudes of 1kN and 0.75kN both at 2Hz both experimentally and in using a CPC-FEM it can be observed that the trends of experimental and simulation were similar however the magnitudes were significantly different with the simulation result being much higher. In both loading cases 2Hz 0.75kN and 2Hz 1kN, the simulated result were almost 3 times the magnitude of the experimental result (at 9MΩ).

In the loading cases of 5Hz 0.75kN and 5Hz 1kN, see Figure 5.21, the trends of experimental and simulated results were somewhat alike, however, again the simulated result were higher in magnitude than the experimental result although to a lesser extent than that of the 2Hz comparison.

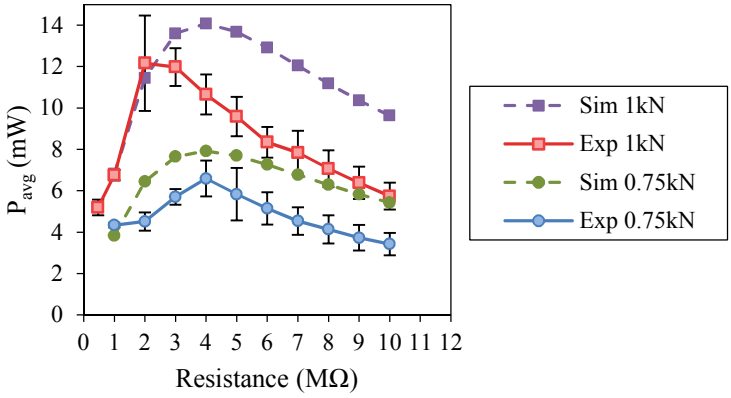

Figure 5.21 Comparision of simulation and experiemntal results of PFT resistance spectrum response, for PFT under a force load at 5Hz over two differnt force loads 1kN and 0.75kN. Simulation is based on worst case senario input parameters for PFT. Experimental results from Section 5.3.2 when PFT was tested in the loading machine.

Both experimental and simulation methods have the capacity to be inaccurate but for different reasons. The simulated result is based on the assumption that the PFTs dimensions and all material properties are exactly accurate, this however is highly unlikely and Figure 5.19 demonstrates the sensitivity of the CPC-FEM to various changes in input parameters. For instance the power output of the PFT CPC-FEM is reduced by 12.3% when reducing the input piezoelectric constants by 5% and when worst case input variables are used the PFT CPC-FEM gives a reduced power output of 44% compared to a model with ideal input values e.g. manufactures material specifications, exact dimensions and no adhesion layers present.

During the experiment there was a piece of equipment that could have resulted in a major systematic error. A 20kN load cell was used to monitor the force exerted on the PFT. The load cell had an unsuitable working force magnitude range for the experiment, thus the results it produced should be viewed as a rough guide. The previous 1.5kN load cell used to measure the force exerted on the Cymbal had been damaged so was not available. Improvements to this experiment would include using a more appropriate load cell. The load cell should be capable of measuring a force magnitude of 0.75-1kN over a force frequency of 2-5Hz. If available it would also be valuable to use a proportional-integral-derivative controller (PID controller) for more accurate measurements for higher force frequencies above 2Hz.

In summary, there was a correlation between the simulation and the experimental results where they showed similar trends, however, their magnitudes were substantially different. Reasons for this difference in magnitude could be because the simulation did not factor for any errors caused by realistic variation for its input parameters, however, the in-appropriately used 20kN load cell was a more likely cause for the magnitudes of the experimental and simulated results being dissimilar.

5.4 Demonstration of PFT in an Application

This section demonstrates the PFT harvesting bio-kinetic energy which was then used to power a wireless sensor module. Initially the PFT was integrated into the sole of a shoe, however, this approach failed (no significant power output) due to a lack of force transfer to the PFT, see Figure 5.22.

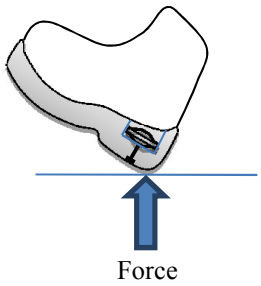

Figure 5.22 Reaction force from ground was obstructed from making contact with PFT due to the thickness of the sole material.

The PFT was then moved further down the sole of the shoe, shown in Figure 5.23 (b). With the PFT moved further down the sole of the shoe, only a small increase in power output from the PFT was gained. To further increase the force transfer from the ball of foot to the PFT a metal plate was then joined to the PFT, shown in Figure 5.23 (c). The addition of the metal plate provided a significant improvement to power output and therefore it was this configuration that was chosen finial testing.

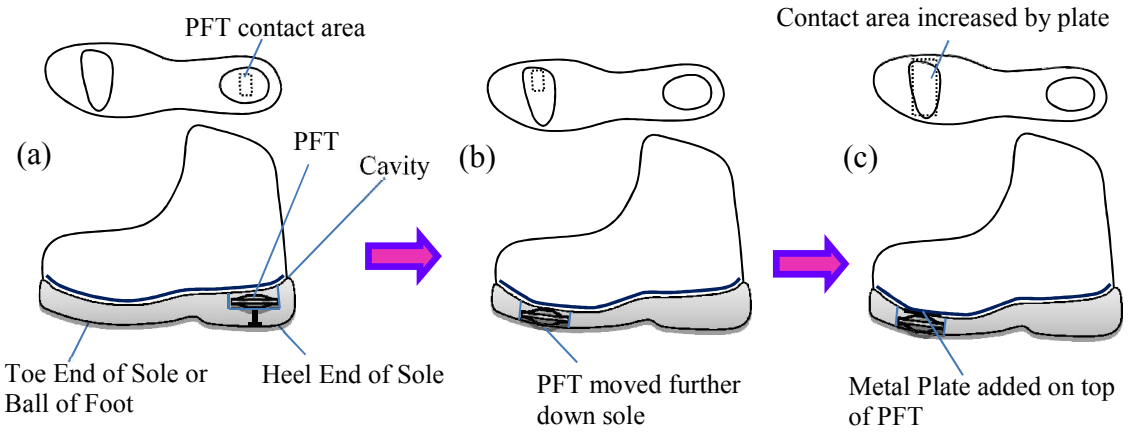

Figure 5.23 (a)-(c) Sketches showing progression of PFT positing within shoe/boot.

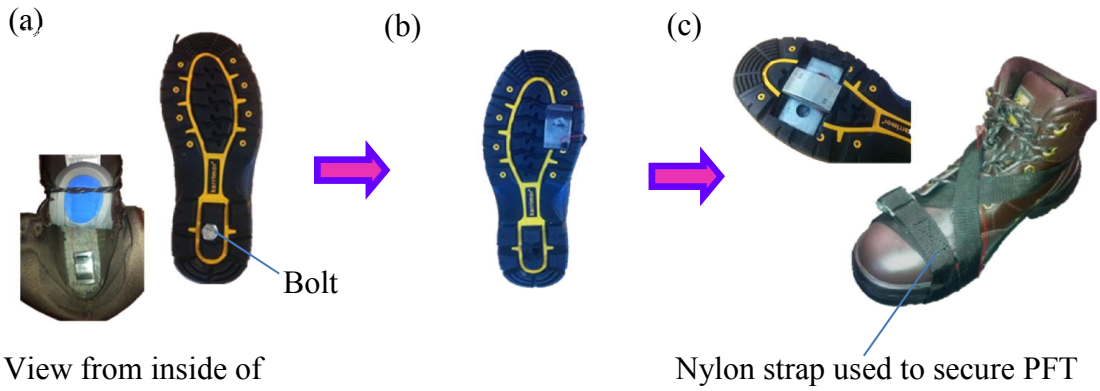

Figure 5.24 (a)-(c) Photographs showing progression of PFT positing within shoe/boot.

5.4.1 **Demonstration set-up**

The aim of the testing was to establish whether the PFT could be successfully integrated into the sole of a shoe/boot to harvest bio-kinetic energy and proceed to a power wireless sensing module. Figure 5.25 depicts the PFT within the context of an application, the system level perspective shows how energy harvested by the PFT is used to power a wireless sensor module, the module collects sensor data and then wirelessly transmits it to a base station.

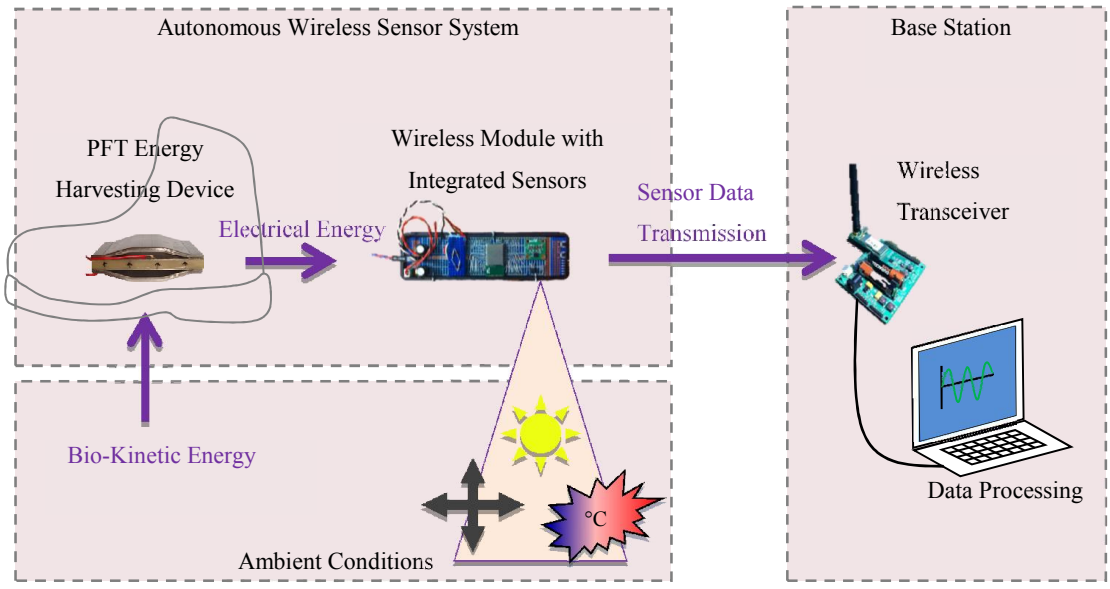

Figure 5.25 System level flow; PFT converting Bio-kinetic energy to electrical energy to power a wireless sensor module which in-turn transmits sensor data to a base station.

The module used was a 'Low power wireless comunication system' developed by Giuliano *et al* [115]. The system was designed and built whilst targeting power consumption on three levels: hardware, software and data transmision. Its sensor array includes an accelerometer, thermometer and light sensor. After senosor data is collected it is transmitted wirelessly to a Jennic LtD wireless intergrated transiever, which was powered from the laptop.

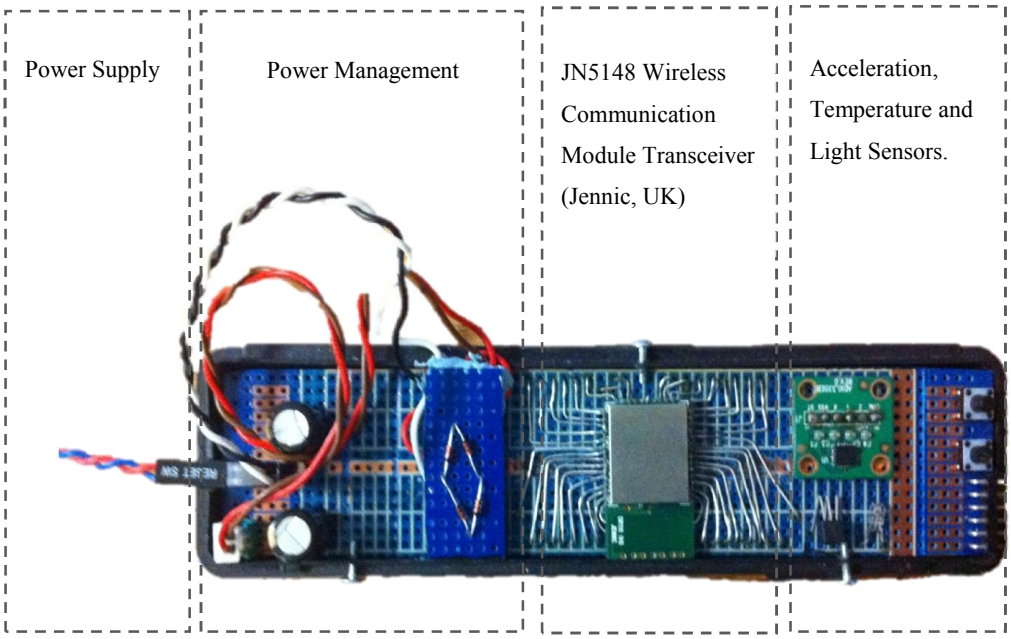

Figure 5.26 Low power consuming wirless module with intergrated sensor array [115].

Figure 5.27 Jennic LtD wireless intergrated transiever compliant with IEEE 802.15.4 protocol at 2.4GHz frequency.

Only one device was integrated into one of the boots, however for comfort and balance both boots were worn during testing. Wearing a pair of shoes, one with an integrated PFT, see Figure 5.24 (c), the subject was then asked to run on a treadmill in order that the frequency gait could be closely monitored. To calculate the frequency of gait the number of steps were counted manually and time taken for those steps was measured using a stopwatch.

Two tests were carried out. Test 1 was to measure the performance of the PFT without any wireless module connected; instead the PFT was connected to a load resistor on a prototype board (PB) which was mounted on the side of the treadmill. The PB was in turn connected to a multi-meter so that the voltage across the resistor could be measured. A range of resistors were used to get a resistance spectrum response graph. Although not shown in Figure 5.28 (a), a laptop was used to record the voltage and also to calculate the rms voltage from the signal provided by the multi-meter. Since, the peaks in the voltage signal varied making it hard to calculate Vrms using a basic approach, the same equation that was used in previous tests was used for averaging the voltage signal,

$$V_{rms} = \frac{1}{N}\sqrt{\sum_{i=1}^{N} x_i^2} \qquad (23)$$

Where, N is the number of samples and x is the magnitude of the voltage sample.

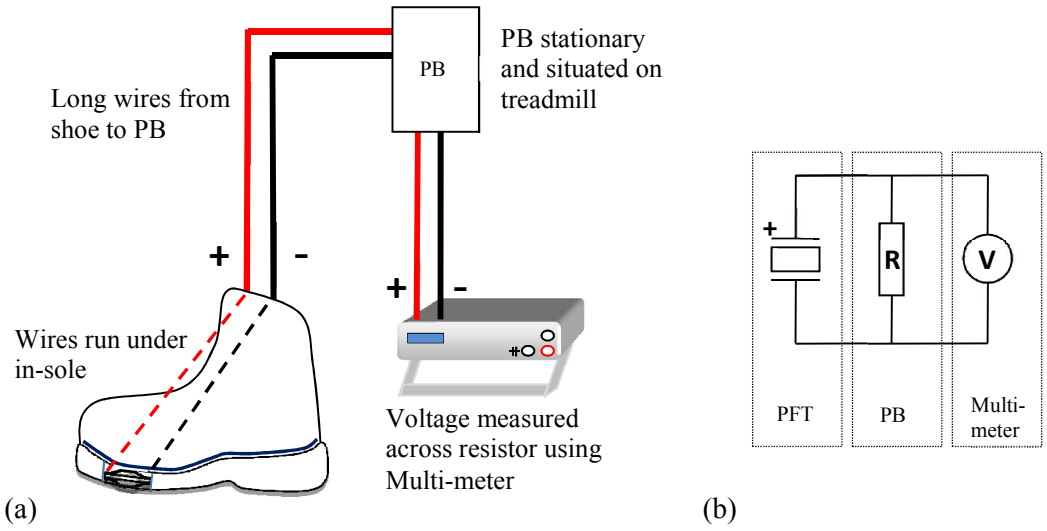

Figure 5.28 (a) Test 1: Establishing the electrical performance of the PFT when connected to a load resistor in parallel, the voltage across the load resistor was measured whilst the subject was running on the treadmill, (b) simplified circuit diagram.

In Test 2 the wireless module was exchanged for the PB. The subject was asked to run until the wireless module transmitted data. This meant that the subject had to run until the module gained enough charge in its capacitors for it to meet the electrical threshhold for transmitting the sensor data. The transmissions were received via a transceiver which was connected to a laptop, the laptop was used to view the sensor data that the transceiver received. The transmissions were monitored in two ways, 1) voltage fluctuations across the wireless module's internal capacitor were used to identify transmissions, and 2) when the transceiver received the sensor data and it was viewed on screen, this was further and more conclusive proof that transmission were occurring and sensors were functioning. Calibration of the sensors was not carried out as part of the testing preparation. The time it took for the initial charge of the capacitor to occur was called the cold-start time. This cold-start time decreases if the power into the module is increased. After the cold-start time had passed the transmissions commenced.

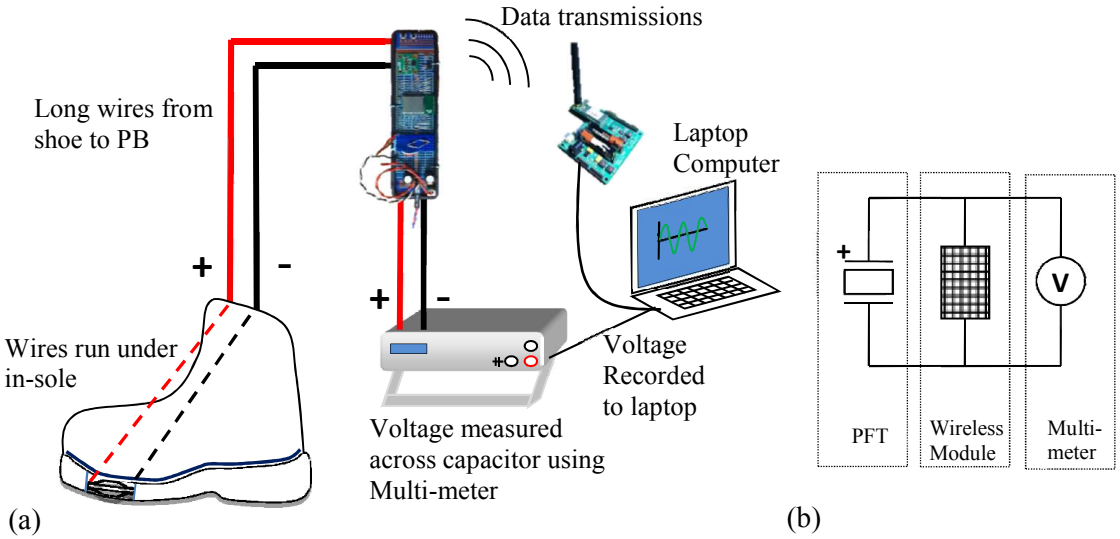

Figure 5.29 (a) Test 2: Ascertaining the cold-start time and time between each transmission by interpreting the voltage measured across the wireless modules internal capacitor using a multi-meter, sensor data was also recorded on the laptop, (b) simplified circuit diagram.

During test 2 the subject also wore the wireless sensor module, which was tucked securely in his trouser pocket, Figure 5.30 (b). The wires that carried charge from the PFT to the wireless sensing module tracked up the leg with intermediate securing bands of insulation tape Figure 5.30 (c).

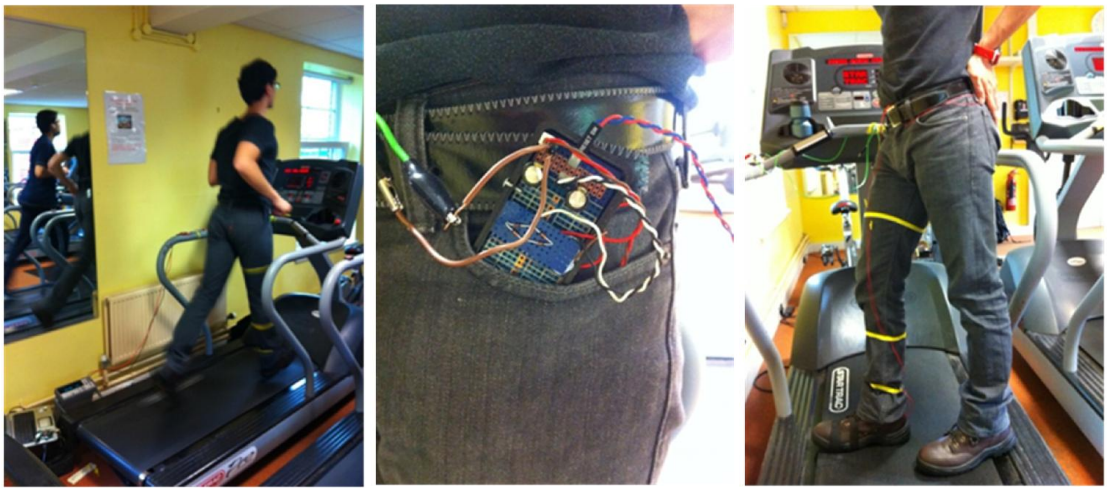

(a) (b) (c)

Figure 5.30 (a) Treadmill used for test the energy harvesting system, (b) wireless module stored in pocket of subject during testing and, (c) wires transferring power between wireless module and PFT tracked up leg and held in place with insulation tape.

5.4.2 **Results & discussions**

5.4.2.1 Test 1

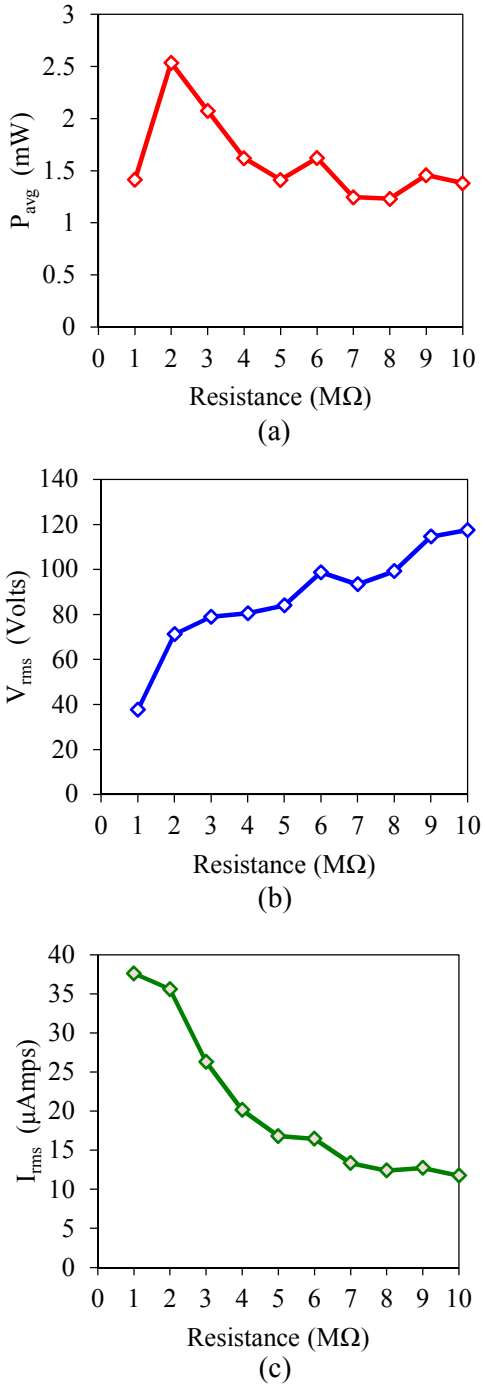

Figure 5.31 Test 1: Voltage measured across a range of resistors connected in parallel to PFT (in shoe). Subject was exerting a 760N force at a frequency of 1.4Hz, (a) calculated power (b) measured voltage, and (c) calculated current.

In test 1 where the PFT was retrofitted into the shoe and the subject was asked to run, the PFT was able to produce a maximum peak power of 2.5mW over 2MΩ ($71V_{rms}$ $36\mu A_{rms}$). Figure 5.31 shows the power, voltage and current output of the PFT over a range of load resistors, where the subject exerted 760N at 1.4Hz. A 1.4Hz force exertion frequency corresponds to a person running at 2.8Hz (when counting strides from both feed during movement) this equates to an average running speed of 3.1mph.

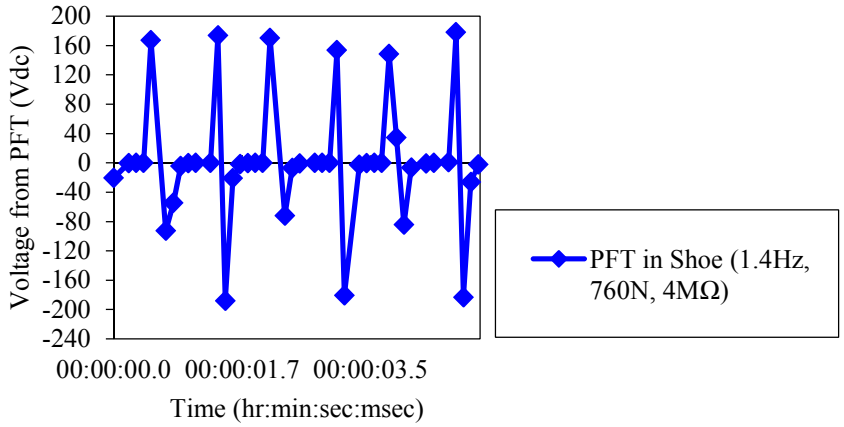

Figure 5.32 Test 1: Voltage measured across a 4MΩ resistor connected in parallel to PFT. Subject was exerting a 760N force at a frequency of 1.4Hz.

The graph in Figure 5.32 is a small sample of the voltage produced by the PFT where the voltage peaks correspond to foot strikes. The voltage was measured over a 4MΩ resistor which was connected to the PFT as an external resistor load replacing the wireless module. The voltage signal shown graph in Figure 5.32 is a small sample which is the reason why there is a difference in rms voltage between results in Figure 5.32 and Figure 5.31 (b) and therefore Figure 5.32 is not representative of the general electrical performance of the PFT. The fluctuations suggest that the PFT was under a complex force loading pattern.

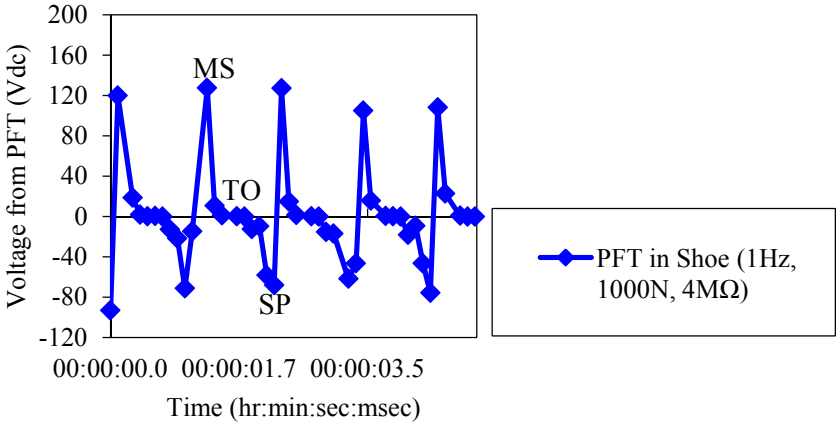

Figure 5.33 Test 1: Voltage measured across a 4MΩ resistor connected in parallel to PFT. Subject was exerting a 1000N force at a frequency of 1Hz. MS, TO and SP denote the mid-stance, toe-off and swing-phase periods of the gait cycle.

Figure 5.33 shows the voltage fluctuations produced by the PFT at a walking pace. The subject was wearing a backpack that increased their downward force to 1000N. The fluctuations in voltage are similar to those seen in a previous study involving a shoe-based piezoelectric energy harvester by Almusallam *et al* [52].

With the PFT situated in the sole of the shoe (closer to the toes) the larger voltage peak of 120Vdc, shown in Figure 5.33, may seem most likely to be due to the toe-off (TO) stage in the gait cycle where by over 75% of all energy generated is in this period [49], this TO period is described as the A2 stage in the graph by Winter *et al* shown in Figure 2.10. The TO is associated with producing 75% of the energy involved in gait, however, this is a closed loop perspective and does not account for interactions such as the energy dissipated during the impact of the feet to the ground during heel strike. Aside from energy expended by the body in TO other possible contributions of input kinetic energy to the PFT are the heel-strike (HS) and mid-stance (MS) when only one foot is in contact with the ground and therefore bearing 100% of the body's weight.

The voltage profile in Figure 5.33 shows an initial peak at 120Vdc followed by a fast step decrease that stagnates somewhat before passing through 0V and then going to a lesser negative peak of ~80Vdc. Considering the position of the PFT in the sole of the shoe, the 120Vdc peak in voltage could be due to the initialising of the MS and the slow

stagnation to 0Vdc due to some kinetic energy contribution from the TO, it then follows that the negative voltage peak could occur during the swing-phase (SP) of the foot where by the PFT with no force loading (due to swing phase) allows the PFT to elastically relieve itself from a compressed state and in doing so cause a voltage with a negative polarity.

5.4.2.2 Test 2

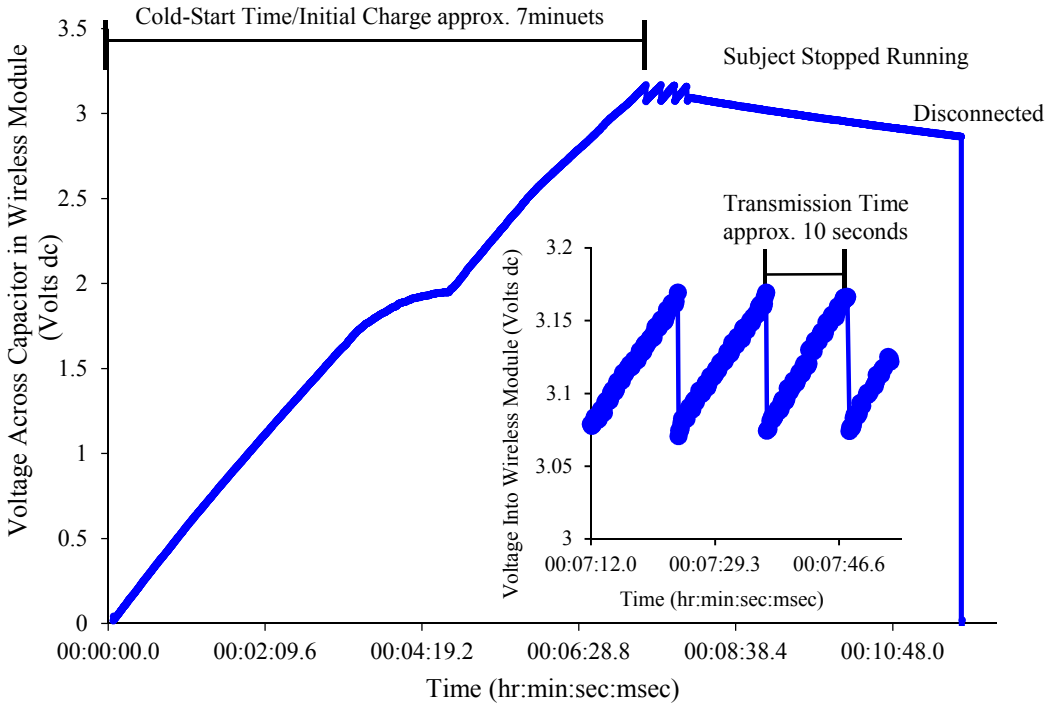

Figure 5.34 Test 2: Voltage across 2mF wireless module capacitor due to power supplied by PFT when subject ran at 1.4Hz exerting approximately 760N on PFT. Inset, magnified plot of voltage fluctuations, fluctuations due to power used by each transmission.

In test 2 the PFT was successful in powering the wireless module so that it could transmit its sensor data. Figure 5.34 shows the voltage across the 2mF capacitor connected to a wireless module with respect to time. The initial cold-start time of 7minutes, meant that the subject had to run for 7minuets continuously (exerting a force of 760N at 1.4Hz on the PFT) to initially charge the capacitor. As soon as the capacitor reached the wireless module functioning threshold-voltage, ~3.2V, sensor reading and transmission of the data were performed. The wireless module warm-start is represented

in the graph by the ascending voltage from ~3.08V to ~3.2V when the capacitor is recovering energy between module sensor readings and data transmission. The energy level provided by the subject running was enough to provide a short warm-start of approximately 10s. The inset graph in Figure 5.34 shows a magnified view of these voltage fluctuations due to the transmissions, were by transmission were sent every 10 seconds. The power consumed by the wireless module during sensor reading and data transmission is represented as a voltage drop from ~3.2V to ~3.08V. When the subject stopped running the voltage dropped to zero. The data from each sensor was received at the laptop base station and recorded.

```
Start Coordinator

Sensor Address [Hex]       : 0x1234
Payload lenght [Byte]      : 15
Temperature reading [øC]   : -20.1
Battery Voltage [mV]       : 3120
Acceleration Voltage reading [mV]   : 1542
Acceleration Voltage reading [mV]   : 1536
Acceleration Voltage reading [mV]   : 1589
ZERO=1560 SENSE=312
X [g]=1 0.0
Y [g]=1 0.0
Z [g]=0 0.0
Light reading [Lux]        : 14
Battery Voltage [mV]       : 3113
Signal Pw. Quality [0-255] : 144
Reception Sensitivity [dBm]: -48.10
CH.(11-26) Pw. Lvl.[0-255] : 132 123 60 93 60 60 63
75 84 84 87 105 60 66 54 54

Sensor Address [Hex]       : 0x1234
Payload lenght [Byte]      : 15
Temperature reading [øC]   : -19.0
Battery Voltage [mV]       : 3113
Acceleration Voltage reading [mV]   : 825
Acceleration Voltage reading [mV]   : 2015
Acceleration Voltage reading [mV]   : 1536
ZERO=1556 SENSE=311
X [g]=1 2.3
Y [g]=0 1.4
Z [g]=1 0.0
Light reading [Lux]        : 14
Battery Voltage [mV]       : 3110
Signal Pw. Quality [0-255] : 147
Reception Sensitivity [dBm]: -47.05
CH.(11-26) Pw. Lvl.[0-255] : 141 66 132 75 63 57 63
132 72 84 99 66 87 60 57 60
```

Figure 5.35 Test 2: Two transmissions of sensor data received via the transceiver.

Figure 5.35 shows the sensor data that was wirelessly sent from the wireless module to the transceiver, a laptop computer was used to interpret the transceiver data. Figure 5.35 shows that transmissions of the acceleration (*x*-, *y*- and *z*-), light intensity and the temperature were all made during test 2.

5.5 Summary

There were two main phases of testing the PFT, firstly, using a loading machine to generate the energy for the PFT to harvest and secondly with the PFT retrofitted into a shoe so that it could harvest bio-kinetic energy from gait.

Initial testing where the loading machine was used, showed the PFT to be capable of producing 2.1mW under force load of 1kN at 2Hz (5MΩ) and 12.2mW under force load of 1kN at 5Hz (2MΩ). Results confirmed no difference in performance between PFTs fabricated with endcap-substrate that were laser weld and PFTs fabricated with endcap-substrates that were resistance spot welded. Tests showed that electrode coverage area had no effect for PFTs excited at 2Hz but at 5Hz there was a small but noticeable difference. The PFTs with a partial electrode at 5Hz produced a higher voltage and a higher current (and therefore higher power) than the PFTs with a full electrode. When comparing loading machine results to the CPC-FEM there was a correlation between the simulation and the experimental results as they showed similar trends, however, their magnitudes were substantially different, this was put down to systematic errors.

When the PFT was retrofitted into the shoe—and subject asked to run exerting 760N at 1.4Hz on the PFT—it produced a maximum of power 2.5mW over a 2MΩ resistor ($71V_{rms}$ $36\mu A_{rms}$). The shoe with retrofitted PFT was then demonstrated in an application were it was shown to power data transmissions of a wireless sensor module, information of acceleration, light intensity and temperature of the subject wearing the module was all transmitted. The transmission rate was 1 transmission every 10 seconds.

CHAPTER 6

Discussions & Conclusions

This chapter is devoted to concluding this research by highlighting the main contributions made in the thesis, summarising the thesis in a conclusion section and finally suggesting further work that could be carried out as a result of limitations in this thesis. The structure of the discussions will follow the objectives set out by this thesis. In discussing each objective the main outcomes and contributions of each chapter are therefore highlighted.

A brief outline of this chapter is as follows:

- Discussion of results, their outcomes and contributions
- Thesis conclusions
- Further work

6.1 Discussions

Objective 1

The first objective was to identify key parameters of the existing Cymbal device that affected its suitability and performance as an EHD using a CPC-FEM as an analytical and design tool.

By analysing the strain behaviour using the CPC-FEM it was demonstrated why a Cymbal was more effective than simply using a piezoelectric disk in the d_{33} mode. Essentially, the endcaps helped the Cymbal to allow for increased elastic deformation of the piezo-disk which corresponded to a greater charge generated by the piezoelectric disk. The mechanism in which the endcaps increased elastic deformation in the piezo-disk could have been because the endcaps suspended the piezo-disk so that more of the

piezo-disk was able to elastically deform with the exception of the join area. The shape factor which involved coupling the d_{33} and d_{31} modes with their respective strain component went some way to demonstrate the amplification strain effect of the endcaps.

Using the CPC-FEM it was found that the physical parameters of the Cymbal had significant effects on the power output from the Cymbal. Reducing the thickness, join length and angle of the endcaps led to higher power outputs. In terms of changing parameters relating to the piezoelectric disk, in general when increasing the piezoelectric thickness the voltage increased, the current decreased and the curve of power reached a peak with a steady decline. Changing the piezoelectric material led to complex electrical outcomes due to the complex nature of piezoelectric material. Certain mechanical and electrical properties of piezoelectric material vary depending on direction. In addition to this, piezoelectric material exhibits resistive, capacitive and inductive characteristics which are in turn affected by physical/dimensional changes.

Although the aim of this thesis was to develop an EHD that could harvest bio-kinetic energy, the Cymbal designed in Chapter 3 was only designed to withstand an applied force of 50N due to the limitation of the endcap adhesion. The Cymbal could have been retrofitted into a shoe, however, extra force buffers would be required to withstand human body weight. The CPC-FEM showed that the Cymbal device developed in this thesis with dimensions of Ø30×4.6mm and an endcap thickness of 0.33mm could to harvest 0.12mW of power under a 50N force at 2Hz (10MΩ).

Contributions made

The Cymbal in thesis had varied success when comparing to other Cymbal in the literature. The Cymbal in this thesis produced a 0.12mW power output for an applied force of 50N at 2Hz but for the lowest frequency test of a Cymbal by Kim *et al* [7] at 10Hz their Cymbal produced approx. 0mW. The Cymbal in this thesis did not produce a higher power than a Cymbal in a study by Palosaari *et al* [82] were it was reported that testing of a Cymbal at 1.19Hz under a force of 27.1N produced 0.27mW (measured over parallel resistor of $3.5M\Omega_{optimal}$). However, the Cymbal in this thesis was able to

withstand higher forces which may widen its range for application. It is likely that the Cymbal made by Palosaari *et al* [82] was only able to harvest forces force up to 27.1N due to the type of materials chosen and the geometry, in particular thickness. This maximum force allowed of 27.1N is most likely a limit based on strength of materials; it is also possible that this limit could be based on experimental testing of the Cymbals. Arguably this Cymbal by Palosaari *et al* [82] could have been designed to withstand higher forces, however, efficiency or effectiveness of the device would also change. It is likely that the Cymbal made by Palosaari *et al* [82] was only able to harvest forces force up to 27.1N due to the type of materials chosen and the geometry, in particular thickness. This maximum force allowed of 27.1N is most likely a limit based on strength of materials; it is also possible that this limit could be based on experimental testing of the Cymbals. Arguably this Cymbal by Palosaari *et al* [82] could have been designed to withstand higher forces, however, efficiency or effectiveness of the device would also change.

Previous studies included Kim *et al* [7] who suggested that the Cymbal was 40 times more efficient than a PZT disk alone, and CPC-FEM results in this thesis showed that a Cymbal produced a voltage 39 times higher than using a disk alone, giving further rigour to this statement.

Kim at al [7] also introduced a d_{33}^{eff} ($d_{33}^{eff} = d_{33} + \left| A\ d_{31} \right|$) which suggested that the increased effectiveness of the Cymbal could in part be attributed to this amplification factor applied only to the d_{31}. The amplification factor in this instance relates to the endcap geometry and thus inherently some leverage effects that may occur due to changes in either of the variables in the amplification factor equation (*A*=cavity radius/cavity depth).

This thesis also attempted to demonstrate the amplification effects of the endcaps by developing a shape factor. The shape factor includes contributions from d_{31} and d_{33} by coupling the two main strains of the piezo-disk with their respective d modes ($\varphi = d_{33}\ \varepsilon_y + \left| d_{31}\ \varepsilon_x \right|$). The simulated voltage produced by the PZT disk alone was approx.

98% smaller than the simulated voltage produced by the Cymbal device. This shows that the Cymbal has a greater ability to generate charge for the same input force. Furthermore, the shape factor for the PZT disk alone was approx. 93% smaller than the shape factor for the Cymbal device. Therefore, the difference in voltage between the PZT disk alone and the Cymbal device was similar to the difference in shape factor between the PZT disk alone and the Cymbal device, suggesting that using the strain was a more accurate quantity to represent the angle amplification effects of the endcaps than using the method described by Kim at al [7]. The shape factor—developed in this thesis—highlights how the extent of elastic deformation, in the form of strain, in the PZT disk due to the endcaps allows the Cymbal device to have a higher power output than a PZT alone.

Objective 2

The second objective was to fabricate and test an existing Cymbal device with the intention of validating the CPC-FEM developed in this thesis. In Chapter 3 the model was validated by way of experiment; comparing the voltage output of the Cymbal in experiment with modelled results. Results from the CPC-FEM of the existing Cymbal were in good agreement with experimental data. This validation—based on a comparison of voltage output, derived current and power—provided a credible design platform for proceeding work.

Contributions made

A previous study found that results from a CPC-FEM of a bio-morph cantilever beam based EHD were in good agreement with experimental data, this EHD had a force input of low magnitude and high frequency (0.23g and 80-100Hz)[14]. The data used to compare experimental and modelled results was based on the electrical output of the EHD, therefore validated in terms of the electrical outputs and not mechanical outputs. Another validation study of the CPC-FEM was carried out by Pozzi *et al* [116] for a

device including bio-morph piezoelectric cantilever beams, where experimental results showed good agreement with the CPC-FEM results when comparing voltage output and also piezoelectric cantilever beams tip velocity.

In Chapter 3 of this thesis, a CPC-FEM of a Cymbal was validated by experiment. This demonstrated that the CPC-FEM could accurately be used to predict the electrical output performance of a Cymbal device and be used as a design tool to improve the electrical performance of the Cymbal whilst also taking into account structural limits i.e., yield stress. Furthermore, the CPC-FEM of the Cymbal could also be used to apply different working conditions where by the input/applied force magnitude and frequency could be varied. The CPC-FEM can also be used to simulate the Cymbal in off-resonance working conditions. Although previous work has been published using the CPC-FEM approach, this thesis developed the first 3D CPC-FEM of a Cymbal and also validated the CPC-FEM by experiment. This is significant as the CPC-FEM is able to simulate a realistic model that includes mechanical inputs and meaningful electrical outputs such as current, voltage and power.

Objective 3

Material selection is crucial when designing a piezoelectric energy harvesting transducer with design performance in mind. When designing a piezoelectric transducer its material properties of the electrical, mechanical and electrical-mechanical coupling are of particular significance. Thus, a study was implemented to try and identify which piezoelectric material properties had strong relationships with power output performance. This led to the third objective which was to develop a piezoelectric material selection criteria using the CPC-FEM developed for the Cymbal study, however the harvester structure that was used was different from the Cymbal. No clear relationship was concluded from the study, instead a criteria or set of rules were concluded for the designer. The study in Chapter 4 looked at the power outputs of 25 different piezoelectric materials, including single crystal, PVDF, and soft and hard PZT materials. The power outputs associated with key piezoelectric material properties of

s_{11}, d_{31}, g_{31}, ε_{r33}^{T}, and associated material properties of FOM and k_{31} were also studied. It was found that (1) d_{31} was a more dominant material property over other material properties for enhanced power output, (2) FOM was a more linear related property to power output than either the coupling coefficient k_{31} or d_{31} alone, and (3) the relative dielectric constant ε_{r33}^{T} had some role when comparing materials with an identical piezoelectric strain constant d_{31}; a lower relative dielectric constant ε_{r33}^{T} was preferred. No single materials parameter were able to be recommended, combined high values of FOM with d_{31} materials properties was recommended for selection of piezoelectric material for a higher power outputs in the context of energy harvesting of low frequency energy sources. Using the comparison data of 25 different material properties a high power producing material was able to be chosen, called DL-53HD (d_{31} 300x10^{-12} m/V, FOM 2.64, 2.96mW), for more detail see Table 4.1. Life cycle analysis or failure analysis of the energy harvesting structures designed was beyond the scope of this thesis, however, it should be noted that the manufacturer of the piezoelectric material chosen suggested it be used instead of a higher performing material DL-54HD (d_{31} 320x10-12 m/V, FOM 2.51, 3.47mW), for more detail see Table 4.1. The manufacturer recommended DL-53HD due to its consistent performance over time i.e., its material properties deviated less from those measured at its inception.

Contributions made

A number of research scientists have carried out research in this area, Bilgen *et al* [103] did a study based on cantilevered unimorph beams and an experimental approach to investigate the actuation and energy harvesting capability of a number of different piezoelectric materials, and concluded that, for the same type of materials, the MFC type of unimorph beams had the highest actuation capability but the lowest energy harvesting capability. Priya [104] provided a dimensionless figure of merit (DFOM) to try to answer the question of which piezoelectric composition is better to be used for energy harvesting based on similar beams but using an analytical approach, which can

be used in routine material evaluation. Kim *et al* [7] used the first physical principle approach to analyse how the electrical power available in piezoelectric transducers is related to piezoelectric material properties of the FOM and g, and further based on 5 different materials, including PVDF, PZN-PT, hard PZT and soft PZT, and high g, to conclude that a material with a higher FOM and a higher g can generate a higher voltage and a higher power when the piezoelectric material is directly used either for energy harvesting or for sensing. The CPC-FEM used in this thesis was therefore used to develop a new criteria or set of rules for the designer, however, this approach varies from previous studies and includes a more extensive quantitative study on how the piezoelectric material properties were related to energy harvesting capability. The contribution of this study was the insight it provided into the relationship between the key material parameters studied and their associated power output, moreover, it enabled a criteria or set of design rules to aid the designer. The design guidance was a combination of using existing criterion (FOM), which was shown to be a fairly precise indicator of performance, coupled with choosing the highest d_{31}, where FOM takes precedence and d_{31} is the secondary indicator. A benefit of using two parameters is in avoiding the confusion of which material to choose if both FOM are identical; having more than one performance parameter is a back-up i.e., if the FOMs are the same or very similar choose the material that also has the higher d_{31}. It may seem that there are parallels between the criteria proposed by Kim *et al* [7] with the criteria set out in this thesis, however, results in this thesis showed that the g constant had a poor correlation with power output when studied over 25 different piezoelectric materials. Instead of using FOM and g this thesis concluded that FOM and d_{31} was a more useful coupling that reflected a stronger correlation with power output.

Objective 4

The 4th objective was to design a new EHD whilst considering key performance related parameters identified in the Cymbal study, the new EHD was required to be able to withstand forces associated with human gait (1kN at 2Hz). A new EHD based on the

Cymbal was designed called the Piezoelectric Flex Transducer (PFT). The PFT, unlike the Cymbal, had an extra two substrate layers at the top and bottom of the piezo-element, although this feature stiffened the device as a whole—therefore reducing the overall force applied to the piezo-element and wasting some input kinetic energy—its addition meant that delamination would be less likely between the piezo-element and the outer amplification frame (the substrate layer spread the applied force over a larger area reducing the stress present in the adhesion layer). By reducing the chance of delamination the force applied to the device could then be increased and thus the PFT was designed to withstand 1kN at 2Hz. Initially the PFT was designed for retrofitting into the heel of a shoe, therefore its shape was made rectangular so that it could make the best use of space filling in as much space as possible. Depending on the application a possible side benefit of this rectangular shape may be that it has an increased packing factor.

This design analysis Section 0 focused on studying key dimensional parameters to use in the final PFT design with the aid of CPC-FEM. The design analysis of the PFT included work from previous chapters by way of material selection and some key dimensional parameters highlighted by studying the Cymbal. The material selection of the piezo-element and endcaps were based on works carried out in Chapter 4 were by the CPC-FEM was used to help select stainless steel for the endcaps and DL-53HD for the piezo-element. The substrate material was kept identical to the endcap material for simplicity, and both being metallic allowed for a strong welded join for later fabrication purposes. The dimensional parameters used in refining the design of the PFT were:

- Thickness of piezoelectric material
- Endcap internal angle.
- Join length.

Parameters from cymbal study repeatedly used in designing PFT.

- Thickness of endcap in conjunction with endcap internal angle.
- Electrode coverage.
- Substrate layer.

Although the Cymbal differs in shape from the PFT, they have a very similar working principle. Both are sandwich structures with a central piezoelectric element and metallic

outer structures that redirect and amplify the applied force so as to make the piezo-element fluctuate between force states of neutral and tension during their operation. Because the Cymbal and PFT have strong similarities in terms of their structural elements and function, some of the parameters in the Cymbal study were used for the PFT designing; these are the first three parameters in the list above and were selected due to their significant influence on power output of the Cymbal. In the studied range, the thicker the piezo-elements tended to produce a higher power output. The trend of power output showed a peak that decayed slowly, this meant that for relatively thick piezo-elements there was a small variation in power output. However, the difference in internal impedance over the range of piezo-thicknesses did change substantially i.e., the thicker the piezo-element the higher the internal impedance. The piezo-thickness chosen was 4mm. As the endcap thickness and internal angle are inherent to one another it was decided that their interaction should also be investigated, thus, the endcap thickness and internal angle were studied when designing the PFT. It was found that thinner endcaps enhanced the positive effects of smaller internal angles. Both reducing thickness of the endcaps and reducing the internal angle gave higher power outputs, the values of 2mm and 8.7° were chosen. Other parameters studied in the designing of the PFT were the electrode coverage and the substrate layering. As expected it was found that thinner substrates gave higher power outputs, thus the thinnest substrate possible of 0.6mm was used with the main limiting factor being endcap-substrate welding area/volume. The join area shared this limitation and smaller join lengths were desired for higher power outputs, were 6mm was chosen. Based on the idea that a partial electrode increased device efficiency by excluding inactive areas of the piezo-element a partial electrode of 40mm was chosen this excluded covering the piezo-volume between the join areas, indeed the CPC-FEM showed that a partial electrode gave a higher power output than a full electrode, interestingly the voltage and current followed the same trend as the power output. Under an applied force of 1kN and frequency 2Hz the CPC-FEM predicted that the PFT could produce up to 5.6mW (4MΩ).

Contributions made

The main contribution to this objective was that a new EHD was developed in this thesis, published and shared with the research community. The new device was inspired by the advantages of an existing device called 'the Cymbal' and was designed using a CPC-FEM to withstand a higher force input. A key difference between the new PFT and the traditional Cymbal is that the new PFT has the addition of the substrate layering to increase the adhesion strength between the piezo-element and its surrounding amplification frame. The CPC-FEM was used to refine the PFT design by studying certain dimensions which were chosen due to their close relationship with power output; the thickness of piezoelectric element, the join length, the electrode coverage, the thickness of endcap in conjunction with endcap internal angle and the thickness of the Substrate layer.

It has been demonstrated that CPC-FEMs similar to the one used in this thesis have been used in literature for the study of other piezoelectric EHDs [14][116], the CPC-FEM used in this thesis was used to design the PFT and gain an understanding of the device (at lower frequencies). Furthermore, the CPC-FEM was used to model a simplified structure of energy harvester to help with piezoelectric material selection.

Objective 5

Built on the foundation of former objectives, the 5th objective was to fabricate and demonstrate the PFT by retrofitting it into the sole of a shoe to harvest bio-kinetic energy from gait to power a wireless sensor module.

The PFTs built for testing were made using very basic techniques including sheet metal bending for the endcaps, welding to join the endcaps to the substrates and structural adhesive to connect the piezo-element with the substrates. Based on a batch size of 8 PFTs the unit cost excluding labour was approximately £51.83. There was a range of PFTs built for testing with some physical variations including; the electrode coverage and the type of welding used to join the endcaps and substrates together.

In early testing of the PFT using a loading machine results showed that there is no difference in electrical performance between PFTs that had laser welded endcaps and substrates with PFTs that had resistance spot welded endcaps and substrates, testing was carried out over three different forces of 0.5,0.75 and 1kN and two frequencies 2Hz and 5Hz. The loading machine testing also showed how the electrode area coverage had no effect on performance at 2Hz which was contrary to results produced by the CPC-FEM. The electrode coverage did however show some effect on the power output at the higher frequency tested at 5Hz. The performance of the PFT in the loading machine, showed that the PFT is capable of producing 2.1mW under a lower force frequency of 2Hz (with at force magnitude of 1kN over 5MΩ resistor) and 12.2mW under a higher force frequency of 5Hz (with a force magnitude of 1kN over 2MΩ resistor).

The sensitivity of the model was investigated by varying some of the input parameters, for instance, when the piezoelectric stiffness was artificially increased by 15% from its original value, the power reduced by almost 1mW from 5.7mW to 4.8mW. During the brief investigation into testing the sensitivity of the model, it was observed that when running a simulation with all of the changes applied to the input parameters listed in Table 5.10 their combined effects on the output power gave an overall decrease in power of 44%. Through this investigation it was also demonstrated that some input paramters of the CPC-FEM are dependant on one another suggesting that optimisation software would be benificial as an improvement to the existing design approach taken in this thesis.

The results obtained from the loading machine testing of the PFTs were compared to the simulation results from the CPC-FEM. Although the CPC-FEM and experimental results showed a similar trend, their magnitudes were quite different. Compared to the validation results of the Cymbal CPC-FEM, the PFT CPC-FEM validation results were relatively poor, this was due to a systematic error caused by the equipment in the experimental set-up, where a 20kN load cell was used, it is too big for the testing and so it is not precise to characterise the load. A more desirable smaller load cell would have been better to accurately measure forces from 0.75-1kN, but at the time, such a load cell was not available.

After the loading machine experiments the PFT was first integrated into the heel of the shoe—as this was the part of the shoe with the most space for retrofitting—however sufficient force was not able to be transmitted to the PFT due to the apex-bolt configuration being too far from the heel impact point. The apex is the area of endcap that input force is applied onto. Subsequently the PFT was moved down to the sole of the shoe and modified with a metal plate to increase its effectiveness of absorbing force from foot impacts.

A human subject wearing shoes with one shoe retrofitted with a PFT was asked to run—on a treadmill—which provided a force applied to the PFT of approximately 760N at a frequency of 1.4Hz, the PFT gave an electrical output over a 10MΩ resistor in parallel of $1.3mW_{avg}$, $117V_{rms}$ and $12\mu A_{rms}$. The maximum power output of the PFT with this same set-up was $2.5mW_{avg}$ (over a 2MΩ resistive load). This demonstrated that the PFT was able to produce a power output when retrofitted into a shoe. Following this, the PFT was then put under the same conditions but instead connected to a wireless sensor module, with the intention of providing a sole source of power to the module. The PFT was able to power the sensors on the module and also the essential data transmissions, information of acceleration, light intensity and temperature of the subject wearing the module was all transmitted. The transmission rate was 1 transmission every 10 seconds, however, the initial time to power the module from a zero energy state (internal capacitor at 0V) was 7 minutes.

Contributions made

It was demonstrated that a novel piezoelectric mobile EHD could produce an output power of $2.1mW_{avg}$ (1kN, 2Hz) when tested in a loading machine. Following this, the PFT was retrofitted into a shoe and shown to harvest bio-kinetic energy from gait of $2.5mW_{avg}$ (0.76kN, 1.4Hz), the PFT was also used to power a wireless sensor module.

The PFT design proposed in this thesis cannot produce as much power compared to other piezoelectric shoe-integrated devices for instance the hydraulic force amplifier actuated piezoelectric stack integrated into the shoe by Antaki *et al* [53] where experiments suggested that 6.2W could be generated or the cog wheel which in-turn

deflects four PZT-5A bimorph stacks simultaneously by Howells *et al* [58] that generated an electrical energy of up to 90mW. There was also a device integrated into the shoe producing 8.4mW from piezoelectric unimorph and 1.3mW from stave by Shenck *et al* [47]. Although the PFT cannot produce as higher output as other piezoelectric shoe-integrated devices, it does have two advantages in combination which are 1) a small more compact configuration at 52x30x16.3mm, and 2) a robust structure that can withstand 1kN. A significant contribution of this thesis is the approach that was used to design the novel PFT. This approach included the following:

- developing a 3D CPC-FEM,
- identifying key parameters of the harvester relating to power performance by using the CPC-FEM as an analysis tool,
- refining the design based on these findings,
- designing a physically robust harvester using stress analysis from the CPC-FEM, and
- using the CPC-FEM a material selection tool.

6.2 Conclusions

The aim of this thesis has been to design, analyse and develop an EHD capable of harvesting sufficient energy from movements of the human body to power a wireless sensor module.

Short summary of thesis

Knowledge of Cymbal gained; how key design parameters related to its electric and mechanical behaviour using CPC-FEM as a design tool.

A Cymbal was fabricated and used to validate the CPC-FEM, however, the Cymbal was not able to be used to harvest bio-kinetic energy due to the high working forces involved (over designed working loads).

The CPC-FEM was used to compare the performance of 25 different piezoelectric materials. This work provides a good resource for the designers

and is a robust guide for which material properties and/or performance values (FOM) are indicators of high power outputs.

A novel harvester is presented. It was designed using a CPC-FEM, tested and demonstrated in an application. It has a small and compact configuration at 52x30x16.3mm making it ideal for retrofit applications or integration into small spaces, it also has a robust structure that can withstand up to 1kN.

Detailed summary of thesis

By choosing an existing device as a start point and using a logical design method i.e., identifying and utilising key dimensional parameters and key material properties affecting performance, a novel PFT device was developed. The primary design tool was the CPC-FEM which allowed analysis of parameters affecting performance without having to fabricate any prototypes.

Initial focus was on an existing device called the Cymbal, were dimensional parameters that related to electrical performance were analysed using a CPC-FEM. After summarising some main key parameters of the Cymbal and identifying that its structural configuration made it unsuitable for higher force applications a new device was designed. Inspired by the function of the Cymbal, the piezoelectric flex transducer (PFT) was designed using CPC-FEM, its square-like form and additional substrate layer—for increased strength—is what made it differ to the Cymbal. Material selection for the PFT included using the CPC-FEM to compare different materials in the specific context of energy harvesting. Guidelines were developed based on a comparison of piezoelectric materials where the CPC-FEM was used to identify which piezoelectric material properties had strong correlations with power output. Ultimately this aided the piezoelectric material selection for the PFT. Other bulk materials for the PFT were chosen based on electrical performance results found when using the CPC-FEM. Following the detailed design process of the PFT it was then fabricated, tested and demonstrated in an application. The PFT was retrofitted into a shoe and used to power a wireless sensor module, the PFT essentially converted bio-kinetic energy from gait/foot fall directly to electrical energy to be used by the module. Through this thesis a novel device has been presented called the PFT which harvested 2.5mW_{avg} from bio-kinetic

energy from gait, this corresponds to a running speed of approximately 3.1mph (5kmph).

6.3 Challenges

There were three main challenges during this thesis, the first, was to develop a new device, this required creativity yet at the same time having to apply the logic needed for a workable solution. This challenge was overcome through a process of generating many design ideas, reviewing the designs, extracting workable solutions from the designs and then combing the beneficial ideas.

The second most prominent challenge was inadequate equipment during load cell testing of the PFT where by the load cell was not appropriate and no replacement was available that suited the force range.

The final challenge during this thesis was using piezoelectric material. The brittle characterises of piezoelectric material limits the mechanical strain that material can withstand before mechanical failure. This is a problem because for energy harvesting, in general, there needs to be a high strain as the higher the strain applied to piezoelectric material the more charge it is able to produce. The performance of a piezoelectric harvester can be increased by extensive design refinements as shown in this thesis, but what may have a larger impact on performance than any other factor is the energy conversion efficiency of the piezoelectric material itself.

6.4 Further Work

Based on limitations in this thesis this short section makes suggestions of further work that would help to improve the robustness of this thesis and also further work that may contribute to research.

Validating the PFT CPC-FEM

The accuracy of the results from the comparison of the PFT CPC-FEM with its experimental equivalent could be improved by running the experiment again with one

change in the equipment; the load cell used should be able to accurately measure the force magnitude and frequency intended for the experiment (1kN at 2-5Hz).

Improving the PFT

- Power output of PFT could be increased by using slotted endcaps to reduce energy wastage through reducing unneeded bulk, this approach could still maintain an appropriate join area between endcap and substrate for a realistic difficulty level of fabrication.
- The weight of the PFT could be reduced by using titanium instead of stainless steel for the endcaps and substrates.
- Power output of PFT could be increased by reducing the volume of substrate by reducing the thickness of the mid-section (cavity area), this would reduce energy wastage by allowing for more elastic deformation yet still keep an appropriate join thickness between endcap and substrate for a realistic difficulty level of fabrication.
- The PFT could have been made with a multi-layered piezoelectric element for reduced internal impedance. This would make the PFT more efficient in battery charging circuits where internal impedance is substantially lower than that of the PFT in this thesis.
- More shape considerations could be investigated for instance answering the question; what effect does changing the shape of the piezo-element have on power output and structural integrity?

Optimisation

As the design platform in this thesis was computer based the CPC-FEM could have been linked with an optimization algorithm. With the ANSYS APDL code some work was started with linking it to modeFRONTIER®—an integration platform for multi-objective and multi-disciplinary optimisation—with the view of using a genetic optimisation algorithm to further study the PFT, however time constraints diminished this opportunity. It would also be of benefit to the research community to use the CPC-

FEM with an optimisation algorithm to look further into the piezoelectric material selection criteria.

Life cycle analysis

A limitation of this study was fatigue analysis of the PFT, it would be beneficial to run a life cycle analysis of the PFT in order to identify more complex failure modes, this may then lead to design refinements. Having life cycle analysis results would also provide an insight into the life span of the PFT to determine whether it would be a cost effective alternative to using batteries cells as the energy source.

Material selection

The conclusion from using the CPC-FEM to compare piezoelectric materials that d_{31} was one of the most influential material properties effecting power output may instead be interpreted as; the CPC-FEM had a high sensitivity for variations in d_{31}, therefore in reality the correlations of d_{31} with power output may be less pronounced. Experimental work testing samples of identical geometry but different piezoelectric materials should be carried out to validate the CPC-FEM or instead determine its accuracy. The background theory of the CPC-FEM could also be scrutinised and multiple finite element modelling software's could be compared.

Other Applications

Although the focus was to use the PFT to harvest bio-kinetic energy there are wider applications for the PFT for instance, it could be used to harvest energy from sources with higher force frequencies. Suggested postdoctoral work could involve fitting the PFTs, one at each automotive engine mount to harvest the high force high frequency combustion engine vibrations. This vibration energy would prove a rich, continuous and relatively predictive source of energy that could contribute towards the substantial electrical energy needs of the automotive vehicles of the 21st century.

REFERENCES

[1] Versatile ultra-low power biomedical signal processor [Online], Available: http://www.energyharvestingjournal.com/articles/versatile-ultra-low-power-biomedical-signal-processor-00003133.asp, (Accessed: 2011) Press Release, Energy Harvesting Journal, Belguin.

[2] Li Huang, V Pop, R de Francisco, R Vullers, G Dolmans, H de Groot, et al., Ultra low power wireless and energy harvesting technologies — An ideal combination, Communication Systems (ICCS), 2010 IEEE International Conference on. (2010) 295-300.

[3] PD Bradley, An ultra-low power, high performance Medical Implant Communication System (MICS) transceiver for implantable devices, Biomedical Circuits and Systems Conference, 2006. BioCAS 2006. IEEE. (2006) 158-161.

[4] P Robert, B Gosselin, AE Ayoub, M Sawan, An Ultra-Low-Power Successive-Approximation-Based ADC for Implantable Sensing Devices, Circuits and Systems, 2006. MWSCAS '06. 49th IEEE International Midwest Symposium on. 1 (2006) 7-11.

[5] A Chandrakasan, SE7: Next generation energy scavenging systems, Solid-State Circuits Conference - Digest of Technical Papers, 2009. ISSCC 2009. IEEE International. (2009) 519-519.

[6] V Marsic, A Giuliano, M Zhu. Low Power Consumption Wireless Sensor Communication System Integrated with an Energy Harvesting Power Source, Sensors and Transducers. 18 (2013) 156-165.

[7] H Kim, S Priya, H Stephanou, K Uchino. Consideration of impedance matching techniques for efficient piezoelectric energy harvesting, IEEE Trans.Ultrason.Ferroelectr.Freq.Control. 54 (2007) 1851-1858.

[8] R Heeks. The next phase of applying ICT for international development , IEEE Computer. 41 (2008) 26-33.

[9] Wan-Young Chung, Young-Dong Lee, Sang-Joong Jung, A wireless sensor network compatible wearable u-healthcare monitoring system using integrated ECG, accelerometer and SpO2, Engineering in Medicine and Biology Society, 2008. EMBS 2008. 30th Annual International Conference of the IEEE. (2008) 1529-1532.

[10] R Appell Private., Photo, Operation Herrick XV, Nahr-e Saraj (North), Helmand Province, Afghanistan. (31/01/12).

[11] A Daniels, Interview of Lance Corpral Mathew Sampson by Alice Daniels, UK [Previously Unpublished], (2013).

[12] BionicPower, [Online], www.bionic-power.com/app_military.html, (Accessed: Feb 2011).

[13] Q Li, V Naing, JM Donelan. Development of a biomechanical energy harvester, Journal of NeuroEngineering and Rehabilitation. 6 (2009).

[14] M Zhu, E Worthington, Design and testing of piezoelectric energy harvesting devices for generation of higher electric power for wireless sensor networks, Proceedings of IEEE Sensors. (2009) 699-702.

[15] T Starner. Human-powered wearable computing, IBM Syst J. 35 (1996) 618-629.

[16] D Jia, J Liu. Human power-based energy harvesting strategies for mobile electronic devices, Frontiers of Energy and Power Engineering in China. 3 (2009) 27-46.

[17] S Priya. Advances in energy harvesting using low profile piezoelectric transducers, Journal of Electroceramics. 19 (2007) 165-182.

[18] A Delnavaz, J Voix, Electromagnetic micro-power generator for energy harvesting from breathing, IECON 2012 - 38th Annual Conference on IEEE Industrial Electronics Society. (2012) 984-988.

[19] V Leonov, T Torfs, P Fiorini, C Van Hoof. Thermoelectric converters of human warmth for self-powered wireless sensor nodes, IEEE Sensors Journal. 7 (2007) 650-656.

[20] G Xu, Y Yang, Y Zhou, J Liu. Wearable thermal energy harvester powered by human foot, Frontiers in Energy. 7 (2013) 26-38.

[21] SR Platt, S Farritor, K Garvin, H Haider. The use of piezoelectric ceramics for electric power generation within orthopaedic implants, Mechatronics, IEEE/ASME Transactions on. 10 (2005) 455-461.

[22] J Andrysek, G Chau. An Electromechanical Swing-Phase-Controlled Prosthetic Knee Joint for Conversion of Physiological Energy to Electrical Energy: Feasibility Study, Biomedical Engineering, IEEE Transactions on. 54 (2007) 2276-2283.

[23] SH Collins, AD Kuo. Recycling energy to restore impaired ankle function during human walking, PLoS ONE. 5 (2010).

[24] MA Karami, DJ Inman. Powering pacemakers from heartbeat vibrations using linear and nonlinear energy harvesters, Appl.Phys.Lett. 100 (2012).

[25] A Zurbuchen, A Pfenniger, A Stahel, CT Stoeck, S Vandenberghe, VM Koch, et al. Energy harvesting from the beating heart by a mass imbalance oscillation generator, Ann.Biomed.Eng. 41 (2013) 131-141.

[26] P Roberts, G Stanley, J Morgan, Harvesting the energy of cardiac motion to power a pacemaker, 81st Annual Scientific Session of the American-Heart-Association. 118 (2008) 679-680.

[27] D Cohen, E Givler. Magnetomyography: Magnetic fields around the human body produced by skeletal muscles, Appl.Phys.Lett. 21 (1972) 114-116.

[28] JB Burch, M Clark, MG Yost, CTE Fitzpatrick, AM Bachand, J Ramaprasad, et al. Radio Frequency Nonionizing Radiation in a Community Exposed to Radio and Television Broadcasting, Environ.Health Perspect. 114 (2006) 248.

[29] B Fair Store [Online], Available: http://shop.b-fair.net/?p=4085, (Accessed: Feb 2013).

[30] M Rasmussen, RE Ritzmann, I Lee, AJ Pollack, D Scherson. An implantable biofuel cell for a live insect, J.Am.Chem.Soc. 134 (2012) 1458-1460.

[31] E Romero, RO Warrington, MR Neuman. Energy scavenging sources for biomedical sensors, Physiol.Meas. 30 (2009) R35-R62.

[32] WH Ko, Piezoelectric energy converter for electronic implants, United stated patent office. 3456134 (1969).

[33] Penglin Niu, P Chapman, L DiBerardino, E Hsiao-Wecksler, Design and optimization of a biomechanical energy harvesting device, Power Electronics Specialists Conference, 2008. PESC 2008. IEEE. (2008) 4062-4069.

[34] K Sasaki, Y Osaki, J Okazaki, H Hosaka, K Itao. Vibration-based automatic power-generation system, Microsystem Technologies. 11 (2005) 965-969.

[35] J Liu, P Fei, J Zhou, R Tummala, ZL Wang. Toward high output-power nanogenerator, Applied Physics Letters. 92 (2008).

[36] B CAVALLIER, P Berthelot, H Nouira, E Foltete, L Hirsinger, S Ballandras, Energy harvesting using vibrating structures excited by shock, Ultrasonics Symposium, 2005 IEEE. 2 (2005) 943-945.

[37] P Miao, PD Mitcheson, AS Holmes, EM Yeatman, TC Green, BH Stark. Mems inertial power generators for biomedical applications, Microsystem Technologies. 12 (2006) 1079-1083.

[38] T von Büren, G Tröster. Design and optimization of a linear vibration-driven electromagnetic micro-power generator, Sens Actuators A Phys. 135 (2007) 765-775.

[39] BE Lewandowski, KL Kilgore, KJ Gustafson. Design Considerations for an Implantable, Muscle Powered Piezoelectric System for Generating Electrical Power, Annals of biomedical engineering. 35 (4) (2007) 631-641.

[40] T Tsutsumino, Y Suzuki, N Kasagi, Y Sakane, Seismic Power Generator Using High-Performance Polymer Electret, Micro Electro Mechanical Systems, 2006. MEMS 2006 Istanbul. 19th IEEE International Conference on. (2006) 98-101.

[41] G Gorge, M Kirstein, R Erbel. Microgenerators for energy autarkic pacemakers and defibrillators: Fact or Fiction? Hertz. 26 (2001) 64-68.

[42] Jiabin Wang, Weiya Wang, GW Jewell, D Howe. Design of a miniature permanent-magnet generator and energy storage system, IEEE Transactions on Industrial Electronics. 52 (2005) 1383-1390.

[43] Q Li, V Naing, JA Hoffer, DJ Weber, AD Kuo, JM Donelan, Biomechanical energy harvesting: Apparatus and method, Proceedings - IEEE International Conference on Robotics and Automation. (2008) 3672-3677.

[44] JR Slade, J Bowman, R Kornbluh, Bio-kinetic energy harvesting using electroactive polymers, Proceedings of SPIE - The International Society for Optical Engineering. 8383 (2012).

[45] J Hitt, W Brechue, A Boehler, J Ward, K Hollander, M Holgate, et al., Dismounted soldier biomechanical power regeneration, Army Science Conference. (2010).

[46] LC Rome, L Flynn, EM Goldman, TD Yoo. Generating Electricity While Walking with Loads, Science. 309 (2005) 1725-1728.

[47] NS Shenck, JA Paradiso. Energy scavenging with shoe-mounted piezoelectrics, Micro, IEEE. 21 (2001) 30-42.

[48] J Feenstra, J Granstrom, H Sodano. Energy harvesting through a backpack employing a mechanically amplified piezoelectric stack, Mechanical Systems and Signal Processing. 22 (2008) 721-734.

[49] DA Winter. Foot trajectory in human gait: A precise and multifactorial motor control task, Phys.Ther. 72 (1992) 45-56.

[50] K Ylli and D Hoffmann and B Folkmer and,Y.Manoli. Design, fabrication and characterization of an inductive human motion energy harvester for application in shoes, Journal of Physics: Conference Series. 476 (2013) 012012.

[51] D Hoffmann and B Folkmer and,Y.Manoli. Human Motion Energy Harvester for Biometric Data Monitoring, Journal of Physics: Conference Series. 476 (2013) 012103.

[52] A Almusallam and R N Torah and D Zhu and M J Tudor and,S.P.Beeby. Screen-printed piezoelectric shoe-insole energy harvester using an improved flexible PZT-polymer composites, Journal of Physics: Conference Series. 476 (2013) 012108.

[53] JF Antaki, GE Bertocci, EC Green, A Nadeem, T Rintoul, RL Kormos, et al. A Gait-Powered Autologous Battery Charging System for Artificial Organs, Asaio Journal,ASAIO J. 41 (1995) 588-595.

[54] M Duffy, D Carroll, Electromagnetic generators for power harvesting, Power Electronics Specialists Conference, 2004. PESC 04. 2004 IEEE 35th Annual. 3 (2004) 2075-2081 Vol.3.

[55] J Kymissis, C Kendall, J Paradiso, N Gershenfeld, Parasitic power harvesting in shoes, Wearable Computers, 1998. Digest of Papers. Second International Symposium on. (1998) 132-139.

[56] RD Kornbluh, R Pelrine, H Prahlad, A Wong-Foy, B McCoy, S Kim, et al., From boots to buoys: Promises and challenges of dielectric elastomer energy harvesting,

Proceedings of SPIE - The International Society for Optical Engineering. 7976 (2011).

[57] Penglin Niu, P Chapman, Design and Performance of Linear Biomechanical Energy Conversion Devices, Power Electronics Specialists Conference, 2006. PESC '06. 37th IEEE. (2006) 1-6.

[58] CA Howells. Piezoelectric energy harvesting, Energy Conversion and Management. 50 (2009) 1847-1850.

[59] A Cimpian and G Ó Laighin and,M.Duffy. Analysis of Pulsed vs. Continuous Power Delivery from an Electromagnetic Generator, Journal of Physics: Conference Series. 476 (2013) 012058.

[60] H Kim, S Priya, K Uchino. Modeling of piezoelectric energy harvesting using cymbal transducers, Japanese Journal of Applied Physics, Part 1: Regular Papers and Short Notes and Review Papers. 45 (2006) 5836-5840.

[61] YB Jeon, R Sood, J- Jeong, S- Kim. MEMS power generator with transverse mode thin film PZT, Sensors and Actuators A: Physical. 122 (2005) 16-22.

[62] M Renaud, P Fiorini, R van Schaijk, C van Hoof, An impact based piezoelectric harvester adapted to low frequency environmental vibrations, Solid-State Sensors, Actuators and Microsystems Conference, 2009. TRANSDUCERS 2009. International. (2009) 2094-2097.

[63] S Kwon. A T-shaped piezoelectric cantilever for fluid energy harvesting, Applied Physics Letters. 97 (2010) 164102-164102-3.

[64] CR Saha, T O'Donnell, H Loder, S Beeby, J Tudor. Optimization of an Electromagnetic Energy Harvesting Device, Magnetics, IEEE Transactions on. 42 (2006) 3509-3511.

[65] R Tashiro, N Kabai, K Katayama, Y Ishizuka, F Tsuboi, K Tsuchiya. Development of an electrostatic generator that harnesses the motion of a living body, JSME. 43 (2000) 916-922.

[66] L Wang, F Yuan, Structural vibration energy harvesting by magnetostrictive materials, Zhejiang University Press, The 4th China-Japan-US Symposium on Structural Control and Monitoring, Hangzhou, China. (2006) 147-152.

[67] JA Paradiso, T Starner. Energy scavenging for mobile and wireless electronics, IEEE Pervasive Computing. 4 (2005) 18-27.

[68] J Gakkestad, L Hanssen, Powering Wireless Sensor Networks Nodes in Northern Europe Using Solar Cell Panel for Energy Harvesting, New Technologies, Mobility and Security (NTMS), 2011 4th IFIP International Conference on. (2011) 1-5.

[69] M Muramatsu, H Koizumi, An experimental result using RF energy harvesting circuit with Dickson charge pump, Sustainable Energy Technologies (ICSET), 2010 IEEE International Conference on. (2010) 1-4.

[70] A Khaligh, Peng Zeng, Xiaochun Wu, Yang Xu, A hybrid energy scavenging topology for human-powered mobile electronics, Industrial Electronics, 2008. IECON 2008. 34th Annual Conference of IEEE. (2008) 448-453.

[71] T Wacharasindhu, JW Kwon. A micromachined energy harvester from a keyboard using combined electromagnetic and piezoelectric conversion, J Micromech Microengineering. 18 (2008).

[72] A Bayrashev, WP Robbins, B Ziaie. Low frequency wireless powering of microsystems using piezoelectric–magnetostrictive laminate composites, Sensors and Actuators A: Physical. 114 (2004) 244-249.

[73] A Dogan, S Yoshikawa, K Uchino, RE Newnham, Effect of geometry on the characteristics of the moonie transducer and reliability issue, Proceedings of the IEEE Ultrasonics Symposium. 2 (1994) 935-939.

[74] S Chen, G Lin, Improvements on PLZT cymbal hydrophone, 2009 4th IEEE Conference on Industrial Electronics and Applications, ICIEA 2009. (2009) 3277-3281.

[75] JF Tressler, RE Newnham, WJ Hughes. Capped ceramic underwater sound projector: The 'cymbal' transducer, J.Acoust.Soc.Am. 105 (1999) 591-600.

[76] R Gosain, EA Gurdal, Y Zhuang, S- Park, S- Lee, K Uchino. Piezoelectric pump using a cymbal transducer, Japanese Journal of Applied Physics. 49 (2010).

[77] J Luis, E- Park, RJ Meyer Jr., NB Smith, Rectangular cymbal arrays for ultrasonic transdermal insulin delivery, Proceedings - IEEE Ultrasonics Symposium. (2007) 840-843.

[78] Y Ke, T Guo, J Li. A new-style, slotted-cymbal transducer with large displacement and high energy transmission, IEEE Trans.Ultrason.Ferroelectr.Freq.Control. 51 (2004) 1171-1177.

[79] KH Lam, CL Sun, HLW Chan, XZ Zhao, CL Choy. A Piezoelectric-Metal-Cavity (PMC) actuator, Journal of Electroceramics. 18 (2007) 251-253.

[80] JP Choi, KH Lee, HJ Lee, NK Lee, BH Kim, Static and dynamic characteristics of modified cymbal mechanism in micro punching system, ICSMA 2008 - International Conference on Smart Manufacturing Application. (2008) 200-204.

[81] B Ren, SW Or, X Zhao, H Luo. Energy harvesting using a modified rectangular cymbal transducer based on 0.71Pb(Mg1/3Nb2/3)O3–0.29PbTiO3 single crystal, Journal of Applied Physics. 107 (2010) 034501-034501-4.

[82] J Palosaari, M Leinonen, J Hannu, J Juuti, H Jantunen. Energy harvesting with a cymbal type piezoelectric transducer from low frequency compression, Journal of Electroceramics. 28 (2012) 214-219.

[83] A Dogan, E Uzgur. Size and material effects on cymbal transducer for actuator applications, Ferroelectrics. 331 (2006) 53-63.

[84] Peng Haijun, Zhang Kai, Du Yiqun, Design method of cymbal transducer structure parameters based on finite element analysis, Computer Design and Applications (ICCDA), 2010 International Conference on. 4 (2010) V4-269-V4-273.

[85] RJ Meyer, WJ Hughes, TC Montgomery, RE Newnham. Design of and Fabrication Improvements to the Cymbal Transducer Aided by Finite Element Analysis, Journal of Electroceramics. 8 (2002) 163-174.

[86] Shilin Wu, Qi Zhang, Zhiping Huang, Jiulong Xiong, Research on Frequency Characteristics of Spherical-Cymbal Transducers, Measuring Technology and Mechatronics Automation, 2009. ICMTMA '09. International Conference on. 1 (2009) 514-518.

[87] P Ochoa, M Villegas, JF Fernández, Effective piezoelectric coefficient calculation of cymbal piezocomposite, Ferroelectrics. 273 (2002) 315-320.

[88] JF Tressler, RE Newnham. Doubly resonant cymbal-type transducers, Ultrasonics, Ferroelectrics and Frequency Control, IEEE Transactions on. 44 (1997) 1175-1177.

[89] J Palosaari, M Leinonen, J Hannu, J Juuti, H Jantunen. Energy harvesting with a cymbal type piezoelectric transducer from low frequency compression, J Electroceramics. 28 (2012) 214-219.

[90] P Ochoa, JL Pons, M Villegas, JF Fernandez. Mechanical stress and electric potential in cymbal piezoceramics by FEA, Journal of the European Ceramic Society. 25 (2005) 2457-2461.

[91] H Zhao, J Yu, J Ling. Finite element analysis of Cymbal piezoelectric transducers for harvesting energy from asphalt pavement, Journal of the Ceramic Society of Japan. 118 (2010) 909-915.

[92] HW Kim, A Batra, S Priya, K Uchino, D Markley, RE Newnham, et al. Energy harvesting using a piezoelectric "cymbal" transducer in dynamic environment, Japanese Journal of Applied Physics, Part 1: Regular Papers and Short Notes and Review Papers. 43 (2004) 6178-6183.

[93] N DUTOIT, B WARDLE, S KIM. Design Considerations for MEMS-Scale Piezoelectric Mechanical Vibration Energy Harvesters, Integrated Ferroelectrics. 71 (2005).

[94] A Erturk, DJ Inman. Issues in mathematical modeling of piezoelectric energy harvesters, Smart Mater.Struct. 17 (2008).

[95] NG Elvin, AA Elvin. A general equivalent circuit model for piezoelectric generators, J Intell Mater Syst Struct. 20 (2009) 3-9.

[96] S Roundy, PK Wright. A piezoelectric vibration based generator for wireless electronics, Smart Mater.Struct. 13 (2004) 1131-1142.

[97] Y Yang, L Tang. Equivalent circuit modeling of piezoelectric energy harvesters, J Intell Mater Syst Struct. 20 (2009) 2223-2235.

[98] NG Elvin, AA Elvin. A coupled finite elementg€"circuit simulation model for analyzing piezoelectric energy generators, J Intell Mater Syst Struct. 20 (2009) 587-595.

[99] Meiling Zhu, E Worthington, J Njuguna. Analyses of power output of piezoelectric energy-harvesting devices directly connected to a load resistor using a coupled piezoelectric-circuit finite element method, Ultrasonics, Ferroelectrics and Frequency Control, IEEE Transactions on. 56 (2009) 1309-1317.

[100] M Pozzi, M Zhu. Plucked piezoelectric bimorphs for knee-joint energy harvesting: Modelling and experimental validation, Smart Mater.Struct. 20 (2011).

[101] X Chen, CHJ Fox, S Mcwilliam. Optimization of a Cantilever Microswitch with Piezoelectric Actuation ournal of Intelligent Material Systems and Structures. 15 (2004) 823-834.

[102] PD Mitcheson, EM Yeatman, GK Rao, AS Holmes, TC Green. Energy Harvesting From Human and Machine Motion for Wireless Electronic Devices, Proceedings of the IEEE. 96 (2008) 1457-1486.

[103] O Bilgen, Y Wang , D Inman. Electromechanical comparison of cantilevered beams with multifunctional piezoceramic devices, Mechanical Systems and Signal Processing. 27 (2012) 763-777.

[104] S Priya. Criterion for material selection in design of bulk piezoelectric energy harvesters, Ultrasonics, Ferroelectrics and Frequency Control, IEEE Transactions on. 57 (2010) 2610-2612.

[105] A Daniels, A Giuliano, M Zhu, A Tiwari, Modeling, Validation and Design Analyses of a Piezoelectric Cymbal Transducer for Non-resonant Energy Harvesting, Green Computing and Communications (GreenCom), 2013 IEEE and Internet of Things (iThings/CPSCom), IEEE International Conference on and IEEE Cyber, Physical and Social Computing. (2013) 1665-1667.

[106] WP Mason. An Electromechanical Representation of a Piezoelectric Crystal Used as a Transducer, Proceedings of the Institute of Radio Engineers. 23 (1935) 1252-1263.

[107] T Jordan L., Z Ounaies, Piezoelectric Ceramics Characterization, NASA/CR-2001-211225 (2001).

[108] DeL Piezo Specialties LLC, Material Specification, [Online], Avaliable: http://delpiezo.com/yahoo_site_admin/assets/docs/Material_Specification_Sheet.254613.pdf , (Accessed: 12 Mar 2013).

[109] Sumitomo Metal (SMI) Electronic Devices Inc, SPEM Sumitomo piezpelectric material, [Online], Available: http://www.datasheetarchive.com/3--LW6-datasheet.html, (Accessed: 12 Mar 2013).

[110] Piezo Systems Inc, Piezoceramic Properties, [Online], Available: http://www.piezo.com/prodmaterialprop.html, (Accessed: 12 Mar 2013).

[111] Steiner & Martins Inc, Piezo Material Properties, [Online], Available: http://www.steminc.com/, (Accessed: 12 Mar 2013).

[112] MatWeb-Material Property Data, 304 Stainless Steel, [Online], Available: http://www.matweb.com/search/DataSheet.aspx?MatGUID=abc4415b0f8b490387e3c922237098da&ckck=1, (Accessed: 03 Jul 2013).

[113] D William, J Callister, Materials science and engineering an introduction, 7th ed., John Wiley & Sons, Inc. 2007.

[114] JK Kim, HS Kim, DG Lee. Adhesion characteristics of carbon/epoxy composites treated with low- and atmospheric pressure plasmas, J.Adhes.Sci.Technol. 17 (2003) 1751-1771.

[115] A Giuliano, V Marsic, M Zhu, Implementation and testing of an elastic strain powered wireless sensing system for energy-autonomous applications, Proceedings of the IEEE International Conference on Internet of Things. (2012).

[116] M Pozzi, MSH Aung, M Zhu, RK Jones, JY Goulermas, The pizzicato knee-joint energy harvester: Characterization with biomechanical data and the effect of backpack load, Smart Materials and Structures. 21 (2012).

[117] IEEE Standard on Piezoelectricity, ANSI/IEEE Std 176-1987. (1988) 0_1.

APPENDICES

APPENDIX 1

APDL code used in material selection study

```
!!**Harmonics
!/BATCH
FINISH
/CLEAR
/PREP7
/OUTPUT, TERM
/UNITS, SI
/SHOW
!BCSOPTION,,incore  !CHANGES MEMORY SETTINGS
BCSOPTION,,minimum  !CHANGES MEMORY SETTINGS
!*use,'EL.MAC'  !make sure its uptodate
!PFT WITH FULL MONOLITHIC LAYER EVEN UNDER JOIN BUT PARTIAL
ELECTRODE UP UNTIL JOIN.
!INCLUDES
!
! ******************************
! Geometrty Name
!******************************
!c=caps= metalic end caps that suspend and suround PZT disc,
!p=piez= piezoelectric disc
!Ho=outside height. From the PZT disc to the outside of the endcaps
!Hi=inside height. From PZT disc to inside the endcap
/UNITS, SI
!******************************
! Basic Unit
!******************************
mm=1e-3
microns=1e-6
eps_0=8.854e-12                    ! Permittivity of free space
kv=1000
!******************************
! Geometrty & Mesh paramters
!******************************
!___VARIABLES___
!
!
!
!
!
!
!*use,'EL.MAC'
```

```
!||||||||||)))
Resistance=10e6 !0.5 next      !load resistor (Ohm) best is 2.5 Mohm
!||||||||||)))
elec=40*mm
!capacitance=1e-12
Force=-1000  !applied force (N)
Segment_arc=360   !Arc length of cymbal section (degree) CANNOT BE ZERO
Segment_div=20     !section division for segment
!___pft SIZE___
Fw=30*mm
FS=0*mm  !Fibre spacing
PFTDepth=30*mm ! this depth help match the capacitance of PCT5
Dp=52*mm
Da=14*mm
Dc=40*mm
tc=0.5*mm
tp=4*mm      !Pzt Thickness
sub=(0.6)*mm      !substrate thickness sub=1.43*3=4.29
fillet_radius=3*mm
Hi=(3.5)*mm
Fpl=Dc
Fpw=PFTDepth
Ft=tp
J=(Dp-Dc)/2 !8
meshsize=3*mm
meshL=3*mm
meshw=3*mm
meshH=3*mm
!___CYMBAL SIZE___
!Dp=50*mm
!Da=6*mm
!Dc=30*mm
!tc=0.33*mm
!tp=1*mm
!sub=1*mm      !substrate thickness
!fillet_radius=3*mm
!the following are to make things easier later on
Ra=Da/2
Rc=Dc/2
Rp=Dp/2
!Hi=(1.5)*mm
Ho=Hi+tc
tph=tp/2
subh=sub/2
pztlayers=2
tpi=tp/pztlayers
!Dp=30*mm
```

```
!Da=6*mm
!Dc=25.5*mm
!tc=0.33*mm
!tp=1*mm
!fillet_radius=3*mm
!Ra=Da/2
!Rc=Dc/2
!Rp=Dp/2
!Ho=(1.85)*mm
!Hi=Ho-tc
!*******************************
! material reference number
!*******************************
!material 1 = cap
!material 2= pzt
!material 4= resistor
!*******************************
! material properties
!*******************************
! * Pzt DL-53HD
! ANISOTROPIC ELASTIC STIFFNESS
!K31 =  0.42
s11=15.1E-12
s12=-4.5E-12
s13=-9.4E-12
s33=24.8E-12
s44=37.1E-12
!s11=((15.1E-12)*0.15)+15.1E-12
!s12=((-4.5E-12)*0.15)-4.5E-12
!s13=((-9.4E-12)*0.15)-9.4E-12
!s33=((24.8E-12)*0.15)+24.8E-12
!s44=((37.1E-12)*0.15)+37.1E-12
NIPZT=(S44/(2*S11))-1
s66=39.2E-12
!PERMITTIVITY constant stress
ep11_T=3550
ep33_T=3850
!ep11_T=(3550)+(3550*0.1)
!ep33_T=3850+(3850*0.1)
! DENSITY, KG/M3
dens_p=7900
! PIEZOELECTRIC STRAIN COEFFICIENTS, C/N
D15=810E-12
D31=-300E-12
D33=680E-12
!D15=((-810E-12)*0.05)+810E-12
!D31=((+300E-12)*0.05)-300E-12
```

```
!D33=((-680E-12)*0.05)+680E-12
Q=20
/NOPR
/PREP7
!The material properties were sourced from www.piezo.com
! * Pzt (VIBRIT 420) JOHNSON MATTHEY
! ANISOTROPIC ELASTIC STIFFNESS
!s11=15.4E-12  !64.935 GPa
!s12=-5.7E-12
!s13=-6.5E-12  !153.846 GPa
!s33=18.7E-12  !53.46 GPa
!s44=45E-12
!NIPZT=(S44/(2*S11))-1
!s66=2*(1+NIPZT)*S33  !=2(1+V)S33
!! PERMITTIVITY constant stress
!ep11_T=1600
!ep33_T=1600
!! DENSITY, KG/M3
!dens_p=7600
!! PIEZOELECTRIC STRAIN COEFFICIENTS, C/N
!D15=525E-12
!D31=-160E-12
!D33=355E-12
!D15m=-525E-12
!D31m=+160E-12
!D33m=-355E-12
!Q=100
!/NOPR
!/PREP7
! * Cap (c=cap) Red Brass, UNS C23000
!dens_c=8750                          ! Density in kg/m^3
!young_c=115e9                        ! Young's modulus in Pa yeild at 550MPa so
conservative 275MPa
!poiss_c=0.307
! * Cap (c=cap) Soft Lead Brass (matweb)
!dens_c=8500                          ! Density in kg/m^3
!young_c=97e9                         ! Young's modulus in Pa
!poiss_c=0.311
! * Caps Stainless Steel AISI Type 450 (matweb)
!dens_c=7800                          ! Density in kg/m^3
!young_c=215e9                        ! Young's modulus in Pa
!poiss_c=0.283
! * Caps Steel kim et al
!dens_c=7800                          ! Density in kg/m^3
!young_c=215e9                        ! Young's modulus in Pa
!poiss_c=0.3
! * Caps Stainless Steel AISI Type 450 (matweb)
```

```
!dens_s=7800                          ! Density in kg/m^3
!young_s=215e9                        ! Young's modulus in Pa
!poiss_s=0.283
! * Caps Stainless Steel 304  Yeild 251MPa SF4 62.75MPa 70% max elogation at break
dens_s=8030                           ! Density in kg/m^3
young_s=193e9                         ! Young's modulus in Pa
poiss_s=0.24
! * Caps Stainless Steel 304  Yeild 251MPa SF4 62.75MPa 70% max elogation at break
dens_c=8030                           ! Density in kg/m^3
young_c=193e9                         ! Young's modulus in Pa
poiss_c=0.24
! * Caps Al 1100 /yeild=34MPa
!dens_c=2710                          ! Density in kg/m^3
!young_c=69e9                         ! Young's modulus in Pa
!poiss_c=0.33
! * Caps Cu Alloy c17200 /yeild=195-380MPa
!dens_c=8250                          ! Density in kg/m^3
!young_c=128e9                        ! Young's modulus in Pa
!poiss_c=0.3
! * Caps Ti Alloy Ti-5Al-2.5Sn  /yeild=760MPa
!dens_c=4480                          ! Density in kg/m^3
!young_c=110e9                        ! Young's modulus in Pa
!poiss_c=0.34
! * Caps Stainless Steel 304 / Yeild=205MPa to 515MPa
!dens_c=8000                          ! Density in kg/m^3
!young_c=193e9                        ! Young's modulus in Pa
!poiss_c=0.3
! material declaration
!*****************************
!___CAPS___
MP, EX, 1, young_c
MP, DENS, 1, dens_c
MP, NUXY, 1, poiss_c
!___SUBSTRATE___
MP, EX, 4, young_s
MP, DENS, 4, dens_s
MP, NUXY, 4, poiss_s
!___+y PZT___
!for pzt poled in the +y direction
!   [s11 s13 s12  0  0  0 ]       [ 0 d31  0 ]     [ep11  0    0  ]
!   [s13 s33 s13  0  0  0 ]       [ 0 d33  0 ]     [  0  ep33  0  ]
!   [s12 s13 s11  0  0  0 ]       [ 0 d31  0 ]     [  0   0   ep11]
!   [ 0   0   0  s44 0  0 ]       [d15 0   0 ]
!   [ 0   0   0   0 s44 0 ]       [ 0  0  d15]
!   [ 0   0   0   0  0 s66]       [ 0  0   0 ]
TB,ANEL,2,,,1                 ! ANISOTROPIC ELASTIC COMPLIANCE MATRIX
TBDATA, 1, s11
```

```
TBDATA, 2, s13
TBDATA, 3, s12
TBDATA, 7, s33
TBDATA, 8, s13
TBDATA, 12, s11
TBDATA, 16, s44
TBDATA, 19, s44
TBDATA, 21, s66
TB,PIEZ,2,,,1              ! PIEZOELECTRIC STRAIN MATRIX
TBDATA, 2, d31
TBDATA, 5, d33
TBDATA, 8, d31
TBDATA, 10, d15
TBDATA, 15, d15
TB,DPER,2,,,1
TBDATA,1,EP11_t   !AT CONSTANT STRESS
TBDATA,2,EP33_t
TBDATA,3,EP11_t
MP,DENS,2,dens_p           ! DENSITY kg/m^3
!__-y PZT___
!for pzt poled in the -y direction
!   [s11 s13 s12  0  0  0 ]       [ 0 d31  0 ]     [ep11  0    0  ]
!   [s13 s33 s13  0  0  0 ]       [ 0 d33  0 ]     [  0  ep33  0  ]
!   [s12 s13 s11  0  0  0 ]       [ 0 d31  0 ]     [  0   0   ep11]
!   [ 0   0   0  s44 0  0 ]       [d15 0   0 ]
!   [ 0   0   0   0 s44 0 ]       [ 0  0  d15]
!   [ 0   0   0   0  0 s66]       [ 0  0   0 ]
TB,ANEL,3,,,1              ! ANISOTROPIC ELASTIC COMPLIANCE MATRIX
TBDATA, 1, s11
TBDATA, 2, s13
TBDATA, 3, s12
TBDATA, 7, s33
TBDATA, 8, s13
TBDATA, 12, s11
TBDATA, 16, s44
TBDATA, 19, s44
TBDATA, 21, s66
TB,PIEZ,3,,,1              ! PIEZOELECTRIC STRAIN MATRIX
TBDATA, 2, d31m
TBDATA, 5, d33m
TBDATA, 8, d31m
TBDATA, 10, d15m
TBDATA, 15, d15m
TB,DPER,3,,,1
TBDATA,1,EP11_t   !AT CONSTANT STRESS
TBDATA,2,EP33_t
TBDATA,3,EP11_t
```

```
MP,DENS,3,dens_p            ! DENSITY kg/m^3
!___ELEMENT TYPES___
ET,1,PLANE82
ET,2,SOLID95
ET,3,SOLID226,1001
ET,4,CIRCU94,0
!ET,5,CIRCU94,2
!__Real Values assigned__
R,3,RESISTANCE
R,5,0.01
!R,4,capacitance
!*********************************
! Modelling
!*********************************
!___DRAW Metal caps____
!_TOPCAP
!apex
KSEL,NONE
ASEL,NONE
k,,0,(tp/2)+Hi+SUB,-Ra
k,,0,(tp/2)+Ho+SUB,-Ra
k,,0,(tp/2)+Ho+SUB,Ra
k,,0,(tp/2)+Hi+SUB,Ra
*GET,KPNUM,KP,,NUM,MAX
a,KPNUM-3,KPNUM-2,KPNUM-1,KPNUM
!rest of cap
KSEL,NONE
ASEL,NONE
k,,0,tp/2+SUB,Rc
k,,0,(tp/2)+SUB+tc,Rc
k,,0,(tp/2)+SUB+tc,Rp
k,,0,tp/2+SUB,Rp
*GET,KPNUM,KP,,NUM,MAX
a,KPNUM-3,KPNUM-2,KPNUM-1,KPNUM
KSEL,NONE
k,,0,(tp/2)+SUB+Hi,Ra
k,,0,(tp/2)+SUB+Ho,Ra
k,,0,(tp/2)+SUB+tc,Rc
k,,0,tp/2+SUB,Rc
*GET,KPNUM,KP,,NUM,MAX
a,KPNUM-3,KPNUM-2,KPNUM-1,KPNUM
ARSYM,Z,ALL
!_BOTCAP
!apex
KSEL,NONE
ASEL,NONE
k,,0,-((tp/2)+Hi+SUB),-Ra
```

```
k,,0,-((tp/2)+Ho+SUB),-Ra
k,,0,-((tp/2)+Ho+SUB),Ra
k,,0,-((tp/2)+Hi+SUB),Ra
*GET,KPNUM,KP,,NUM,MAX
a,KPNUM-3,KPNUM-2,KPNUM-1,KPNUM
!rest of cap
ASEL,NONE
KSEL,NONE
k,,0,-((tp/2)+SUB),Rc
k,,0,-((tp/2)+tc+SUB),Rc
k,,0,-((tp/2)+tc+SUB),Rp
k,,0,-(tp/2+SUB),Rp
*GET,KPNUM,KP,,NUM,MAX
a,KPNUM-3,KPNUM-2,KPNUM-1,KPNUM
KSEL,NONE
k,,0,-((tp/2)+Hi+SUB),Ra
k,,0,-((tp/2)+Ho+SUB),Ra
k,,0,-((tp/2)+tc+SUB),Rc
k,,0,-(tp/2+SUB),Rc
*GET,KPNUM,KP,,NUM,MAX
a,KPNUM-3,KPNUM-2,KPNUM-1,KPNUM
ARSYM,Z,ALL
ALLS
VEXT,ALL,,,PFTDepth
! lengthways seed
LSEL,S,LINE,,50
LSEL,A,LINE,,92
LSEL,A,LINE,,66
LSEL,A,LINE,,108
LSEL,A,LINE,,42
LSEL,A,LINE,,84
LPLOT
LESIZE,ALL,MESHL
! widthways seed
LSEL,S,LINE,,55
LSEL,A,LINE,,63
LSEL,A,LINE,,62
LSEL,A,LINE,,80
LSEL,A,LINE,,72
LSEL,A,LINE,,71
LSEL,A,LINE,,47
LSEL,a,LINE,,96
LSEL,A,LINE,,104
LSEL,A,LINE,,101
LSEL,A,LINE,,117
LSEL,A,LINE,,118
LSEL,A,LINE,,110
```

```
LSEL,A,LINE,,88
LPLOT
LESIZE,ALL,MESHW
! mesh caps
ESIZE,meshsize
VATT,1,,2  !num is material then el type
vmesh,all
CM,caps,VOLU
cm,caps,elem
CMSEL,S,caps
CM,CAPSN,NODE
ALLS
EPLOT
!MESH NOTES: the key relationships is between the join ((dp-dc)/2) and the substrate. As long as these
!line up then the mesh works. I put the dimensions into excel and change the mesh num until i
!found an even number of meshsize divisions into the join length and substrate
subL/mesh and join/mesh
!___DRAW Spacer Sides___
Lsel,none
KSEL,NONE
ASEL,NONE
NSEL,NONE
ESEL,NONE
VSEL,NONE
CMSEL,NONE
!metal spacer sides of pzt
ASEL,NONE
ksel,none
k,,0,-(tp/2),Rc
k,,0,+(tp/2),Rc
k,,0,+(tp/2),Rp
k,,0,-(tp/2),Rp
*GET,KPNUM,KP,,NUM,MAX
a,KPNUM-3,KPNUM-2,KPNUM-1,KPNUM
ARSYM,Z,ALL
ksel,none
!___DRAW Substrates____
!*lower
!left split
k,,0,-(tp/2),-Rp
k,,0,-((tp/2)+sub),-Rp
k,,0,-((tp/2)+sub),-Rc
k,,0,-(tp/2),-Rc
*GET,KPNUM,KP,,NUM,MAX
a,KPNUM-3,KPNUM-2,KPNUM-1,KPNUM
```

```
k,,0,-(tp/2),-Rc
k,,0,-((tp/2)+sub),-Rc
k,,0,-((tp/2)+sub),Rc
k,,0,-(tp/2),Rc
*GET,KPNUM,KP,,NUM,MAX
a,KPNUM-3,KPNUM-2,KPNUM-1,KPNUM
!right split
k,,0,-(tp/2),Rc
k,,0,-((tp/2)+sub),Rc
k,,0,-((tp/2)+sub),Rp
k,,0,-(tp/2),Rp
*GET,KPNUM,KP,,NUM,MAX
a,KPNUM-3,KPNUM-2,KPNUM-1,KPNUM
!*upper
!left split
k,,0,(tp/2),-Rp
k,,0,((tp/2)+sub),-Rp
k,,0,((tp/2)+sub),-Rc
k,,0,(tp/2),-Rc
*GET,KPNUM,KP,,NUM,MAX
a,KPNUM-3,KPNUM-2,KPNUM-1,KPNUM
k,,0,(tp/2),-Rc
k,,0,((tp/2)+sub),-Rc
k,,0,((tp/2)+sub),Rc
k,,0,(tp/2),Rc
*GET,KPNUM,KP,,NUM,MAX
a,KPNUM-3,KPNUM-2,KPNUM-1,KPNUM
!right split
k,,0,(tp/2),Rc
k,,0,((tp/2)+sub),Rc
k,,0,((tp/2)+sub),Rp
k,,0,(tp/2),Rp
*GET,KPNUM,KP,,NUM,MAX
a,KPNUM-3,KPNUM-2,KPNUM-1,KPNUM
!___MESH Lower Substrates
lsel,none
ASEL,NONE
NSEL,NONE
ESEL,NONE
VSEL,NONE
CMSEL,NONE
ASEL,S,,,64
ASEL,A,,,65
ASEL,A,,,63
VEXT,ALL,,,PFTDepth
CM,LLSUB,LINE
CMSEL,S,LLSUB
```

```
LSEL,R,LOC,Z,RC
LESIZE,ALL,MESHW
CMSEL,S,LLSUB
LSEL,R,LOC,Z,RP
LESIZE,ALL,MESHW
CMSEL,S,LLSUB
LSEL,R,LOC,Z,-RC
LESIZE,ALL,MESHW
CMSEL,S,LLSUB
LSEL,R,LOC,Z,-RP
LESIZE,ALL,MESHW
ESIZE,meshsize
VATT,4,,2    !Assign material properties
vmesh,all
cm,lsub,elem
CM,lSUBN,NODE
alls
eplot
!___MESH upper Substrates
lsel,none
ASEL,NONE
NSEL,NONE
ESEL,NONE
VSEL,NONE
CMSEL,NONE
ASEL,S,,,66
ASEL,A,,,67
ASEL,A,,,68
VEXT,ALL,,,PFTDepth
CM,LUSUB,LINE
CMSEL,S,LUSUB
LSEL,R,LOC,Z,RC
LESIZE,ALL,MESHW
CMSEL,S,LUSUB
LSEL,R,LOC,Z,RP
LESIZE,ALL,MESHW
CMSEL,S,LUSUB
LSEL,R,LOC,Z,-RC
LESIZE,ALL,MESHW
CMSEL,S,LUSUB
LSEL,R,LOC,Z,-RP
LESIZE,ALL,MESHW
ESIZE,meshsize
VATT,4,,2    !Assign material properties
vmesh,all
cm,usub,elem
CM,uSUBN,NODE
```

```
alls
eplot
!___MESH Sides
lsel,none
ASEL,NONE
NSEL,NONE
ESEL,NONE
VSEL,NONE
CMSEL,NONE
ASEL,S,,,61
ASEL,A,,,62
VEXT,ALL,,,PFTDepth
lplot
!Seeding mesh
CM,LSPLIT,LINE
CMSEL,S,LSPLIT
LSEL,R,LOC,Z,RC
LESIZE,ALL,MESHW
CMSEL,S,LSPLIT
LSEL,R,LOC,Z,-RC
LESIZE,ALL,MESHW
ESIZE,meshsize
VATT,2,,3   !MAT,REAL,TYPE  !Assign material properties
vmesh,all
CM,SPACER_NODES,NODE
CM,SPACER,ELEM
CM,SPACERN,NODE
alls
eplot
! * Pzt layers
LSEL,NONE
ASEL,NONE
NSEL,NONE
ESEL,NONE
VSEL,NONE
CMSEL,NONE
!needed for do loops
!Fibre_Unit=Fw+FS
!No_Fib=Fpw/Fibre_Unit
!No_Fib2=No_Fib-Fibre_Unit              !needed as I will be mirroring
!No_Fib3=No_Fib2/2                     !half of number of fibres
!No_Fib_Half=NINT(No_Fib3)             !returns an integer
!Num_of_Fibers=((No_Fib_Half)*2)+1 !checking aid
!for all meshing
!No_Fib_Halff=No_Fib_Half-1
!ActiveFibreWidth=(Num_of_Fibers*Fw)+(No_Fib_Halff*2*fs)
!meshseed=ActiveFibreWidth/2   !/Ad
```

```
Fibre_Unit=Fw+FS
No_Fib=NINT(Fpw/Fibre_Unit)
!draws first middle area for fibres
! ASEL,STAT    Displays active areas
! ASEL,S,AREA,....
! *GET,KREF,KP,,NUM,MAX
 !K,KREF+1,-Fw/2,-Ft/2,-Fpl/2
 !K,KREF+2,-Fw/2,Ft/2,-Fpl/2
 !K,KREF+3,Fw/2,Ft/2,-Fpl/2
 !K,KREF+4,Fw/2,-Ft/2,-Fpl/2
 !A,KREF+1,KREF+2,KREF+3,KREF+4 !231
*GET,FIRST_FIBRE_AREA,AREA,,NUM,MAX ! correlates to first middle fibre area
! *STATUS,FIRST_FIBRE_AREA
move=0
*Do,Fibre,1,No_Fib
K,,(+move),-Ft/2,-Fpl/2
 *GET,KREFA,KP,,NUM,MAX
K,,(+move),Ft/2,-Fpl/2
 *GET,KREFB,KP,,NUM,MAX
K,,(+move+Fw),Ft/2,-Fpl/2
 *GET,KREFC,KP,,NUM,MAX
K,,(+move+Fw),-Ft/2,-Fpl/2
 *GET,KREFD,KP,,NUM,MAX
 A,KREFA,KREFB,KREFC,KREFD
move=move+Fibre_Unit
*Enddo
! * PZT MESH & extruding
*GET,LAST_FIBRE_AREA,AREA,,NUM,MAX !235
VEXT,ALL,,,,,Fpl
CM,PZTL,LINE
LSEL,R,LOC,Y,TP/2
LSEL,R,LOC,Z,-RC
LESIZE,ALL,MESHW
CMSEL,S,PZTL
CMPLOT
LSEL,R,LOC,Y,TP/2
LSEL,R,LOC,Z,RC
LESIZE,ALL,MESHW
LPLOT
CMSEL,S,PZTL
LSEL,R,LOC,Z,RC
LSEL,R,LOC,X,FPW
LESIZE,ALL,MESHH
ESIZE,meshsize
VATT,2,,3   !MAT,REAL,TYPE
VMESH,ALL
CM,PZTT,elem
```

```
CM,PZTN,node
CM,PZTK,KP
CMSEL,NONE
CMSEL,S,SPACER,ELEM
CMSEL,A,PZTT,ELEM
CM,PZT,ELEM
!CHECK MESHING BETWEEN PZT AND SPACER
CMSEL,NONE
CMSEL,S,SPACER,ELEM
CMSEL,A,PZT,ELEM
CMPLOT,ALL
alls
NUMMRG, NODE, 1.0E-10
!___Delete unused elements___
!ALLSEL, ALL       !this ET was used to make 3D mesh
!EPLOT
!ESEL, U, TYPE, , 1 !but is now not used in model
!NUMMRG, NODE, 1.0E-10
!nummrg,kp,1e-7
!*************************************************************
! Boundary Conditions
!*************************************************************
alls
!___Fixed Base___
NSEL,S,LOC,Y,-((tp/2)+sub+Ho)
D,ALL,UY,0
D,ALL,UX,0
!selects top apex
NSEL,S,LOC,Y,(tp/2)+sub+Ho
CP,NEXT,UY,ALL
!*****************************************
! Loading
!*****************************************
!___FORCE___
CSYS,0  !ensures that were're in cartesian
NSEL,S,LOC,Y,(tp/2)+SUB+Ho !selects top apex
*get,numnode,node,0,count
F,ALL,FY,(force/numnode)
!*****************************************
! Circuit
!*****************************************
!*****************************************
! Circuit
!*****************************************
!___ELECTRODE COUPLING___
!
!
```

```
!    | |____/   \ /   \ /   \ /   \_____| |
!    |__|
!

! top electrode connect point
VSEL,NONE
NSEL,NONE
ESEL,NONE
CMSEL,NONE
CSYS,0
CMSEL,S,PZTN,NODE
CMSEL,a,SPACERN,NODE
NPLOT
NSEL,R,LOC,Y,TP/2
NSEL,R,LOC,z,-elec/2,elec/2
NPLOT
*GET,node_s1,NODE,,NUM,MIN
CM,signal_1,NODE
! bottom electrode connect point
VSEL,NONE
NSEL,NONE
ESEL,NONE
CMSEL,NONE
!
CMSEL,S,PZTN,NODE
CMSEL,a,SPACERN,NODE
NPLOT
NSEL,R,LOC,Y,-TP/2
NSEL,R,LOC,z,-elec/2,elec/2
NPLOT
*GET,node_g1,NODE,,NUM,MIN
CM,Ground_1,NODE
! couples all +ve flats
VSEL,NONE
NSEL,NONE
ESEL,NONE
CMSEL,NONE
CMSEL,S,signal_1,NODE
CMPLOT
CP,NEXT,volt,ALL
! Couples and grounds all -ve flats
VSEL,NONE
NSEL,NONE
ESEL,NONE
CMSEL,NONE
CMSEL,S,Ground_1,NODE
CMPLOT
```

```
CP,NEXT,volt,ALL
D,ALL,volt,0
!___Colecting number of elements to help when getting ESOL's___
ALLS
*GET,ENUM,ELEM,,NUM,MAX
EPLOT
!___RESISTOR___
TYPE,4
REAL,3          !assigns resistive value
E,node_s1,node_G1
NSEL,ALL
ALLS
EPLOT
/SOLU
!*********************************************
!Results
!*********************************************
!     |
!     |        *
!   P |      *   *
!   O |    *       *
!   W |   *         *
!   E |  *            *
!   R | *               *
!     |*                  *
!     |_____________________________
!            RESISTANCE
khz=1000
f_min=0 !FOR RESISTANCE
f_max=2
subs=1
KECI=1/(2*Q)
EQSLV,SPARSE,1E-13
ANTYPE,HARMIC
HROPT,FULL
OUTRES,ESOL,ALL
HROUT,ON
OUTPR,ALL,1
!___Printing results as amplitudes and phaes angles___
OUTRES,ALL,ALL
HARFRQ,f_min,f_max
NSUBST,subs
KBC,1
DMPRAT,KECI
ALLSEL,ALL
!___Delete unused elements___
ALLSEL, ALL        !this ET was used to make 3D mesh
```

```
ESEL, U, TYPE, , 1 !but is now not used in model
solve
FINISH
!/EXIT,NOSAVE
SAVE
/POST26
NUMVAR,200
LINES,5000
alls
eplot
!___CALCULATIONS___
ESOL,32,ENUM+1,,SMISC,1,V_RES   !ITEM=SMISC, E=1, COMPONENT FIELD
IS SMUN (N)
ESOL,31,ENUM+1,,SMISC,2,I_RES
ESOL,33,ENUM+1,,NMISC,1,P_RES
PRCPLX,1
PRVAR,V_RES
!IMAGIN,51,32
!REALVAR,52,32 CANT GET TO WORK
! * MAKING COMPLEX POST26 VARIABLE VARABLES INTO PARAMETERS
FOR LATER USE
!INITIALISE MATRIX
*DIM,REALVOL,,1,1
*DIM,IMAGVOL,,1,1
!*STATUS,REALVOL
!*STATUS,IMAGVOL
!PICK REAL AND IMAG PART OF VOLTAGE VARIABLE ND PLACE INTO
ARRAY PARAMETER
VGET,REALVOL(1,1),32,2,0   !PUTS REAL PART OF VOLT INTO ARRAY
VGET,IMAGVOL(1,1),32,2,1    !PUTS IMAG PART OF VOL INTO ARRAY
!COMBINE REAL AND IMAG TO GET AMPLITUDE OF VOLTAGE
VPUT,REALVOL,40,2,0  !CONVERT ARRAY PARAMETERS INTO VARIABLES
VPUT,IMAGVOL,45,2,0  !CONVERT ARRAY PARAMETERS INTO VARIABLES
PROD,41,40,40  !REAL^2
PROD,46,45,45  !IMAG^2
ADD,47,41,46    !REAL^2 + IMAG^2
SQRT,48,47     !SQRT(REAL^2 + IMAG^2)
*GET,V_AMP,VARI,48,EXTREM,VMAX !MAKES VARIABLE INTO
PARAMETER
```

APPENDIX 2

Input of Piezoelectric Material Constants into ANSYS

ANSYS assumes linear piezoelectric behaviour. In linear piezoelectricity the equations of linear elasticity are coupled with the charge equation of electrostatics by way of the piezoelectric constants [117]. The piezoelectric constants involved are c^E, e and ε^S which are the elastic, piezoelectric and dielectric constants, respectively. The electromechanical constitutive equations are represented in ANSYS by the following,

$$\{T\} = [c^E]\{S\} - [e]\{E\} \tag{24}$$

$$\{D\} = [e]^T\{S\} + [\varepsilon^S]\{E\} \tag{25}$$

Or equivalently,

$$\begin{Bmatrix} \{T\} \\ \{D\} \end{Bmatrix} = \begin{bmatrix} [c^E] & [e] \\ [e]^T & -[\varepsilon^S] \end{bmatrix} \begin{Bmatrix} \{S\} \\ -\{E\} \end{Bmatrix} \tag{26}$$

Where,

$\{T\}$ = stress vector

$\{D\}$ = electric flux density vector

$\{S\}$ = strain vector

$\{E\}$ = electric field vector

$[c^E]$ = elasticity matrix, super-script *E* signifies it's evaluation at constant electric field

$[e]$ = piezoelectric matrix relating stress and electric field, where super-script *T* outside brackets signifies a transposed matrix

$[\varepsilon^S]$ = dielectric matrix super-script *S* signifies it's evaluation at constant strain

However, there are alternative forms of the constitutive equations discussed in the IEEE standard on piezoelectricity [117]. One such alternative form was used in a NASA paper

on piezoelectric characterisation [107] and is as follows,

$$\{S\} = [s^E]\{T\} + [d]\{E\} \tag{27}$$

$$\{D\} = [d]^T\{T\} + [\varepsilon^T]\{E\} \tag{28}$$

Where,

$\{T\}$ = stress vector

$\{D\}$ = electric flux density vector

$\{S\}$ = strain vector

$\{E\}$ = electric field vector

$[s^E]$ = compliance matrix, super-script *E* signifies it's evaluation at constant electric field

$[d]$ = piezoelectric matrix relating strain and electric field, where super-script *T* outside brackets signifies a transposed matrix

$[\varepsilon^S]$ = dielectric matrix super-script *S* signifies it's evaluation at constant strain

This constitutive form is also present in manufacturing therefore influencing the forms of material constants that are published, hence why in this Thesis the piezoelectric strain constant *d* was studied. The constants input into the ANSYS model in this thesis are the elastic compliances (s), piezoelectric strain constants (d), the dielectric permittivity's (ε) and the density (ρ). According to the specific element type used in ANSYS the dielectric permittivity ε must be input with the correct syntax identifying whether it at constant stress or strain. Moreover, there are further restrictions to be considered for legacy elements. ANSYS states that 'legacy elements' tend to be less robust and have fewer capabilities than 'current technology elements'.

The methods of how the constants were input into the ANSYS model will now follow. Either the elastic compliance *s* or the stiffness *c* can be input and ANSYS will carry out the conversion. The type of constant must be declared so ANSYS can take the correct action.

$$\left[s^E\right] = \left[c^E\right]^{-1} \tag{29}$$

In manufacturing piezoelectric elastic compliance data (at constant electric field) is often based on the following format matrix,

$$\left[s_z^E\right] = \begin{bmatrix} s_{11}^E & s_{12}^E & s_{13}^E & s_{14}^E & s_{15}^E & s_{16}^E \\ s_{21}^E & s_{22}^E & s_{23}^E & s_{24}^E & s_{25}^E & s_{26}^E \\ s_{31}^E & s_{32}^E & s_{33}^E & s_{34}^E & s_{35}^E & s_{36}^E \\ s_{41}^E & s_{42}^E & s_{43}^E & s_{44}^E & s_{45}^E & s_{46}^E \\ s_{51}^E & s_{52}^E & s_{53}^E & s_{54}^E & s_{55}^E & s_{56}^E \\ s_{61}^E & s_{62}^E & s_{63}^E & s_{64}^E & s_{65}^E & s_{66}^E \end{bmatrix} \frac{C}{N} \tag{30}$$

Now reducing the matrix to only the independent components, expressing the symmetry of the matrix and assuming the relations $s_{22}=s_{11}$, $s_{55}=s_{44}$, $s_{23}=s_{13}$ and $s_{66}=2(s_{11}- s_{12})$),

$$\left[s_z^E\right] = \begin{bmatrix} s_{11}^E & s_{12}^E & s_{13}^E & & & \\ & s_{11}^E & s_{13}^E & & & \\ & & s_{33}^E & & & \\ & & & s_{44}^E & & \\ & & & & s_{44}^E & \\ & & & & & s_{66}^E \end{bmatrix} \frac{C}{N} \tag{31}$$

To convert this into an ANSYS format before entering the constants into ANSYS the bottom three rows are changed as follows,

- row 4-5
- row 5-6, and
- row 6-4.

$$\left[s^{E}_{ANSYS_Z}\right]=\begin{bmatrix} s^{E}_{11} & s^{E}_{12} & s^{E}_{13} & & & \\ & s^{E}_{11} & s^{E}_{13} & & & \\ & & s^{E}_{33} & & & \\ & & & s^{E}_{66} & & \\ & & & & s^{E}_{44} & \\ & & & & & s^{E}_{44} \end{bmatrix}\frac{C}{N} \tag{32}$$

Drawing related APDL commands such as RECTNG and PTXY, which are used to draw rectangles and polygons/prisms, respectively, are only available to be used in the *x*-*y* plane. Using these commands becomes problematic when trying to draw a circular based shape. For example, if a half cross-section of a Cymbal, as in Figure 6.1, is drawn on the *x*-*y* plane, then revolving the 2D drawing by 360° would result in the thickness of the piezoelectric disk to be parallel with the *y*-axis.

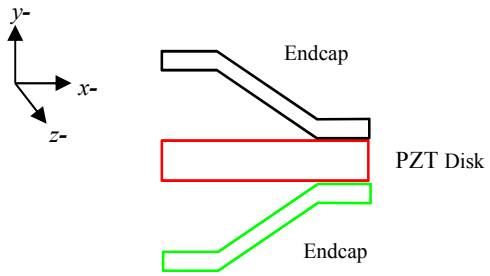

Figure 6.1 Drawing of half cross-section of Cymbal structure.

Hence, there is a need to input material properties into ANSYS with axis co-ordination different to the default. An alternative of using restrictive drawing commands is to define key points, draw lines connecting the key points and then make an area in the space that is confined by the lines. In this thesis the piezoelectric material was poled in the *y*-direction thus a further conversion to the input material constants was required:

- Z data becomes Y data
- Y data becomes Z data
- X data remains the same

The ANSYS matrix indexing order with regards to the co-ordinate system is different from the standard form,

$$STANDARD = \begin{matrix} \\ x \\ y \\ z \\ yz \\ xz \\ xy \end{matrix} \begin{matrix} \begin{matrix} x & y & z & yz & xz & xy \end{matrix} \\ \end{matrix} \qquad ANSYS = \begin{matrix} \\ x \\ y \\ z \\ xy \\ yz \\ xz \end{matrix} \begin{matrix} \begin{matrix} x & y & z & xy & yz & xz \end{matrix} \\ \end{matrix} \tag{33}$$

To convert from *z*- to *y*-poling the following terms were swapped:

- y,y with z,z
- x,y with x,z
- xy,xy with xz,xz

To give,

$$\left[s^E_{ANSYS\ y}\right] = \begin{bmatrix} s^E_{11} & s^E_{13} & s^E_{12} & & & \\ & s^E_{33} & s^E_{13} & & & \\ & & s^E_{11} & & & \\ & & & s^E_{44} & & \\ & & & & s^E_{44} & \\ & & & & & s^E_{66} \end{bmatrix} \frac{C}{N} \tag{34}$$

Considering the ANSYS input order for the elastic compliance matrix in combination with the APDL input command TB and TBDATA,

$$ANSYS\ \ INPUT\ \ ORDER\ \ FOR\ \ TBDATA = \begin{matrix} 1 & 2 & 3 & 4 & 5 & 6 \\ & 7 & 8 & 9 & 10 & 11 \\ & & 12 & 13 & 14 & 15 \\ & & & 16 & 17 & 18 \\ & & & & 19 & 20 \\ & & & & & 21 \end{matrix} \tag{35}$$

The following APDL code was used to input the elastic compliance components into their ANSYS compatible matrix:

```
TB,ANEL,2,,,1              ! ANISOTROPIC ELASTIC COMPLIANCE MATRIX
TBDATA, 1, s11
TBDATA, 2, s13
TBDATA, 3, s12
TBDATA, 7, s33
TBDATA, 8, s13
TBDATA, 12, s11
TBDATA, 16, s44
TBDATA, 19, s44
TBDATA, 21, s66
```

In manufacturing piezoelectric strain constant data is often based on the following matrix format,

$$\left[d_z\right] = \begin{bmatrix} d_{11} & d_{12} & d_{13} & d_{14} & d_{15} & d_{16} \\ d_{21} & d_{22} & d_{23} & d_{24} & d_{25} & d_{26} \\ d_{31} & d_{32} & d_{33} & d_{34} & d_{35} & d_{36} \end{bmatrix} \tag{36}$$

To convert to the ANSYS input compatible format it must first be transposed,

$$\left[d_z\right]^T = \begin{bmatrix} d_{11} & d_{21} & d_{31} \\ d_{12} & d_{22} & d_{32} \\ d_{13} & d_{23} & d_{33} \\ d_{14} & d_{24} & d_{34} \\ d_{15} & d_{25} & d_{35} \\ d_{16} & d_{26} & d_{36} \end{bmatrix} \tag{37}$$

Then reduced and assuming the relationships of $d_{32} = d_{31}$ and $d_{24} = d_{15}$,

$$\left[d_z\right]^T = \begin{bmatrix} & & d_{31} \\ & & d_{31} \\ & & d_{33} \\ & d_{15} & \\ d_{15} & & \\ & & \end{bmatrix} \tag{38}$$

The bottom three rows are changed as follows,

- row 4-5
- row 5-6, and
- row 6-4.

$$\left[d_{ANSYS_Z}\right] = \begin{bmatrix} & & d_{31} \\ & & d_{31} \\ & & d_{33} \\ & & \\ & d_{15} & \\ d_{15} & & \end{bmatrix} \tag{39}$$

Considering the ANSYS indexing order for the co-ordinates and to convert from *z*- to *y*-poling the following terms were swapped:

- x,z with x,y
- z,z with y,y
- y,z with z,y
- yz,y with yz,z

- xz,x with xy,x

$$ANSYS = \begin{matrix} & x & y & z \\ x & & & \\ y & & & \\ z & & & \\ xy & & & \\ yz & & & \\ xz & & & \end{matrix} \tag{40}$$

To give,

$$\left[d_{ANSYS\ y}\right] = \begin{bmatrix} & d_{31} & \\ & d_{33} & \\ & d_{31} & \\ d_{15} & & \\ & & d_{15} \\ & & \end{bmatrix} \tag{41}$$

Considering the ANSYS input order for the piezoelectric strain constant matrix in combination with the APDL input command TB and TBDATA,

$$ANSYS\ INPUT\ ORDER = \begin{bmatrix} 1 & 2 & 3 \\ 4 & 5 & 6 \\ 7 & 8 & 9 \\ 10 & 11 & 12 \\ 13 & 14 & 15 \\ 16 & 17 & 18 \end{bmatrix} \tag{42}$$

The following APDL code was used to input the piezoelectric strain constants into their ANSYS compatible matrix:

```
TB,PIEZ,3,,,1                    ! PIEZOELECTRIC STRAIN MATRIX
TBDATA, 2, d31m
TBDATA, 5, d33m
TBDATA, 8, d31m
TBDATA, 10, d15m
TBDATA, 15, d15m
```

In manufacturing the relative dielectric constant component data (at constant stress) is often based on the following matrix format which is the same as the ANSYS format in this case,

$$\left[\varepsilon^{T}_{r_Z}\right]=\begin{bmatrix}\varepsilon^{T}_{r11} & & \\ & \varepsilon^{T}_{r22} & \\ & & \varepsilon^{T}_{r33}\end{bmatrix} \tag{43}$$

Assuming $\varepsilon_{22}=\varepsilon_{11}$, leads to,

$$\left[\varepsilon^{T}_{rANSYS_Z}\right]=\begin{bmatrix}\varepsilon^{T}_{r11} & & \\ & \varepsilon^{T}_{r11} & \\ & & \varepsilon^{T}_{r33}\end{bmatrix} \tag{44}$$

To convert from *z*- to *y*-poling the following terms was swapped:

- y,y with z,z

$$\left[\varepsilon^{T}_{rANSYS\ y}\right]=\begin{bmatrix}\varepsilon^{T}_{r11} & & \\ & \varepsilon^{T}_{r33} & \\ & & \varepsilon^{T}_{r11}\end{bmatrix} \tag{45}$$

The following APDL code was used to input the relative dielectric constants into their ANSYS matrix:

```
TB,DPER,3,,,1
TBDATA,1,EP11_t   !AT CONSTANT STRESS
TBDATA,2,EP33_t
TBDATA,3,EP11_t
```

The following APDL code was used to input the piezoelectric material's density into the ANSYS model:

```
MP,DENS,3,dens_p
```

APPENDIX 3

Cymbal device before fabrication

APPENDIX 4
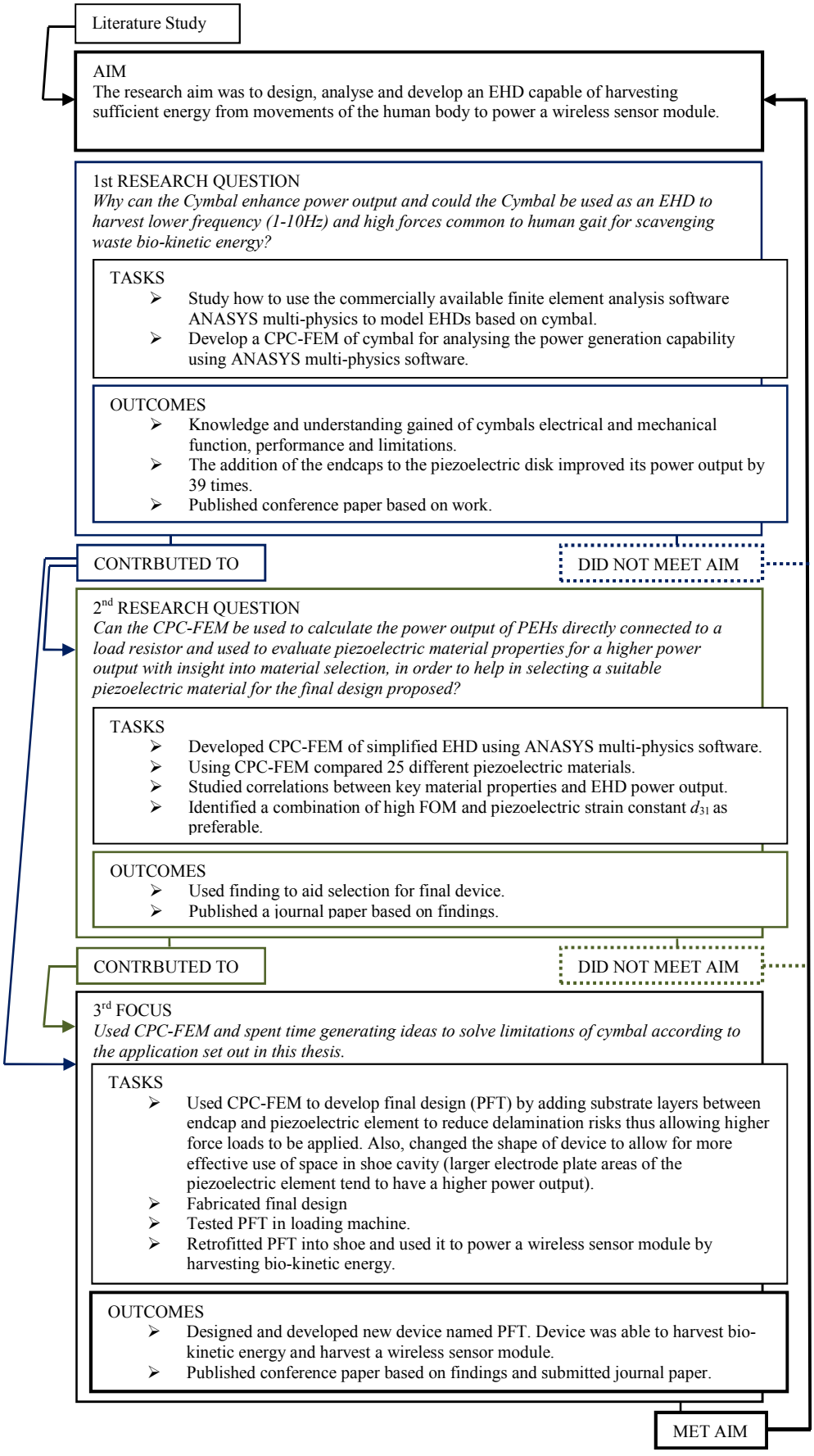
Methodology